STUDIES OF CHARGE TRANSFER AT SEMICONDUCTOR/LIQUID JUNCTIONS

Thesis by

Katherine Elizabeth Pomykal

In Partial Fulfillment of the Requirements

for the Degree of

Doctor of Philosophy

California Institute of Technology

Pasadena, California

1998

(Submitted September 23, 1997)

Acknowledgements

Acknowledgement #1: There is no possible way I will remember everyone I should thank for getting me through the last four years, so I apologize in advance to anyone I forgot in the list below. I'm sure you all remember or will experience the feeling, as Janet once told me, that you "don't have two brain cells left to rub together" while finishing your degree, so I'm sure you will forgive the omission. Caltech should have people send in their acknowledgements a year after they graduate so these things don't happen.

Acknowledgement #2: Even if I do remember all you that you did for me, if I put everyone's name in here, the acknowledgements will be longer than my thesis. So just because your name became part of "...and others," doesn't mean I appreciate what you did for me any less. Thanks.

Now to get (somewhat) more serious, I'll start by thanking people who helped me on a professional level. First and foremost, without Dr. John Reynolds at Lawrence Livermore National Laboratory I never would have ended up doing chemistry research, and without Dr. Michael Sailor at UC San Diego I never would have ended up in Nate's group at Caltech. Therefore, Mike and John deserve all the credit (or blame, depending on my mood) for getting me here in the first place. Both of them were great and caring advisors, and Mike especially has continued to give me helpful advice on dealing with various aspects of life. Working (and playing) with the Sailor group has been one of the most fun periods of time in my life.

This is not to say I haven't also worked with a terrific bunch of people in the Lewis group. I've always been thankful that we have maintained a good group dynamic throughout the coming and goings of postdocs and graduate students, and I have interacted with many intelligent, creative, and fun people during my time here. Special thanks go to Arnel Fajardo, who co-authored two papers with me, and to Geneviève Sauvé and George Coia, my present collaborators. These people helped tremendously with constructive

criticism, experimental data, and useful discussion. Although many people have offered good insights and helped in revising proposals and manuscripts, I'd like to also single out Gary Shreve and Rob Rossi as two people I could always count on to look at my work thoroughly and gently but honestly point out all the strengths and weaknesses. I'd also like to especially thank William Royea for always keeping us entertained with stories of his exploits--there's never a dull moment when Will is around.

One of the hardest parts in writing one's acknowledgements seems to be what to say about your thesis advisor. For me, no matter how frustrated I get with Nate sometimes, he has always come through when I really needed him to. I'd also like to echo the sentiment of many former students that working in this group definitely teaches one how to be a good scientist. Any paper coming out of this group is written to withstand the highest standards of scientific rigor, and most of the time we are more critical of ourselves than anyone else would be, which is as I think things should be.

Of course, most of us need to get out of the lab sometimes to keep our sanity (or at least find insanity in other ways). Fortunately, I have had many people throughout the years who have helped me keep perspective. Thanks to all who have pounded the pavement with me, especially my fellow marathon training partners Dave Liberles, Aimee Wyatt, and Doug Sutton. A special thanks to Michelle Parks, who not only dragged me on enough long runs to eventually convince me to try marathoning, but was also a good friend and confidante during the long hours on the roads as well as at other times. A special thanks also to "honorary runner" Tom Dakan, who provided music and entertainment while biking with us and kept Michelle and me going on those 26-milers.

The Caltech Masters Swim Team has also provided some much-needed diversion from graduate school, and I'd like to thank all of the members. Before mentioning any teammates names, however, I have to thank Chris Kenyon for getting me riled up enough to get back in swimming shape in the first place. If he hadn't insulted me that day, I might

have never gotten to know a great group of people. I especially want to express my gratitude to my coach, Kenny Grace, for his caring, and to Dan and Lori Stein, without whom I might have been homeless my last month of graduate school. Kenny can put a smile on anyone's face no matter how bad one's mood is, and I can't express my thanks enough to Dan and Lori for letting me impose on them. Thanks also to Jordan Kaplan, who was an inspiration to us all and whose life inspires me still.

Last, but certainly not least, I want to thank my friends and family not already mentioned above. Along with Michelle, Janet Kesselman was one of my best friends in graduate school, as well as a fellow UCSD and Lewis group alumna. Thanks for all the lunchtime talks and weekend expeditions. Andy and I were also lucky enough to have several family friends in the So. Cal. area; thanks to them for providing a "home away from home" several times a year. I have also been incredibly fortunate to be blessed with two wonderful and supportive sets of parents; my own, Tom and Karen Nelson, as well as my in-laws Glenn and Glynice Pomykal who treat me like their own daughter. I'd also like to thank my little sister Carolyn for entertaining me with her various trials and tribulations; even though she has had almost as many exploits as Will, I'm still proud of her. My sisters-in-law and their families also treat me like one of the family, and thanks to Susan and Carey for being "big sisters." Most importantly, a million thanks to the most vital person in my life, my husband Andy, without whom I would be completely lost. His love and support has meant everything to me.

Abstract

Steady-state current-voltage measurements on two types of semiconductor/liquid junction solar cells are presented. Results of these and other experiments on single-crystal electrodes are discussed in terms of present kinetic theory on charge transfer at these junctions.

Nanoporous titanium dioxide electrodes have been sensitized with a series of dyes with varying ground state reduction potentials. The spectral response and current-voltage properties of these electrodes have been measured. The trends can be explained by the differences in absorption spectra and ground state potentials. The effect of pH on the conduction band edge position of nanoporous titanium dioxide has been examined through current-voltage measurements and luminescence studies on dye-sensitized electrodes. The results are discussed in the framework of current theories on increasing efficiency of these electrodes. Studies involving charge separation at the back electrode contact were also performed.

Predictions of the Marcus/Gerischer theory for photoelectrode stability have been investigated experimentally for n-Si/CH_3OH photoelectrochemical cells. Specifically, a semiconductor electrode is predicted to be more stable if the reorganization energy of the stabilizing agent is decreased (in the normal region of the Marcus behavior), thereby increasing the rate of minority carrier capture by the stabilizer. This prediction was quantified experimentally by monitoring the branching ratio between two competing reactions at a semiconductor/liquid interface. The experimental observations can be consistently explained through this predicted influence of the minority carrier acceptor reorganization energy on the interfacial charge transfer rate constant.

Interfacial charge transfer rate constants at indium phosphide/liquid junctions were investigated using current density-potential and differential capacitance-potential methods. The measured electron transfer rate constants, k_{et}, for these systems were $\approx 10^{-16}$ cm^4 s^{-1},

in excellent agreement with previous theoretical predictions. Contacts which did not display bimolecular kinetic behavior still yielded upper bounds on the charge transfer rate constants, which were also consistent with limits predicted by theory. The current density-potential behavior of n-InP and p-InP/$Fe(CN)_6^{3-/4-}$(aq) junctions was also examined in order to assess the validity of prior kinetic measurements on these interfaces.

Table of Contents

List of Schemes and Figures

Chapter 3.

Chapter 4.

Chapter 5.

List of Tables

Summary

Since Fujishima and Honda published their work on titanium dioxide as a photoanode in water in 1975, much interest has been generated in the field of semiconductor/liquid junctions as a useful source of energy. Semiconductor/liquid junction technology is also important in the electronics industry in terms of etching and other chemical processing steps. These junctions have also shown promise in photocatalytic applications such as toxic waste remediation and in sensor applications. A fundamental understanding of the chemistry at these junctions is thus vital for a number of technological areas. This thesis examines steady-state charge transfer at semiconductor/liquid junctions and uses experimental data to evaluate existing theory on charge transfer rate constants. Chapter 1 will present a general overview of semiconductor/liquid junction technology and some background on electron transfer theory at these junctions.

The basic organization of this thesis was developed to move from more qualitative studies to quantitative measurements of charge transfer rate constants. One fairly new approach to solar energy conversion is the use of highly porous, dye-sensitized electrodes. Grätzel and others have reported efficiencies of up to 10% with titanium dioxide electrodes of this type. However, this field is still in comparatively early stages and many gaps remain in understanding the behavior of these cells. Due to the complexity of this system, many of its properties cannot be directly correlated to those of the more typical single-crystal semiconductor/liquid junctions and must be looked at separately. Some of these characteristics will be examined in Chapter 2. Systematic studies are described regarding changing the ground state reduction potential and central metal of the dye molecule, as well as examining the pH dependence of the current-voltage behavior of the cells. The spectral response and current-voltage properties of electrodes modified with a series of dyes are compared. The trends can be explained by the differences in absorption spectra and ground state potentials. The effect of pH on the conduction band edge position of nanoporous

titanium dioxide has been examined through current-voltage measurements and luminescence studies on dye-sensitized electrodes. The results are discussed in the framework of current theories on increasing efficiency of these electrodes. Studies involving charge separation at the back electrode contact were also performed.

Chapters 3-5 involve single crystal electrodes in contact with non-aqueous solutions. Theoretical analyses of charge transfer rates have been published on these systems, but until recently little experimental data was available to evaluate the theory. In Chapter 3, the dependence of the hole transfer rate constant from the semiconductor to the liquid is examined as a function of the reorganization energy of the electron donor in solution. An n-type semiconductor electrode is predicted to be more stable to passivation or corrosion reactions if the reorganization energy of the electron donor is decreased (in the normal region of the Marcus behavior) because the rate constant for hole transfer to the desired electron donor is increased. This prediction was quantified experimentally by monitoring the branching ratio between two competing reactions at a semiconductor/liquid interface: hole transfer from a Si photoanode to the electron donor in solution vs. passivation of the Si photoanode through hole transfer to water. Dimethylferrocene (Me_2Fc), ruthenium(II) pentaammine 4,4'-bipyridine ($Ru(NH_3)_5(4,4'\text{-bipy})^{2+}$), and cobalt(II) *tris*(2,2'-bipyridine) ($Co(2,2'\text{-bipy})_3^{2+}$) were used as electron donors because of their very similar standard electrochemical potentials but varying solvent reorganization energies. Also, charge transfer with these species is known to proceed by an outer-sphere mechanism and none of these donors adsorb to the electrode surface. At constant electron donor concentration, constant driving force for reaction, constant photocurrent density, and constant water concentration in CH_3OH, the stability of n-Si photoelectrodes decreased in the order $Me_2Fc^{+/0}$>$Ru(NH_3)_5(4,4'\text{-bipy})^{3+/2+}$>$Co(2,2'\text{-bipy})_3^{3+/2+}$. This observation can be consistently explained through the theoretically predicted influence of the minority carrier acceptor reorganization energy on the interfacial charge transfer rate constant.

In Chapters 4 and 5, electron transfer rate constants are compared with the maximum possible rate constant predicted by theory. Chapter 4 contains some modifications of the original theory and upper limits on the electron transfer rate constant measured experimentally. Theoretical expressions for the charge transfer rate constant at a semiconductor/liquid junction have been modified to include the effects of adiabaticity and the existence of a Helmholtz layer at the solid/liquid interface. These expressions have yielded an estimate of the maximum interfacial charge transfer rate constant, at optimal exoergicity, for a semiconductor in contact with a random distribution of non-adsorbing, outer-sphere redox species. An experimental upper bound on this interfacial charge transfer rate constant has been obtained through the determination of key energetic and kinetic measurements for stable semiconductor electrodes in contact with outer-sphere redox species. The upper limits for the interfacial charge transfer rate constant at several semiconductor/liquid contacts were found to be consistent with the upper limits predicted by theory. The current density-potential behavior of n-InP and p-InP/$Fe(CN)_6^{3-/4-}$(aq) junctions was also examined and compared to the behavior of stable, non-aqueous InP photocells in order to assess the validity of prior kinetic measurements on these interfaces.

Chapter 5 describes quantitative measurements of electron transfer rate constants at n-type indium phosphide/methanol junctions and relates these results to the theory. Steady-state methods are used to measure interfacial electron transfer rate constants at n-type indium phosphide/liquid junctions which displayed bimolecular kinetic behavior in which the observed current density was first order in the concentration of electrons at the semiconductor surface and in the concentration of acceptors in the solution. Differential capacitance-potential measurements were used to determine the energetics for the charge transfer process as well as to determine the concentration of electrons at the semiconductor surface as a function of applied potential. These measurements also indicated that the voltage dropped across the semiconductor space charge region varied ideally with the

change in cell potential. The measured charge transfer rate constants, k_{et}, for these systems were $\approx 10^{-16}$ cm^4 s^{-1}, in excellent agreement with previous theoretical predictions.

Chapter 1:
Basics of Semiconductor/Liquid Junctions

I. Introduction

Charge transfer processes at semiconductor/liquid interfaces are the fundamental steps in developing efficient photoelectrochemical energy storage systems,[1-5] chemical sensors,[6,7] selective photoelectrochemical etching systems,[8,9] and photocatalytic degradation processes for toxic waste remediation.[10-15] Although electron transfer between fixed donor-acceptor species in solution[16-19] and at metal electrodes[20-24] has been well-characterized, relatively little comparison between theory and experiment is available for charge transfer processes involving semiconductor electrode surfaces.[25-32] This lack of information can largely be ascribed to difficulties involved in rigorously controlling the chemical composition of semiconductor electrode surfaces, difficulties in developing measurement methods that are sensitive to the desired interfacial charge transfer kinetic processes, and difficulties in identifying electrode/electrolyte combinations that would allow an unambiguous comparison between experimental measurements and theoretical predictions.[1-4,25-44] Despite these problems, this area has attracted considerable attention by both theoretical and experimental chemists[26,29,30,32,45-50] because of the importance of understanding these processes, and because understanding how different variables affect the charge transfer rate constant could also provide insight into solid-state semiconductor contacts.

This chapter will provide a background in current theory on semiconductor-liquid interfaces in the context of solar energy conversion. Since Chapters 3-5 deal with predictions involving charge transfer rate constants, a general discussion of theoretical treatments of the rate constant will also be included here. Specific aspects of such theories will be left to the chapters pertaining to them. An alternate approach to solar energy conversion which will be introduced here will be more thoroughly examined in Chapter 2.

The basic problem in semiconductor/liquid junction solar cell technology is the trade-off between stability and conversion efficiency. Semiconductors such as silicon, indium phosphide, and gallium arsenide have small bandgaps which overlap well with the

terrestrial solar spectrum but are unstable in water. Wide bandgap semiconductors such as titanium dioxide are stable in aqueous solutions but do not absorb visible light, resulting in very low terrestrial conversion efficiencies. There are two approaches to overcoming these problems: extending the absorption spectrum of semiconductors such as titanium dioxide to better match the terrestrial solar spectrum, or finding a way to stabilize semiconductors such as silicon in solution. This thesis examines aspects of both approaches to semiconductor/liquid junction energy conversion.

One approach to solar energy conversion is to sensitize wide bandgap semiconductors with dyes which absorb visible light. Early attempts to do this with single-crystal electrodes were not very successful because one monolayer of dye proved insufficient to absorb much of the incident light,[51,52] while multiple layers of dye resulted in self-quenching of the dye and inefficient injection.[53] To overcome these problems, high-surface area electrodes were used instead of single-crystals. In this way, one monolayer of dye can absorb most of the incident light while still achieving efficient electron injection. Grätzel and others have had a great deal of success in this area using high-surface area titanium dioxide electrodes.[54] Using nanoporous TiO_2 electrodes in conjunction with ruthenium-based dyes, efficiencies of up to 10% have been reported.[55] Although many papers have been published investigating such systems, answers to some fundamental questions remain unclear. Chapter 2 will address some of these issues.

One solution to the problem of stabilizing solar cells fabricated with small-bandgap semiconductors is to use non-aqueous electrolyte solutions. Although initial papers reported high resistive losses and low efficiencies,[56-58] optimizing solvent-electrolyte combinations and electrode configurations resulted in stable, efficient cells. Efficiencies of up to 14% have been reported for silicon electrodes in contact with methanolic solutions.[59] This approach is still not commercially viable due to the toxicity and cost of the solvents and electrolyte combinations used; however, these systems are ideal for study due to their simplicity. Single crystal electrodes can be manufactured with very low surface defect

densities and nearly perfect junctions with liquids are easily obtained, in contrast with solid-state junctions which are very difficult to make atomically perfect. Chapters 3, 4 and 5 discuss various aspects of charge transfer across these types of semiconductor/liquid junctions.

II. Theory

Many review articles[5,26,60-62] have been written on charge separation and recombination mechanisms at single-crystal semiconductor/liquid junctions; therefore this topic will be only briefly described here to clarify other areas of the theory. The traditional method by which semiconductor/liquid junctions create electrical power from light is illustrated in Scheme 1.1. Although this scheme and the following discussion describe the case of an n-type semiconductor, an analogous model is readily derived for p-type semiconductors. The electrochemical potential of the semiconductor before immersion is known as its Fermi level, $\mathbf{E}_f$, and is a function of the dopant density N_d. When the semiconductor is placed in contact with a liquid containing a redox-active species of Nernstian potential $E(A/A^-)$, the electrochemical potentials of the two phases must equilibrate. The potential drop required to attain this equilibrium develops primarily across the semiconductor, in which dopant atoms are ionized. The resulting electric field separates photogenerated carriers, directing charges of opposite sign in opposite directions.

Although photogenerated electrons are driven away from the surface by the electric field described above, there are always a finite concentration of electrons at the surface of the semiconductor, given by a Boltzmann exponential term. These electrons have sufficient driving force to cross the interface into the solution despite the electric field present; thus, the rate constant for this process is very important to the overall efficiency of the junction. Very rapid majority carrier charge transfer is undesirable for photoelectrochemical devices, since rapid collection of majority carriers (electrons in the case of n-type semiconductors) by species in solution would result in significant recombination of charge carriers and would thus limit the efficiency of a photoelectrochemical energy conversion device.

However, very slow capture of minority carriers (holes) is also undesirable, because any appreciable current would require a large overpotential and would result in wasteful voltage losses in the cell. For these reasons, an understanding of both majority and minority charge transfer rate constants at these interfaces is essential. An understanding of the factors affecting interfacial charge transport processes should also allow design of systems that kinetically direct charge carriers in the solid to react with the desired redox molecules in the solution, thereby improving electrode stability and decreasing deleterious electrode passivation or corrosion reactions.

For charge transfer processes between molecular donor and molecular acceptor reagents in homogeneous solution, the theoretical behavior predicted by Marcus has been widely verified by experiment.[16-19] In addition, data on metal electrodes have yielded insight into heterogeneous charge transfer processes.[20-24] In contrast, relatively little linkage between theory and experiment has been attained for delocalized carriers in a semiconducting solid transferring into localized, molecular acceptors in a liquid electrolyte.[25-32]

Recent theoretical treatments of charge transfer processes at semiconductor/liquid interfaces have yielded expressions for the electron transfer rate constant, k_{et}, between a charge carrier in the semiconductor and an outer-sphere redox species in the electrolyte.[29,46] Starting with Marcus' treatment of liquid-liquid interfaces,[63] and modifying the result to describe the situation in which one species is a delocalized electron in the semiconducting solid and the other is an electron acceptor dissolved in homogeneous solution, yields:[29]

$$k_{et} = \nu_n \kappa_{el} \kappa_n \tag{1.1}$$

with

$$\kappa_{el} = \pi\left[\frac{2(r_A + r_e)}{\beta^3} + \frac{6}{\beta^4}\right] \tag{1.2}$$

and

$$\kappa_n = e^{-(\lambda_A + \Delta G^{o'})^2/(4kT\lambda_A)} \quad (1.3)$$

In this transition state theory description of the interfacial rate constant the attempt frequency, ν_n, is the relevant nuclear vibrational frequency, taken to be approximately 10^{13} s^{-1}. κ_{el} and κ_n are the electronic and nuclear factors, respectively. In the expression for κ_{el}, r_A and r_e are the effective radii of the acceptor in solution and of the electron in the solid, respectively, and β is the electronic coupling decay constant. In the nuclear term, λ_A is the total reorganization energy of the acceptor molecule, $\Delta G^{o'}$ is the free energy of reaction for the electron transfer, k is the Boltzmann constant, and T is the temperature. Similar expressions can be derived for hole transfer rate constants.

Some authors have criticized this approach and the upper limit on the charge transfer rate constant predicted by this theory.[64] A theoretical treatment which accurately predicts the rate constant is important due to interest in "hot" charge carrier transfer processes. Normally, even when an n-type semiconducting crystal is irradiated with light above the bandgap energy, the excited electrons thermalize to the energy of the conduction band edge before charge transfer can occur, resulting in a constant driving force for charge transfer with respect to the incident wavelength. "Hot" electrons would be able to transfer into solution before complete thermalization, potentially resulting in higher energy efficiencies.

Experiments are needed to test the predictive power of the Marcus theory approach as well as to validate or disprove any other theoretical treatments. Due to the difficulty in measuring these rate constants directly, many of the conclusions reached from earlier data in the literature are strongly dependent on interpretation. In the work described in this thesis, experiments were carefully designed to avoid the possibility of misinterpretation of the data. For the rate constant studies described in Chapters 3-5, single crystal electrodes

with very few surface defects were used in cells which were known to be stable over long time periods.

An alternate approach to solar energy conversion, developed by Grätzel,[54] is illustrated in Scheme 1.2. Unlike the systems described above, in which the photon absorption and charge separation all occur within the semiconductor, Grätzel's approach to the conversion of photons into electrical energy involves two distinct materials. An adsorbed dye absorbs photons to create electron-hole pairs, while titanium dioxide nanoparticles accept the excited state electron and separate them from the holes. Normally the counter electrode would be unable to efficiently regenerate the dye due to diffusion problems, so a redox couple is added to the solution to accept electrons from the counter electrode and reduce the dye to complete the circuit. Many aspects of the cell must be considered in order to optimize its performance. The dye's excited state must be sufficiently energetic to efficiently inject an electron into the TiO_2 conduction band, while the reduction potential of the solution species must be energetic enough to efficiently reduce the dye. Simultaneously, the dye must overlap closely with the solar spectrum, and the potential difference between the solution redox potential and the conduction band edge should be maximized for greater photovoltages.

A complicating aspect in studying these films is that due to the nanocrystalline character of the semiconducting electrodes, many of the equations used to describe single-crystal electrode systems are not easily applied to dye-sensitized TiO_2 systems. In a single-crystal system, the interface is clearly defined and is only two-dimensional. In contrast, the titanium dioxide/liquid junction is a randomly twisting, three-dimensional interface. The presence of two redox-active species, the dye and the redox couple in solution, also complicate kinetic analyses of these systems. Finally, the nanocrystals which make up the TiO_2 electrode are probably not large enough to support an electric field, so it is likely that transport of electrons through the film is driven by a concentration gradient. Due to the complex nature of these films, a detailed rate constant analysis will not be presented here,

but rather a more basic approach will be used to qualitatively describe charge transfer processes at the electrode surface.

Although the body of literature on dye-sensitized, nanocrystalline titanium dioxide is immense, many fundamental questions remain unanswered. The characteristics of the semiconductor/liquid junction can vary with the preparation of the TiO_2 colloids, the dye used, the pH of the electrolyte solution, humidity, and countless other details. Systematic changes in the dye and solution pH will be examined, while other variables such as water content and colloid preparation will be held as constant as possible.

Scheme 1.1: Charge separation at a semiconductor/liquid junction. Integrating the charge distribution caused by the ionization of dopant atoms with respect to position yields the electric field strength. A second integration yields the electric potential difference.

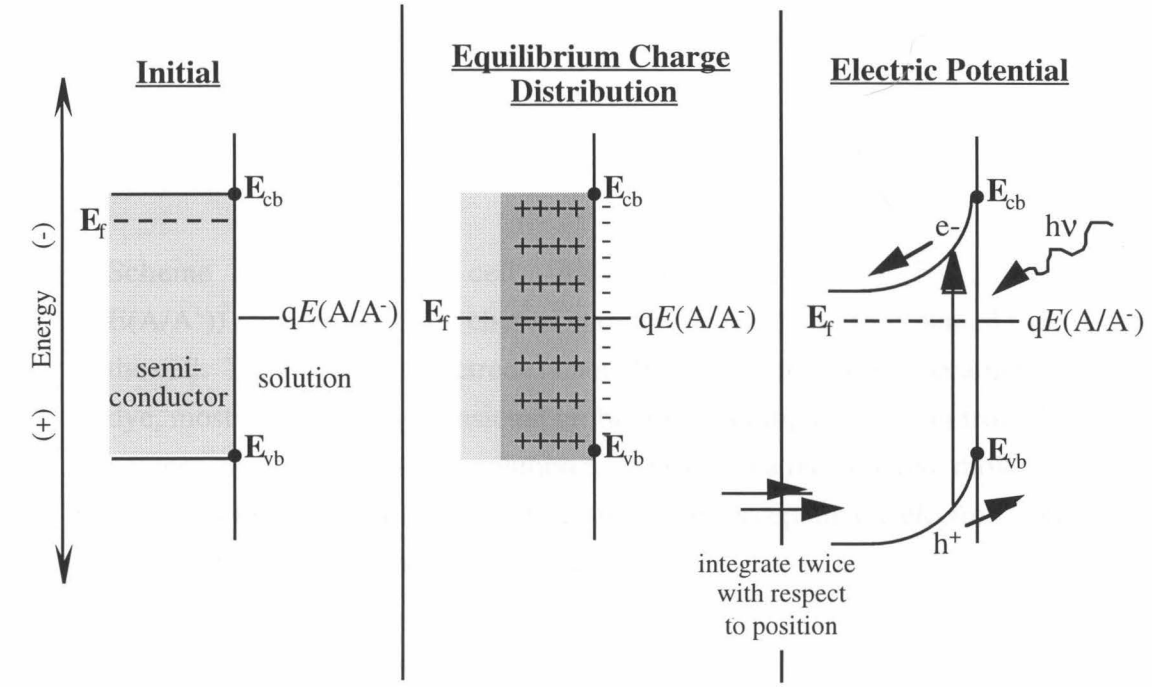
Initial
Equilibrium Charge Distribution
Electric Potential
Energy
(-)
(+)
E_{cb}
E_f
E_{vb}
$qE(A/A^-)$
semi-conductor
solution
e-
hν
h^+
integrate twice with respect to position

Scheme 1.1

Scheme 1.2: The Grätzel cell. All of the energy levels (Dye, Dye*, $E(A/A^-)$) must be carefully chosen in order for energy to be obtained from the cell. The Pt counter electrode is not efficient at directly regenerating the dye, most likely due to diffusional problems in getting an electron from the counter electrode across the solution to the dye, so a redox active molecule is needed in solution to act as an electron shuttle, accepting the electron from the counter electrode and regenerating the dye.

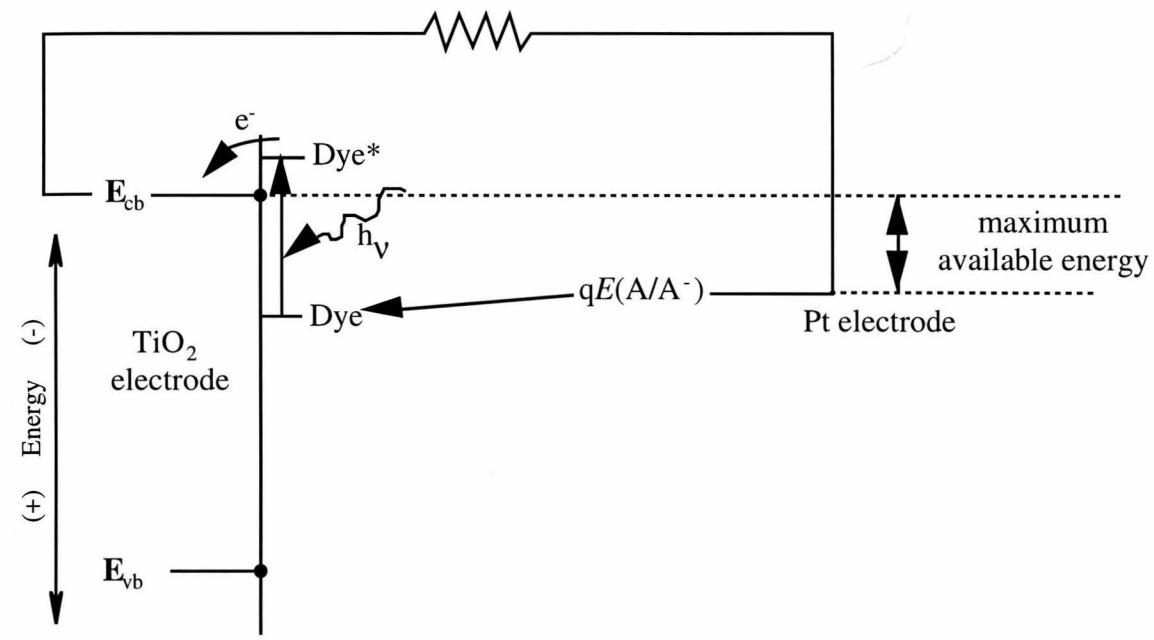
e-
Dye*
Ecb
hν
maximum
available energy
qE(A/A-)
Dye
Pt electrode
TiO2
electrode
(-)
Energy
(+)
Evb

Scheme 1.2

III. References

(1) Wrighton, M. S. *Acc. Chem. Res.* **1979**, *12*, 303.

(2) Rajeshwar, K. *J. Appl. Electrochem.* **1985**, *15*, 1.

(3) Parkinson, B. *Acc. Chem. Res.* **1984**, *17*, 431.

(4) Finklea, H. O. *Semiconductor Electrodes*; Elsevier: New York, 1988.

(5) Tan, M. X.; Laibinis, P. E.; Nguyen, S. T.; Kesselman, J. M.; Stanton, C. E.; Lewis, N. S. *Prog. Inorg. Chem.* **1994**, *41*, 21.

(6) Hafeman, D. G.; Parce, J. W.; McConnell, H. M. *Science* **1988**, *240*, 1182.

(7) de Rooij, N. F.; van de Vlekkert, H. H. In *Chemical Sensor Technology*; N. Yamazoe, Ed.; Kodansha, Ltd.: Tokyo, 1991; Vol. 3; 213.

(8) Elliott, D. J. *Integrated Circuit Fabrication Technology*; Mc-Graw Hill: New York, 1989.

(9) Kohl, P. A.; Ostermayer, F. W. *Ann. Rev. Mat. Sci.* **1989**, *19*, 379.

(10) Kormann, C.; Bahnemann, D. W.; Hoffmann, M. R. *Environ. Sci. Technol.* **1991**, *25*, 494.

(11) Pruden, A. L.; Ollis, D. F. *Environ. Sci. Technol.* **1983**, *17*, 628.

(12) Draper, R. B.; Fox, M. A. *Langmuir* **1990**, *6*, 1396.

(13) Fox, M. A. In *Photocatalysis and Environment: Trends and Applications*; M. Schiavello, Ed.; Kluwer Academic Publishers: Dordrecht, 1988; Vol. 237; 445.

(14) Minero, C.; Aliberti, C.; Pelizzetti, E.; Terzian, R.; Serpone, N. *Langmuir* **1991**, *7*, 928.

(15) Hidaka, H.; Nohara, K.; Zhao, J.; Serpone, N.; Pelizzetti, E. *J. Photochem. Photobiol. A: Chem.* **1992**, *64*, 247.

(16) Closs, G. L.; Calcaterra, L. T.; Green, N. J.; Penfield, K. W.; Miller, J. R. *J. Phys. Chem.* **1986**, *90*, 3673.

(17) McClendon, G.; Miller, J. R. *J. Am. Chem. Soc.* **1985**, *107*, 7811.

(18) Fox, L. S.; Kozik, M.; Winkler, J. R.; Gray, H. B. *Science* **1990**, *247*, 1069.

(19) Marcus, R. A.; Sutin, N. *Biochim. Biophys. Acta* **1985**, *811*, 265.

(20) Saji, T.; Yamada, T.; Aoyagui, S. *J. Electroanal. Chem. Interfacial Electrochem.* **1975**, *61*, 147.

(21) Saji, T.; Maruyama, Y.; Aoyagui, S. *J. Electroanal. Chem.* **1978**, *86*, 219.

(22) Miller, C.; Grätzel, M. *J. Phys. Chem.* **1991**, *95*, 5225.

(23) Chidsey, C. E. D.; Bertozzi, C. R.; Putvinski, T. M.; Mujsce, A. M. *J. Am. Chem. Soc.* **1990**, *112*, 4301.

(24) Ravenscroft, M. S.; Finklea, H. O. *J. Phys. Chem.* **1994**, *98*, 3843.

(25) Morrison, S. R. *Electrochemistry at Semiconductor and Oxidized Metal Electrodes*; Plenum: New York, 1980.

(26) Koval, C. A.; Howard, J. N. *Chem. Rev.* **1992**, *92*, 411.

(27) Memming, R. *Ber. Bunsenges. Phys. Chem.* **1987**, *91*, 353.

(28) Gerischer, H. In *Physical Chemistry: An Advanced Treatise*; H. Eyring; D. Henderson and W. Yost, Ed.; Academic: New York, 1970; Vol. 9A; 463.

(29) Lewis, N. S. *Ann. Rev. Phys. Chem.* **1991**, *42*, 543.

(30) Bard, A. J.; Mirkin, M. V.; Horrocks, B. R. *J. Phys. Chem.* **1994**, *98*, 2739.

(31) Miller, B.; Menezes, S.; Heller, A. *J. Electrochem. Soc.* **1979**, *126*, 1483.

(32) Rosenwaks, Y.; Thacker, B. R.; Nozik, A. J.; Ellingson, R. J.; Burr, K. C.; Tang, C. L. *J. Phys. Chem.* **1994**, *98*, 2739.

(33) Colell, H.; Alonsovante, N.; Tributsch, H. *J. Electroanal. Chem.* **1992**, *324*, 127.

(34) Willig, F.; Eichengerger, R.; Sundaresan, N. S.; Parkinson, B. A. *J. Am. Chem. Soc.* **1990**, *112*, 2702.

(35) Albery, W. J.; Bartlett, P. N. *J. Electrochem. Soc.* **1981**, *128*, 1492.

(36) Ellis, A. B.; Bolts, J. M.; Kaiser, S. W.; Wrighton, M. S. *J. Am. Chem. Soc.* **1977**, *99*, 2848.

(37) Miller, R. J. D.; Kasinski, J. J.; Gomez-Jahn, L. A.; Min, L. *Springer Ser. Chem. Phys.* **1988**, *48*, 424.

(38) Heller, A. *Acc. Chem. Res.* **1981**, *14*, 154.

(39) Bard, A. J. *J. Phys. Chem.* **1982**, *86*, 172.

(40) Frank, S. N.; Bard, A. J. *J. Am. Chem. Soc.* **1975**, *97*, 7427.

(41) Rosenbluth, M. L.; Lewis, N. S. *J. Am. Chem. Soc.* **1986**, *108*, 4689.

(42) Lantz, J. M.; Corn, R. M. *J. Phys. Chem.* **1994**, *98*, 4899.

(43) Fischer, P. R.; Daschbach, J. L.; Richmond, G. L. *Chem. Phys. Lett.* **1994**, *218*, 200.

(44) Moser, J. E.; Grätzel, M. *Chem. Phys.* **1993**, *176*, 493.

(45) Marcus, R. A. *J. Phys. Chem.* **1990**, *94*, 1050.

(46) Gerischer, H. *J. Phys. Chem.* **1991**, *95*, 1356.

(47) Pomykal, K. E.; Fajardo, A. M.; Lewis, N. S. *J. Phys. Chem.* **1996**, *100*, 3652.

(48) Fajardo, A. M.; Lewis, N. S. *Science* **1996**, *274*, 969.

(49) Smith, B. B.; Nozik, A. J. *Chem. Phys.* **1996**, *205*, 47.

(50) Uhlendorf, I.; Reinekekoch, R.; Memming, R. *J. Phys. Chem.* **1996**, *100*, 4930.

(51) Matsumura, M.; Nomura, Y.; Tsubomura, H. *Bull. Chem. Soc. Jpn.* **1977**, *50*, 2533.

(52) Alonso, N.; Beley, V. M.; Chartier, P.; Ern, V. *Rev. Phys. Appl.* **1981**, *16*, 5.

(53) Eichberger, R.; Willig, F. *Chem. Phys.* **1990**, *141*, 159.

(54) O'Regan, B.; Grätzel, M. *Nature* **1991**, *353*, 737.

(55) Nazeeruddin, M. K.; Kay, A.; Rodicio, I.; Humphry-Baker, R.; Müller, E.; Liska, P.; Vlachopoulos, N.; Grätzel, M. *J. Am. Chem. Soc.* **1993**, *115*, 6382.

(56) Legg, K. D.; Ellis, A. B.; Bolts, J. M.; Wrighton, M. S. *Proc. Natl. Acad. Sci.* **1977**, *74*, 4116.

(57) Kohl, P. A.; Bard, A. J. *J. Am. Chem. Soc.* **1977**, *99*, 7531.

(58) Langmuir, M. E.; Hoenig, P.; Rauh, R. D. *J. Electrochem. Soc.* **1981**, *128*, 2357.

(59) Gibbons, J. F.; Cogan, G. W.; Gronet, C. M.; Lewis, N. S. *Appl. Phys. Lett.* **1984**, *45*, 1095.

(60) Lewis, N. S. *Acc. Chem. Res.* **1990**, *23*, 176.

(61) Lewis, N. S.; Rosenbluth, M. In *Photocatalysis: Fundamentals and Applications*; N. Serpone and E. Pelizzetti, Ed.; John Wiley & Sons: New York, 1989; pp 45.

(62) Nozik, A. J. *Ann. Rev. Phys. Chem.* **1978**, *29*, 189.

(63) Marcus, R. A. *J. Phys. Chem.* **1991**, *95*, 2010.

(64) Smith, B. B.; Halley, J. W.; Nozik, A. J. *Chem. Phys.* **1996**, *205*, 245.

Chapter 2: Steady-State Current-Voltage Characteristics of Dye-Sensitized Titanium Dioxide Electrodes: pH Dependence and Spectral Response

I. Introduction

One approach to the useful conversion of light into electrical energy is the use of wide bandgap semiconductors. These compounds tend to be more stable to air and water oxidation than small bandgap semiconductors such as Si, InP, and GaAs.[1] However, to overcome the poor overlap of wide bandgap semiconductors with the solar spectrum, electrodes made with these materials must be coated with dyes which absorb light in the visible region. Grätzel and others have had a great deal of success in this area using high-surface area titanium dioxide electrodes.[2-5] These systems consist of nanocrystalline titanium dioxide coated onto a conducting glass substrate, the adsorbed dye, a sacrificial electron donor to regenerate the dye, and a platinum counter electrode to reduce the electron donor (Scheme 2.1). When these nanoporous electrodes are sensitized with ruthenium-based dyes, efficiencies of up to 10% have been reported.[6] Although many papers have been published on various aspects of these systems,[5,7-9] answers to some fundamental questions remain unclear.

One possible complication arising from using particulate systems as electrodes is that the individual particles are too small to support an electric field.[5] Since this electric field provides the mechanism for charge separation in traditional solar cells, the high photocurrents and photovoltages observed in the dye-sensitized TiO_2 electrodes were initially surprising. As described in this work, studies were undertaken to determine why the electrons injected from the dye travel towards the conducting glass substrate to be collected. The current-voltage properties of the conducting glass substrate as well as of unsensitized TiO_2 electrodes were characterized in both LiI/I_2 and $Me_2Fc^{+/0}$ in an effort to explain the mechanism for charge separation in these systems.

Next, the synthesis of a series of dyes with varying ground state reduction potentials is reported. The choice of this particular series of dyes serves two purposes. First, by varying the ground state potential, a threshold value for the driving force necessary for the electron donor to regenerate the dye can be obtained. Also, by

synthesizing both the ruthenium and osmium analogs of each dye the effect of changing the metal can be examined. Since the singlet-triplet transition is not as forbidden in osmium complexes as in ruthenium, the osmium dyes have additional absorption bands at higher wavelengths.[10] If the excited electrons produced from these absorbed photons are still sufficiently energetic to inject into the TiO_2, higher photocurrents will be observed. This prediction will be explored through photocurrent-voltage measurements and spectral response data.

A third issue which will be addressed in this work is the effect of various additives on the current-voltage properties of these cells. Additives such as 4-methylmorpholine N-oxide (NMO) and t-butyl pyridine have been found to increase the open-circuit voltages and efficiencies of these electrodes.[6] One hypothesis put forward is that these compounds passivate surface states on the electrode, so that the dark current is decreased and electrode performance is enhanced.[6,11] Another explanation is that since both NMO and t-butyl pyridine can act as bases, these compounds change the effective pH of the solution, moving the band edges of the TiO_2 and changing the energetics of the junction. The present work attempts to differentiate between these two explanations by creating the same improvement using a non-coordinating base. Using Proton Sponge, a non-nucleophilic base, to control the solution pH, any change in the open circuit voltage should be solely the result of the change in pH, since it is unlikely that the Proton Sponge could passivate any surface states.

Scheme 2.1: The Grätzel cell. All of the energy levels (Dye, Dye*, $E(A/A^-)$) must be carefully chosen in relation to E_{cb} so that energy can be obtained from the cell. It has been shown that the Pt counter electrode is not efficient at directly regenerating the dye, most likely due to diffusional problems in getting an electron from the counter electrode across the solution to the dye, so a redox active molecule is needed in solution to act as an electron shuttle, accepting the electron from the counter electrode and regenerating the dye.

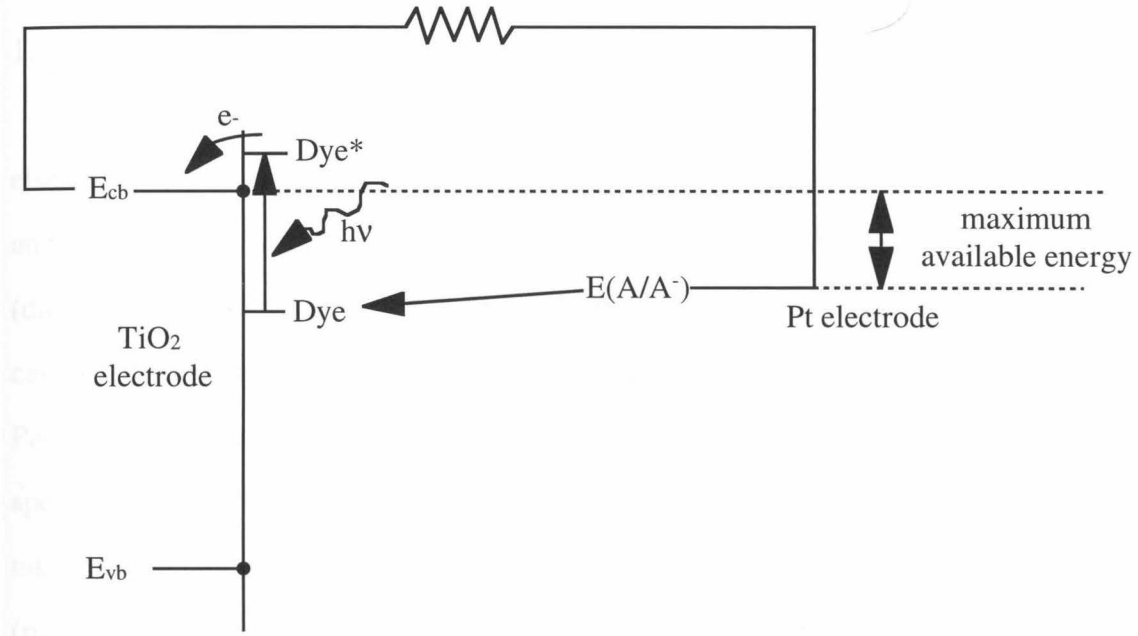
e-
Dye*
Ecb
hν
maximum
available energy
E(A/A-)
Dye
Pt electrode
TiO2
electrode
Evb

Scheme 2.1

II. Experimental Section

A. Materials

The performance of the nanoporous dye-sensitized electrodes has been found to be highly dependent on the method of preparation of the titanium dioxide as well as on the methods of synthesis and purification of the dyes. Therefore, although the electrode preparation used here is similar to that described elsewhere,[6,8] the procedure will be described in detail.

1. *Dye Characterization*

The synthesis and purification of the 8 dyes listed in Table 2.1 is described elsewhere.[12] These organometallic complexes were found to be pure by NMR analysis and elemental analyses for C, H, and N were within 0.4% for all dyes except Ru(4,4'-(dicarboxy)-2,2'-bipyridine)$_2$(CN)$_2$ for which the elemental analysis deviated from the calculated values by 0.6%. Absorption spectra of the dyes were obtained on a Hewlett-Packard Model 8452A Diode Array Spectrophotometer and are shown in Figure 2.1. The spectra for all dyes except the *tris*-[4,4'-(dicarboxy)-2,2'-bipyridine] (L') complexes were taken in ethanolic solutions containing 0.001 M/0.001 M pyridine/pyridinium triflate (py/pyH$^+$). Due to solubility constraints, the spectra for the OsL'$_3$ and RuL'$_3$ were obtained in ethanolic solutions of 0.010 M py$^+$.

2. *Electrodes*

The nanoporous electrodes consist of three distinct layers, where most of the thickness of the film resides in the middle layer, consisting of the TiO_2 colloid. For the other two layers, stock solutions were prepared by adding 0.100 M $TiCl_4$ to isopropanol or 2.00 M $TiCl_4$ to water with vigorous stirring. Once the initial fuming had stopped, these preparations resulted in clear solutions. The isopropanol solution was used as prepared, but immediately before use, an aliquot of the aqueous solution was diluted to 0.20 M.

The preparation of titanium dioxide colloidal solutions was based on the procedure of Smetana. First, 2.6 mL of concentrated nitric acid was added to 375 mL deionized

water. With vigorous stirring, 62.5 mL $Ti(OCH(CH_3)_2)_4$ was added slowly (~30 mL/min.), and a white precipitate formed. This solution was then stirred for 2 hours at room temperature and 8 hours at 80 ˚C to evaporate the propanol. The resulting sol was suction filtered through fine filter paper and then autoclaved at 200 ˚C for 12 hours in a sealed pressure vessel. The final solution was evaporated to a concentration of 160 g L^{-1} in TiO_2. To maintain porosity in the final film, Carbowax 20000 was added to a concentration of 40% weight equivalent of TiO_2 and the sol was stirred overnight. This colloid solution was stored and used as a stock solution for up to 2 months without significant change in electrode properties.

Electrodes were prepared by first depositing a layer of the isopropanol solution onto 3-mm thick glass coated with a conducting layer of F-doped SnO_2 (8-10 Ω/square, L.O.F.). The layer was evenly spread by pulling a glass slide across the surface of the electrode, where Scotch tape on either side of the electrode region acted as a spacer for the slide. After the isopropanol had evaporated, the colloid solution was spread onto the conducting glass in a similar fashion. Once this layer had dried, the electrodes were fired in a tube furnace under flowing air at 450 ˚C for 30 minutes. Once the electrodes had cooled, 100 mL of the freshly made aqueous solution was deposited on each electrode. After the electrodes were covered and allowed to sit overnight, the electrodes were rinsed with isopropanol. Sample electrode thicknesses were approximately 5 μm as measured by profilometry.

Immediately before dye adsorption, each electrode was fired a second time at 450 ˚C for 30 minutes. The electrodes were cooled to 100 ˚C and then were immersed in an ethanolic solution containing 0.0001-0.0005 M of the desired dye. The dye solution was buffered with 0.001 mM pyridine/pyridinium triflate (py/pyH^+). The electrodes were immersed in the dye for at least 4 hours before use in electrolyte solution. An absorption spectrum of each electrode was taken prior to use to quantify the amount of dye adsorbed.

3. *Redox Couples and Electrolytes*

Lithium iodide, iodine, Proton Sponge and pyridinium triflate were purchased from Aldrich. Pyridinium triflate was also synthesized from pyridine by acidification of a solution of pyridine in diethyl ether with triflic acid, and was dried under vacuum before use. Proton Sponge was stored in a nitrogen-purged drybox and was used as received. LiI was dried at 200 °C before use. Iodine and dimethylferrocene were sublimed under vacuum before use. Dimethylferrocenium was synthesized using the method of Hendrickson et al. and was dried under vacuum before use. Absolute ethanol was purchased from EM Science and used as received. Pyridine and acetonitrile were purchased from EM Science and distilled before use. The CH_3CN was distilled first over CaH_2 and then over P_2O_5. Stock solutions containing 0.500 M LiI/0.040 M I_2/0.001 M py/pyH^+ in CH_3CN were prepared for use with the TiO_2 electrodes. For pH studies, aliquots of this solution were added to solid Proton Sponge to yield the desired concentrations.

Initial experiments with TiO_2 electrodes showed poor reproducibility. It was hypothesized that variables such as water concentration and solution pH were affecting the current-voltage behavior of these electrodes, so care was taken to control these variables. All reagents and solutions listed above were stored in a nitrogen-purged box after purification. The pyridinium triflate and pyridinium were added to both the dye and electrolyte solutions in 0.001 M concentrations to maintain a constant initial pH. In pH studies, these buffered solutions were made more basic by adding Proton Sponge. Enough Proton Sponge was added so that the pyridine/pyridinium could no longer act as a buffer. All cells were constructed inside the nitrogen-purged box and sealed to avoid water contamination before being brought out of the box. These precautions led to greatly improved reproducibility.

Table 2.1: Ground state reduction potentials for the dyes used in this work. All values are referenced to a methanol SCE. Abbreviations for the dyes are as follows:

RuL'$_3$=tris(4,4'-(dicarboxy)-2,2'-bipyridyl)ruthenium(II) (hexafluorophosphate salt)

OsL'$_3$=tris(4,4'-(dicarboxy)-2,2'-bipyridyl)osmium(II) (hexafluorophosphate salt)

RuL$_2$L'=bis(2,2'-bipyridyl)(4,4'-(dicarboxy)-2,2'-bipyridyl)ruthenium(II)

OsL$_2$L'=bis(2,2'-bipyridyl)(4,4'-(dicarboxy)-2,2'-bipyridyl)osmium(II)

RuL'$_2$(CN)$_2$=*cis*-dicyanobis(4,4'-(dicarboxy)-2,2'-bipyridyl)ruthenium(II)

OsL'$_2$(CN)$_2$=*cis*-dicyanobis(4,4'-(dicarboxy)-2,2'-bipyridyl)osmium(II)

RuL'$_2$(NCS)$_2$=*cis*-di(isothiocyanato)bis(4,4'-(dicarboxy)-2,2'-bipyridyl)ruthenium(II)

OsL'$_2$(NCS)$_2$=*cis*-di(isothiocyanato)bis(4,4'-(dicarboxy)-2,2'-bipyridyl)osmium(II)

a: from ref. 13

b: from ref. 10

Dye	Reduction Potential (V vs. SCE)
RuL'_3	1.32[a]
OsL'_3	1.01
RuL_2L'	1.24
OsL_2L'	0.84
$RuL'_2(CN)_2$	1.04[b]
$OsL'_2(CN)_2$	0.78
$RuL'_2(NCS)_2$	0.80
$OsL'_2(NCS)_2$	0.42

Table 2.1

Figure 2.1a-h: Absorption spectra of the 8 dyes used in this work, in ethanolic solution.

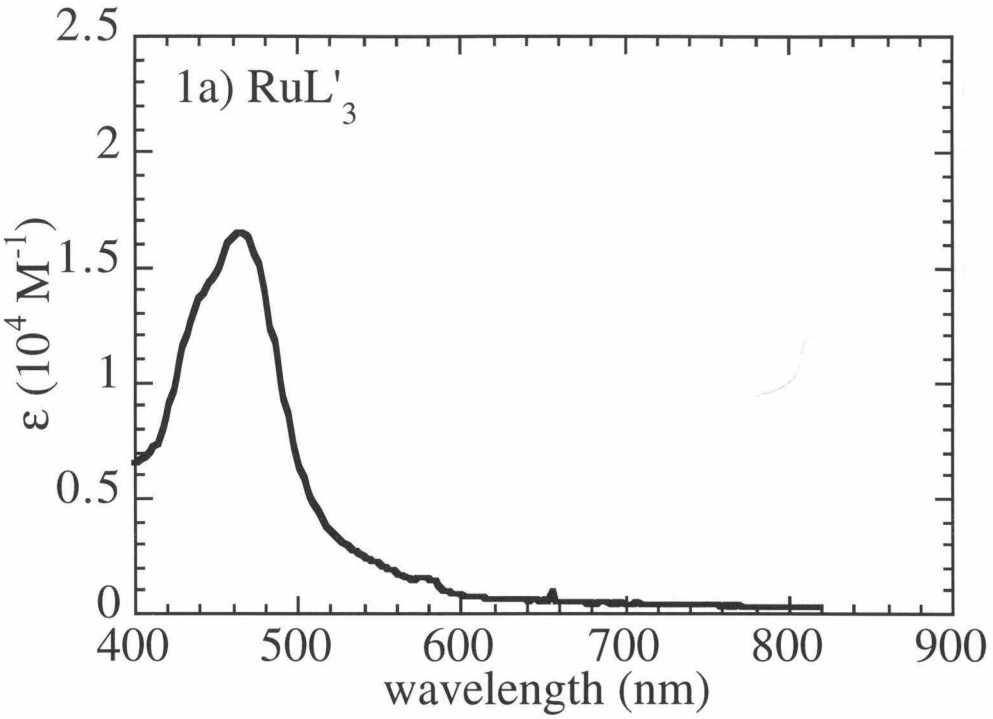
1a) RuL'3
ε (10^4 M^-1)
wavelength (nm)
2.5
2
1.5
1
0.5
0
400
500
600
700
800
900

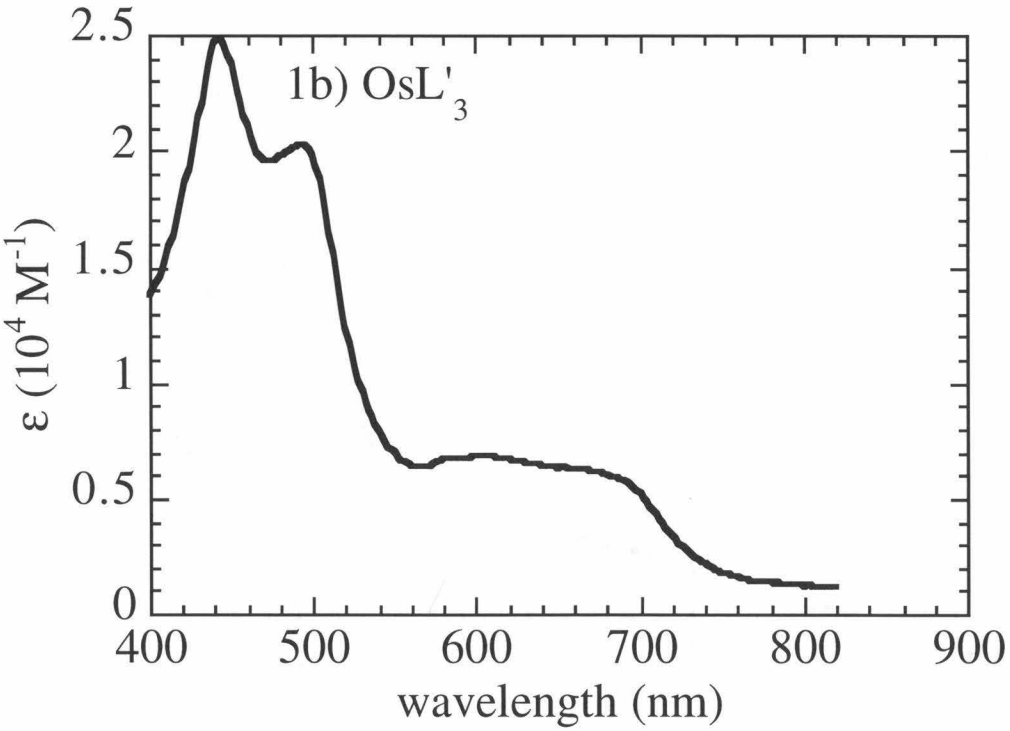
1b) OsL'3
ε (10^4 M^-1)
wavelength (nm)
2.5
2
1.5
1
0.5
0
400
500
600
700
800
900

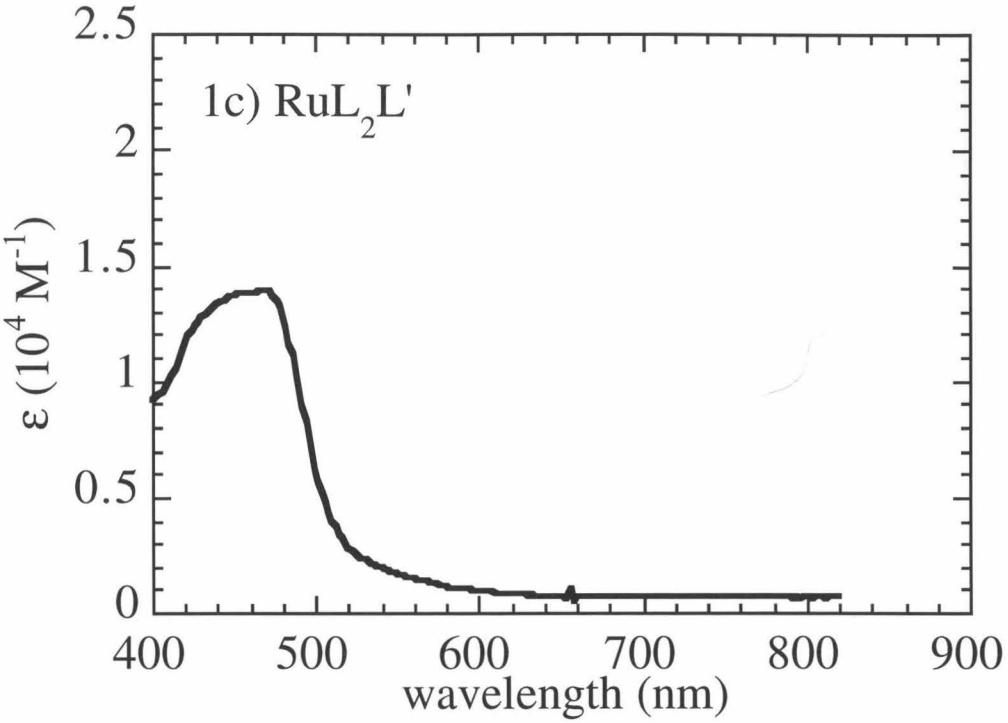
1c) RuL2L'
ε (10^4 M^-1)
wavelength (nm)
2.5
2
1.5
1
0.5
0
400
500
600
700
800
900

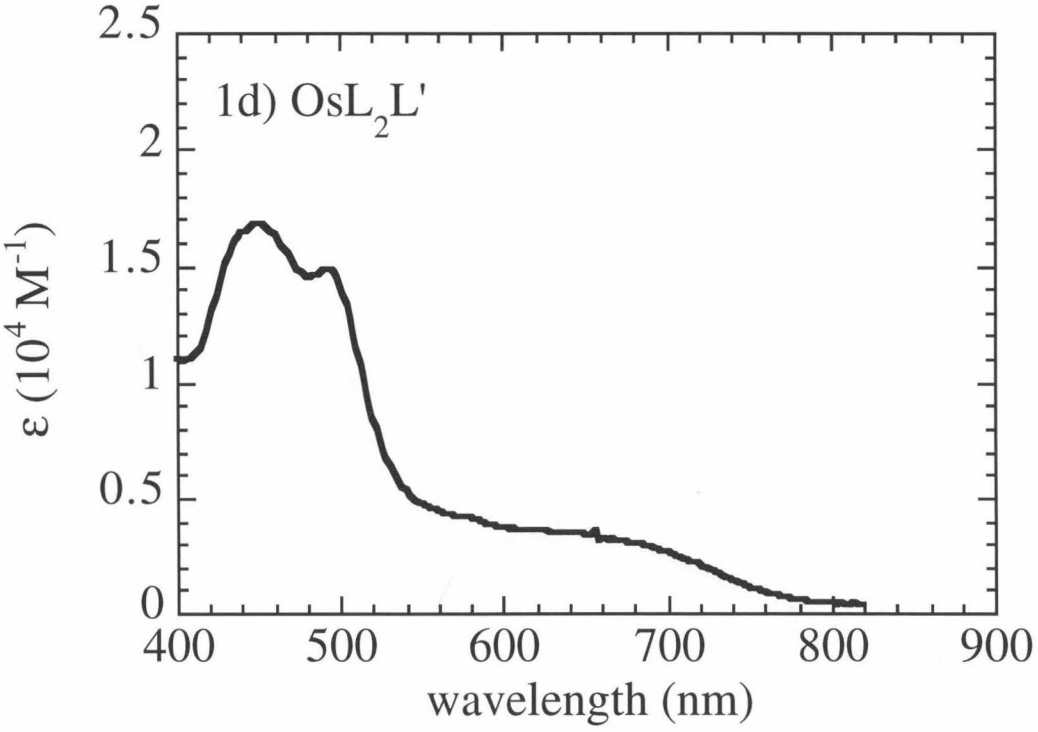
1d) OsL2L'
ε (10^4 M^-1)
wavelength (nm)
2.5
2
1.5
1
0.5
0
400
500
600
700
800
900

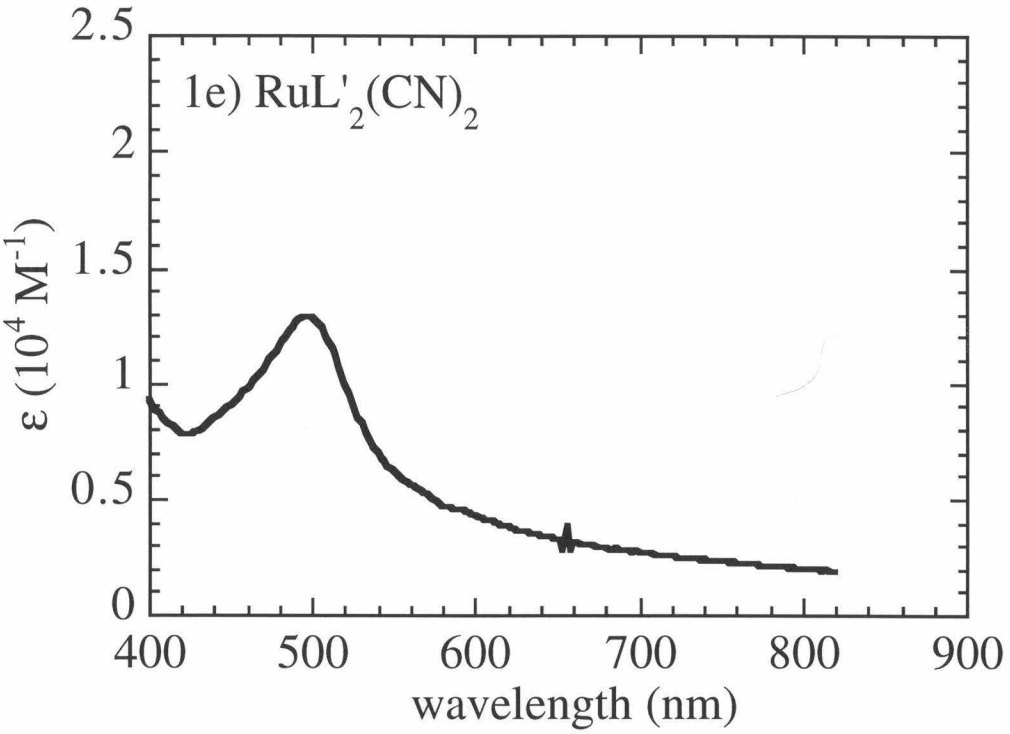
1e) RuL'2(CN)2
ε (10^4 M^-1)
wavelength (nm)
2.5
2
1.5
1
0.5
0
400
500
600
700
800
900

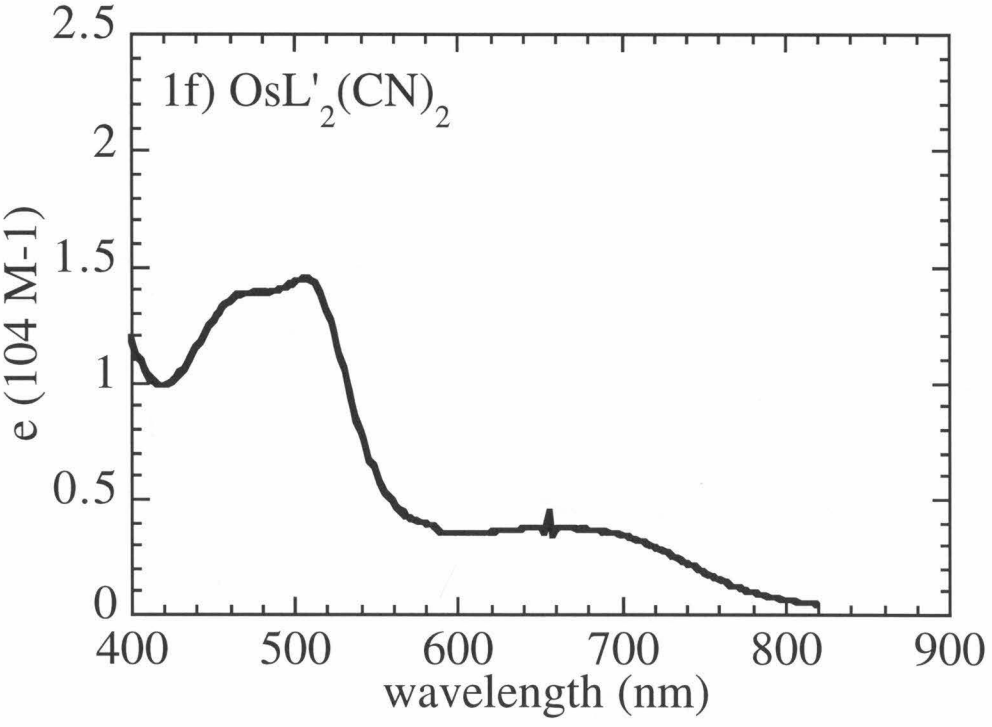
1f) OsL'2(CN)2
e (104 M-1)
wavelength (nm)
2.5
2
1.5
1
0.5
0
400
500
600
700
800
900

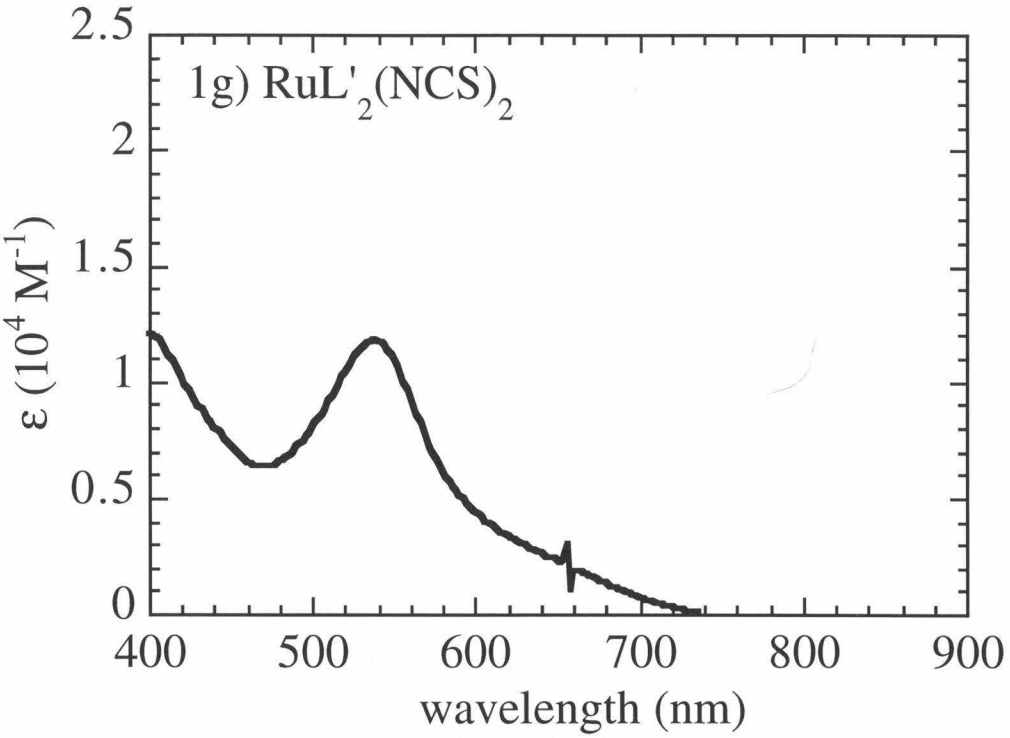
1g) RuL'2(NCS)2
ε (10^4 M^-1)
2.5
2
1.5
1
0.5
0
400
500
600
700
800
900
wavelength (nm)

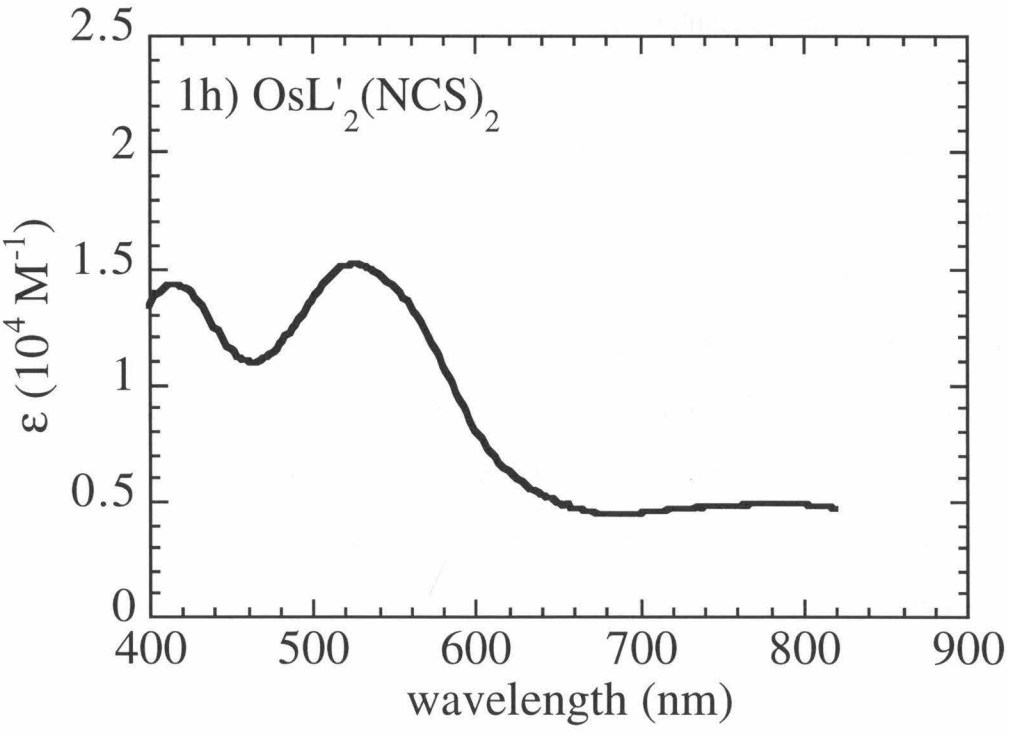
1h) OsL'2(NCS)2
ε (10^4 M^-1)
2.5
2
1.5
1
0.5
0
400
500
600
700
800
900
wavelength (nm)

B. Electrochemical Methods

The ground state reduction potentials of the 8 dyes, shown in Table 2.1, were obtained by cyclic voltametry. All measurements performed in this laboratory were done using an EG&G Princeton Applied Research (PAR) Model 172 Potentiostat in conjunction with a Houston Instruments Omnigraphic 2000 recorder. The cyclic voltametric experiments were done in methanol solutions containing 0.0005-0.001 M in the dye of interest except for the two dyes listed below. The ground state reduction potential of the $RuL'L_2$ dye was measured in acetonitrile. The reduction potential of the fully protonated RuL'_3 was measured by Spitler in aqueous solution.[13] All reduction potentials were referenced to a saturated calomel electrode (SCE).

Current density vs. potential experiments were performed using an EG&G Princeton Applied Research (PAR) Model 362 Potential Controller in conjunction with a Houston Instrument Omnigraphic 2000 recorder. Light intensities were controlled by the use of an ELH W-halogen bulb and were determined by use of a calibrated silicon photodiode (Solarex). A UV cutoff filter was used to avoid direct excitation of electrons in the titanium dioxide. All measurements were performed in a three-electrode potentiostatic set-up, with a Pt wire reference and Pt gauze counter electrode. The distance between the working and counter electrodes was approximately 2 mm and no stirring was performed.

Some dye-electrolyte combinations were found to require some equilibration time to reach a stable open-circuit voltage; therefore, all cells were allowed to equilibrate for at least 30 minutes after exposure to a new solution before data reported here were recorded. After exposure to Proton Sponge, electrodes were allowed to reequilibrate with the buffered I^-/I_2 solution for at least 2 hours. Although the current-voltage properties of these junctions remained stable while the cell was assembled, once the electrodes were removed from the iodine solution they tended to degrade. For this reason, fresh electrodes were used in all experiments.

Spectral response data was obtained by biasing the cell to short circuit and measuring the voltage output from the current monitor on the potentiostat. Monochromatic light was obtained from a Spex 1682A tungsten lamp in conjunction with a Spex 1681B monochromator with 1.25 mm slits. For the TiO_2 electrodes, the dark current tended to drift slightly over time, so the dark current was measured at each wavelength and subtracted from the photocurrent at that wavelength. The light intensity from a beam-split portion of the monochromator output was measured by monitoring the photocurrent at a Si photodiode from United Detector Technology. This diode thus served as a calibration of the lamp intensity. Quantum yields were obtained by placing a calibrated Si photodiode in the same position as the TiO_2 working electrode and measuring the photocurrent at short circuit, then correcting the data from the TiO_2. Current-voltage data at AM 1.0 illumination was obtained before and after each run. Electrodes which showed significant decreases in photocurrent ($\geq 5\%$) were viewed to be defective and were not included in the final analysis.

C. Luminescence Studies

Luminescence data was obtained from dye-sensitized electrodes immersed in a solution of CH_3CN containing 0.0010 M py/pyH^+ and 0 or 0.010 M Proton Sponge. Spectra were collected using a spectrofluorimeter consisting of a 150-watt xenon continuous-arc excitation source, two Spex 1618B Minimate monochromators, a Hamamatsu R955 photomultiplier detector and appropriate collecting and focusing optics. The excitation beam was pulsed at 1.0 kHz using a mechanical chopper, which allowed phase-sensitive detection of the PMT response. A National Instruments PC-LPM-16 interface card was used to provide A/D conversion and monochromator control via an Intel 80386-based computer. The slit widths of the excitation and emission monochromators were set to 2.5 and 1.5 mm, respectively.

Electrodes were positioned in the cell containing the solution, and the cell was rotated approximately 45° relative to both monochromators. The cell was then rotated

slightly away from 45° to avoid deflecting light from the excitation source directly into the PMT. Emission spectra were obtained first in solutions containing no Proton Sponge. First, one scan was taken and the peak intensity was noted. Ten scans were then signal averaged to reduce noise in the spectrum. A final scan was taken and the peak intensity was compared to the initial value to make sure there was no change over the course of the experiment. Then the solution was removed by pipette, taking care not to change the electrode position, and solution containing 0.010 M Proton Sponge was added. The electrode was allowed to equilibrate for 30 minutes and the above procedure was repeated. Finally, the Proton Sponge solution was removed and a new aliquot of the initial solution was added. The electrode was allowed to equilibrate for 2 hours and a third set of emission spectra was taken.

III. Results

A. Characterization of Unsensitized Electrodes

Current-voltage behavior in the dark for a nanoporous titanium dioxide electrode was first compared to the current-voltage behavior for a conducting glass electrode in a solution of LiI/I_2. As seen in Figure 2.2, both reduction and oxidation of the I_2/I^- couple require high overpotentials at the conducting glass electrode and very low currents are observed in either potential direction. In contrast, the TiO_2 electrode shows rectifying behavior and yields much higher dark currents in forward bias than the conducting glass alone. This behavior indicates that the success of this system may be due to the slow kinetics of electron transfer for iodine at the conducting glass surface. Because reduction and oxidation of iodine/iodide is sluggish at the back contact, negligible recombination losses are suffered. Then, since the titanium dioxide is rectifying at the I_2/I^- junction, a large photovoltage is attainable.

To further support this explanation for the success of these electrodes, a similar experiment was performed with $Me_2Fc^{+/0}$ as the redox couple in solution. This redox couple was chosen because the reduction potential of this couple is reasonably close to that

of the I_2/I^-. In this case, very high currents were observed in both potential directions at the conducting glass electrode, as seen in Figure 2.3. At the titanium dioxide electrode, similar behavior was observed. Although data is not shown here, dye-sensitized electrodes immersed in solutions of $Me_2Fc^{+/0}$ developed only low photovoltages and showed little photocurrent at short circuit. This behavior results because in this case, high recombination losses are present at the back contact. Therefore, the ideal redox couple in these cells must not only have the correct reduction potential for efficient regeneration of the dye, but also have slow kinetics at the conducting glass substrate.

Figure 2.2: Current-potential behavior for unsensitized electrodes in CH_3CN/0.040 M I_2/0.500 M LiI in the dark. Filled circles represent the data for the conducting glass used as a substrate for the TiO_2. Open circles show the data for a nanoporous TiO_2 electrode with no dye sensitizer.

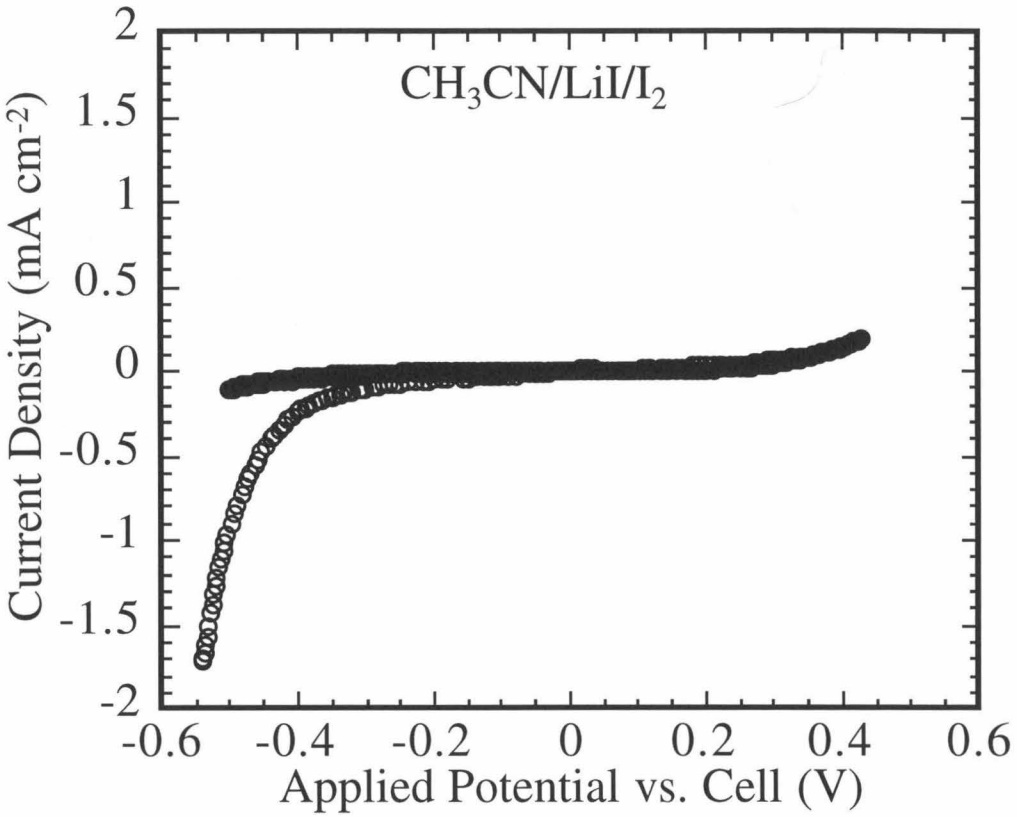
CH3CN/LiI/I2
Current Density (mA cm-2)
Applied Potential vs. Cell (V)
2
1.5
1
0.5
0
-0.5
-1
-1.5
-2
-0.6
-0.4
-0.2
0
0.2
0.4
0.6

Figure 2.2

Figure 2.3: Current-potential behavior for unsensitized electrodes in CH_3CN/(0.100 M/0.100 M) $Me_2Fc^{+/0}$/1.00 M $LiClO_4$ in the dark. Filled circles represent the data for the conducting glass used as a substrate for the TiO_2. Open circles show the data for a nanoporous TiO_2 electrode with no dye sensitizer.

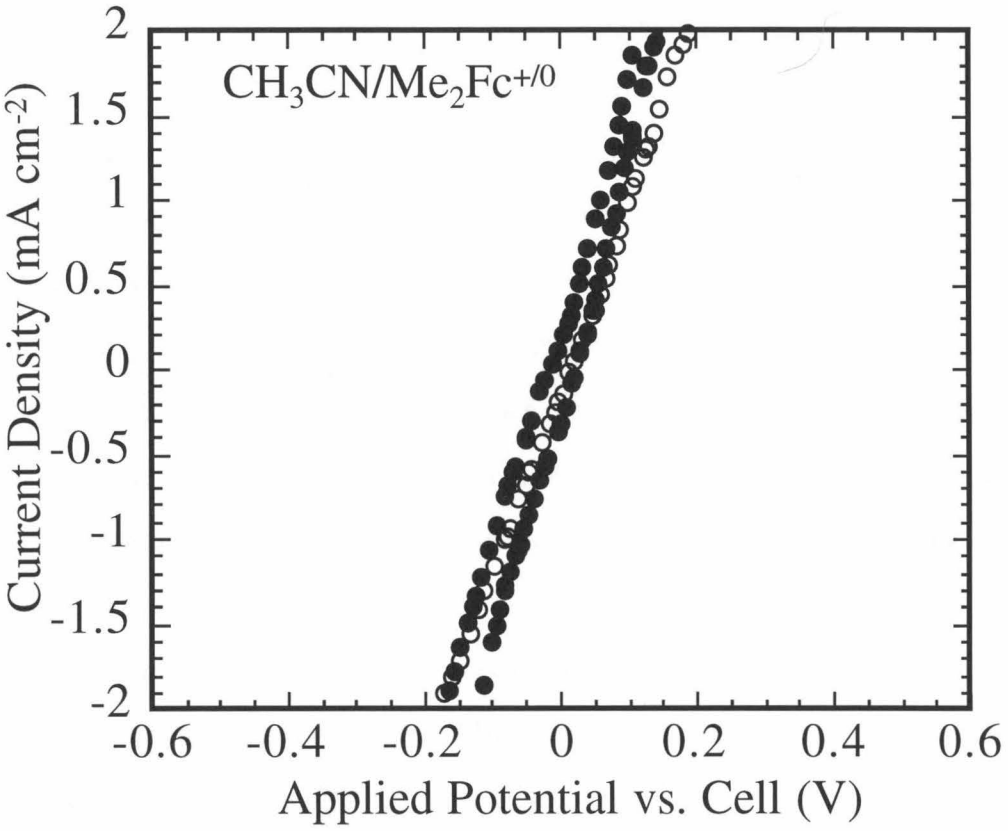
CH3CN/Me2Fc+/0
Current Density (mA cm-2)
Applied Potential vs. Cell (V)
2
1.5
1
0.5
0
-0.5
-1
-1.5
-2
-0.6
-0.4
-0.2
0
0.2
0.4
0.6

Figure 2.3

B. Spectral Response

Spectral response data for electrodes sensitized with the eight dyes characterized above are shown in Figure 2.4. These results can be explained fully by three coinciding factors. First, as expected, the spectral response roughly correlates with the absorption spectrum of each dye. Dyes which adsorb in lower concentrations such as the RuL'_3 and OsL'_3 showed lower current responses. The wavelength at which the maximum photocurrent was observed corresponded to the absorption maximum for each dye. To correct for differences in dye absorption, the spectral response data was divided by the absorption spectrum of the electrode used. The results are shown in Figure 2.5. In most cases, this procedure makes the response much more similar from dye to dye.

Second, within a given set of ligands, the osmium dyes showed much more photocurrent at higher wavelengths. This phenomenon is due to the weak band present in the absorption spectra of the osmium dyes which is not present in the ruthenium dyes and which likely arises due to the direct excitation of photons to triplet states in the osmium dyes. These transitions are more forbidden in the ruthenium analogs and thus low photocurrent is seen at these wavelengths.

The only response which cannot be explained by a combination of these two effects is that of electrodes sensitized with the $OsL'_2(NCS)_2$ dye. Electrodes sensitized with this dye show very high light absorption, yet these electrodes show very poor energy conversion. However, this effect can be explained by examining the ground state reduction potentials of the dyes. Of the dyes examined in this work, the $OsL'_2(NCS)_2$ has the least positive reduction potential and in fact is only 0.18 V positive of the I_2/I^- redox couple. It is likely, therefore, that the smaller driving force for regeneration of the dye limits the efficiency of this dye.

Figure 2.4a-h: Average spectral response for TiO_2 electrodes sensitized with one of the 8 dyes characterized above in CH_3CN/0.040 M I_2/0.500 M LiI/(0.001 M/0.001 M) py/pyH^+. IPCE represents the incident photon-to-electron conversion efficiency and is equivalent to the external quantum yield of the cell.

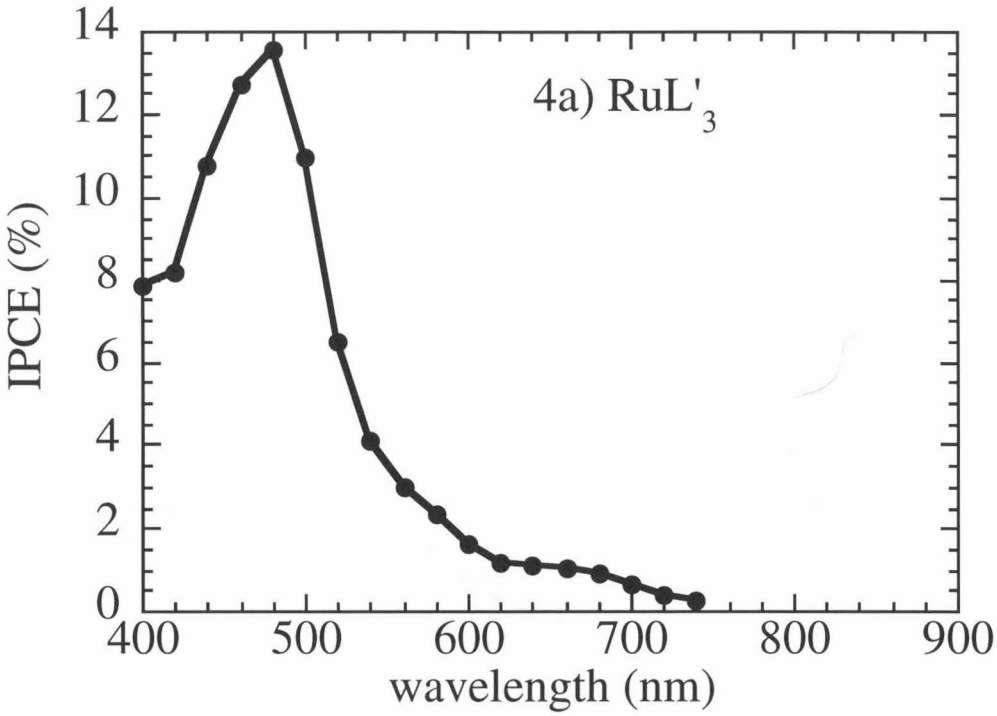
4a) RuL'3
IPCE (%)
wavelength (nm)
0
2
4
6
8
10
12
14
400
500
600
700
800
900

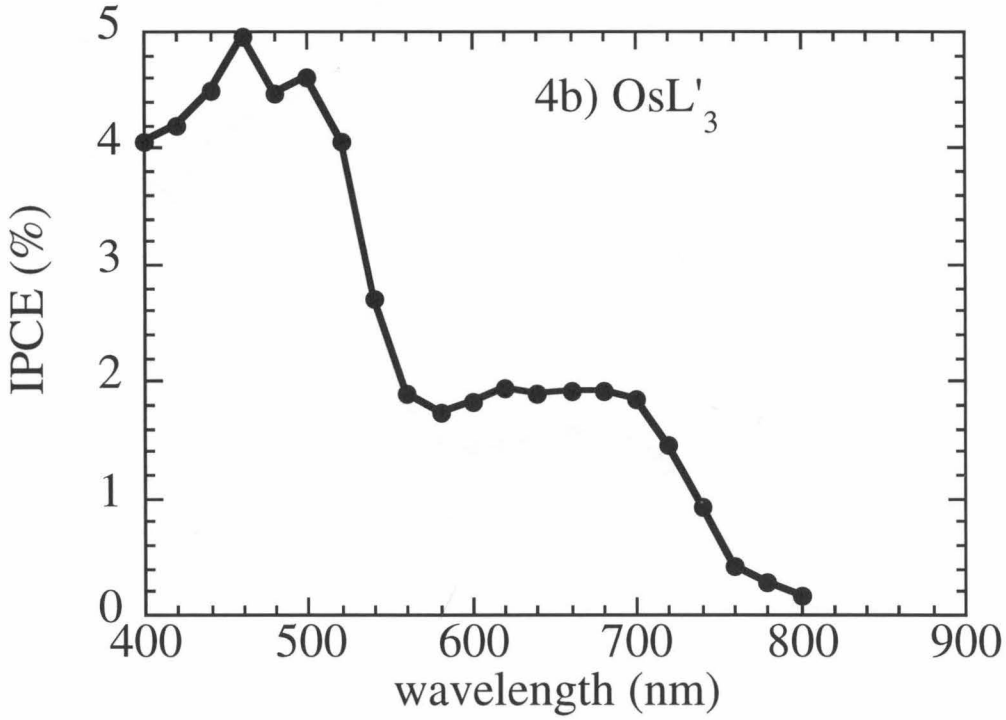
4b) OsL'3
IPCE (%)
wavelength (nm)
0
1
2
3
4
5
400
500
600
700
800
900

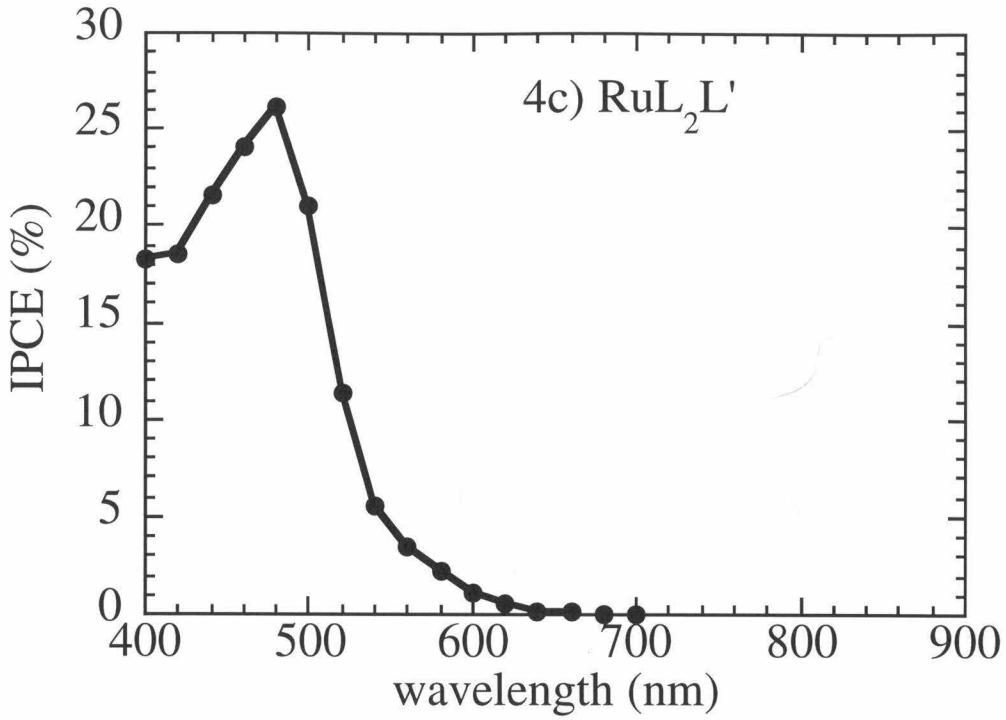
4c) RuL2L'
IPCE (%)
wavelength (nm)
0
5
10
15
20
25
30
400
500
600
700
800
900

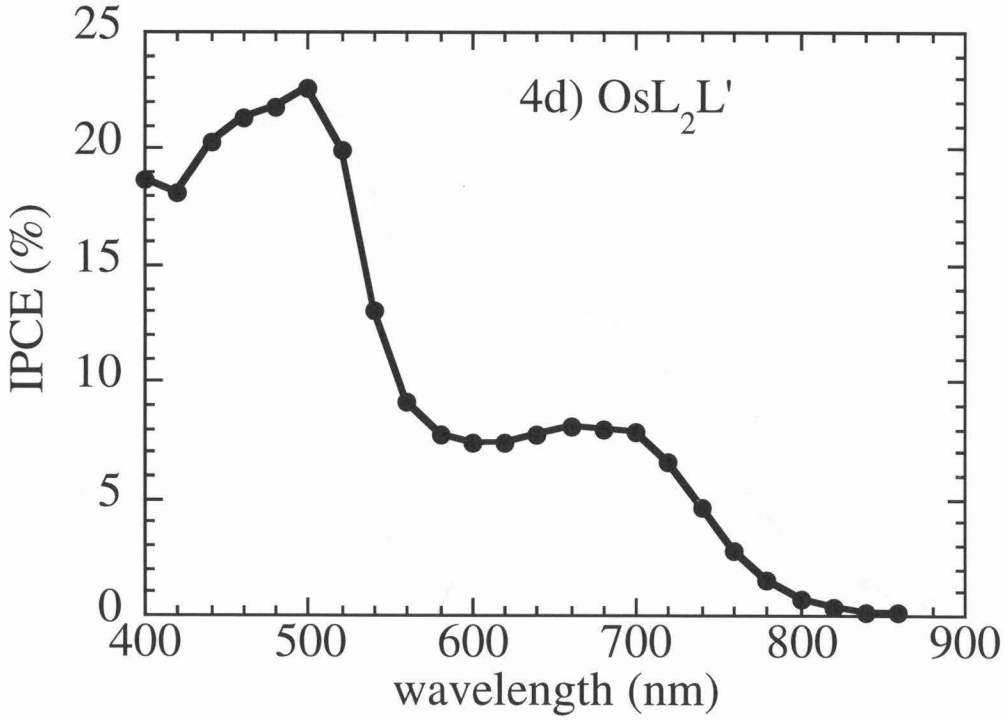
4d) OsL2L'
IPCE (%)
wavelength (nm)
0
5
10
15
20
25
400
500
600
700
800
900

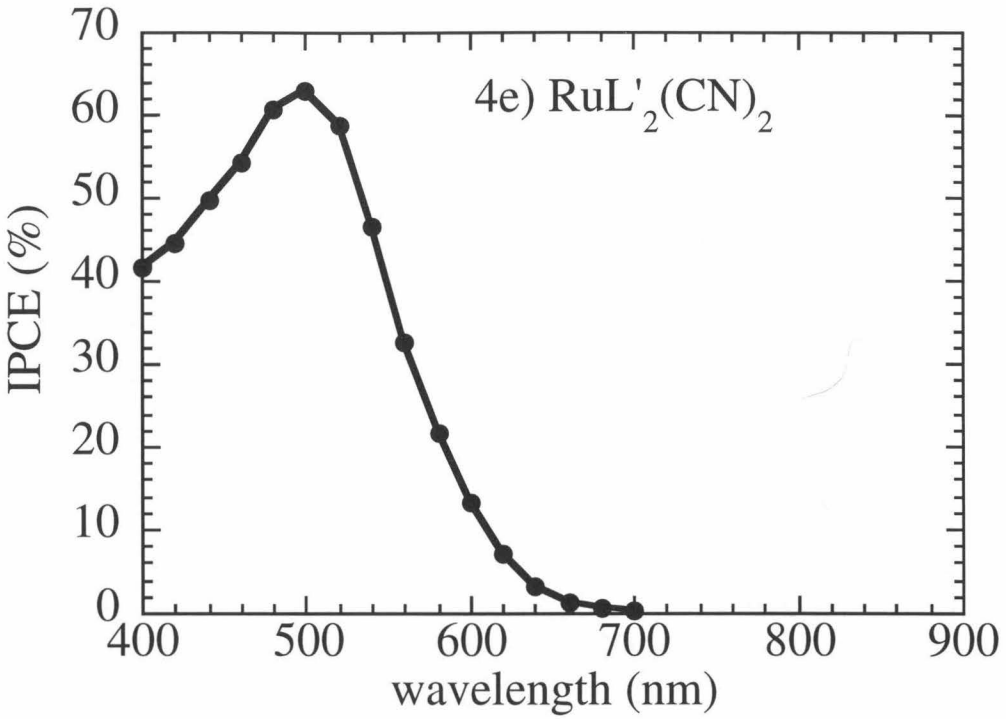
4e) RuL'2(CN)2
IPCE (%)
wavelength (nm)
0
10
20
30
40
50
60
70
400
500
600
700
800
900

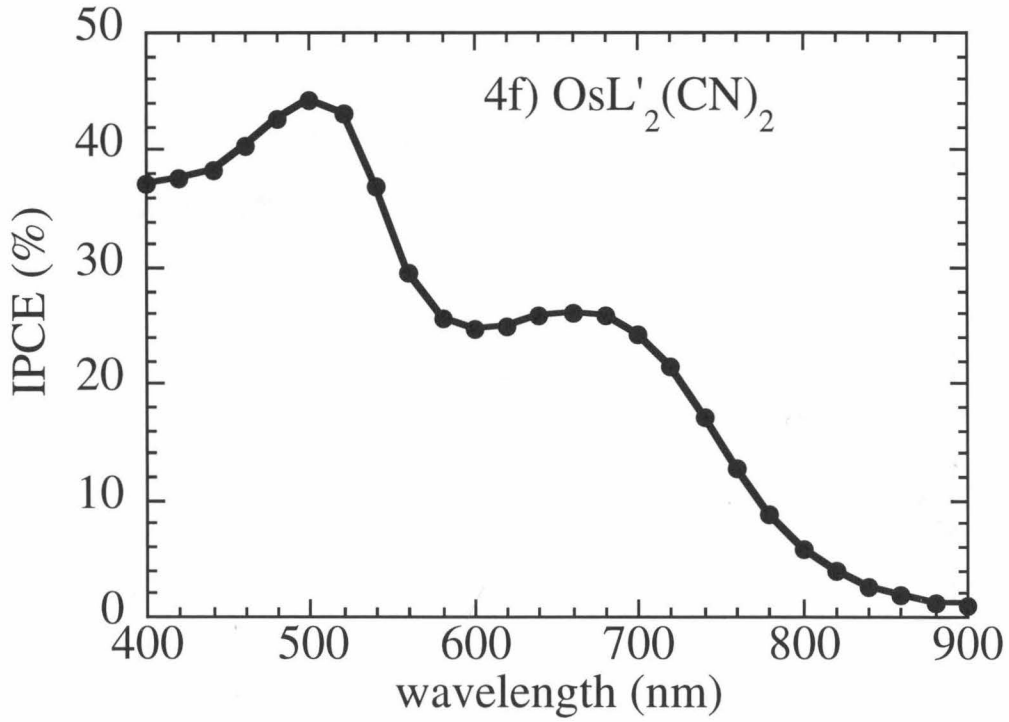
4f) OsL'2(CN)2
IPCE (%)
wavelength (nm)
0
10
20
30
40
50
400
500
600
700
800
900

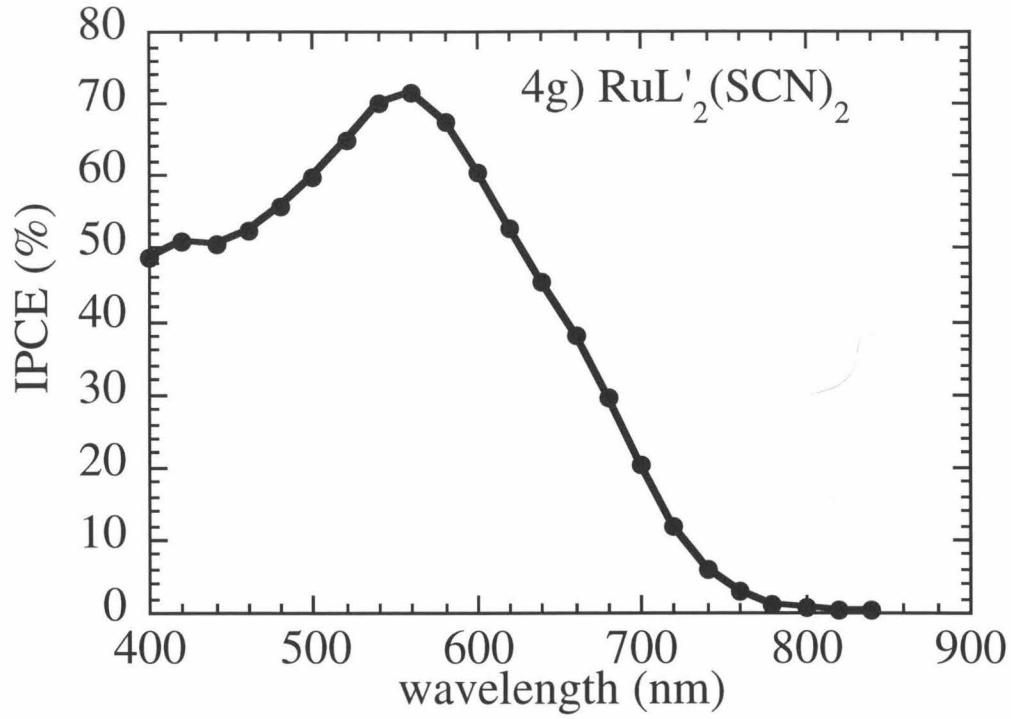
4g) RuL'2(SCN)2
IPCE (%)
wavelength (nm)
0
10
20
30
40
50
60
70
80
400
500
600
700
800
900

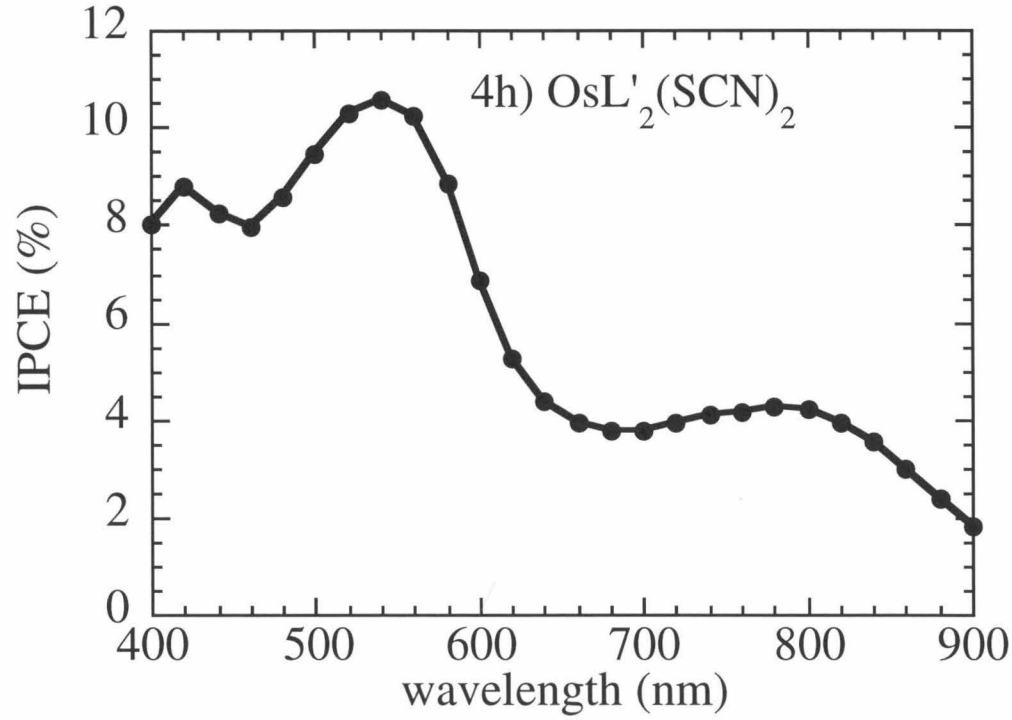
4h) OsL'2(SCN)2
IPCE (%)
wavelength (nm)
0
2
4
6
8
10
12
400
500
600
700
800
900

Figure 2.5a-h: Spectral response data normalized for dye absorption.

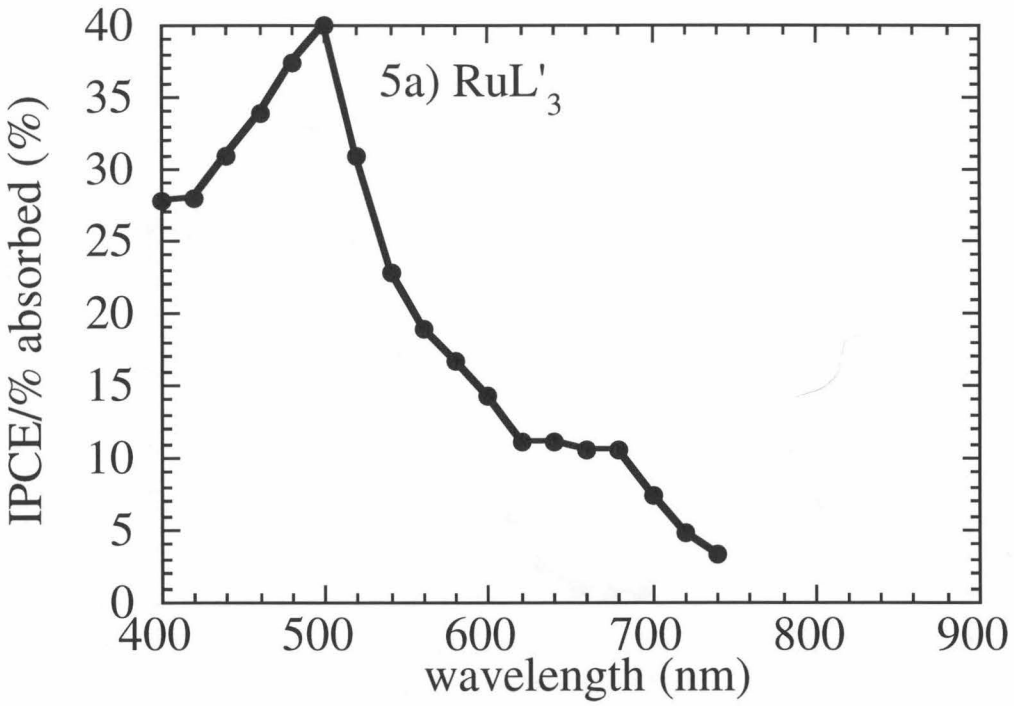
5a) RuL'3
IPCE/% absorbed (%)
wavelength (nm)
0
5
10
15
20
25
30
35
40
400
500
600
700
800
900

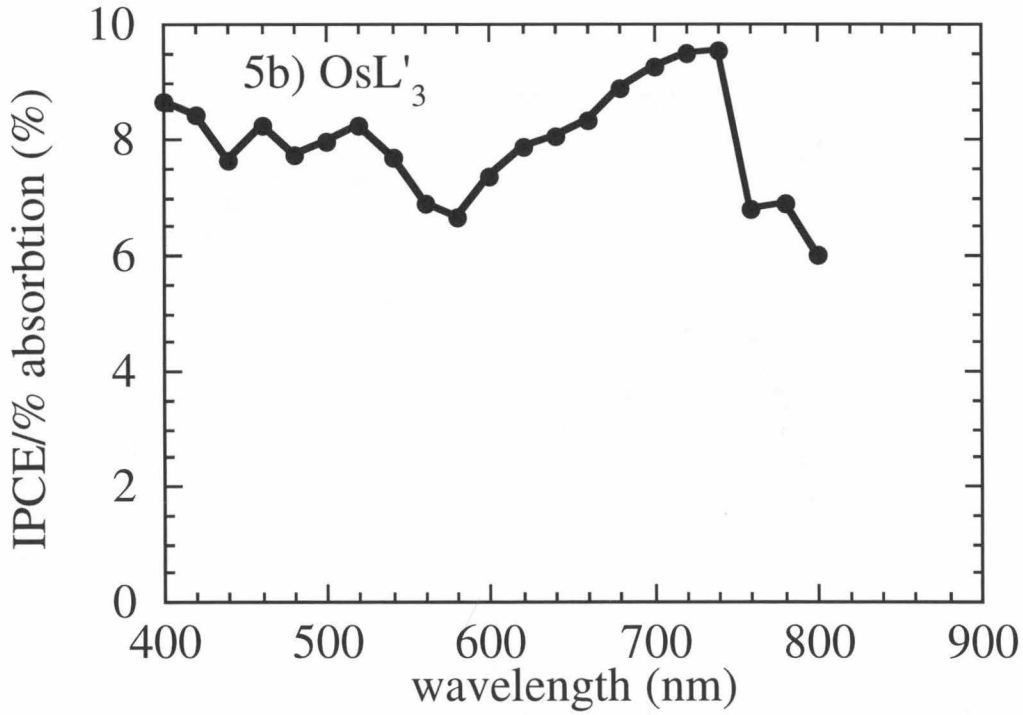
5b) OsL'3
IPCE/% absorbtion (%)
wavelength (nm)
0
2
4
6
8
10
400
500
600
700
800
900

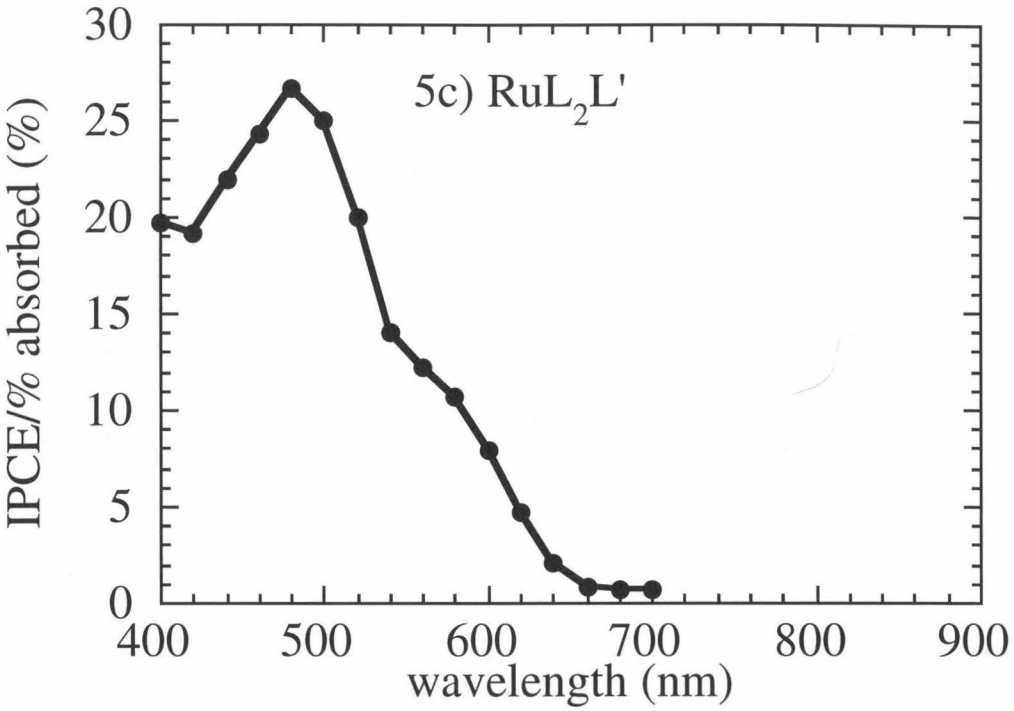
5c) RuL2L'
IPCE/% absorbed (%)
wavelength (nm)
0
5
10
15
20
25
30
400
500
600
700
800
900

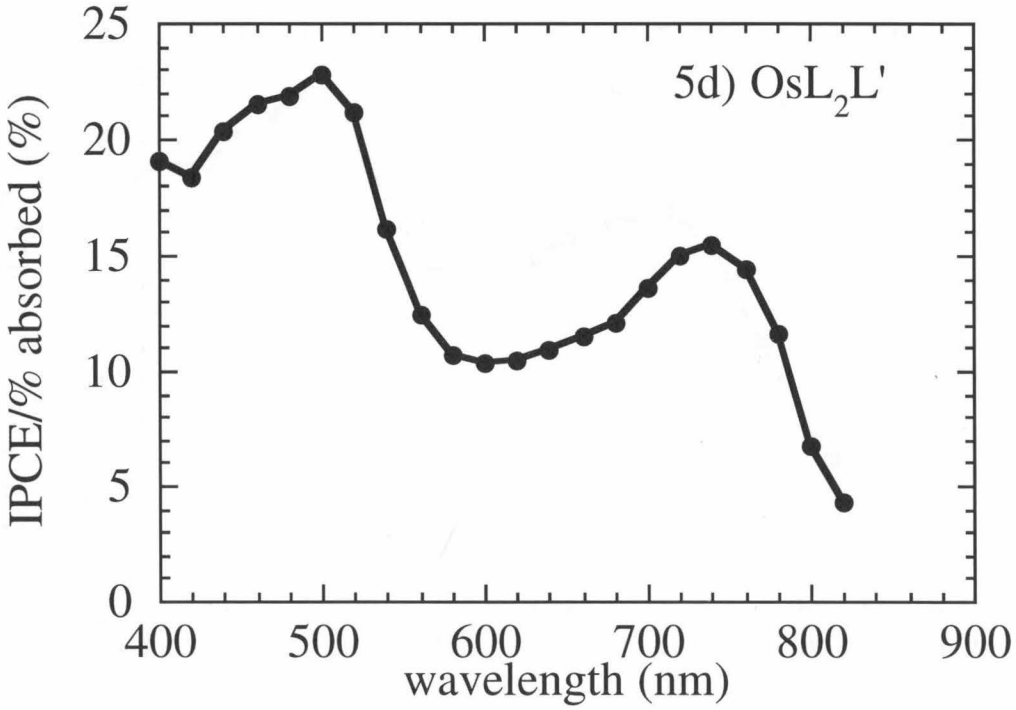
5d) OsL2L'
IPCE/% absorbed (%)
wavelength (nm)
0
5
10
15
20
25
400
500
600
700
800
900

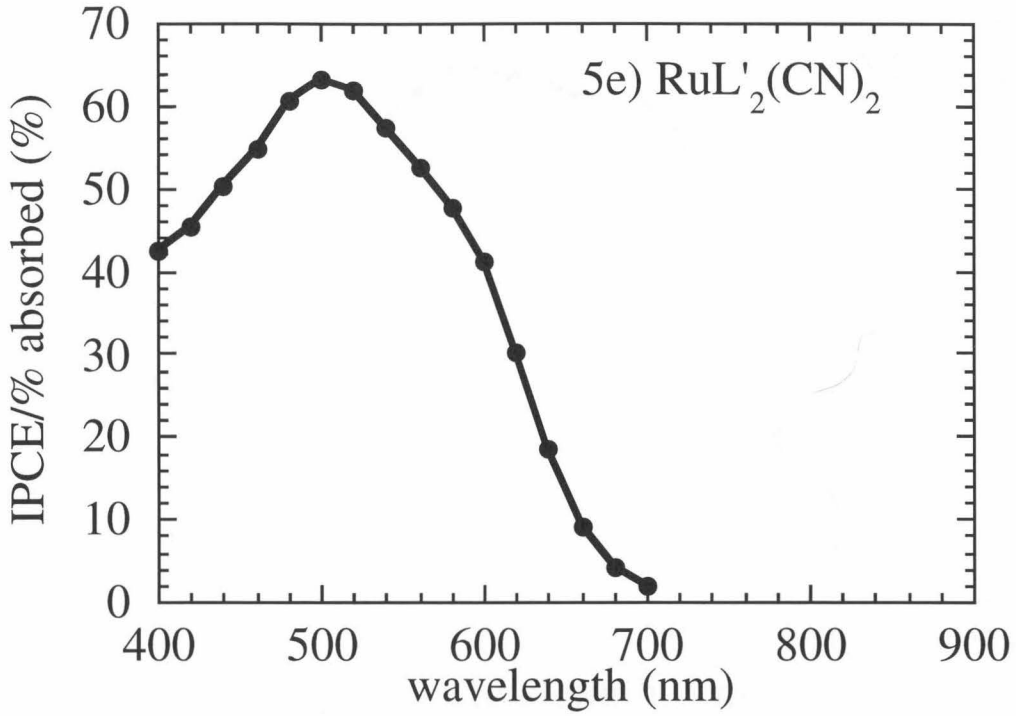
5e) RuL'2(CN)2
IPCE/% absorbed (%)
wavelength (nm)
0
10
20
30
40
50
60
70
400
500
600
700
800
900

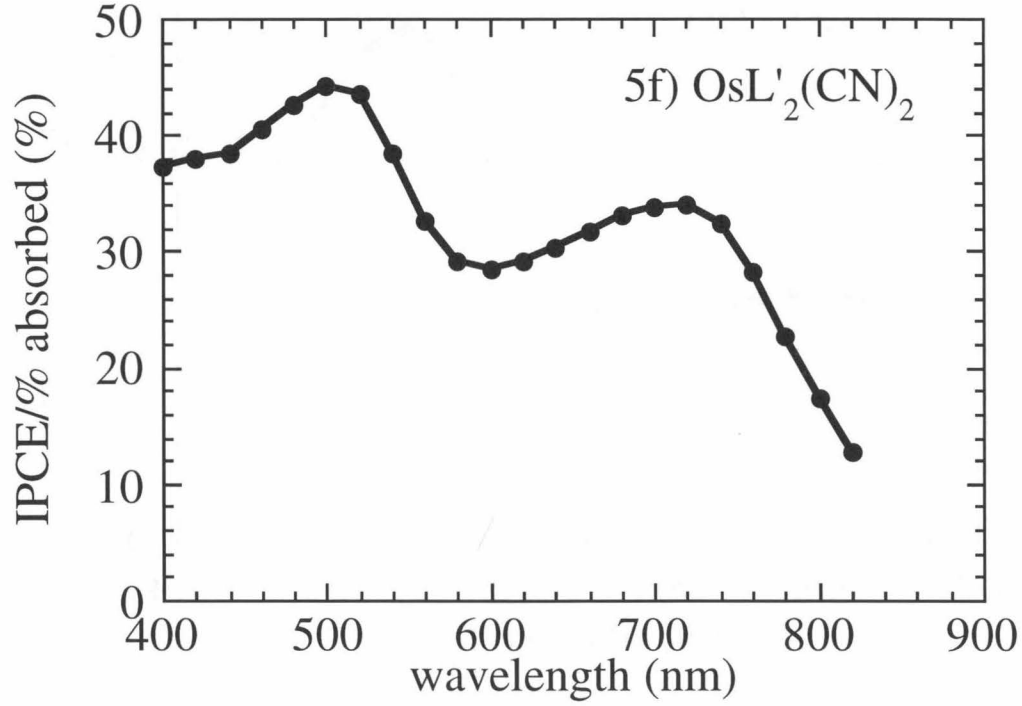
5f) OsL'2(CN)2
IPCE/% absorbed (%)
wavelength (nm)
0
10
20
30
40
50
400
500
600
700
800
900

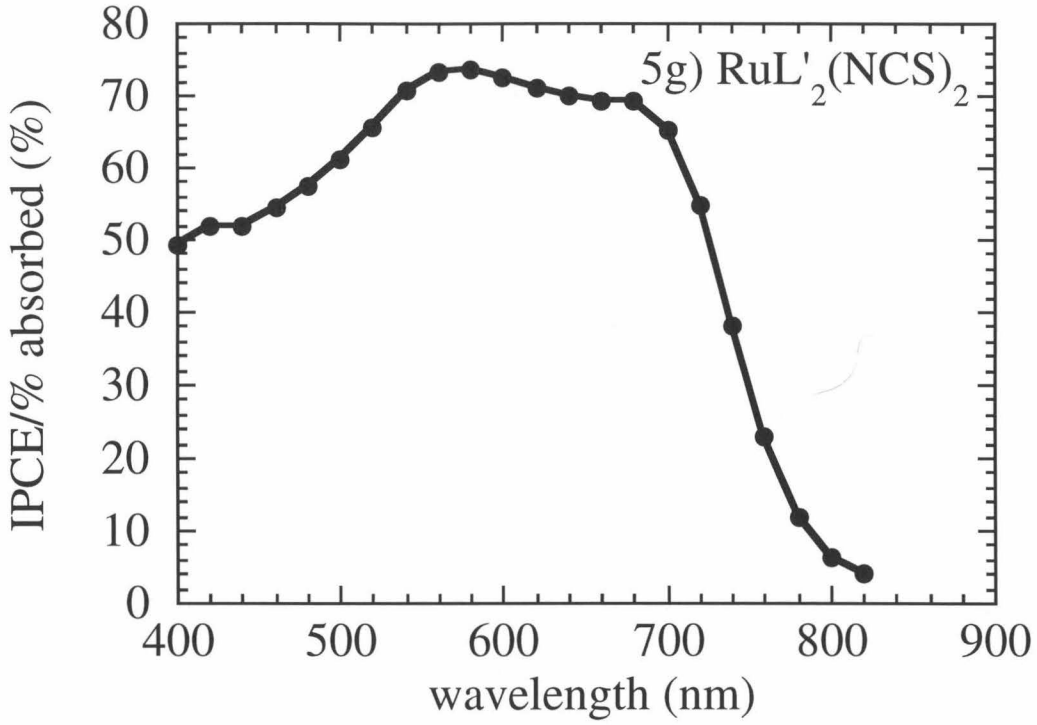
5g) RuL'2(NCS)2
IPCE/% absorbed (%)
wavelength (nm)
0
10
20
30
40
50
60
70
80
400
500
600
700
800
900

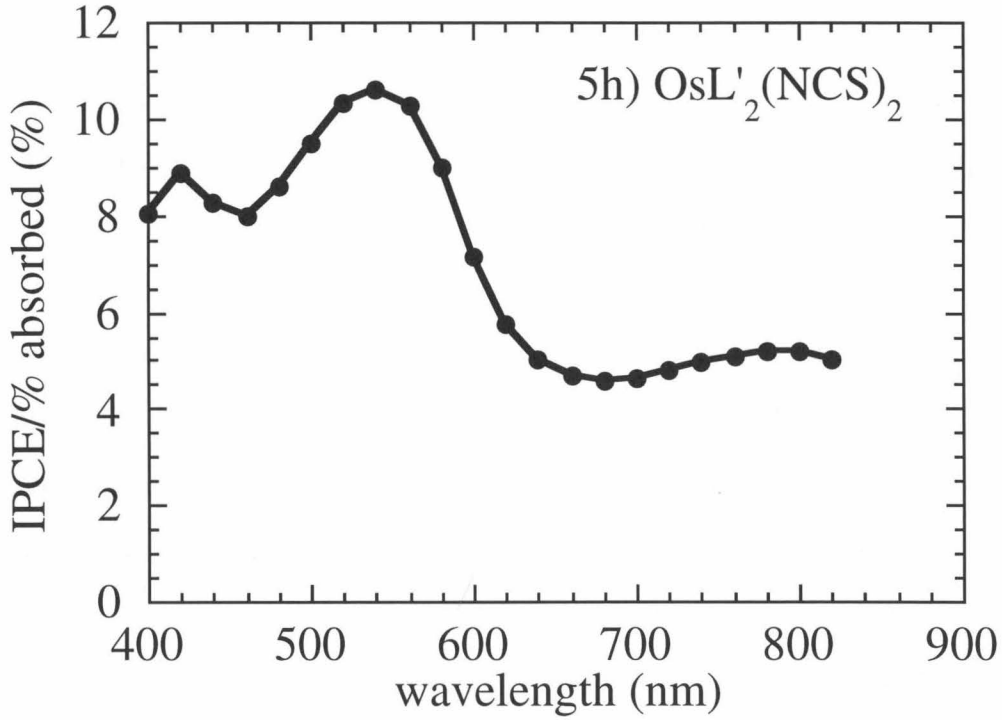
5h) OsL'2(NCS)2
IPCE/% absorbed (%)
wavelength (nm)
0
2
4
6
8
10
12
400
500
600
700
800
900

C. Current-Voltage Curves

Current-voltage behavior for sample electrodes are shown in Figure 2.6. The range of open circuit voltages and short circuit current densities for a series of electrodes are listed in Table 2.2. In each case, the light intensity corresponded to the photon flux present at AM 1.0 illumination as monitored by the calibrated photodiode. As depicted in Figure 2.6, these electrodes showed little degradation in current after being held at short circuit under low light intensity for approximately 30 minutes (the duration of the spectral response measurements). As predicted by Grätzel et al.,[5] electrodes sensitized with the $RuL'_2(NCS)_2$ complex exhibited the highest efficiencies. Table 2.3 shows the relative short circuit current densities predicted by the spectral response for a cell illuminated with 100 mW cm-2 of light. In most cases, the trend in the short-circuit current densities corresponded to the trend in photon-to-current efficiencies. However, some electrodes deviated significantly from the expected behavior. The electrodes sensitized with the OsL'_3 dye exhibited much higher short circuit current densities than would be predicted from the spectral response data. With this dye the spectral response was particularly slow to stabilize; however, the cause of the discrepancy is still unknown.

One question which arises from the data is whether the differences in the open circuit voltages at AM 1.0 illumination between electrodes sensitized with different dyes is due to a difference in the junction energetics or is merely a reflection of the difference in injection efficiency. Since the maximum free energy obtainable from the cell should only be dependent on the difference between the TiO_2 conduction band edge and the redox couple in solution (Scheme 2.1), the open-circuit voltage should not be a function of the dye at a given current density. Assuming the principle of superposition holds, the current-voltage behavior of these cells in the dark should yield information regarding this issue. Figure 2.7 shows the dark current-voltage behavior of the electrodes depicted in Figure 2.6. The curves do not appear to deviate from each other by more than 100 mV, supporting the hypothesis that the differences in the cells in the light are only due to

differences in the number of electrons injected into the TiO_2. Table 2.4 shows the potential required to pass 2.0 mA cm^{-2} of reductive current in the dark and further illustrates the similarities in the electrode behavior. Only the electrodes sensitized with $RuL'_2(NCS)_2$ and $RuL'_2(CN)_2$ require significantly higher voltages than other electrodes. In fact, electrodes sensitized with $RuL'_2(CN)_2$ show the highest voltages, so at a given photocurrent, electrodes sensitized with this dye should exhibit the highest photovoltages.

Figure 2.6a-h: Current-potential curves for a representative TiO_2 electrode for each of the 8 dyes characterized above at a light intensity of AM 1.0 in CH_3CN/0.040 M I_2/0.500 M LiI/(0.001 M/0.001 M) py/pyH^+. Filled circles represent data collected before measuring the spectral response of the electrode while open circles represent data taken after the spectral response measurements.

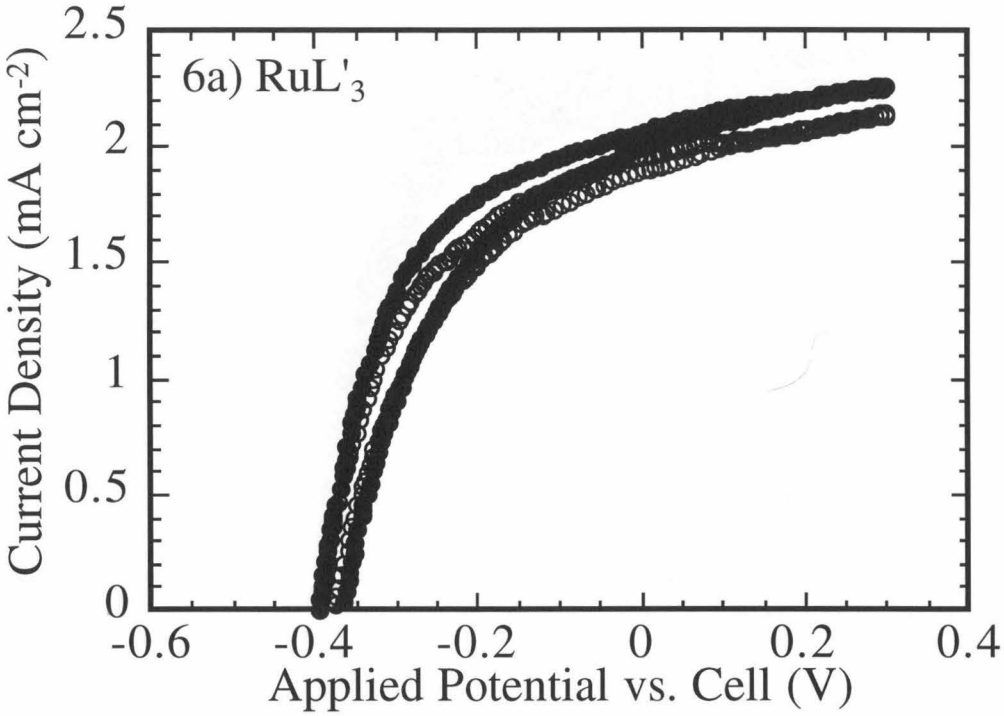
6a) RuL'3
Current Density (mA cm-2)
Applied Potential vs. Cell (V)
2.5
2
1.5
1
0.5
0
-0.6
-0.4
-0.2
0
0.2
0.4

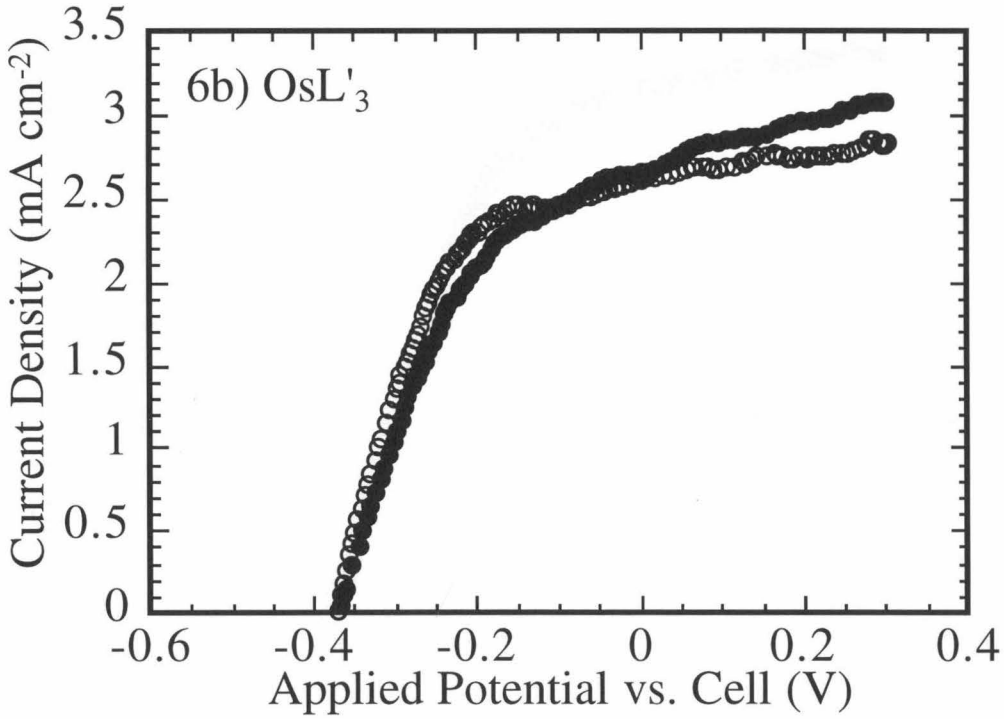
6b) OsL'3
Current Density (mA cm-2)
Applied Potential vs. Cell (V)
3.5
3
2.5
2
1.5
1
0.5
0
-0.6
-0.4
-0.2
0
0.2
0.4

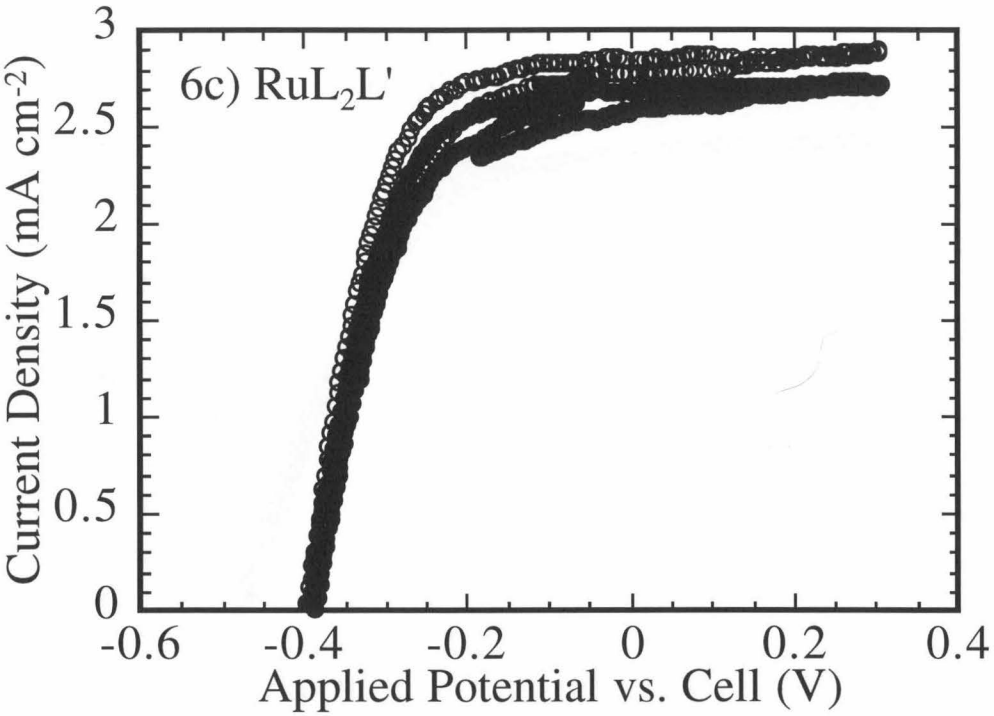
6c) RuL2L'
Current Density (mA cm-2)
Applied Potential vs. Cell (V)
3
2.5
2
1.5
1
0.5
0
-0.6
-0.4
-0.2
0
0.2
0.4

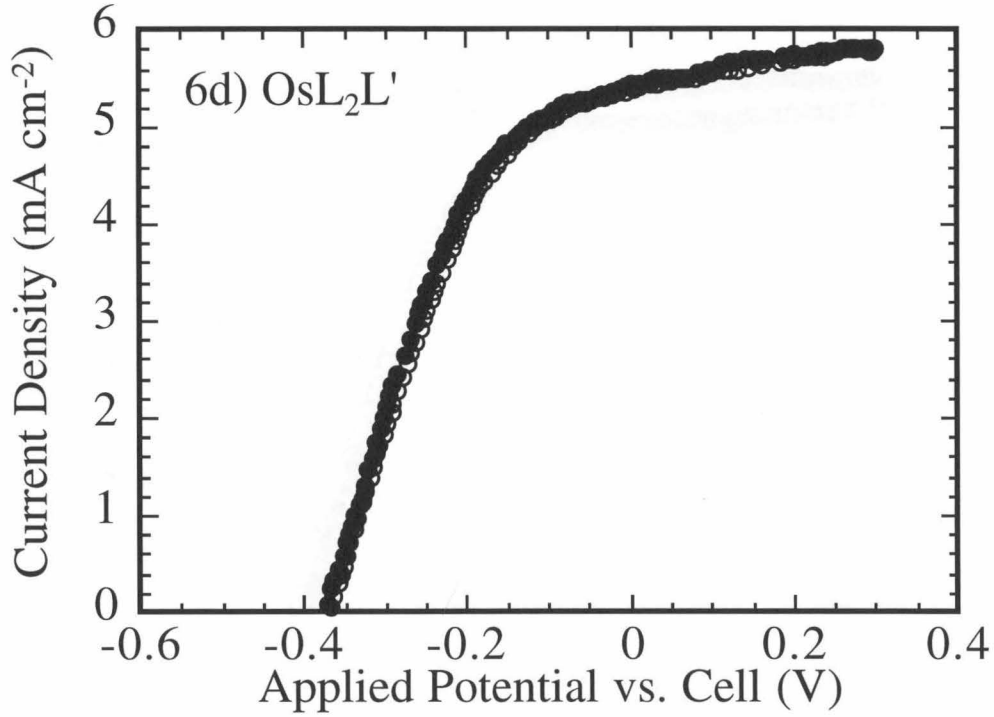
6d) OsL2L'
Current Density (mA cm-2)
Applied Potential vs. Cell (V)
6
5
4
3
2
1
0
-0.6
-0.4
-0.2
0
0.2
0.4

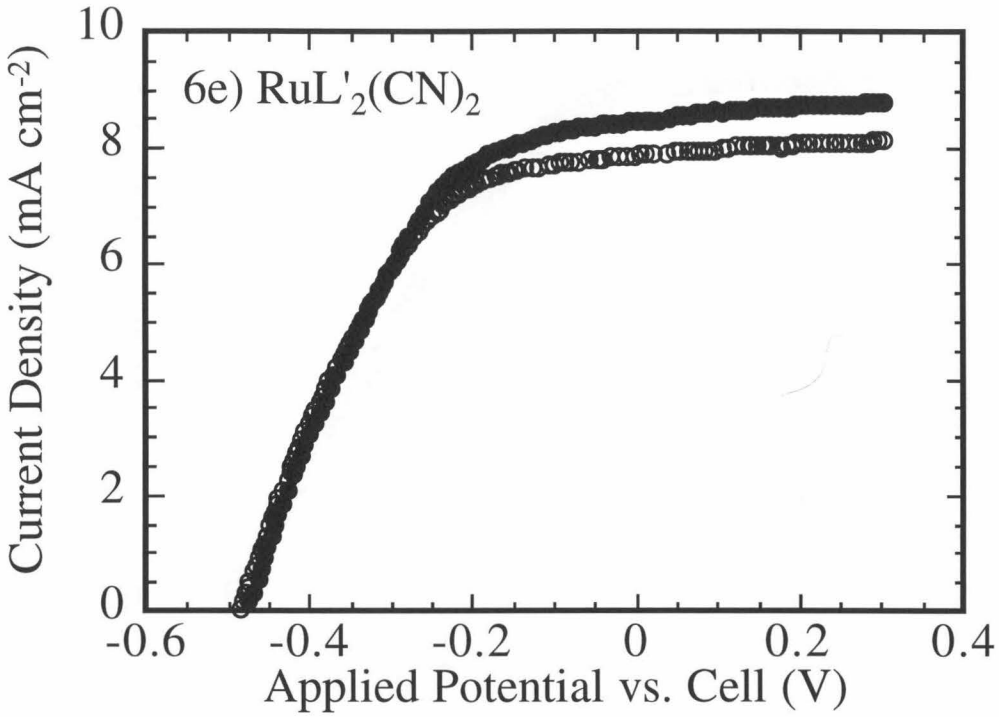
6e) RuL'2(CN)2
Current Density (mA cm-2)
Applied Potential vs. Cell (V)
10
8
6
4
2
0
-0.6
-0.4
-0.2
0
0.2
0.4

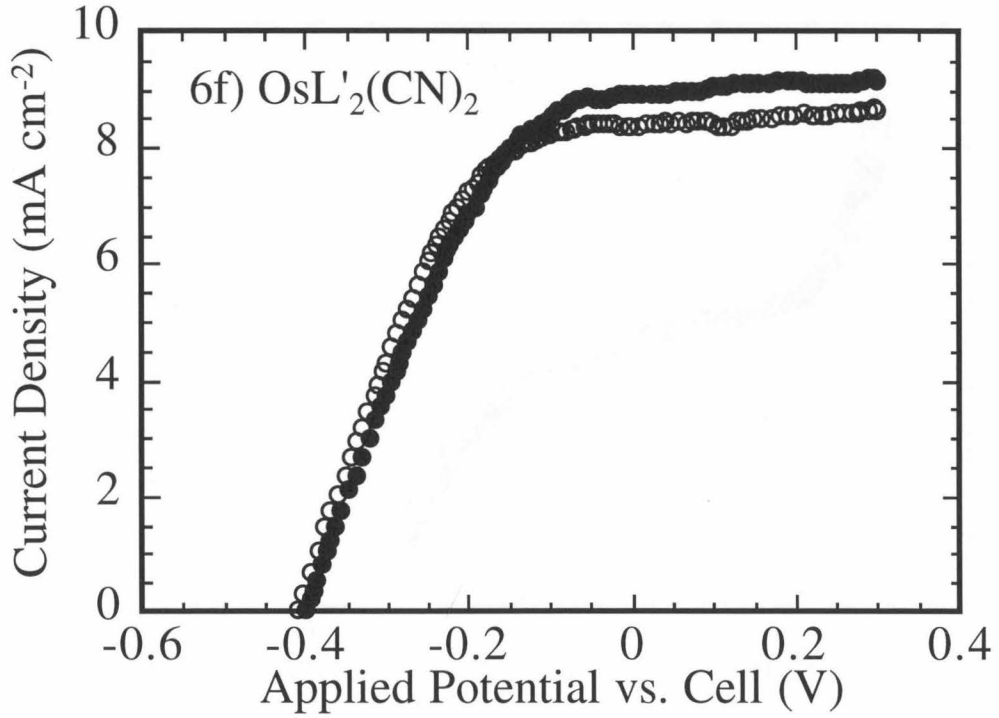
6f) OsL'2(CN)2
Current Density (mA cm-2)
Applied Potential vs. Cell (V)
10
8
6
4
2
0
-0.6
-0.4
-0.2
0
0.2
0.4

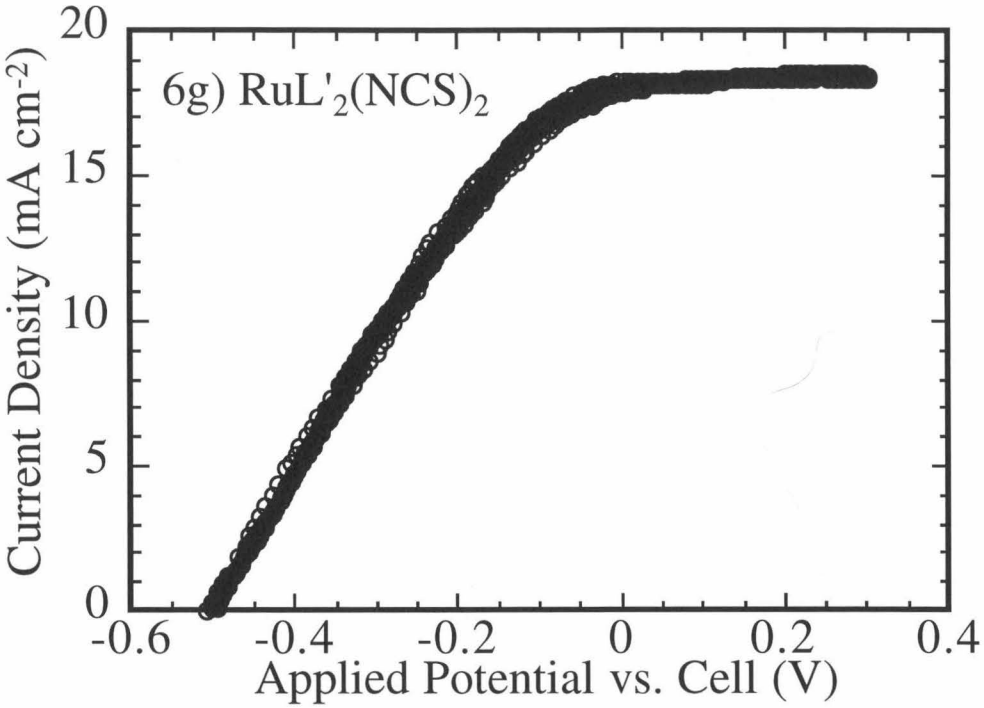
6g) RuL'2(NCS)2
Current Density (mA cm-2)
Applied Potential vs. Cell (V)
20
15
10
5
0
-0.6
-0.4
-0.2
0
0.2
0.4

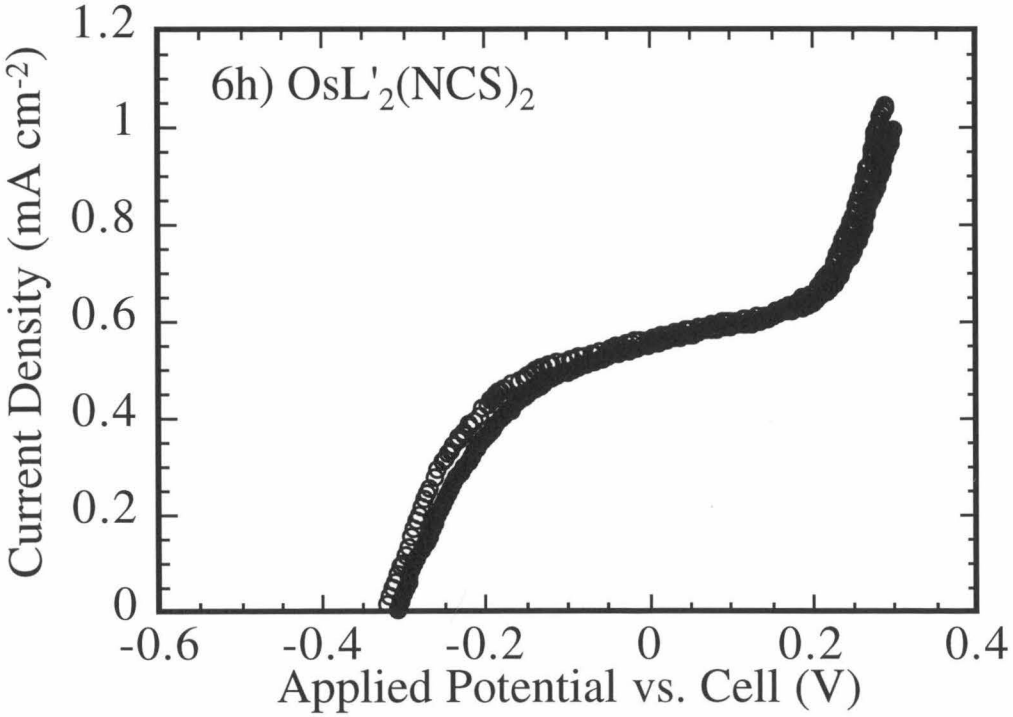
6h) OsL'2(NCS)2
Current Density (mA cm-2)
Applied Potential vs. Cell (V)
1.2
1
0.8
0.6
0.4
0.2
0
-0.6
-0.4
-0.2
0
0.2
0.4

Table 2.2: Open Circuit Voltages (V_{oc}) and Short-Circuit Current Densities (J_{sc}) as a Function of Sensitizer at AM 1.0 illumination. V_{oc} values are listed vs. the cell potential.

Dye	V_{oc} (average, mV)	J_{sc} (average, mA cm^{-2})	V_{oc} (range, mV)	J_{sc} (range, mA cm^{-2})
RuL'_3	370	2.0	365-380	1.3-2.6
OsL'_3	360	4.6	345-375	2.4-5.8
RuL_2L'	390	3.2	385-405	2.7-3.7
OsL_2L'	390	5.4	350-450	4.7-6.2
$RuL'_2(CN)_2$	490	8.4	470-500	8.3-8.5
$OsL'_2(CN)_2$	410	8.2	410	7.5-9.0
$RuL'_2(NCS)_2$	520	17	495-570	15-20
$OsL'_2(NCS)_2$	330	2.1	310-375	2.0-2.2

Table 2.2

Table 2.3: Predicted short circuit current densities at 100 mW cm^{-2} incident illumination based on integrated spectral response data.
a: Calculated using solar spectrum.
b: Calculated using spectrum of Sylvania ELH bulbs used in this work.

Dye	Current Density (mA cm^{-2})[a]	Current Density (mA cm^{-2})[b]
RuL'_3	.96	1.1
OsL'_3	.62	.78
RuL_2L'	1.6	1.7
OsL_2L'	2.8	3.5
$RuL'_2(CN)_2$	5.6	7.0
$OsL'_2(CN)_2$	7.6	9.7
$RuL'_2(NCS)_2$	11	16
$OsL'_2(NCS)_2$	2.0	2.4

Table 2.3

Figure 2.7a-h: Current-potential data taken in the dark for the electrodes represented in Figure 2.6.

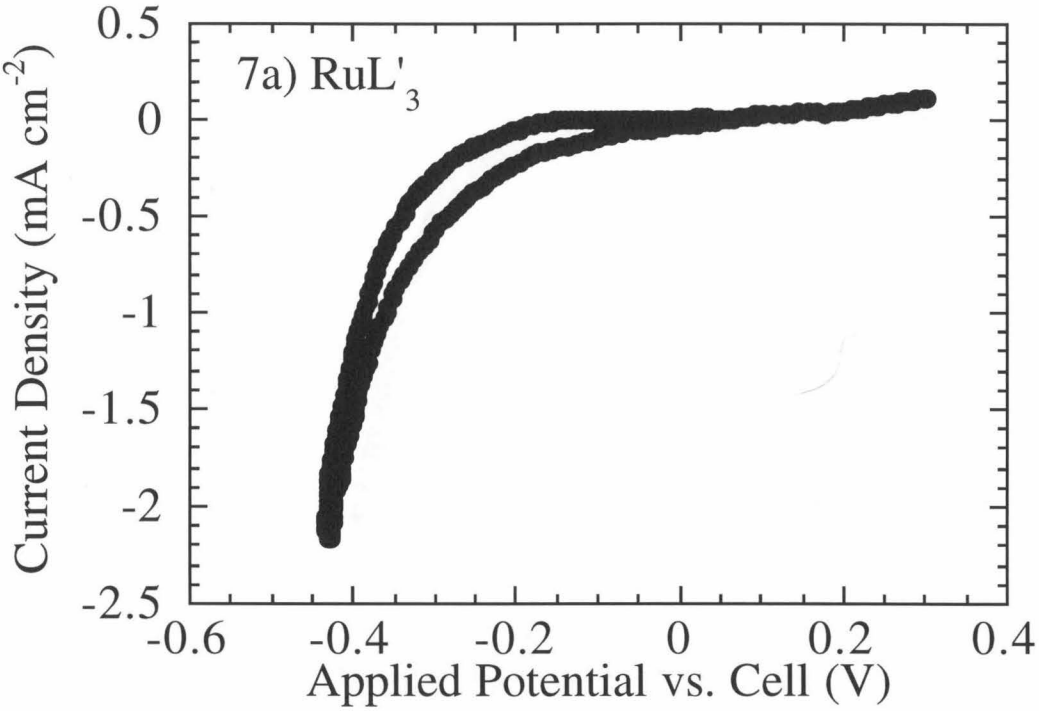
7a) RuL'3
Current Density (mA cm-2)
Applied Potential vs. Cell (V)
0.5
0
-0.5
-1
-1.5
-2
-2.5
-0.6
-0.4
-0.2
0
0.2
0.4

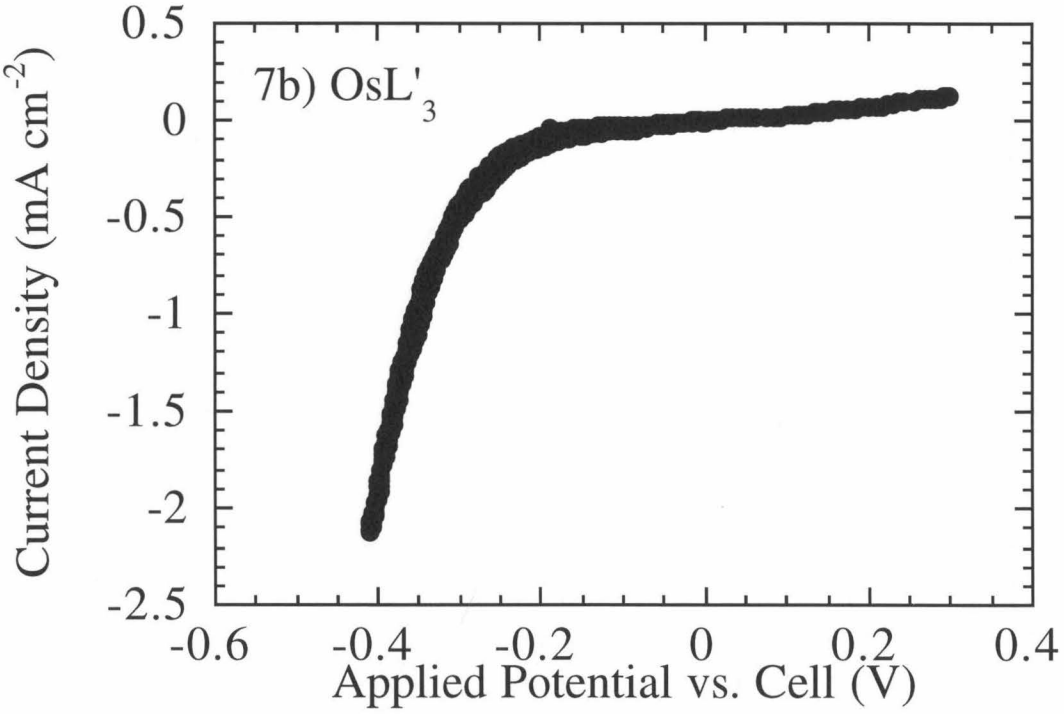
7b) OsL'3
Current Density (mA cm-2)
Applied Potential vs. Cell (V)
0.5
0
-0.5
-1
-1.5
-2
-2.5
-0.6
-0.4
-0.2
0
0.2
0.4

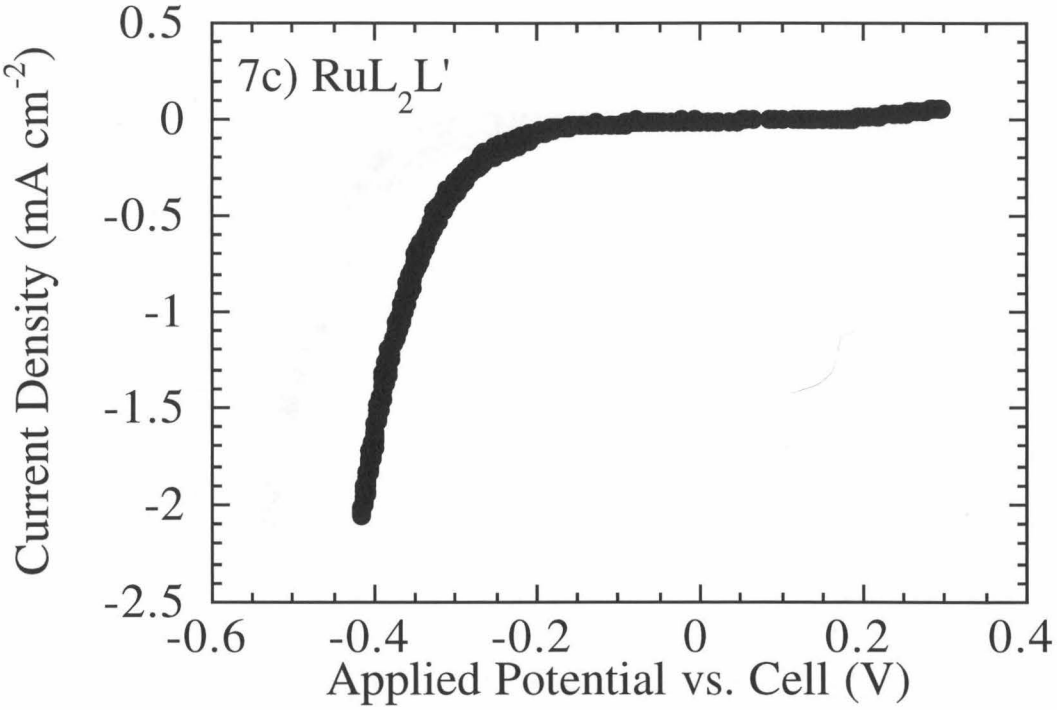
7c) RuL2L'
Current Density (mA cm-2)
Applied Potential vs. Cell (V)
0.5
0
-0.5
-1
-1.5
-2
-2.5
-0.6
-0.4
-0.2
0
0.2
0.4

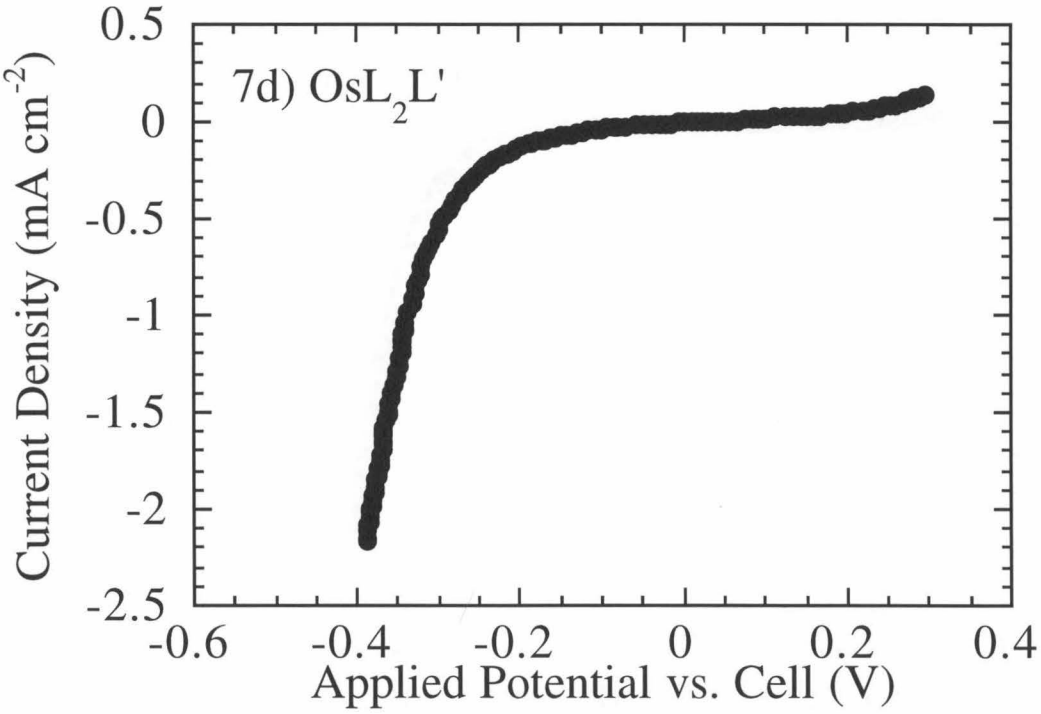
7d) OsL2L'
Current Density (mA cm-2)
Applied Potential vs. Cell (V)
0.5
0
-0.5
-1
-1.5
-2
-2.5
-0.6
-0.4
-0.2
0
0.2
0.4

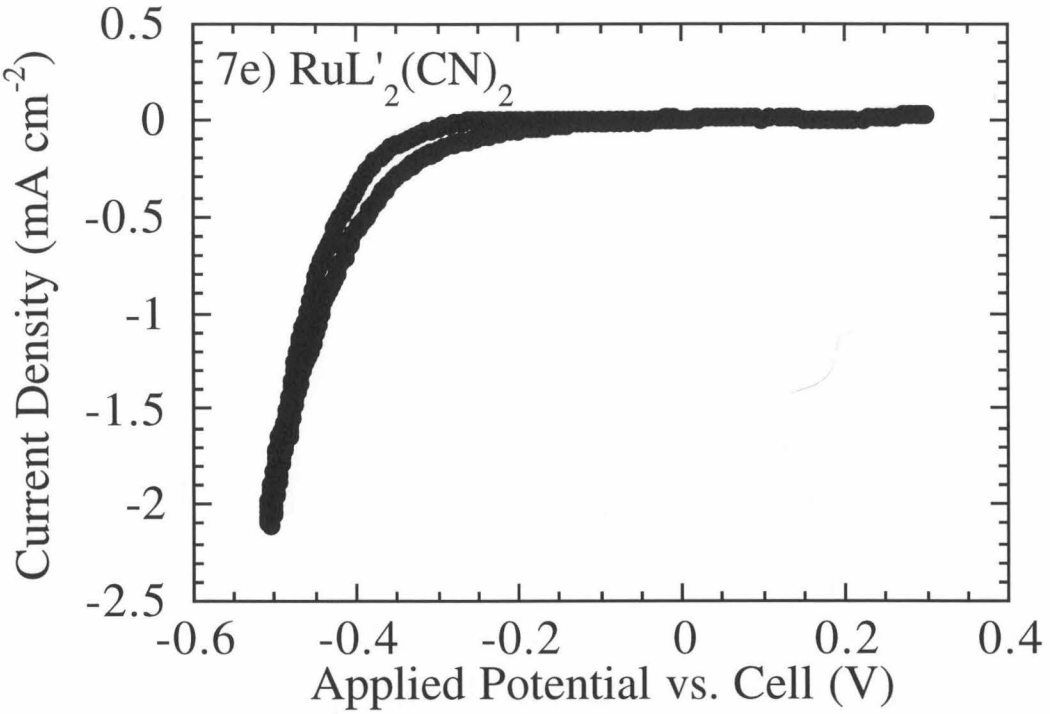
7e) RuL'2(CN)2
Current Density (mA cm-2)
Applied Potential vs. Cell (V)
0.5
0
-0.5
-1
-1.5
-2
-2.5
-0.6
-0.4
-0.2
0
0.2
0.4

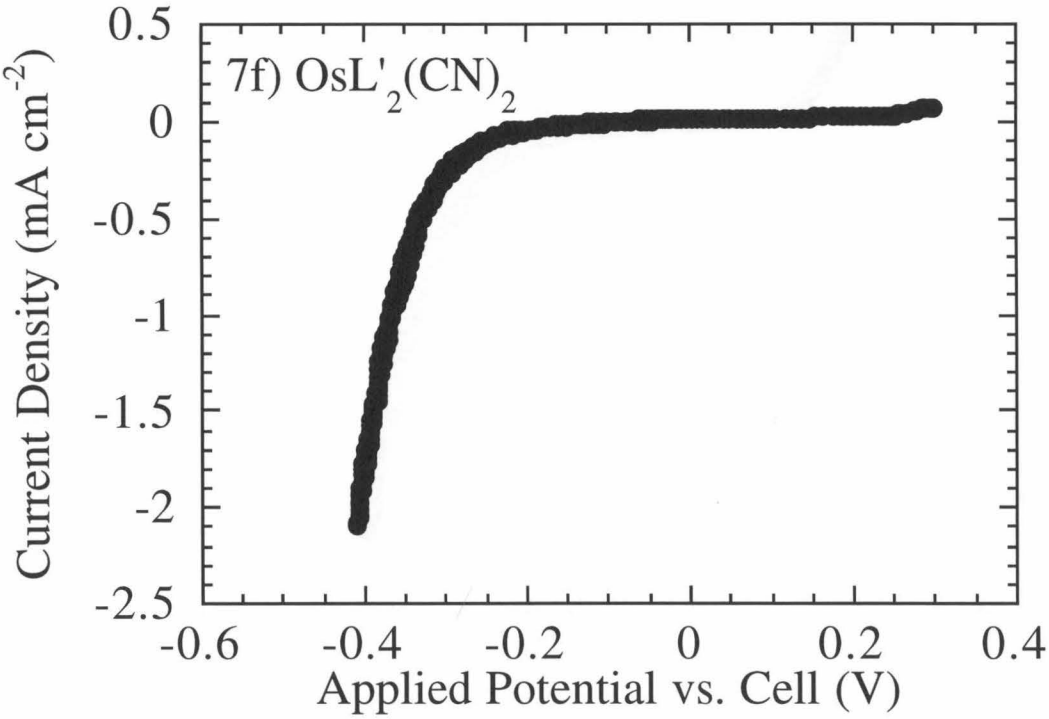
7f) OsL'2(CN)2
Current Density (mA cm-2)
Applied Potential vs. Cell (V)
0.5
0
-0.5
-1
-1.5
-2
-2.5
-0.6
-0.4
-0.2
0
0.2
0.4

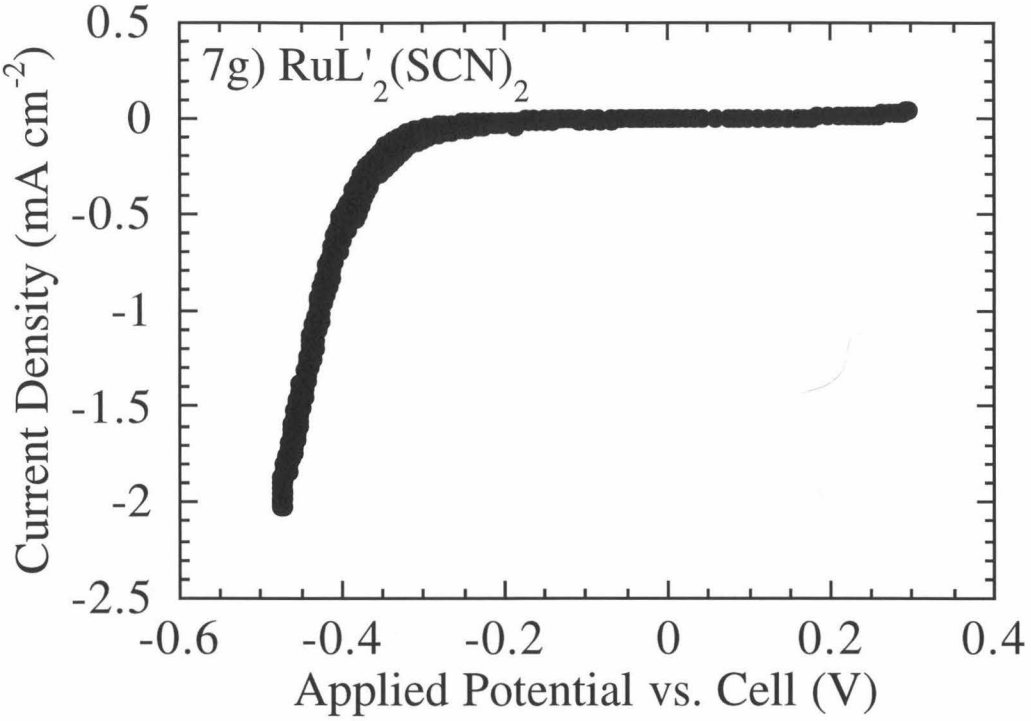
7g) RuL'2(SCN)2
Current Density (mA cm-2)
Applied Potential vs. Cell (V)
0.5
0
-0.5
-1
-1.5
-2
-2.5
-0.6
-0.4
-0.2
0
0.2
0.4

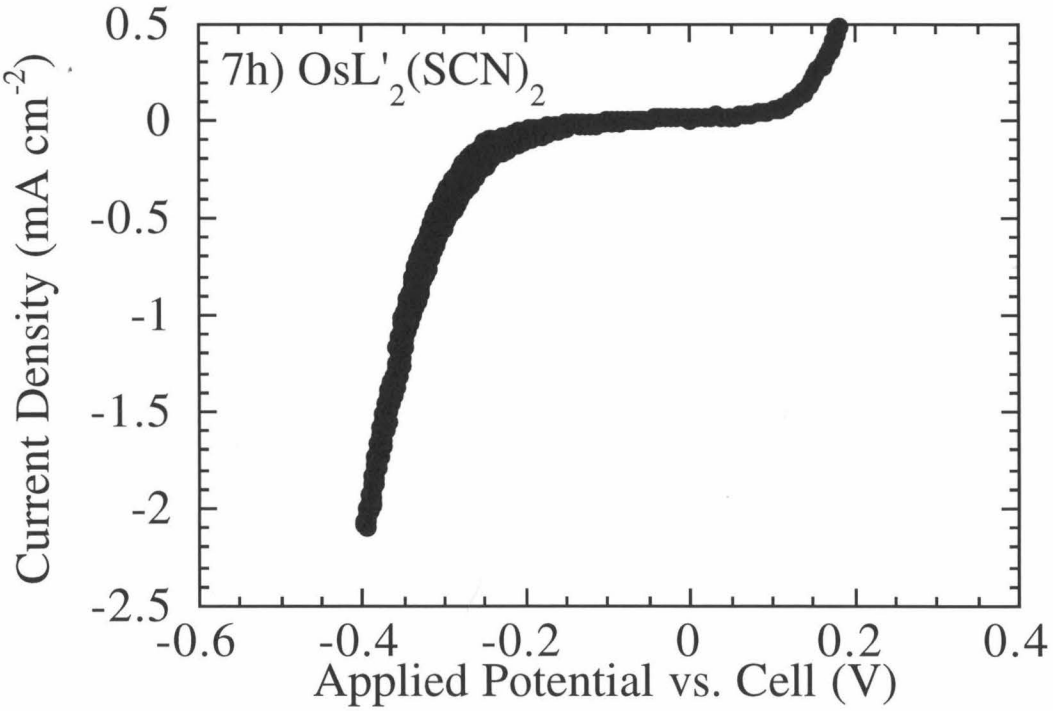
7h) OsL'2(SCN)2
Current Density (mA cm-2)
Applied Potential vs. Cell (V)
0.5
0
-0.5
-1
-1.5
-2
-2.5
-0.6
-0.4
-0.2
0
0.2
0.4

Table 2.4: Applied potential required to sustain 2.0 mA cm^{-2} of reductive current in the dark for TiO_2 electrodes sensitized with each dye.

Dye	Potential vs. Cell (V)
RuL'_3	-0.43
OsL'_3	-0.40
RuL_2L'	-0.41
OsL_2L'	-0.38
$RuL'_2(CN)_2$	-0.50
$OsL'_2(CN)_2$	-0.41
$RuL'_2(NCS)_2$	-0.47
$OsL'_2(NCS)_2$	-0.39

Table 2.4

D. Effect of pH on I-V Curves--$TiO_2/RuL'_2(NCS)_2$ Electrodes

$TiO_2/RuL'_2(NCS)_2$ electrodes were characterized as a function of Proton Sponge concentration to determine whether improvements seen in cells with special additives were due to surface state passivation or some other mechanism or if the effect could be explained solely on the basis of pH change. In initial sets of experiments, each electrode was first characterized in a solution containing only buffered LiI/I_2. As depicted in Figure 2.8a, when Proton Sponge was added, the open circuit voltages increased dramatically and the short circuit currents dropped. This effect is believed to be due to a shifting in the band edge position of the TiO_2 with pH. As the difference between the conduction band edge position of the TiO_2 and the reduction potential of the LiI/I_2 is increased, the open circuit voltage gets larger. If the conduction band edge becomes so negative that the excited dye cannot inject electrons efficiently, the short-circuit current density decreases. However, as shown in Figure 2.8b, when the electrode was reintroduced to the buffered solution, the open-circuit voltages decreased as expected, but the short-circuit current densities did not recover.

As mentioned earlier, once the electrodes were exposed to iodine solution, the removal of the iodine contact caused some irreversible degradation of the electrode which could account for the change between the first and last potential scan. To determine whether the decrease in current upon exposure to Proton Sponge was completely due to emptying the cell and refilling it, current-voltage curves of fresh $TiO_2/RuL'_2(NCS)_2$ electrodes in solutions containing various concentrations of Proton Sponge were examined (Figure 2.9). As seen in the figure, the results for the 10 mM Proton Sponge solution were almost identical to those of electrodes first exposed to buffered solution. Since the dyes are known to desorb in aqueous base, the more basic solutions could cause some loss of dye even in non-aqueous solutions, resulting in lower currents when the electrodes are reimmersed in buffered solution. Although this effect may also account for part of the current decrease, the voltage increases in basic solution cannot be explained by a loss of

dye, thus a band edge shift seems likely. The dark curves for this dye-electrode system show a similar shift in the voltage, further supporting the presence of a band edge shift. Table 2.5 summarizes the open circuit voltages and short circuit current densities as a function of Proton Sponge concentration.

Figure 2.8: Current-potential curves for a $RuL'_2(NCS)_2$-sensitized TiO_2 electrode at a light intensity of AM 1.0. (a) Filled circles represent data for the electrode immersed in a CH_3CN solution containing 0.040 M I_2/0.500 M LiI/(0.001 M/0.001 M) py/pyH^+. Open circles represent data for the same electrode in a solution similar to the initial solution but containing 0.010 M Proton Sponge. (b) Filled squares represent data for a second TiO_2 electrode immersed in the 0.010 Proton Sponge solution. Open triangles represent data for this electrode in CH_3CN/0.040 M I_2/0.500 M LiI/(0.001 M/0.001 M) py/pyH^+ after exposure to the Proton Sponge solution.

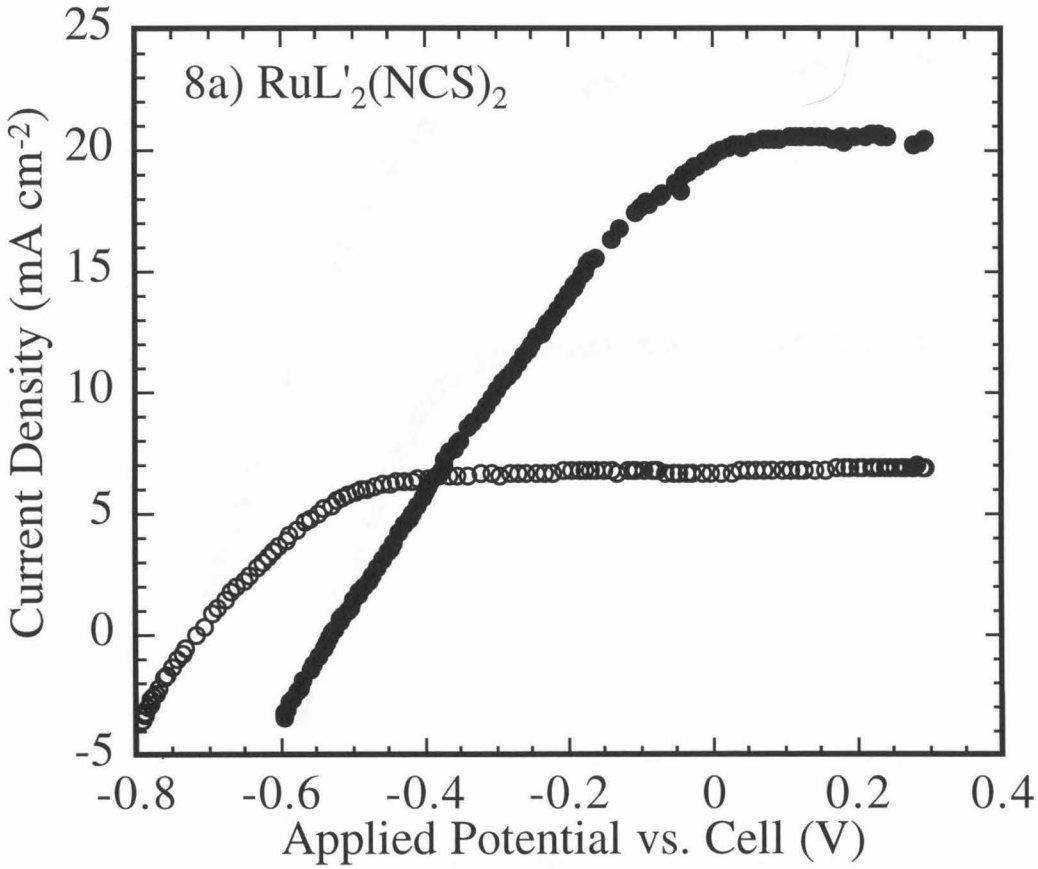
8a) RuL'2(NCS)2
Current Density (mA cm-2)
Applied Potential vs. Cell (V)
25
20
15
10
5
0
-5
-0.8
-0.6
-0.4
-0.2
0
0.2
0.4

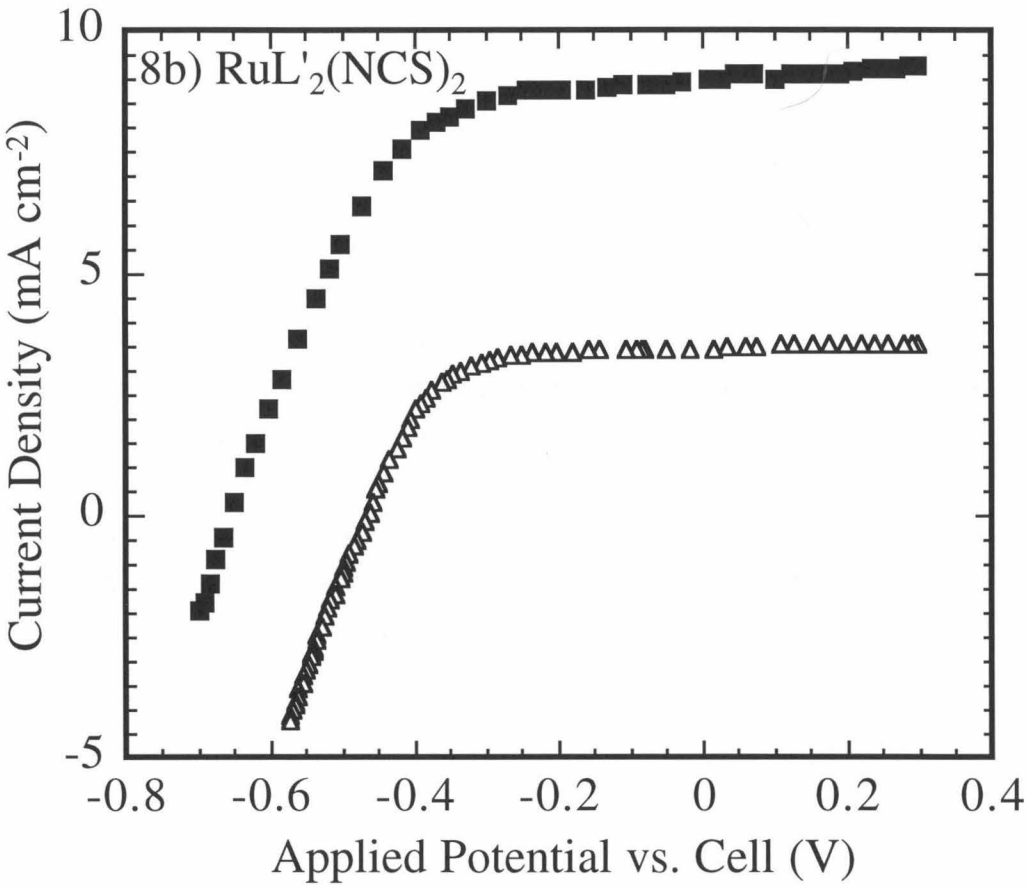
8b) RuL'2(NCS)2
Current Density (mA cm-2)
10
5
0
-5
-0.8
-0.6
-0.4
-0.2
0
0.2
0.4
Applied Potential vs. Cell (V)

Figure 2.9: (a) Photocurrent-potential curves for solutions containing various Proton Sponge concentrations. All light intensities were AM 1.0. Filled squares represent data taken in a solution containing 0.001 M Proton Sponge, open circles represent data taken in a solution containing 0.003 M Proton Sponge, and filled triangles represent data taken in a solution containing 0.010 M Proton Sponge. (b) Dark current-potential curves for an electrode before (filled squares) and after (open squares) exposure to Proton Sponge. Squares represent data taken in the buffered CH_3CN solution while triangles represent data in a solution containing 0.010 M Proton Sponge.

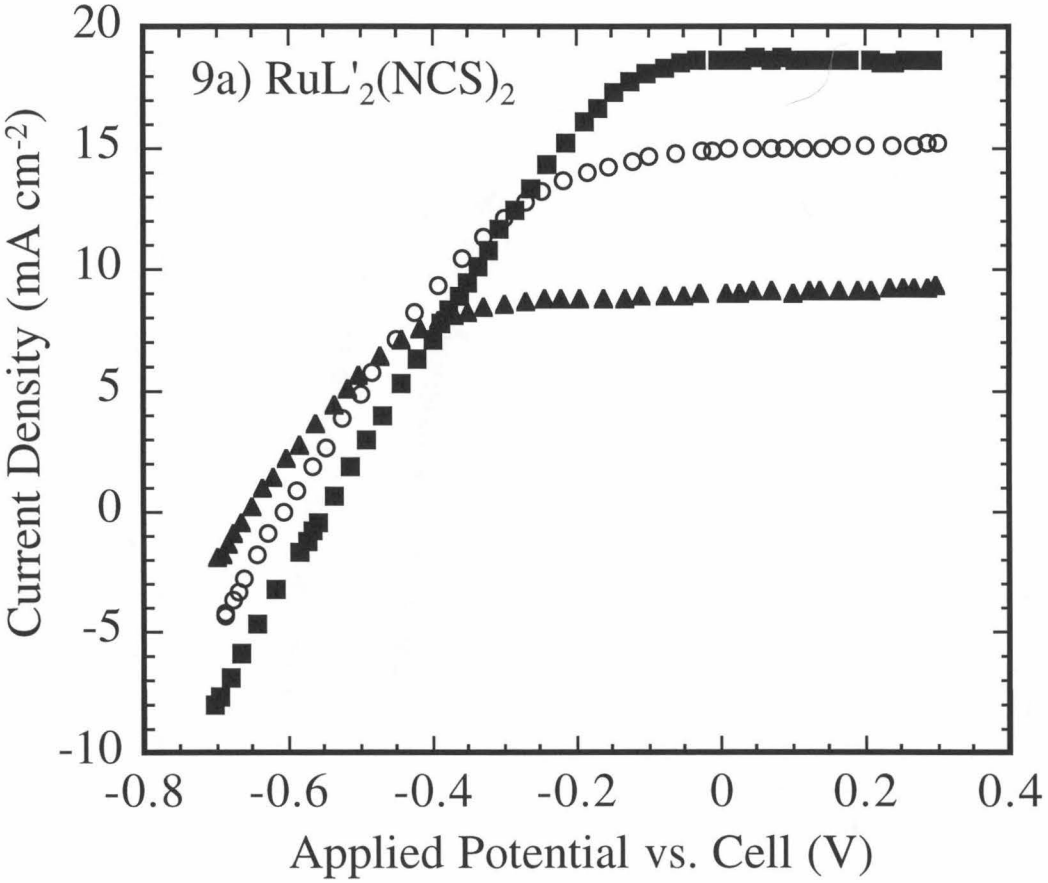
9a) RuL'2(NCS)2
Current Density (mA cm-2)
Applied Potential vs. Cell (V)
20
15
10
5
0
-5
-10
-0.8
-0.6
-0.4
-0.2
0
0.2
0.4

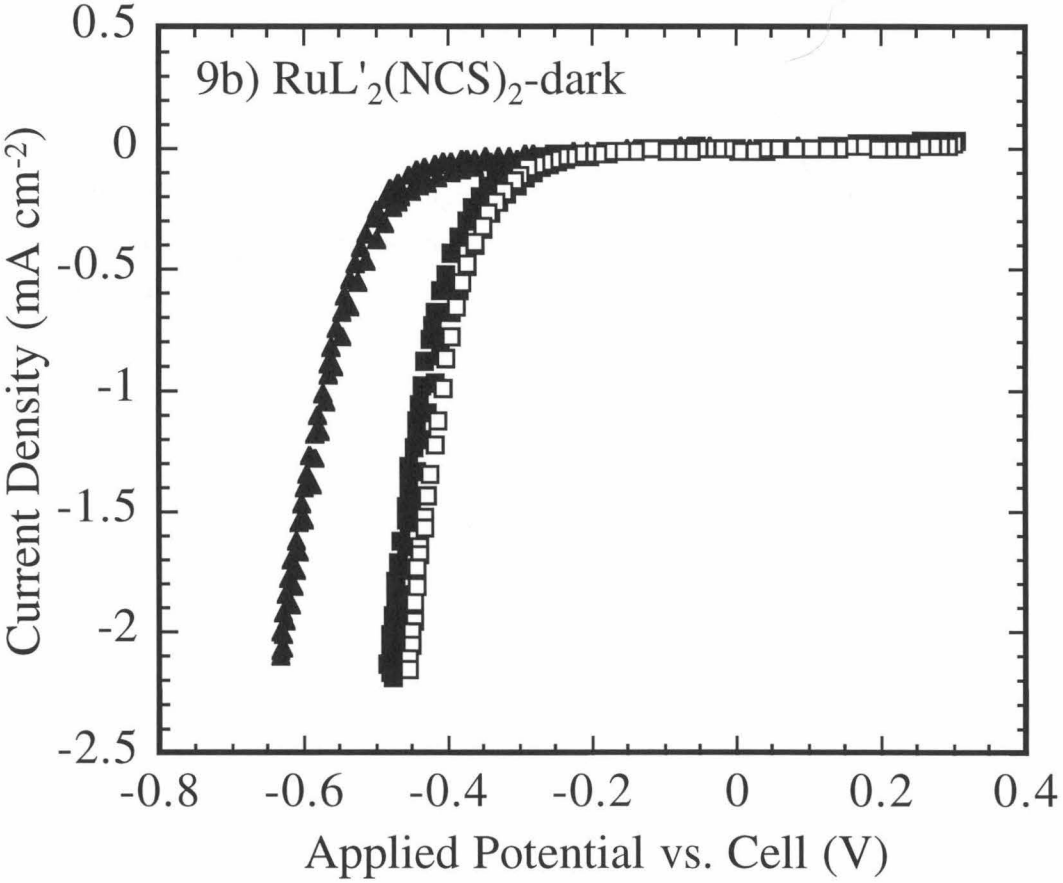
9b) RuL'2(NCS)2-dark
Current Density (mA cm-2)
Applied Potential vs. Cell (V)
0.5
0
-0.5
-1
-1.5
-2
-2.5
-0.8
-0.6
-0.4
-0.2
0
0.2
0.4

Table 2.5: Open circuit voltages and short-circuit current densities for $RuL'_2(NCS)_2$-TiO_2 electrodes as a function of Proton Sponge concentration at AM 1.0 illumination.

Proton Sponge Concentration	V_{oc} (average, mV)	J_{sc} (average, mA cm^{-2})
0 mM	520 ± 20	17 ± 2
1 mM	550 ± 20	18 ± 2
3 mM	590 ± 20	15 ± 1
10 mM	700 ± 20	7.2 ± 1

Table 2.5

E. Effect of pH on luminescence of the adsorbed dye--TiO_2/RuL'_3 electrodes

The effect of pH on the TiO_2 band edge positions was further examined through luminescence studies of the adsorbed dye. The quantum yield for luminescence (Φ) of the dye is given by eq. 2.1, where k_{rad} is the rate constant for radiative decay, k_{nrad} is the rate constant for non-radiative decay, and k_{inj} is the injection rate constant:

$$\Phi = \frac{k_{rad}}{k_{rad} + k_{nrad} + k_{inj}} \qquad (2.1)$$

If a shift in the band edge position causes a decrease in the injection rate constant, resulting in a decrease in photocurrent increase, the quantum yield for luminescence should increase, and thus luminescence intensity should increase as the pH is increased. If the decrease in current observed above was solely due to a loss of dye, the luminescence intensity should decrease due to the smaller amount of dye on the surface of the electrode.

Luminescence studies were first attempted on $TiO_2/RuL'_2(NCS)_2$ electrodes, but the luminescence intensity was very low and the peak was at a wavelength too high to detect with the system available. TiO_2/RuL'_3 electrodes were chosen as an alternate because of the strong luminescence of the L'_3 dyes. The luminescence results are shown in Figure 2.10a. When Proton Sponge is present, the luminescence intensity increases as expected. After 2 hours of immersion in the buffered solution after exposure to the Proton Sponge solution, the luminescence drops back down near the initial value. To minimize the effects of changing solutions, the luminescence experiment was repeated with a new electrode in a CH_3CN solution containing 0.001 M/0.001 M py/pyH^+. In this case, a few drops of glacial acetic acid were then added to the solution to neutralize the Proton Sponge. As shown in Figure 2.10b, an immediate decrease in the luminescence intensity was observed, consistent with an increased dye injection efficiency and a positive conduction band edge shift due to the decreased pH.

To make sure the effect of pH on the current-voltage characteristics was not limited to the $RuL'_2(NCS)_2$ system, J-E curves of the TiO_2/RuL'_3 electrodes were examined as a

function of pH. The results are shown in Figure 2.11. The photocurrents drop significantly when the Proton Sponge concentration is changed from 0 to 0.010 M. The large amount of hysteresis present makes it difficult to quantify the open-circuit voltage change although it appears to increase slightly. As in the previous case, the photocurrents decrease from their initial value on reimmersion and equilibration with the buffered solution. The dark curves show a large negative shift in the voltage when the electrode is exposed to Proton Sponge, similar to the behavior observed with the $TiO_2/RuL'_2(NCS)_2$ electrodes. The dark curves return to their previous position when the electrode is reimmersed in the buffered solution.

Figure 2.10: Luminescence data for a RuL'_3-sensitized TiO_2 electrode immersed in a CH_3CN solution buffered with 0.001 M/0.001 M py/pyH^+. Spectra are corrected for instrument response. (a) Open symbols represent data taken in the buffered solution, while the filled squares represent data taken in a solution with 0.010 M Proton Sponge added. Diamonds represent data taken before exposure to Proton Sponge; circles represent data taken after exposure to Proton Sponge. (b) Open squares represent data taken in a solution with 0.010 M Proton Sponge added; filled circles represent data taken in the same solution with a few drops of glacial acetic acid added.

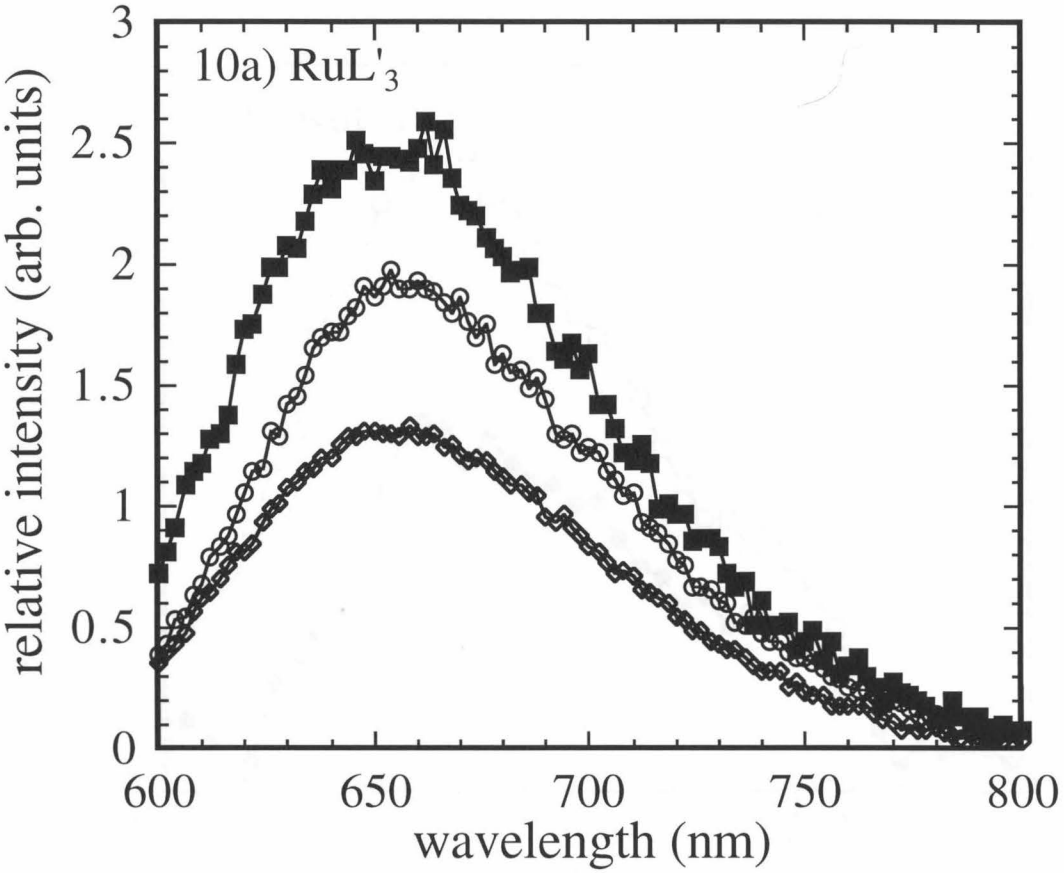
10a) RuL'3
relative intensity (arb. units)
wavelength (nm)
0
0.5
1
1.5
2
2.5
3
600
650
700
750
800

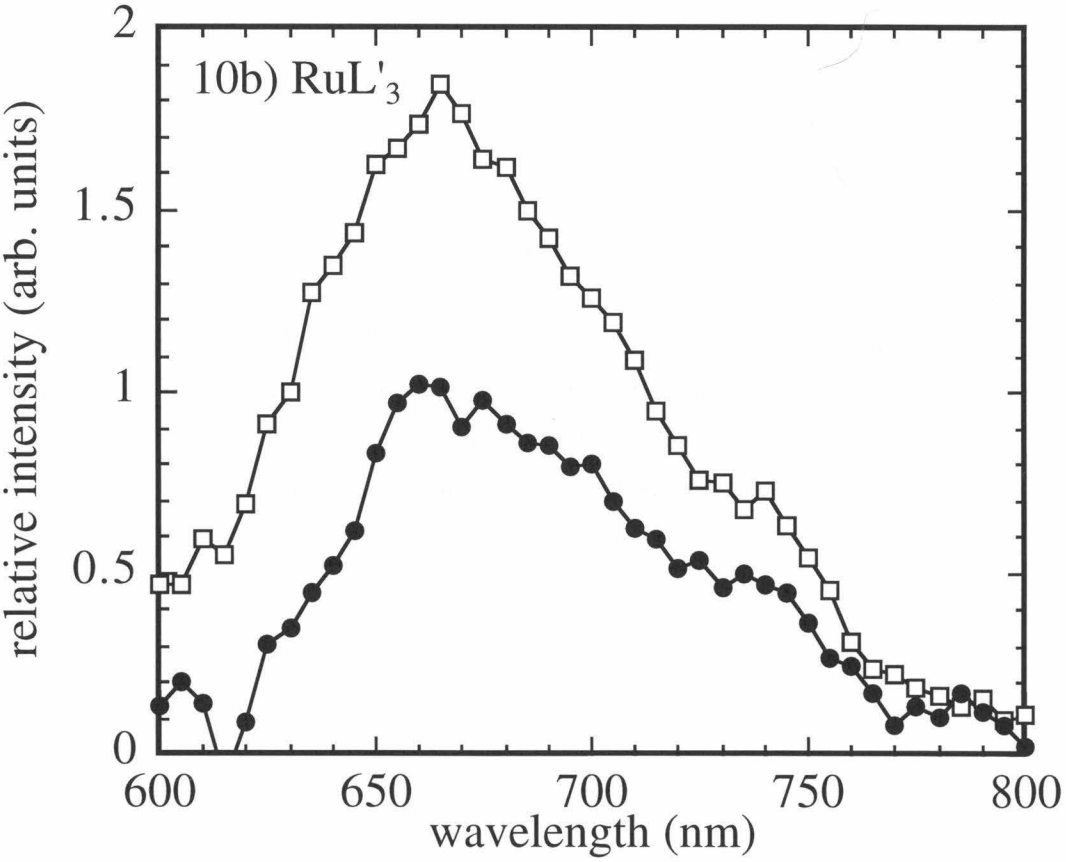
10b) RuL'3
relative intensity (arb. units)
wavelength (nm)
0
0.5
1
1.5
2
600
650
700
750
800

Figure 2.11: Current-potential data for a RuL'_3-sensitized TiO_2 electrode in CH_3CN/0.040 M I_2/0.500 M LiI/(0.001 M/0.001 M) py/pyH^+. Triangles represent data taken in solutions containing only the buffer, while circles represent data taken in a solution with 0.010 M Proton Sponge added. Filled triangles represent data taken before exposure to Proton Sponge; open triangles represent data taken after exposure to Proton Sponge. (a) Photocurrent-potential data. (b) Dark current-potential data.

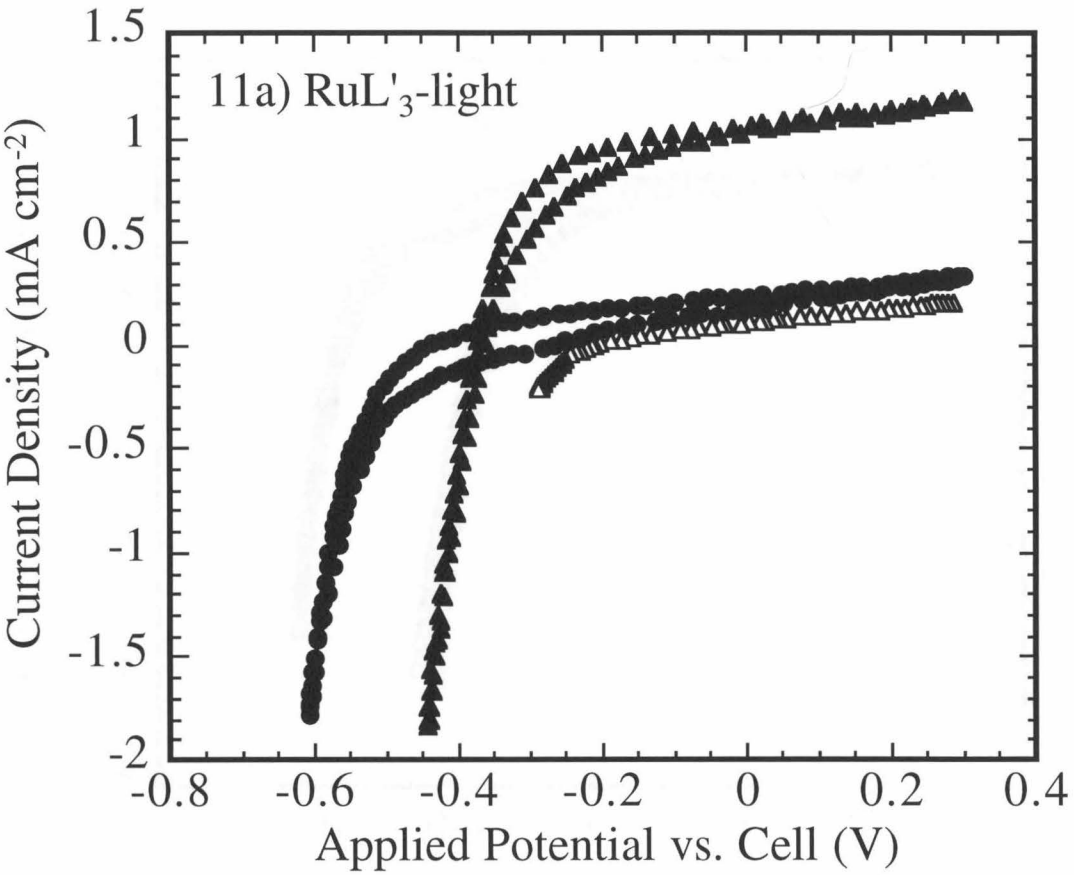
11a) RuL'3-light
Current Density (mA cm-2)
Applied Potential vs. Cell (V)
1.5
1
0.5
0
-0.5
-1
-1.5
-2
-0.8
-0.6
-0.4
-0.2
0
0.2
0.4

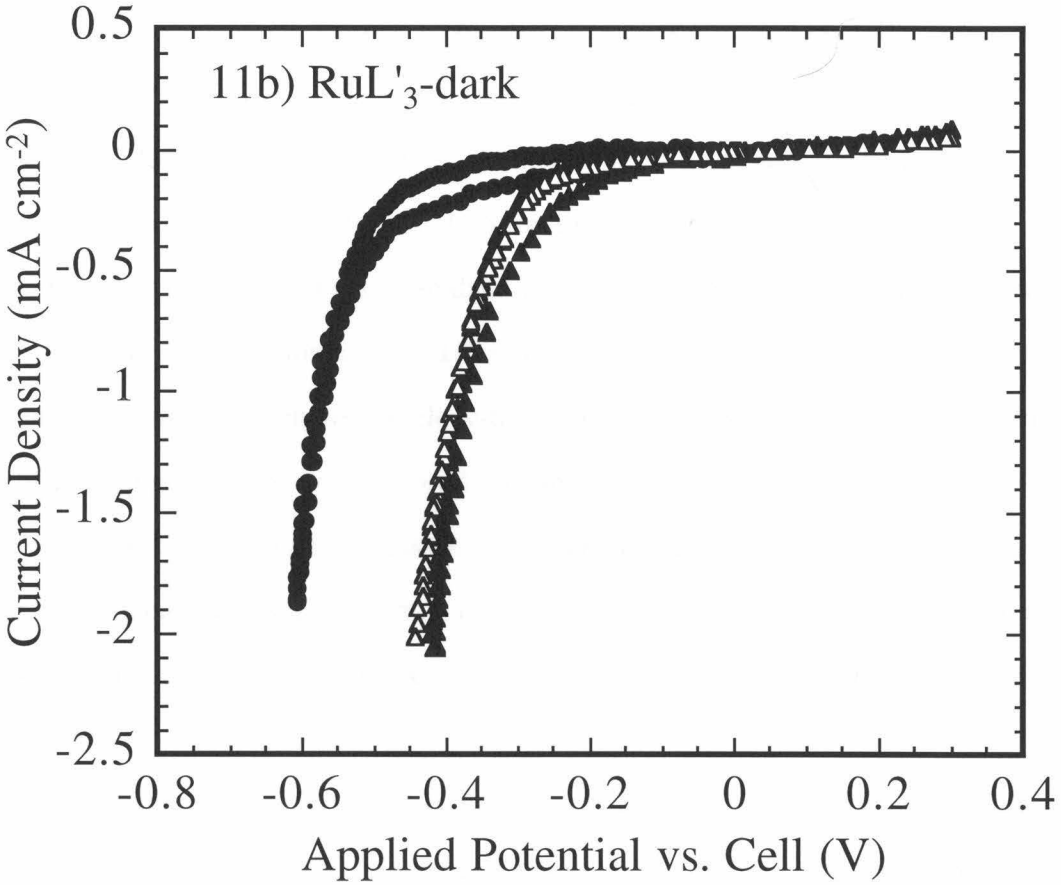
11b) RuL'3-dark
Current Density (mA cm-2)
Applied Potential vs. Cell (V)
0.5
0
-0.5
-1
-1.5
-2
-2.5
-0.8
-0.6
-0.4
-0.2
0
0.2
0.4

IV. Discussion

The data presented here provide a rational approach for design of more efficient nanoporous electrodes. As discussed above, the first requirement for this type of system is slow charge transfer kinetics between the back contact of the electrode and the sacrificial electron donor/acceptor in solution. This condition allows the separation of charge by a diffusion gradient rather than drift. A similar approach has been used in single crystal systems such as Si, in which ohmic selective back contacts were used in conjunction with Si electrodes with very high carrier lifetimes to produce efficient solar cells.[14]

The exploration of alternate dyes also seems promising. As expected, moving down the periodic table from ruthenium to osmium results in a second band in the absorption spectrum. Spectral response data shows that these excess photons absorbed also result in electron injection into the TiO_2. In theory, this effect would result in higher photocurrents from a continuous wavelength source such as the sun. Unfortunately, the effect of changing the metal on the ground state reduction potential must also be considered. The osmium dyes are less easily reduced and thus in certain cases are not efficiently regenerated by the iodine/iodide redox couple. However, careful design of the ligands or changing the solution redox species could improve the photoproperties of these solar cells.

Finally, the effect of solution pH on the interfacial energetics of the junction should be considered. The data demonstrates that changing the solution pH can have a profound effect on the current-voltage properties of the cell even in nonaqueous solutions. Increasing the pH has been shown to result in photovoltage increases of up to 200 mV. Again, though, this parameter needs to be optimized for the system studied. If the conduction band edge moves too negative as a result of changing the pH, the dye excited state may no longer be energetically capable of injecting an electron, and photocurrents will decrease. Another consideration is the stability of the dye adsorption at high pH. Design of a more robust linker on the dye ligands would alleviate this problem.

V. References

(1) Tan, M. X.; Laibinis, P. E.; Nguyen, S. T.; Kesselman, J. M.; Stanton, C. E.; Lewis, N. S. *Prog. Inorg. Chem.* **1994**, *41*, 21.

(2) O'Regan, B.; Grätzel, M. *Nature* **1991**, *353*, 737.

(3) Smestad, G.; Bignozzi, C.; Argazzi, R. *Solar Energy Mater. Solar Cells* **1994**, *32*, 259.

(4) Argazzi, R.; Bignozzi, C. A.; Heimer, T. A.; Castellano, F. N.; Meyer, G. J. *Inorg. Chem.* **1994**, *33*, 5741.

(5) Hagfeldt, A.; Grätzel, M. *Chem. Rev.* **1995**, *95*, 49; and references therein.

(6) Nazeeruddin, M. K.; Kay, A.; Rodicio, I.; Humphry-Baker, R.; Müller, E.; Liska, P.; Vlachopoulos, N.; Grätzel, M. *J. Am. Chem. Soc.* **1993**, *115*, 6382.

(7) Vinodgopal, K.; Hua, X.; Dahlgren, R. L.; Lappin, A. G.; Patterson, L. K.; Kamat, P. V. *Journal Of Physical Chemistry* **1995**, *99*, 10883.

(8) Lindstrom, H.; Rensmo, H.; Sodergren, S.; Solbrand, A.; Lindquist, S. E. *Journal Of Physical Chemistry* **1996**, *100*, 3084.

(9) Fitzmaurice, D. J.; Eschle, M.; Frei, H.; Moser, J. *Journal Of Physical Chemistry* **1993**, *97*, 3806.

(10) Heimer, T. A.; Bignozzi, C. A.; Meyer, G. J. *Journal Of Physical Chemistry* **1993**, *97*, 11987.

(11) Huang, S. Y.; Schlichthorl, G.; Nozik, A. J.; Grätzel, M.; Frank, A. J. *Journal Of Physical Chemistry B* **1997**, *101*, 2576.

(12) Sauvé, G.; Cass, M. E.; Lewis, N. S. *to be submitted* .

(13) Spitler, M. T. *J. Electroanal. Chem.* **1987**, *228*, 69.

(14) Tan, M. X.; Kenyon, C. N.; Wilisch, W. C. A.; Lewis, N. S. *J. Electrochem. Soc.* **1995**, *142*, L62.

Chapter 3: Stability of n-Si/CH_3OH Contacts as a Function of the Reorganization Energy of the Electron Donor

All or part of this text originally appeared in: Pomykal, K. E., Fajardo, A. M., and Lewis, N. S., *J. Phys. Chem.*, **1995**, *99(20)*, pp. 8302-8310.

I. Introduction

In this chapter and those following, experiments are conducted with single crystal electrodes and a more quantitative approach to analysis of semiconductor/liquid junction kinetics is used. This chapter addresses the experimental validation of one key aspect of the Marcus/Gerischer model for charge transfer at semiconductor/liquid contacts as first presented in Chapter 1. Based on the expression for κ_n (Equation 3.2 below), it is obvious that the interfacial charge capture rate of a photogenerated charge carrier in the semiconductor should be highly dependent on λ, the reorganization energy of the molecular reagent in the electrolyte solution.[1-6] Such a correlation is especially important for photogenerated minority carriers in n-type semiconductors because, as discussed earlier, many photoanodes are unstable in the presence of water and undergo deleterious photocorrosion or photopassivation reactions.[7-9] An improved understanding of the factors involved in determining interfacial charge transfer rate constants at semiconducting electrodes should allow more efficient scavenging of photogenerated charge carriers and should thereby enable the construction of more stable, efficient photoelectrochemical cells.

II. Theory

As discussed in Chapter 1, the interfacial charge transfer rate constant for hole transfer to an electron donor, k_{ht}, can be broken down into a vibrational term, ν_n, a nuclear term, κ_n, and an electronic term, κ_{el}:

$$k_{ht} = \nu_n \kappa_n \kappa_{el} \tag{3.1}$$

Only κ_n contains a term that is strongly dependent on the reorganization energy, λ:

$$\kappa_n = e^{-[(\Delta G^{o'} + \lambda)^2/4\lambda kT)]} \tag{3.2}$$

where $\Delta G^{o'}$ equals the driving force of the elementary charge transfer step at the semiconductor/liquid contact, T is the temperature, and k is the Boltzmann constant. Thus, the interfacial charge capture rate of a delocalized, photogenerated charge carrier in the

semiconductor should be highly dependent on λ, the reorganization energy of the molecular reagent in the electrolyte solution.[1-6] Such a correlation is especially important for photogenerated minority carriers in n-type semiconductors because most photoanodes are unstable in the presence of water and undergo deleterious photocorrosion or photopassivation reactions.[7-9] For hole transfer at an n-type semiconductor/liquid interface, $\Delta G^{o'}=\mathbf{E}^{o'}(A/A^-)-\mathbf{E}_{vb}$, where $\mathbf{E}^{o'}(A/A^-)$ is the standard electrochemical potential of the redox couple in solution, and $\mathbf{E}_{vb}$ is the energy of the valence band edge at the semiconductor surface.[5] At constant driving force with $\mathbf{E}_{vb}-\mathbf{E}^{o'}(A/A^-)<\lambda$, the interfacial charge transfer rate constant for capture of minority carriers should therefore decrease as λ increases.

Due to the difficulty in directly measuring k_{ht} for photogenerated minority carriers at an n-type semiconducting photoelectrode,[3,10-12] the approach used here was to evaluate the kinetic competition between passivation and stabilization reactions for a given semiconductor/solvent-electrolyte combination. Three different outer-sphere electron donors, with nearly constant electrochemical potentials but widely varying electron self-exchange rate constants (and thus widely varying λ values) (Table 3.1),[13,14] were used as stabilizing agents for n-Si/CH_3OH-electrolyte interfaces. Water was then deliberately introduced into the dried solvent to provide a controlled, known concentration of passivating agent against which kinetic competition by the various stabilizers could be measured (Figure 3.1). The concentration of redox stabilizer and the light intensity were also maintained constant throughout the photoelectrode experiments, and the driving force for charge transfer was determined to be essentially identical for all three contacts. Under these conditions, the Marcus/Gerischer theory predicts that stabilizers with smaller λ values should possess larger k_{ht} values and therefore should produce improved photoanode stability and increased solar energy conversion efficiency.

Prior work has investigated the electrode stability of some semiconductor/liquid contacts in the presence of redox stabilizers, but has produced mixed results when

compared to theoretical predictions. Gomes and coworkers have studied the stabilization of GaP by $Fe(CN)_6^{4-}$ and by Fe(II) (EDTA) using rotating ring-disk electrode methods.[15] However, comparisons between the two redox couples were performed at different pH values, resulting in a shift of the band edge positions that changed the driving force for charge transfer in the two systems.[16] Schneemeyer and Wrighton examined the efficiencies of $MoSe_2$ electrodes in contact with various halide ions in acetonitrile,[17] but charge transfer processes to the halide redox systems generally involve inner-sphere redox steps and/or multi-step pathways which are not amenable to straightforward comparisons with theory. Here these problems were minimized by use of simple outer-sphere one-electron transfer reagents with nearly identical redox potentials, and controlled amounts of passivation in non-aqueous solvents.

Figure 3.1: Pathways for hole transfer at the Si/liquid interface. $\mathbf{E}(A/A^-)$ is the electrochemical potential of the redox couple in solution, qV_n is defined as the difference in the bulk of the semiconductor between the conduction band energy, $\mathbf{E}_{cb}$, and the Fermi level, $\mathbf{E}_f$, and V_{bi} is the built-in voltage of the junction, which is equal in magnitude to the flat-band potential measured relative to the equilibrium potential of the solution. The barrier height, ϕ_b, is defined as the sum of V_{bi} and V_n. As the self-exchange rate constant of the redox couple A/A^- decreases, k_{ht} decreases, and the corrosion reaction becomes a viable pathway.

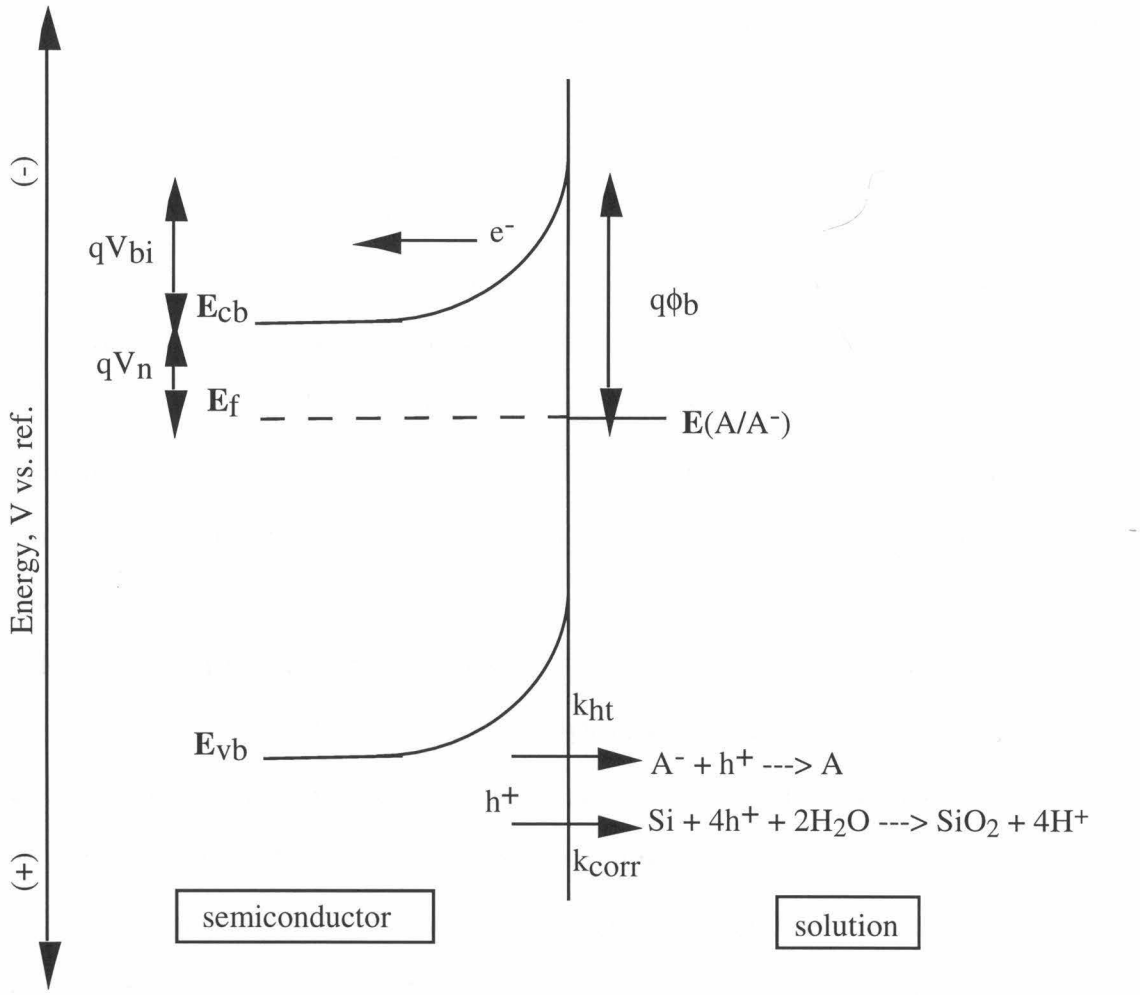
(-)
Energy, V vs. ref.
(+)
qVbi
Ecb
qVn
Ef
e-
qϕb
E(A/A-)
Evb
kht
A- + h+ ---> A
h+
Si + 4h+ + 2H2O ---> SiO2 + 4H+
kcorr
semiconductor
solution

Figure 3.1

III. Experimental Section

A. Electrodes

Single-crystal wafers of (100)-oriented n-type Si (2-6 Ω-cm resistivity, phosphorus-doped, obtained from Silicon Sense Inc., Nashua NH) were cut into squares approximately 4 mm on each side to provide specimens suitable for use as Si electrodes. Ohmic contacts were then formed by scratching Ga:In eutectic into the back (unpolished) side of the Si squares. The samples were attached to a Cu wire with Ag print (GC Electronics), and all metal contacts were insulated from the solutions through the use of white epoxy (1C; Dexter Corp.). The area of each electrode was determined by photographing the electrodes and their insulating epoxy, magnifying the pictures by a known amount, and using a digitizing program to determine the exposed geometric areas. The magnification factor was determined through simultaneous photographs of a microruler.

B. Redox Couples and Electrolytes

Purification of the solvents and electrolytes has been described previously.[18] All electrolytes were dried through heating under vacuum in a Schlenk tube, and methanol was dried over Mg methoxide and then distilled under nitrogen.

The trifluoromethanesulfonate (TFMS) salt of ruthenium(II) pentaammine 4,4'-bipyridine ($Ru(NH_3)_5(4,4'\text{-bipy})^{2+}$) was prepared according to the method of Fleischer and Lavallee,[19] with minor modifications to obtain the TFMS salt instead of the chloride salt. One equivalent of $[Ru(NH_3)_5Cl]Cl_2$ (Strem Chemical Co.) was dissolved in H_2O at 80 °C and two equivalents of AgTFMS (Aldrich) were added to precipitate two equivalents of AgCl. The solution was filtered and the filtrate was then degassed with argon. Zinc amalgam was added to the filtrate to reduce the ruthenium ion, forming $Ru(NH_3)_5H_2O^{2+}(aq)$. In another flask, 4 equivalents of 4,4'-dipyridyl hydrate (Aldrich) were dissolved in hot H_2O. To avoid formation of the unwanted dimeric compound $(Ru(NH_3)_5)_2(4,4'\text{-bipy})^{4+}$, the $Ru(NH_3)_5H_2O^{2+}(aq)$ solution was slowly added to the

dipyridyl solution through a cannula. The solvent was removed by vacuum distillation, and the resulting solid was dissolved in hot ethanol. Diethyl ether was added to precipitate $(Ru(NH_3)_5(4,4'\text{-bipy})(TFMS)_2$, which was isolated by filtration and was dried under vacuum.

The chloride salt of cobalt (II) *tris*(2,2'-bipyridine) ($Co(2,2'\text{-bipy})_3^{2+}$) was prepared by dissolving one equivalent of anhydrous cobalt(II) chloride in dry CH_3OH followed by addition of a solution that contained three equivalents of 2,2'-dipyridyl dissolved in dry CH_3OH.[20] The solvent was removed by vacuum distillation and the product was dried under vacuum.

1,1'-Dimethylferrocene Me_2Fc (Strem Chemical Co.) was purified by sublimation under vacuum. 1,1'-Dimethylferricenium (Me_2Fc^+) was available from previous experiments in this laboratory[18] or was generated *in situ* using controlled potential electrolysis in a three compartment cell. The oxidized forms of the Ru and Co redox couples, $Ru(NH_3)_5(4,4'\text{-bipy})^{3+}$ and $Co(2,2'\text{-bipy})_3^{3+}$, were produced electrochemically from the corresponding reduced Ru(II) and Co(II) complexes that were prepared as described above. Electrolysis was monitored both by counting the number of coulombs passed through the cell and by checking the cell potential and comparing it to the value expected from the Nernst equation, $E(A/A^-)=E^{o'}(A/A^-)+(RT/F)\ln([A]/[A^-])$. In this equation, $E(A/A^-)$ represents the redox potential of the solution, $E^{o'}(A/A^-)$ is the standard potential for reaction between A and A^-, R is the gas constant, and F is Faraday's constant.

Values of $E^{o'}(A/A^-)$ were measured using cyclic voltammetry at a 0.50 cm long, 0.5 mm diameter platinum wire in methanolic solutions of 1.00 M electrolyte and 0.0010-0.0015 M $[A^-]$ (Figure 3.2). A platinum foil was used as a counter electrode, and a CH_3OH SCE, consisting of mercury and mercurous chloride in a saturated methanolic solution of LiCl, was used as the reference electrode. This CH_3OH SCE had a potential of 0.0500 ± 0.0005 V vs. a normal SCE when measured in saturated aqueous KCl. Note that all potentials are referenced against this CH_3OH SCE unless noted otherwise. The

voltammetry experiments showed quasi-reversible behavior for all three redox couples, although the peak-to-peak separation was largest for $Co(2,2'\text{-bipy})_3^{3+/2+}$. $E^{o'}(A/A^-)$ was determined by estimating the mean of the anodic and cathodic peak positions (Table 3.1).

Figure 3.2: Cyclic voltammograms for the redox couples used in this work. (a) 0.0010 M Me_2Fc-1.00 M $LiClO_4$, scan rate = 50 mV s^{-1}; (b) 0.0010 M $Ru(NH_3)_5(4,4'\text{-bipy})^{2+}$-1.00 M LiTFMS, scan rate = 20 mV s^{-1}; (c) 0.0015 M $Co(2,2'\text{-bipy})_3^{2+}$-1.00 M LiCl, scan rate = 50 mV s^{-1}. The reference electrode in (a) and (b) was a methanol SCE; the reference electrode in (c) was a standard SCE. Anodic currents are positive in sign.

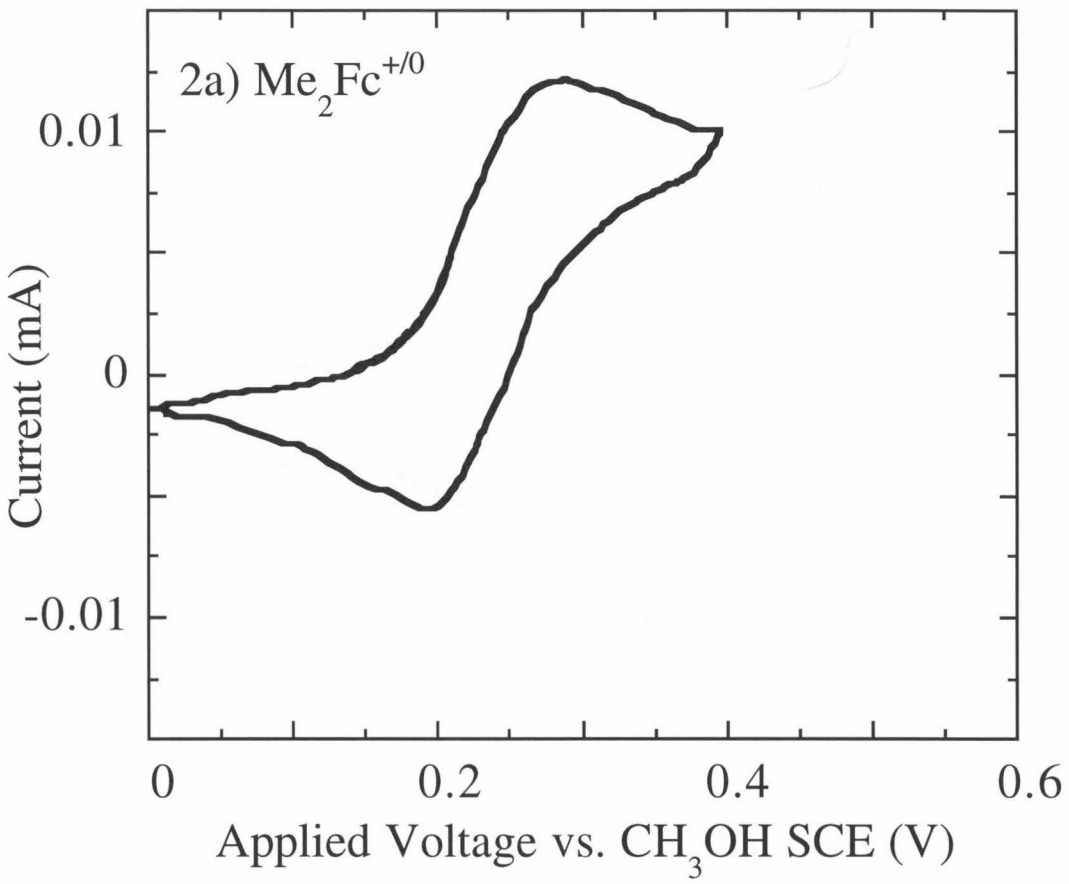
2a) $Me_2Fc^{+/0}$
0.01
0
-0.01
Current (mA)
0
0.2
0.4
0.6
Applied Voltage vs. CH_3OH SCE (V)

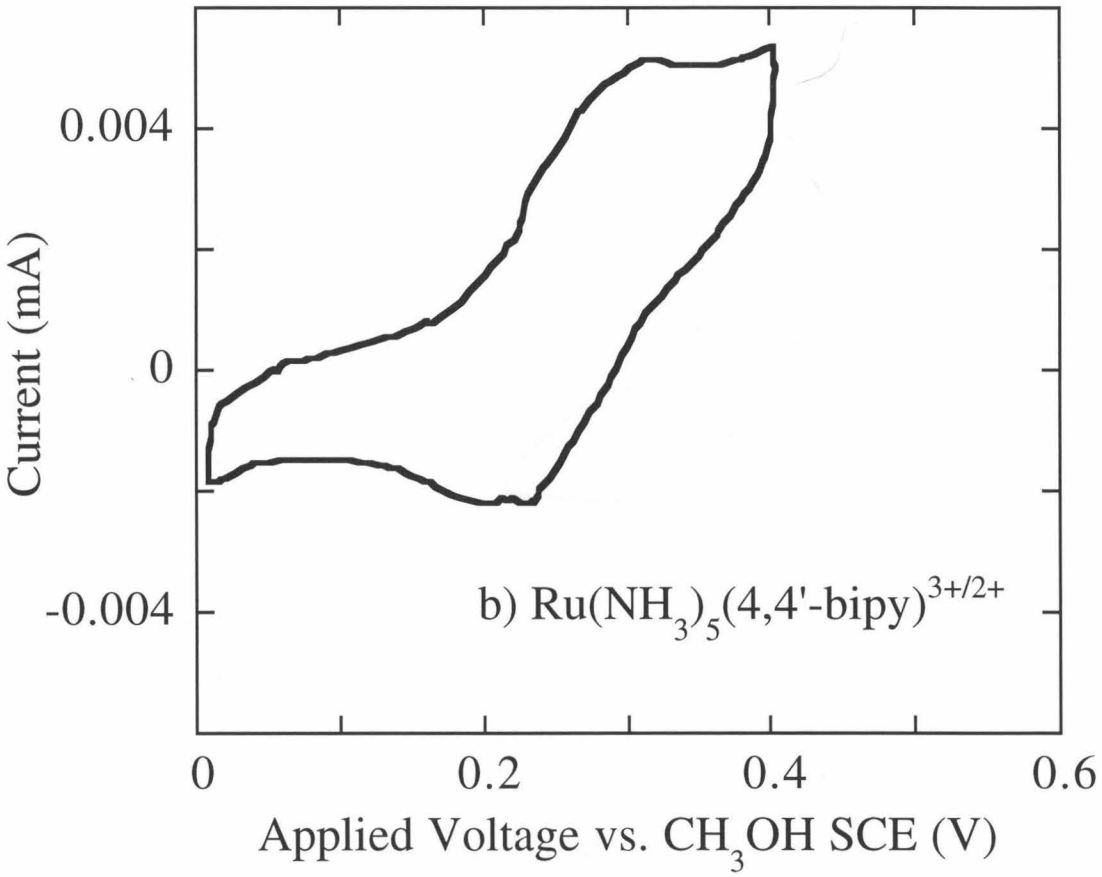
0.004
0
-0.004
Current (mA)
b) Ru(NH3)5(4,4'-bipy)3+/2+
0
0.2
0.4
0.6
Applied Voltage vs. CH3OH SCE (V)

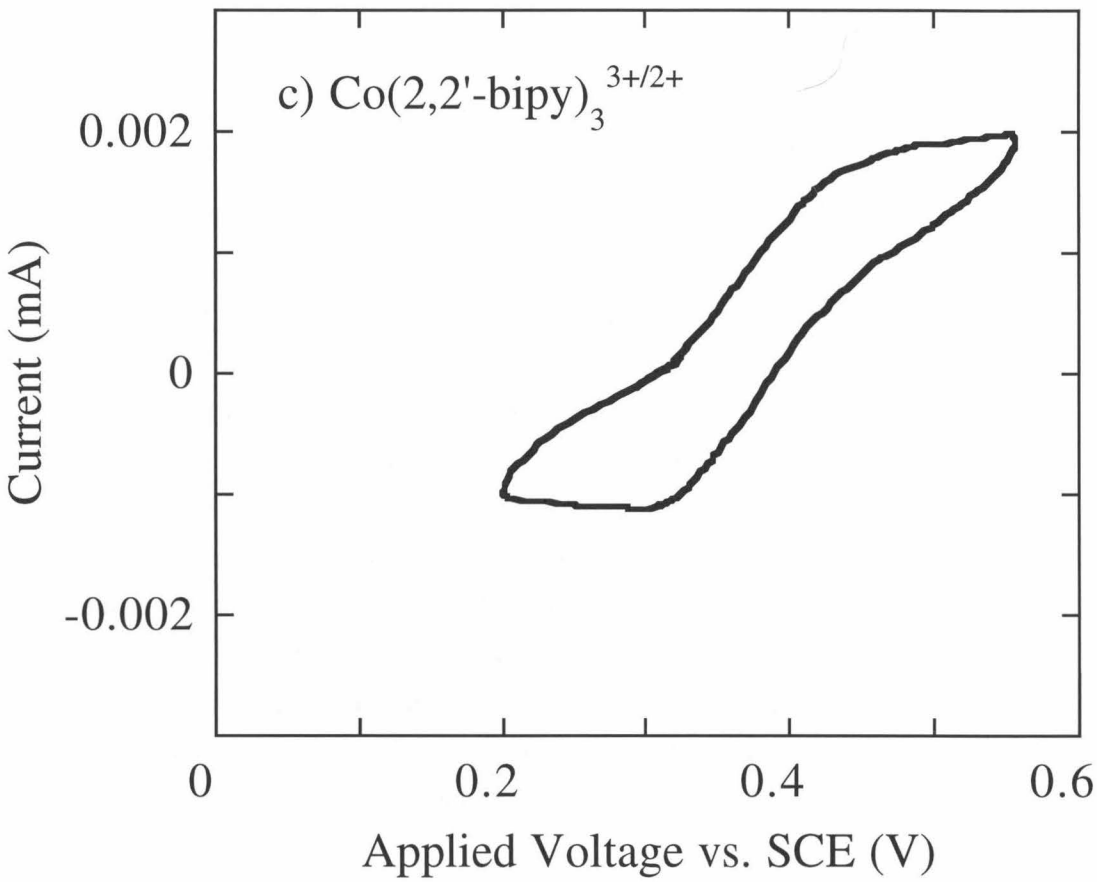
c) Co(2,2'-bipy)3 3+/2+
0.002
0
-0.002
Current (mA)
0
0.2
0.4
0.6
Applied Voltage vs. SCE (V)

Table 3.1. Standard reduction potentials and self-exchange rates for the redox couples used in this work.

a $Co(2,2'\text{-bipy})^{3+/2+}$ = cobalt(III/II) *tris*(2,2'-bipyridine); $Ru(NH_3)_5(4,4'\text{-bipy})^{3+/2+}$ = ruthenium(III/II) pentaammine 4,4'-bipyridine; $Me_2Fc^{+/0}$ = 1,1'-dimethylferricenium/1,1'-dimethylferrocene.

b The values for $E(A/A^-)$ have been corrected for the differences between the CH_3OH SCEs and a standard SCE to give approximate values vs. SCE. The values for the 3+/2+ redox couples have been corrected for charge effects not present in the $Me_2Fc^{+/0}$ redox couple using the correction to infinite ionic strength described by Gray et al.[31,32]

c from ref 53. The measurements of self-exchange rates were done in aqueous solutions; the self-exchange rate for $Ru(NH_3)_5(4,4'\text{-bipy})^{3+/2+}$ was estimated by the self-exchange rate for $Ru(NH_3)_5(py)^{3+/2+}$, where py = pyridine.

d from ref 54. The self-exchange rate was measured in methanol; the self-exchange rate for $Me_2Fc^{+/0}$ was estimated by the self-exchange rate of ferrocene/ferrocenium.

Redox Couples[a]	Self-Exchange Rate	$E^{o'}$(A/A$^-$),[b] V vs. SCE
$Co(2,2'\text{-bipy})_3^{3+/2+}$	50 $M^{-1}s^{-1}$ [c]	0.32
$Ru(NH_3)_5(4,4'\text{-bipy})^{3+/2+}$	1 x 10^6 $M^{-1}s^{-1}$ [d]	0.26
$Me_2Fc^{+/0}$	1 x 10^7 $M^{-1}s^{-1}$ [d]	0.20

Table 3.1

C. Electrochemical Methods

All electrochemical experiments were performed using a Model 173 potentiostat from EG&G Princeton Applied Research (PAR) with a Houston Omnigraphic 2000 recorder and an EG&G PAR Model 175 Universal Programmer. Data were collected in a three-electrode set-up that consisted of a Si working electrode, a Pt foil counter electrode, and a Pt wire reference electrode. The concentrations of the various components of the cell were 1.00 M electrolyte, 0.0010 M of the oxidized form of the redox couple (A), and 0.0240 M of the reduced form of the redox couple (A^-), unless otherwise specified. $LiClO_4$, LiTFMS, and LiCl were the electrolytes for the redox couples $Me_2Fc^{+/0}$, $Ru(NH_3)_5(4,4'\text{-bipy})^{3+/2+}$, and $Co(2,2'\text{-bipy})_3^{3+/2+}$, respectively.

An electrochemical cell was typically prepared by loading 5.00×10^{-4} moles of the reduced form of the desired redox couple and 2.00×10^{-2} moles of the electrolyte into the cell in an inert atmosphere drybox. The cell was then removed from the box and 20.0 mL of CH_3OH were added by syringe while purging the cell with nitrogen. All electrodes were also added and removed while purging the cell with nitrogen. To produce the oxidized form of the redox couple, a Pt foil working electrode and a CH_3OH SCE were immersed in the main solution. A smaller compartment that was separated from the main cell by a Nafion frit and that contained a Pt foil counter electrode was then filled with a 1.00 M solution of electrolyte in methanol. Voltages of 0.20-0.30 V vs. CH_3OH SCE were applied to produce anodic current until the oxidized form of the redox couple reached 0.0010 M, as monitored by the cell potential and by the number of coulombs passed through the cell. A controlled amount of water was then added to the cell, and the potential was allowed to stabilize. It was found that 5-10%(v/v) H_2O (2.8-5.6 M) was the optimal amount for the measurements described herein. At lower H_2O concentrations, the best stabilizing agents prevented essentially all electrode passivation for exposure times up to 60 min, while at higher H_2O concentrations, the poorest stabilizing agents were not able to

compete effectively enough with passivation to obtain meaningful current density vs. voltage curves.

To examine the current density vs. voltage (J-V) behavior of the silicon electrodes as a function of time, the CH_3OH SCE was replaced by a Pt wire, and the Pt foil was removed from the auxiliary electrode compartment and placed into the main cell compartment with the Si working electrode and the Pt wire reference electrode. The potential of the Si electrode was then continuously scanned from -0.500 V to +0.200 V vs. $E(A/A^-)$ at a rate of 50 mV s^{-1}, and the J-V curves were then recorded at predetermined time intervals. A constant light intensity from an ELH-type W-halogen bulb,[21] corresponding to an initial light-limited photocurrent density of $\approx$ 100 $\mu A\ cm^{-2}$, was maintained throughout the J-V scans. Through the course of these experiments, it was discovered that Si electrodes yielded much more stable J-V behavior if they were first immersed into CH_3OH-1.00 M $LiClO_4$-0.15 M Me_2Fc-0.002 M Me_2Fc^+ solutions with the potential being scanned from -0.500 V to +0.200 V vs. $E(A/A^-)$ at a photocurrent density of 100-200 $\mu A\ cm^{-2}$ for 5 minutes. For consistency, all measurements were therefore made after electrodes had undergone this J-V scanning procedure, and fresh electrodes were used for measurements in each new redox couple-electrolyte solution.

The rate of electrochemically-induced oxide growth was measured by X-ray photoelectron spectroscopy (XPS). At the beginning of each experiment, an HF-etched Si electrode was placed into a nitrogen-purged Schlenk tube and was then isolated from nominally identical Si samples that were to be used in the electrochemical measurements. A second HF-etched, $Me_2Fc^{+/0}$ treated Si electrode was then immersed into the electrolyte-redox couple solution for 10 seconds at open circuit and then was also placed into this Schlenk tube. A third, HF-etched, $Me_2Fc^{+/0}$-treated Si electrode was then placed into a solution containing the redox couple of interest. The potential of the working electrode was set to be equal to the redox potential of the cell, and the light intensity was periodically adjusted to maintain a constant photocurrent density of 100 $\mu A\text{-}cm^{-2}$, except when the

photocurrents became so low due to electrode passivation that the lamp could not be moved closer towards the cell without producing significant heating of the sample. J-V curves were taken at the beginning of each experiment and were also collected after a specified amount of time at short circuit. After sufficient passivation had occurred, the Si electrode was removed from the electrolyte solution and was rinsed with CH_3OH. The electrode was then placed into the Schlenk tube that contained the original control specimens. A series of experiments consisted of repeating this passivation procedure with fresh electrodes, all exposed to the electrolyte solution for a different amount of time. At the end of a series, the Schlenk tube was introduced into a nitrogen flushbox, and the electrodes were mounted onto UHV (ultra-high vacuum) sample studs for XPS measurements.

The electrodes were transferred to vacuum through a load-lock that connected directly to the flushbox. A Varian V-200 Turbo Pump was used to evacuate the load-lock to approximately 10^{-7} torr prior to introduction of the samples into the UHV system. The XPS experiments were conducted in an M-Probe Surface Spectrometer (Surface Science Instruments (Fisons)) that was pumped by a CTI-Cryogenics 8 cryo pump. The instrument was maintained at a base pressure of 5×10^{-10} torr, although the operating pressure was slightly higher (5×10^{-9} to 2×10^{-8} torr) due to slow outgassing of the epoxy around the sample. XP spectra were taken by exciting electrons with Al Kα (1486.6 eV) X-rays and collecting data with a hemispherical analyzer. The detector was positioned at an angle of 35° from the plane of the sample surface. Data collection and analysis were done with the M-Probe package software, version 3.4. This instrument has a sensitivity of approximately 0.1 monolayers and a resolution (full width at half maximum for the Au (4f)7/2 peak) of 0.88 ± 0.01 eV.[18] Spectra were taken for three different areas on each electrode surface to verify the uniformity of the oxide layer.

D. Barrier Height Measurements

The barrier heights of the various n-Si/CH_3OH junctions were calculated from the dependence of the differential capacitance of the semiconductor/liquid contact on the

potential applied to the electrode. In a conventional equivalent circuit for the semiconductor/liquid junction,[2] three capacitances are connected in series: the space-charge region capacitance (C_{sc}), the Helmholtz layer capacitance (C_H), and the diffuse layer capacitance (C_d). Since $C_{sc} << C_H$ and $C_{sc} << C_d$, the junction may be described as a single capacitor (C_{sc}) in parallel with a resistor, R_{sc}, where R_{sc} represents the voltage-dependent resistance to faradaic charge transfer. A resistor, R_s, in series with these two elements accounted for any resistances in the cell and completed the electrical circuit . The C_{sc} values could then be determined from experimental impedance data through the equation:

$$\omega C_{sc} = \frac{1 + (1 - 4(\frac{Z_{im}}{R_{sc}})^2)^{1/2}}{2Z_{im}} \qquad (3.3)$$

where Z_{im} is the imaginary part of the impedance for a given frequency f, where the angular frequency $\omega = 2\pi f$.

Impedance spectra were obtained on a computer-controlled Schlumberger Model 1260 frequency response analyzer equipped with a Model 1286 Electrochemical Interface. An impedance measurement consisted of 11 frequency sweeps from 10^6 to 10^3 Hz, each with a 10 mV peak amplitude ac voltage. Each sweep was performed using a different dc reverse bias relative to short circuit, with the dc bias increasing in 50 mV increments from 0.000 to 0.500 V. Results were obtained at seven frequencies between 5.012 kHz and 100 kHz. For each dc bias, the Nyquist plot of the real part of the impedance versus the imaginary part of the impedance was fit to a semicircle, and the diameter of this semicircle was taken to be R_{sc}. The C_{sc} values were then extracted and plotted vs. the applied dc bias, using the well-known Mott-Schottky relationship of C_{sc}^{-2} vs. V for a depleted semiconductor/liquid contact.[22,23] These Mott-Schottky plots were extrapolated to infinite C_{sc} ($C_{sc}^{-2}=0$) to obtain the flat-band potential, and thus the barrier height, ϕ_b, of the

solid/liquid contact. The desired driving force for minority carrier transfer was then calculated using the known value of the band gap, $\mathbf{E}_g$, of Si:

$$\mathbf{E}_{vb} - E^{o'}(A/A^-) = \mathbf{E}_g - q\phi_b - (\frac{RT}{nF})\ln(\frac{[A]}{[A^-]}) \quad (3.4)$$

Frequency dispersion in the capacitance-voltage data was observed when the concentration of acceptor species was 0.0010 M, so the concentrations of both forms of the redox couple were increased to 0.175 M in donor species and 0.009 M in acceptor species for all impedance measurements. This higher redox concentration produced minimal frequency dispersion and indicated that at low redox concentrations, effects of polarization at the counter electrode were important over this frequency range even under potentiostatic control. The final, higher concentration ratios produced approximately the same solution potential as that used in the J-V and stability experiments. A large (0.8-0.9 cm^2) Si electrode area was also required for impedance measurements in order to eliminate errors in the dopant densities calculated from the C^{-2} vs. V plots. Reliable Mott-Schottky plots could not be obtained for $Ru(NH_3)_5(4,4'\text{-bipy})^{3+/2+}$ because the redox system was not sufficiently soluble in CH_3OH, and the C_{sc} vs. V data obtained at the solubility limit of the redox couple were dependent on the ac measurement frequency.

IV. Results

A. Electrode Stability and Current Density vs. Voltage (J-V) Behavior as a Function of the Solvent Reorganization Energy of the Electron Donor

Figure 3.3 presents the J-V data for n-Si/CH_3OH-$Me_2Fc^{+/0}$, n-Si/CH_3OH-$Ru(NH_3)_5(4,4'\text{-bipy})^{3+/2+}$, and n-Si/$CH_3OH$-$Co(2,2'\text{-bipy})_3^{3+/2+}$ contacts. All three redox couples have very similar standard electrochemical potentials, and the concentration of the oxidized form of the redox pair was adjusted to produce identical Nernstian potentials for the three solutions of concern. n-Si/CH_3OH-$Me_2Fc^{+/0}$ contacts (Figure

3.3e) displayed J-V behavior in accord with that reported previously for this well-studied semiconductor/liquid contact. As expected from the similar redox potentials of $Ru(NH_3)_5(4,4'\text{-bipy})^{3+/2+}$ and $Me_2Fc^{+/0}$, very similar open circuit voltages (V_{oc}) and J-V characteristics were observed for these two redox couples. Use of $Co(2,2'\text{-bipy})_3^{3+/2+}$ yielded similar V_{oc} values but produced a somewhat lower fill factor than was observed for n-Si/CH_3OH-$Me_2Fc^{+/0}$ or n-Si/CH_3OH-$Ru(NH_3)_5(4,4'\text{-bipy})^{3+/2+}$ contacts. Pre-treating electrodes in the $Me_2Fc^{+/0}$ solutions[18] improved the fill factors as well as the stability of electrodes in contact with $Co(2,2'\text{-bipy})_3^{3+/2+}$ solutions (Figure 3.4).

n-Si/CH_3OH-$Me_2Fc^{+/0}$ and n-Si/CH_3OH-$Ru(NH_3)_5(4,4'\text{-bipy})^{3+/2+}$ contacts exhibited stable J-V behavior over 20 min time scales, but n-Si/CH_3OH-$Co(2,2'\text{-bipy})_3^{3+/2+}$ contacts were unstable even over these short time periods. Repeated attempts to thoroughly purify the solvent and to exclude water from the cells did not produce stability of n-Si/CH_3OH-$Co(2,2'\text{-bipy})_3^{3+/2+}$ contacts over 20 min time scales. As seen in Figure 3.3, Si electrodes became very resistive after 20 minutes of continuous scanning in the light in $Co(2,2'\text{-bipy})_3^{3+/2+}$. After 60 minutes, even electrodes cycled in CH_3OH-$Ru(NH_3)_5(4,4'\text{-bipy})^{3+/2+}$-2.8 M H_2O began to fail (Figure 3.3d). In contrast, n-Si/CH_3OH-$Me_2Fc^{+/0}$ junctions were stable for much longer periods even when no precautions were taken to exclude air or water from the components of the cell (Figure 3.3e, f). These observations qualitatively suggested that the three different redox systems had greatly different stabilities towards photopassivation reactions due to oxide growth.

Figure 3.3: J-V curves for untreated electrodes in CH_3OH. The electrolyte concentration was 1.00 M, the concentration of the reduced form of the redox couple was 0.0240 M, and the concentration of the oxidized form of the redox couple was 0.0010 M. All redox potentials are measured vs. a CH_3OH SCE: (a) Co(2,2'-bipy)$_3^{3+/2+}$-LiCl (E(A/A$^-$) = 300 ± 2 mV); (b) Co(2,2'-bipy)$_3^{3+/2+}$-LiCl, 2.8 M H_2O; (c) Ru(NH_3)$_5$(4,4'-bipy)$^{3+/2+}$-LiTFMS (E(A/A$^-$) = 225 ± 2 mV); (d) Ru(NH_3)$_5$(4,4'-bipy)$^{3+/2+}$-LiTFMS, 2.8 M H_2O; (e) $Me_2Fc^{+/0}$-$LiClO_4$ (E(A/A$^-$) = 180 ± 2 mV); (f) $Me_2Fc^{+/0}$-$LiClO_4$, 2.8 M H_2O. (a)-(f): solid line = start. (a), (b): dashed line = after 20 minutes of continuous scanning. (c)-(f): dashed line = after 60 minutes.

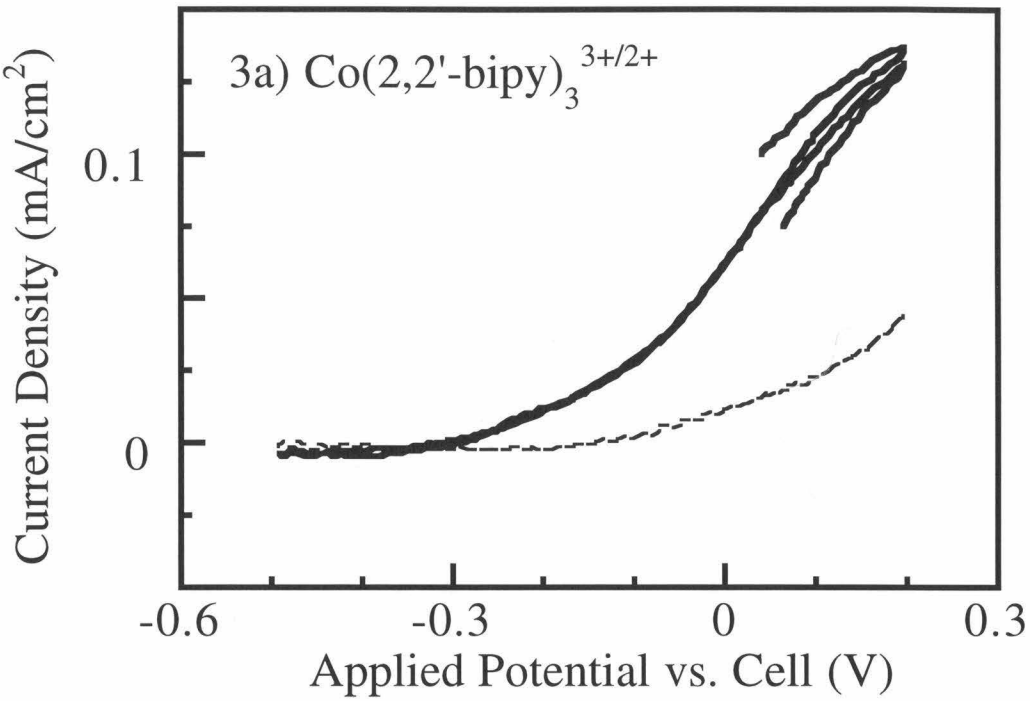
3a) Co(2,2'-bipy)$_3^{3+/2+}$
Current Density (mA/cm^2)
0.1
0
-0.6
-0.3
0
0.3
Applied Potential vs. Cell (V)

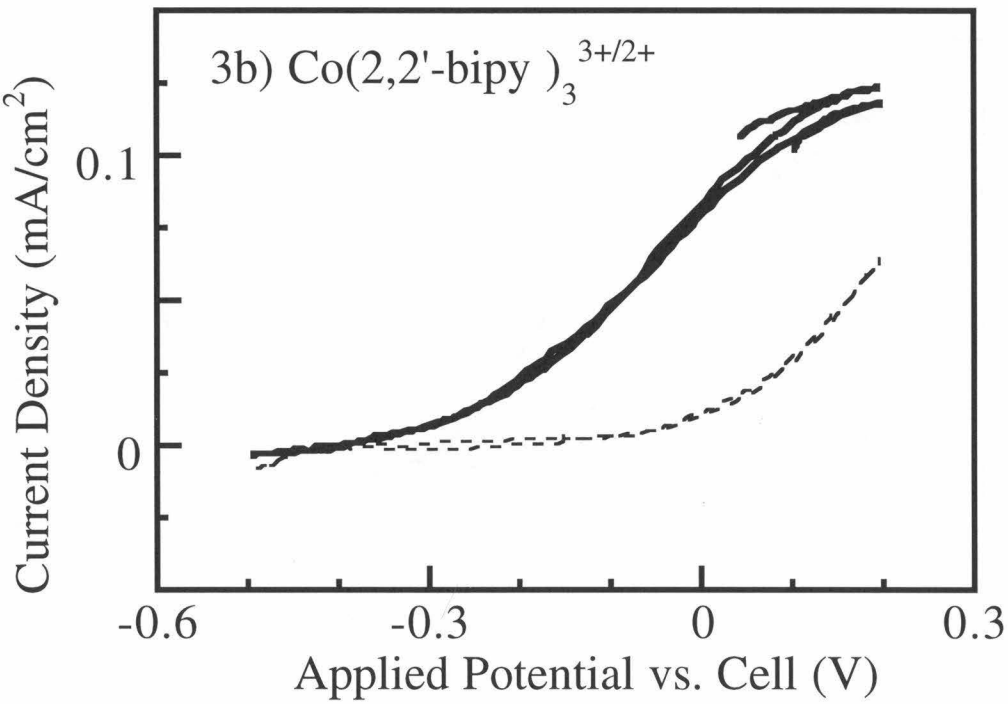
3b) Co(2,2'-bipy)$_3^{3+/2+}$
Current Density (mA/cm^2)
0.1
0
-0.6
-0.3
0
0.3
Applied Potential vs. Cell (V)

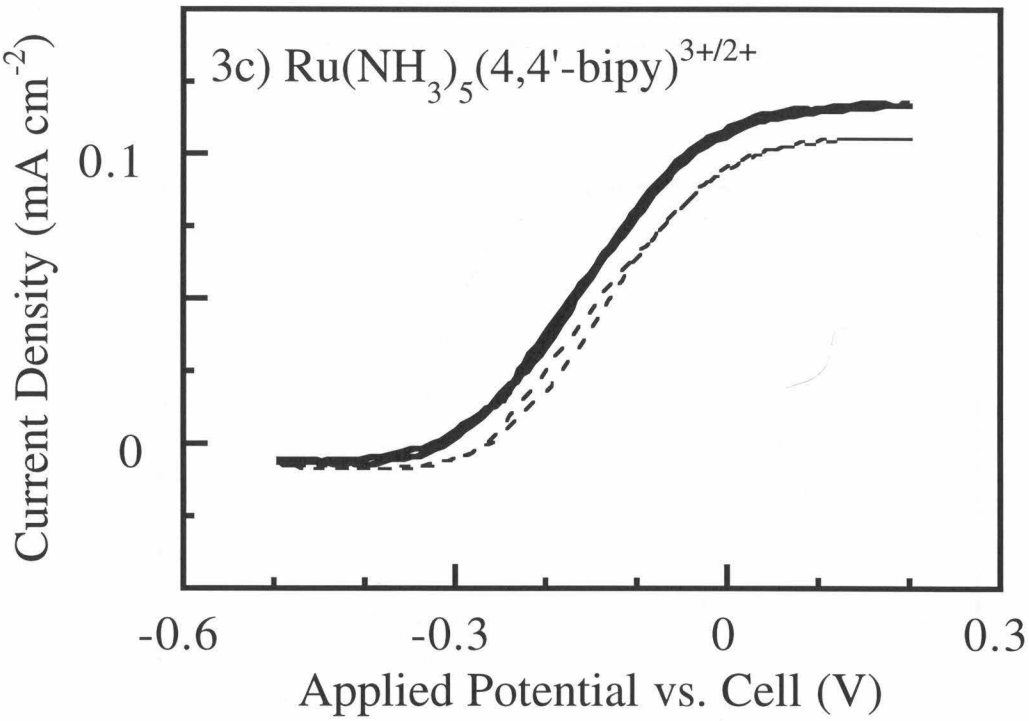
3c) Ru(NH3)5(4,4'-bipy)3+/2+
Current Density (mA cm-2)
0.1
0
-0.6
-0.3
0
0.3
Applied Potential vs. Cell (V)

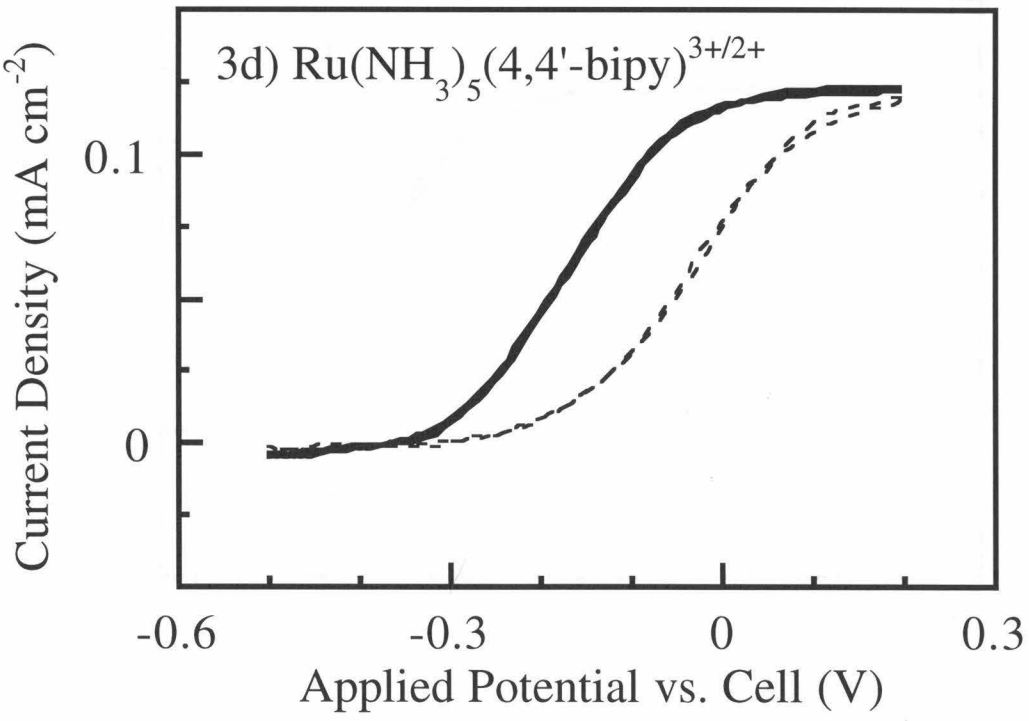
3d) Ru(NH3)5(4,4'-bipy)3+/2+
Current Density (mA cm-2)
0.1
0
-0.6
-0.3
0
0.3
Applied Potential vs. Cell (V)

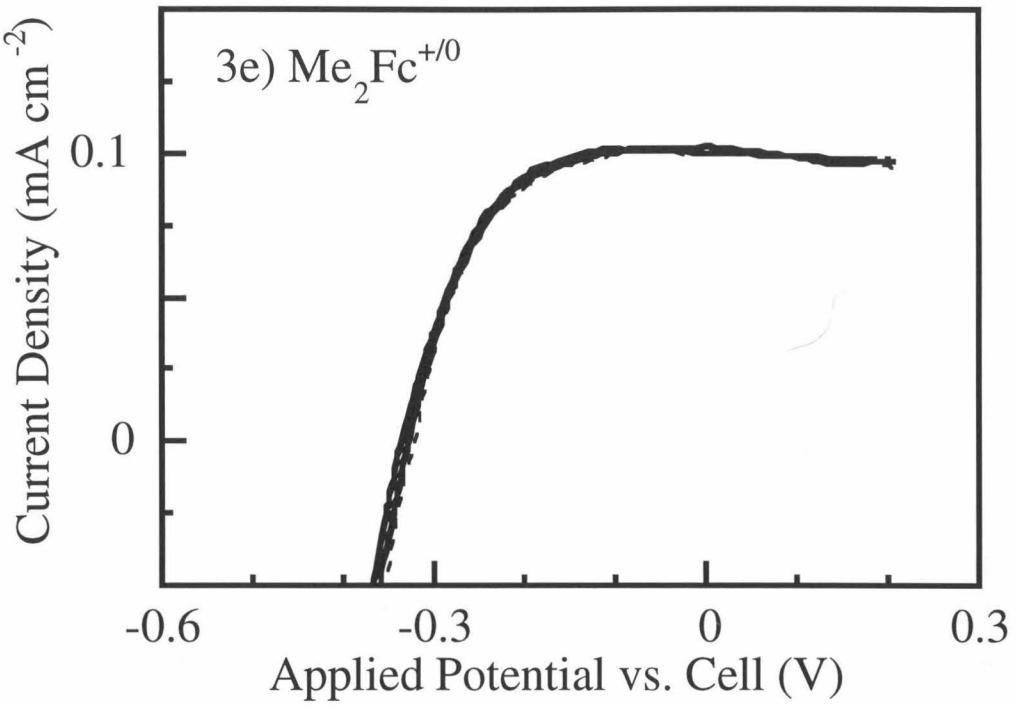
3e) $Me_2Fc^{+/0}$
Current Density (mA cm^{-2})
0.1
0
-0.6
-0.3
0
0.3
Applied Potential vs. Cell (V)

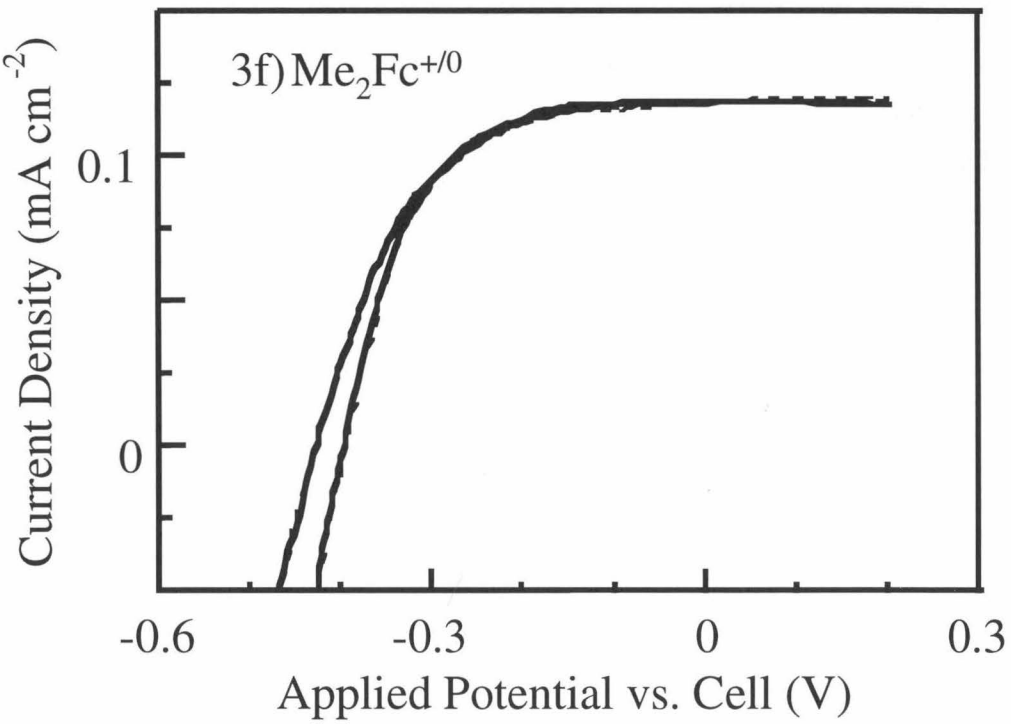
3f) $Me_2Fc^{+/0}$
Current Density (mA cm^{-2})
0.1
0
-0.6
-0.3
0
0.3
Applied Potential vs. Cell (V)

Figure 3.4: J-V curves for treated electrodes in CH_3OH. The electrolyte concentration was 1.00 M, the concentration of the reduced form of the redox couple was 0.0240 M, and the concentration of the oxidized form of the redox couple was 0.0010 M: (a) Co(2,2'-bipy)$_3^{3+/2+}$-LiCl (E(A/A$^-$) = 300 ± 2 mV); (b) Co(2,2'-bipy)$_3^{3+/2+}$-LiCl, 2.8 M H_2O; (c) Co(2,2'-bipy)$_3^{3+/2+}$-LiCl, 5.6 M H_2O; (d) Ru$(NH_3)_5$(4,4'-bipy)$^{3+/2+}$-LiTFMS (E(A/A$^-$) = 225 ± 2 mV); (e) Ru$(NH_3)_5$(4,4'-bipy)$^{3+/2+}$-LiTFMS, 2.8 M H_2O; (f) Ru$(NH_3)_5$(4,4'-bipy)$^{3+/2+}$-LiTFMS, 5.6 M H_2O; (g) $Me_2Fc^{+/0}$-$LiClO_4$ (E(A/A$^-$) = 180 ± 2 mV); (h) $Me_2Fc^{+/0}$-$LiClO_4$, 2.8 M H_2O; (i) $Me_2Fc^{+/0}$-$LiClO_4$, 5.6 M H_2O. (a)-(i): solid line = start. (a)-(c): dashed line = after 45 minutes of continuous scanning. (d)-(i): dashed line = after 60 minutes.

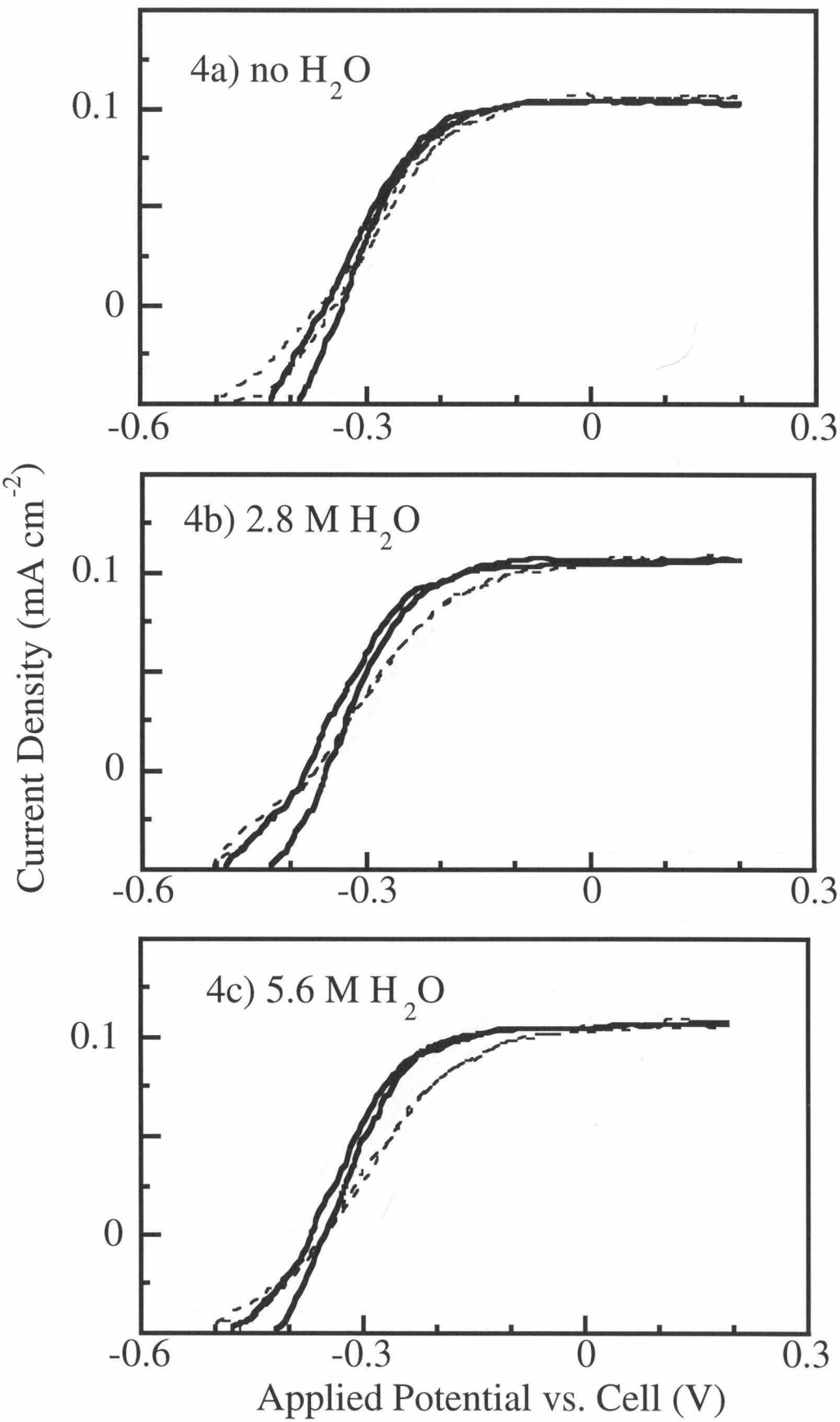
4a) no H_2O
4b) 2.8 M H_2O
4c) 5.6 M H_2O
0.1
0
-0.6
-0.3
0
0.3
Current Density (mA cm^{-2})
Applied Potential vs. Cell (V)

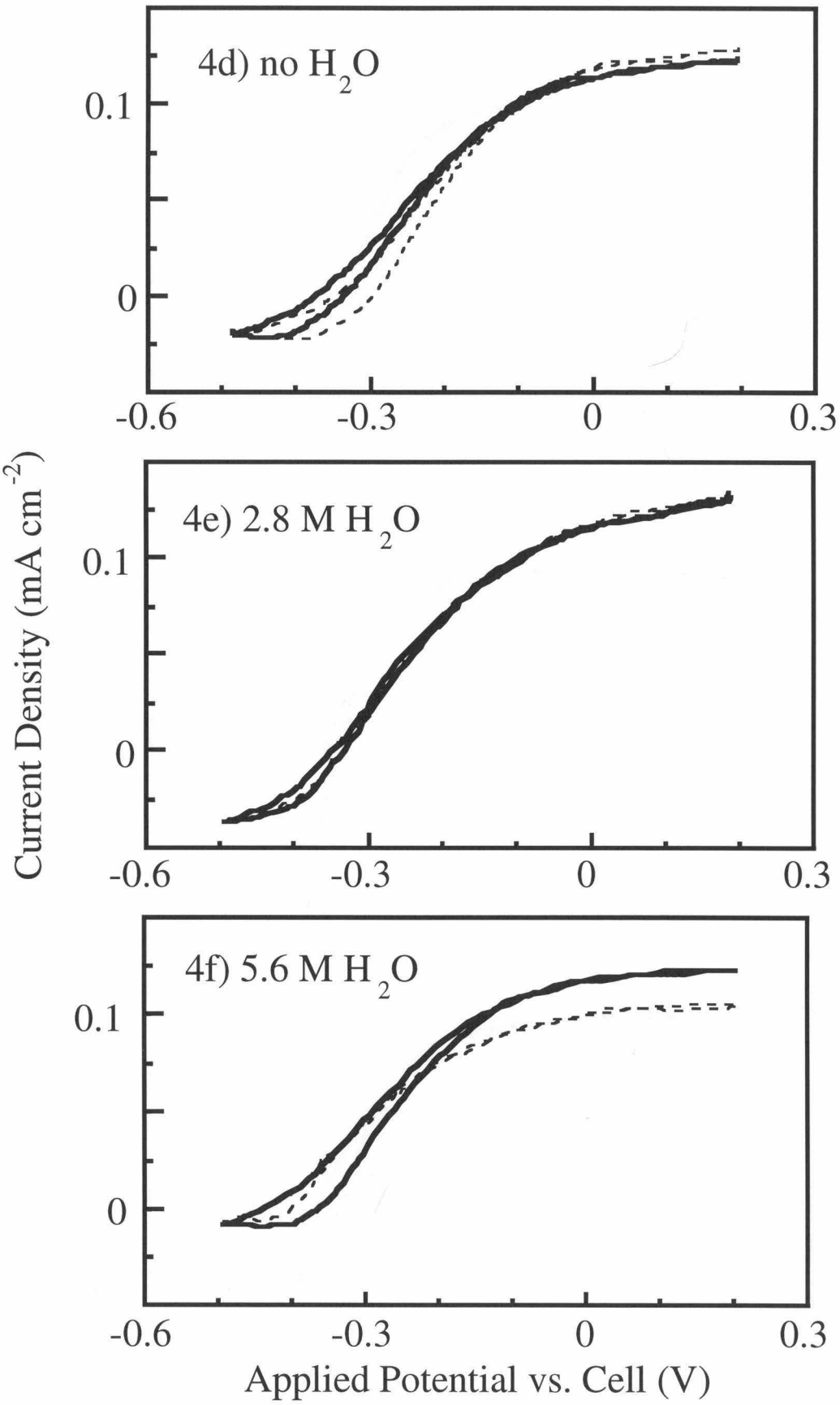
4d) no H2O
4e) 2.8 M H2O
4f) 5.6 M H2O
0.1
0
-0.6
-0.3
0
0.3
Current Density (mA cm-2)
Applied Potential vs. Cell (V)

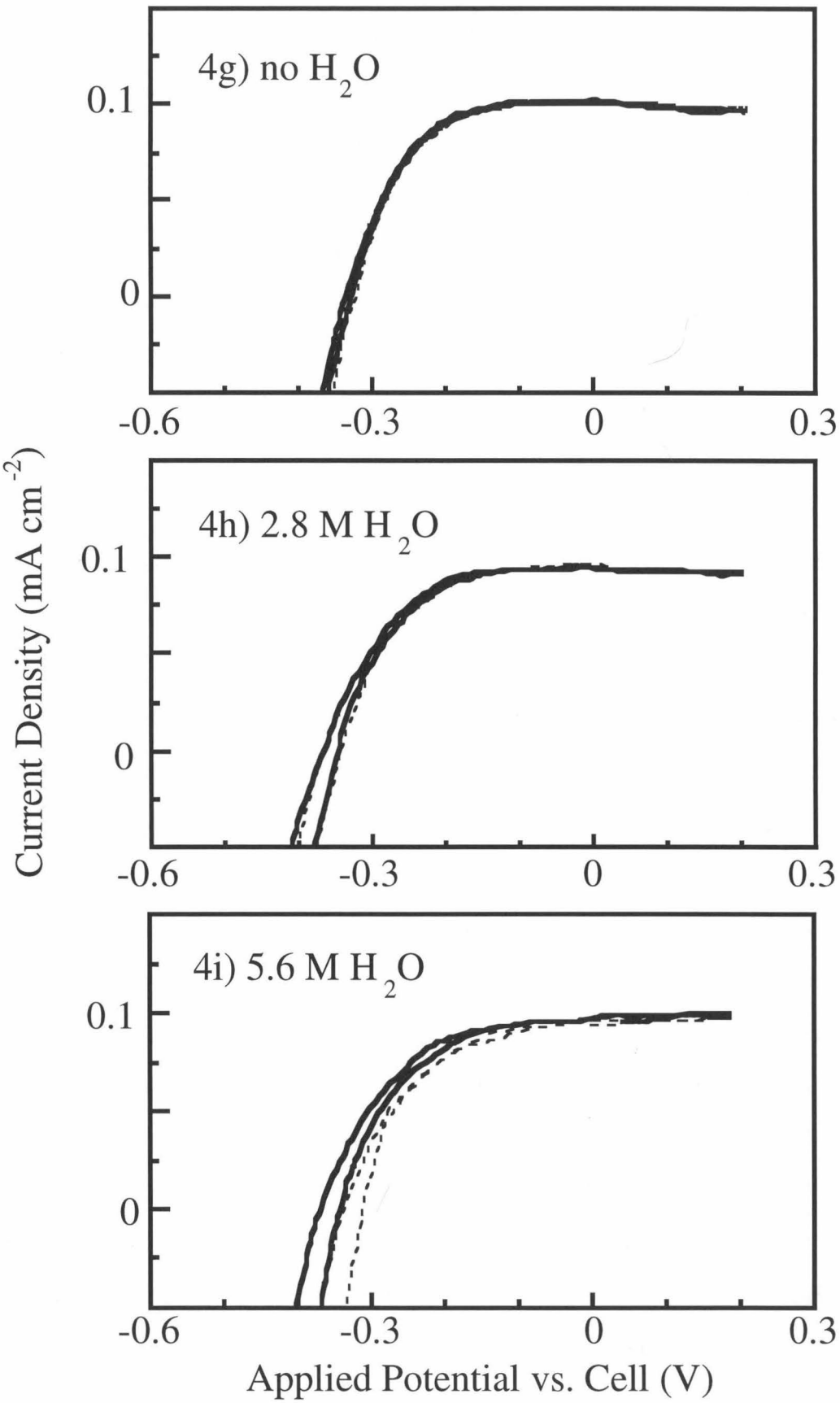
4g) no H2O
4h) 2.8 M H2O
4i) 5.6 M H2O
0.1
0
-0.6
-0.3
0
0.3
Current Density (mA cm-2)
Applied Potential vs. Cell (V)

B. XPS Investigations of Electrochemical Oxide Growth

A more quantitative measure of the relative photoanode stability was obtained by examining the rate of silicon oxide formation for the three various n-Si/CH_3OH contacts. These investigations were performed using a high-resolution X-ray photoelectron spectrometer that was interlocked to an anaerobic transfer system. This system allowed manipulation of samples, and their subsequent introduction into a UHV chamber, without significant oxide growth during the handling and analysis steps.

To minimize variations in stability that might have resulted from variations in the amount of uncontrolled, adventitious water in the solvent, the water concentration was deliberately increased to 2.8 M (5% by volume) in each system. This decreased the stability of the n-Si/CH_3OH-$Me_2Fc^{+/0}$ contact, but produced conditions under which the oxide growth rate could be evaluated and compared for all three redox couples. To minimize possible errors due to the increased resistance of the passivated electrode surface, stability measurements were restricted to time scales that produced relatively thin (<15 Å) oxide layers. During oxide growth, the electrode potential was maintained at short circuit vs. the Nernstian potential of the cell to ensure similar driving forces and similar photogenerated hole concentrations at the electrode surface for all three redox systems.

Survey scans to determine the elemental composition of the surface were taken before focusing on the Si region to determine the amount of oxide growth. These survey scans typically showed peaks corresponding to Si, O, and C. No Fe, Ru, or Co was detected on the surface within the instrument sensitivity limit of less than 0.1 monolayers.

Figure 3.5 shows representative XPS data of the Si 2p region for $Me_2Fc^{+/0}$-treated Si electrode surfaces that had been exposed to CH_3OH-2.8 M H_2O solutions, each containing 0.0240 M of one of the three redox couple donors and 0.0010 M of the corresponding acceptor. Also included in Figure 3.5 are XPS data for n-Si/CH_3OH-2.8 M H_2O-0.0960 M $Co(2,2'\text{-bipy})_3^{2+}$-0.0040 M $Co(2,2'\text{-bipy})_3^{3+}$ contacts. Samples that had been reserved as controls, or had only been immersed at open circuit into the electrolyte

solutions, showed no detectable oxide and only displayed the characteristic Si 2p doublet at a binding energy of 99.7 ± 0.2 eV (Figure 3.5, dashed lines). In contrast, after passage of anodic photocurrent in the three solutions, all XP spectra showed a new peak with a binding energy approximately 3.7 eV larger than the substrate Si 2p peak (Figure 3.5). Since these electrodes were held at short circuit instead of continuously scanned, the current decayed more quickly, especially for electrodes in contact with the Co(2,2'-bipy)$_3^{3+/2+}$ redox couple, than it did in the J-V experiments described above. J-V curves for the Co(2,2'-bipy)$_3^{3+/2+}$ redox couple are shown in Figure 3.6 for both n-Si/CH_3OH-2.8 M H_2O-0.0240 M Co(2,2'-bipy)$_3^{2+}$-0.0010 M Co(2,2'-bipy)$_3^{3+}$ and n-Si/CH_3OH-2.8 M H_2O-0.0960 M Co(2,2'-bipy)$_3^{2+}$-0.0040 M Co(2,2'-bipy)$_3^{3+}$ cells.

The peak position of the higher binding energy signal of Si in the XPS data has been well-documented to be characteristic of SiO_2. Using a peak fitting program to determine the relative areas of the Si 2p substrate and SiO_2 peaks, the thickness of the oxide was calculated as:

$$d = (\lambda_{es} \times \cos\theta)[\ln(1 + (\frac{I^{\circ}_S}{I^{\circ}_A})(\frac{I_A}{I_S}))] \qquad (3.5)$$

where d is the oxide thickness, λ_{es} is a tabulated attenuation factor based on the escape depth of the photoelectrons produced in the material of study, and θ is the angle from the surface of the sample to the detector relative to normal incidence.[24,25] $I^{\circ}_S / I^{\circ}_A$ is an instrument normalization factor related to the ratio of the signals expected for pure Si vs. pure SiO_2, and I_A and I_S are the measured areas of the SiO_2 and Si peaks, respectively. Inserting the known parameters for the instrument and samples used in these experiments (λ=26Å,[26] I°_S/I°_A=1.3,[27] and θ=55°) allowed calculation of the equivalent thickness of the oxide overlayer. This value is designated as an equivalent thickness because use of

Equation 3.5 implicitly assumes that the overlayer is homogeneous and uniform over the electrode surface.[24,25]

Figure 3.7 shows a summary of the oxide thickness data deduced from application of Equation 3.6 to the XPS data. Contact with CH_3OH-H_2O-$Co(2,2'\text{-bipy})_3^{3+/2+}$ clearly produced the most rapid Si oxide growth, while CH_3OH-H_2O-$Me_2Fc^{+/0}$ and CH_3OH-H_2O-$Ru(NH_3)_5(4,4'\text{-bipy})^{3+/2+}$ contacts were similar to each other and produced significantly less oxide over the same time period. The error bars in the plot are representative of both the variation between the measurements for the three areas of each electrode and the possible change in θ due to difficulties in mounting the electrodes perfectly parallel to the sample studs. Although not pictured in Figure 3.7, the line representing XPS data for n-Si/CH_3OH-2.8 M H_2O-0.0040 M $Co(2,2'\text{-bipy})_3^{3+}$-0.0960M $Co(2,2'\text{-bipy})_3^{2+}$ contacts fell between the line for CH_3OH-2.8 M H_2O-0.0010 M $Ru(NH_3)_5(4,4'\text{-bipy})^{3+}$-0.024 M $Ru(NH_3)_5(4,4'\text{-bipy})^{2+}$ contacts and CH_3OH-2.8 M H_2O-0.0010 M $Co(2,2'\text{-bipy})_3^{3+}$-0.0240M $Co(2,2'\text{-bipy})_3^{2+}$ contacts. These oxide formation data were therefore in accord with the stability trends deduced from the time-dependence of the J-V data, and indicated that the $Me_2Fc^{+/0}$ and $Ru(NH_3)_5(4,4'\text{-bipy})^{3+/2+}$ redox systems significantly improved the electrode stability relative to the $Co(2,2'\text{-bipy})_3^{3+/2+}$ redox system.

Figure 3.5: XP Spectra of Si photoelectrodes. (a) electrode cycled in $Me_2Fc^{+/0}$ solution (0.0010 M / 0.0240 M), 100 min.; (b) electrode cycled in $Ru(NH_3)_5(4,4'\text{-bipy})^{3+/2+}$ (0.0010 M / 0.0240 M), 60 min.; (c) electrode cycled in $Co(2,2\text{-bipy})_3^{3+/2+}$ (0.0010 M / 0.0240 M), 20 min.; (d) electrode cycled in $Co(2,2\text{-bipy})_3^{3+/2+}$ (0.0040 M / 0.0960 M), 30 min. The XP spectrum of a freshly etched n-Si electrode is included as a dashed line in panel.

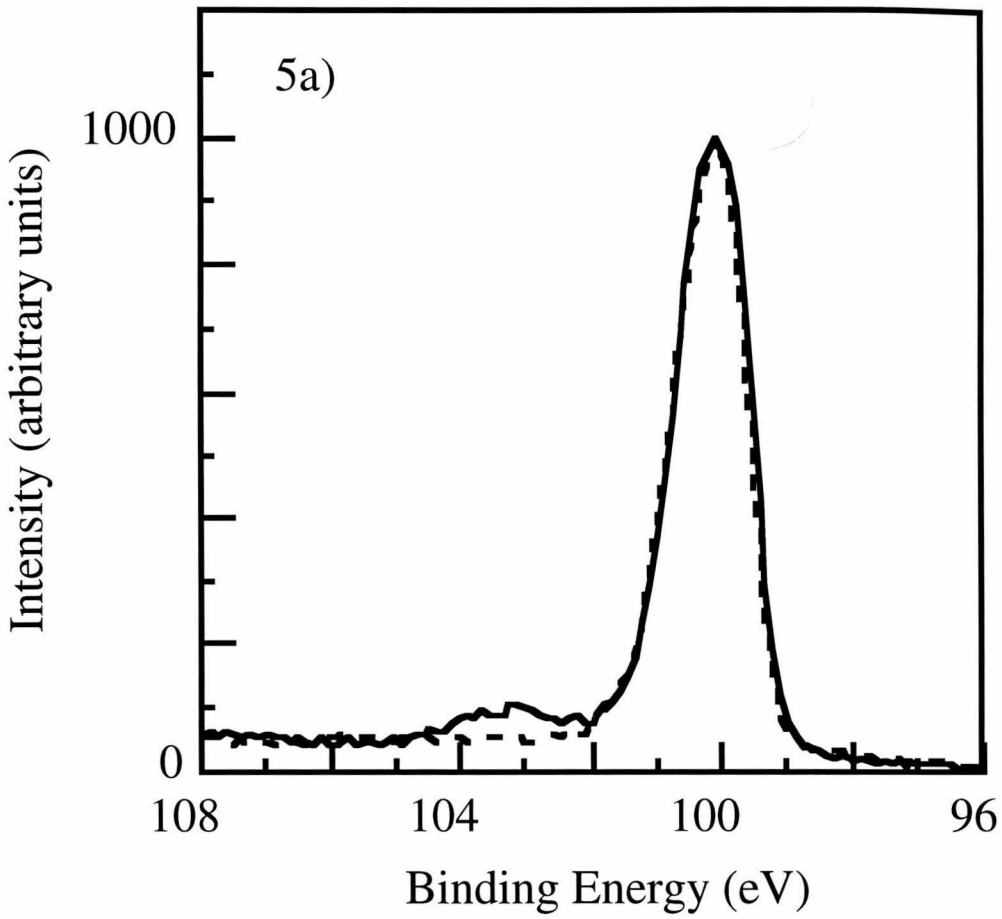
5a)
1000
0
Intensity (arbitrary units)
108
104
100
96
Binding Energy (eV)

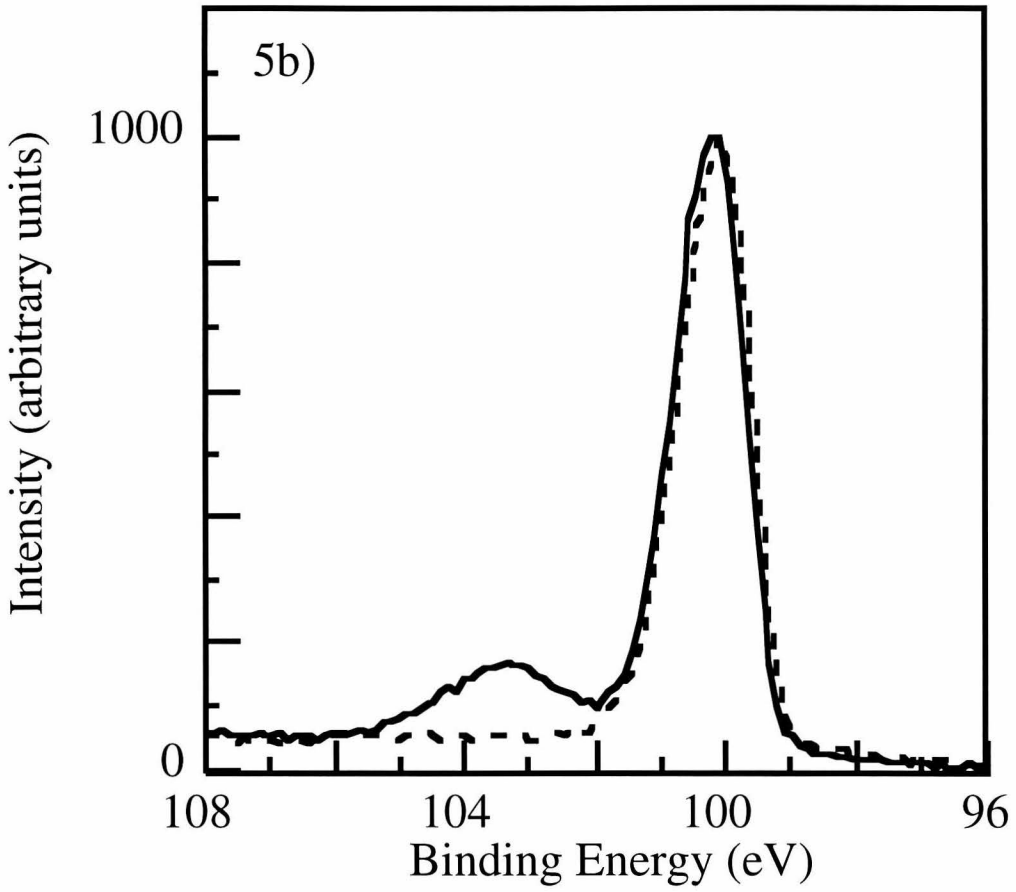
5b)
1000
0
Intensity (arbitrary units)
108
104
100
96
Binding Energy (eV)

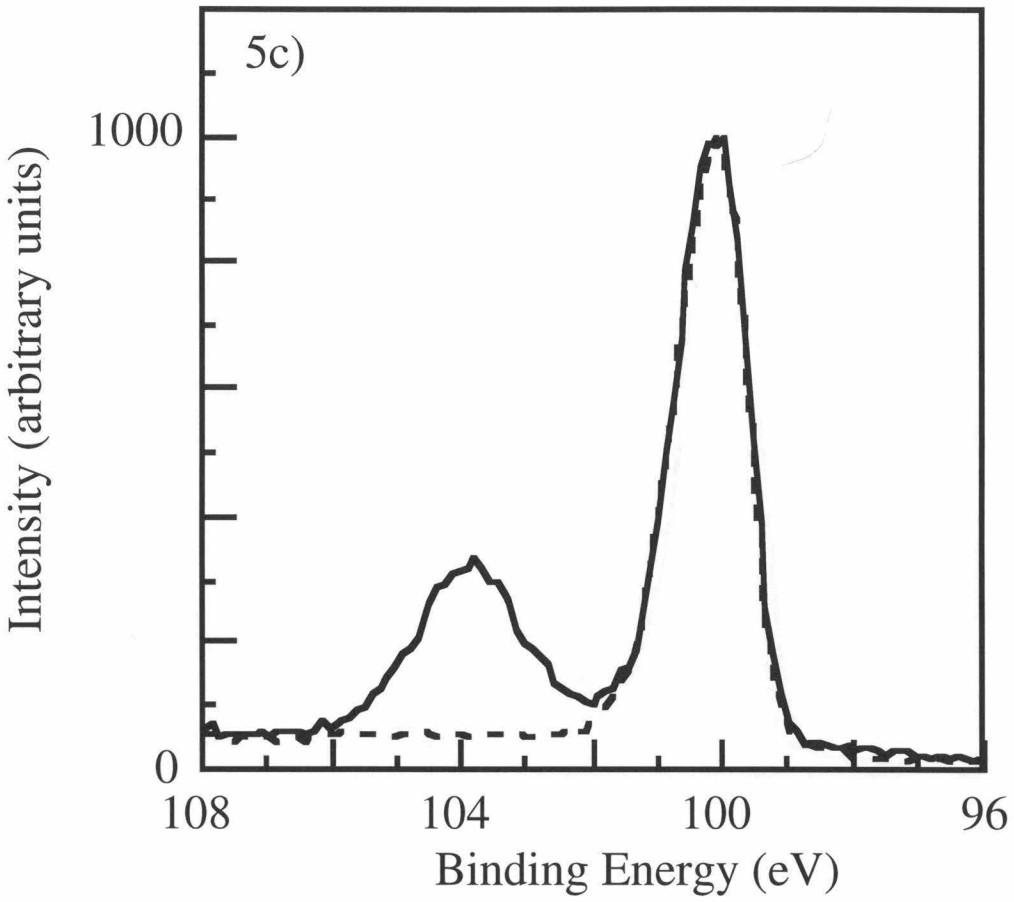
5c)
1000
0
Intensity (arbitrary units)
108
104
100
96
Binding Energy (eV)

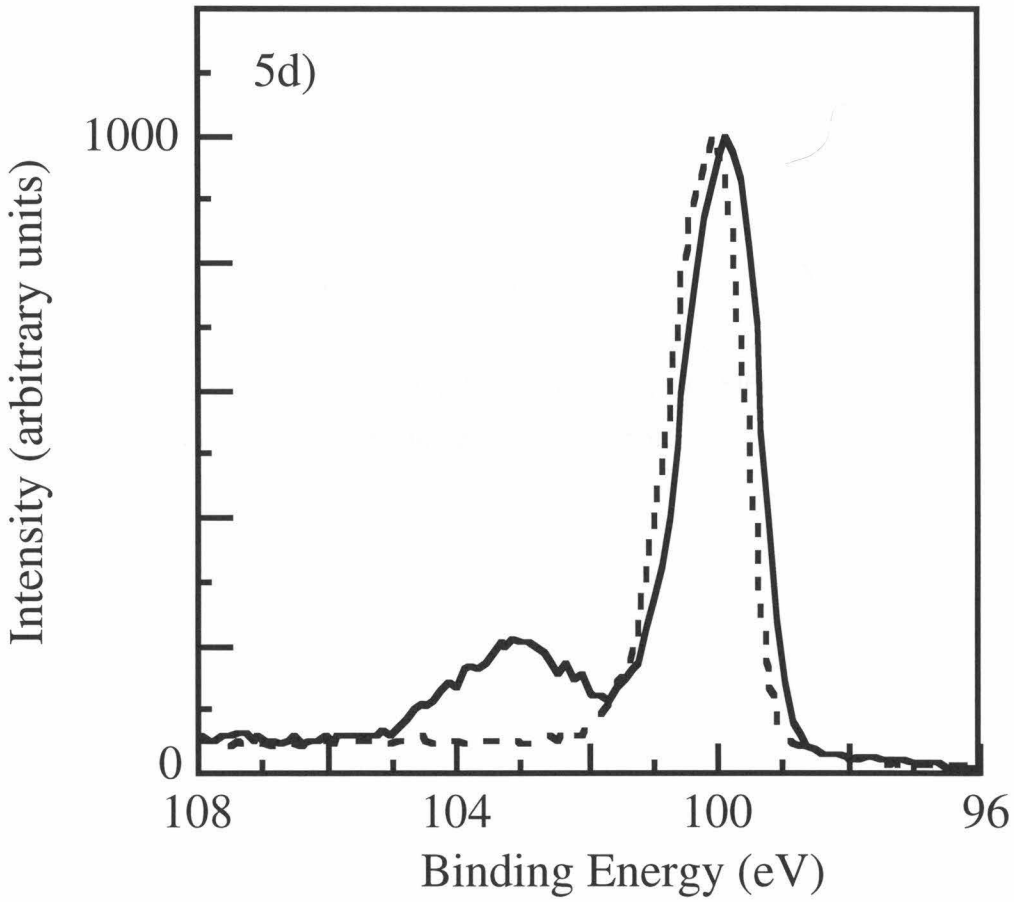
5d)
1000
0
Intensity (arbitrary units)
108
104
100
96
Binding Energy (eV)

Figure 3.6: J-V curves, treated electrodes. (a) $Co(2,2'\text{-bipy})_3^{3+/2+}$ (0.0010 M / 0.0240 M), solid line = start, dashed line = after 20 minutes at short circuit; (b) $Co(2,2'\text{-bipy})_3^{3+/2+}$ (0.0040 M / 0.0960 M), solid line = start, dashed line = after 30 minutes at short circuit.

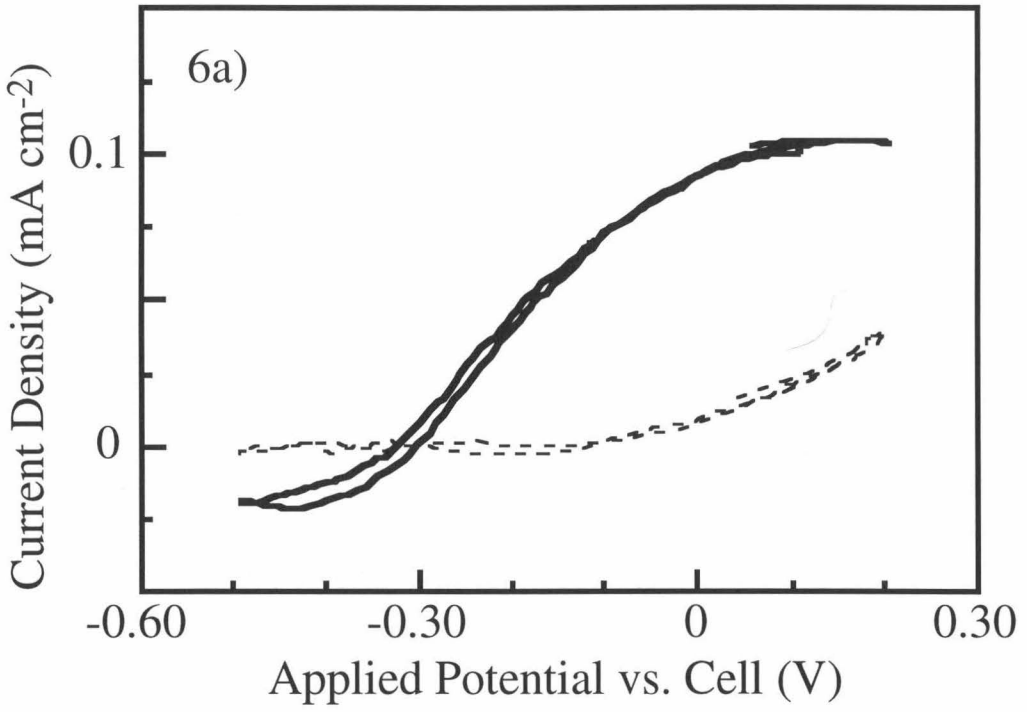
6a)
Current Density (mA cm-2)
0.1
0
-0.60
-0.30
0
0.30
Applied Potential vs. Cell (V)

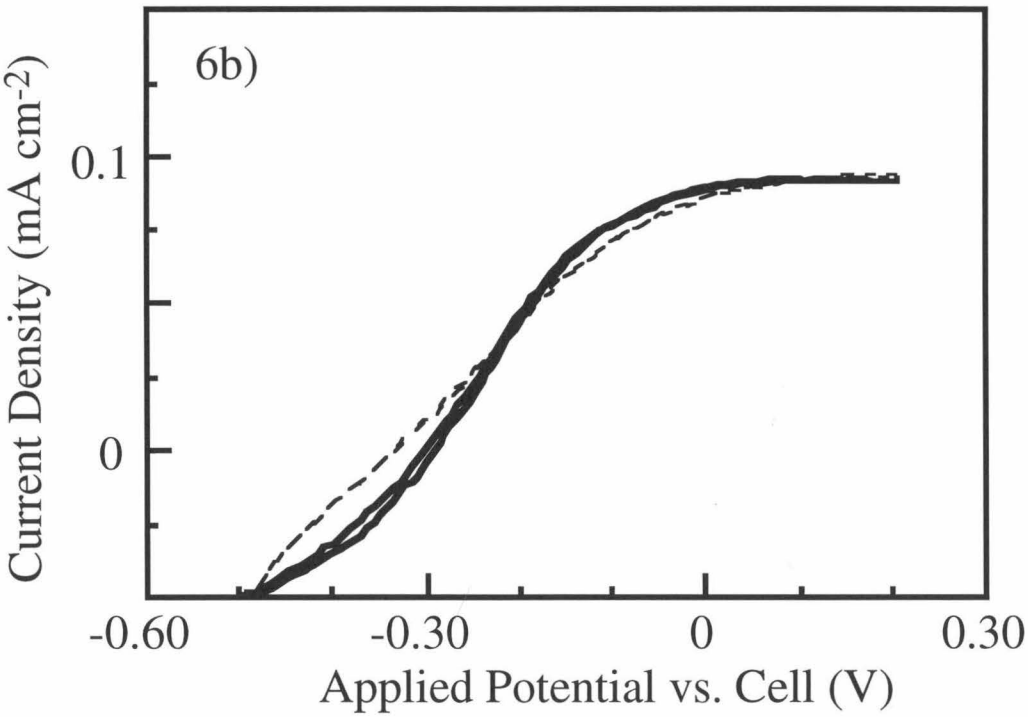
6b)
Current Density (mA cm-2)
0.1
0
-0.60
-0.30
0
0.30
Applied Potential vs. Cell (V)

Figure 3.7: Summary of XPS data; oxide growth over time. (a) $Me_2Fc^{+/0}$, 0.0010 M/0.0240 M (solid squares); (b) $Ru(NH_3)_5(4,4'\text{-bipy})^{3+/2+}$, 0.0010 M/0.0240 M (open squares); (c) $Co(2,2\text{-bipy})_3{}^{3+/2+}$, 0.0010 M/0.0240 M (diamonds).

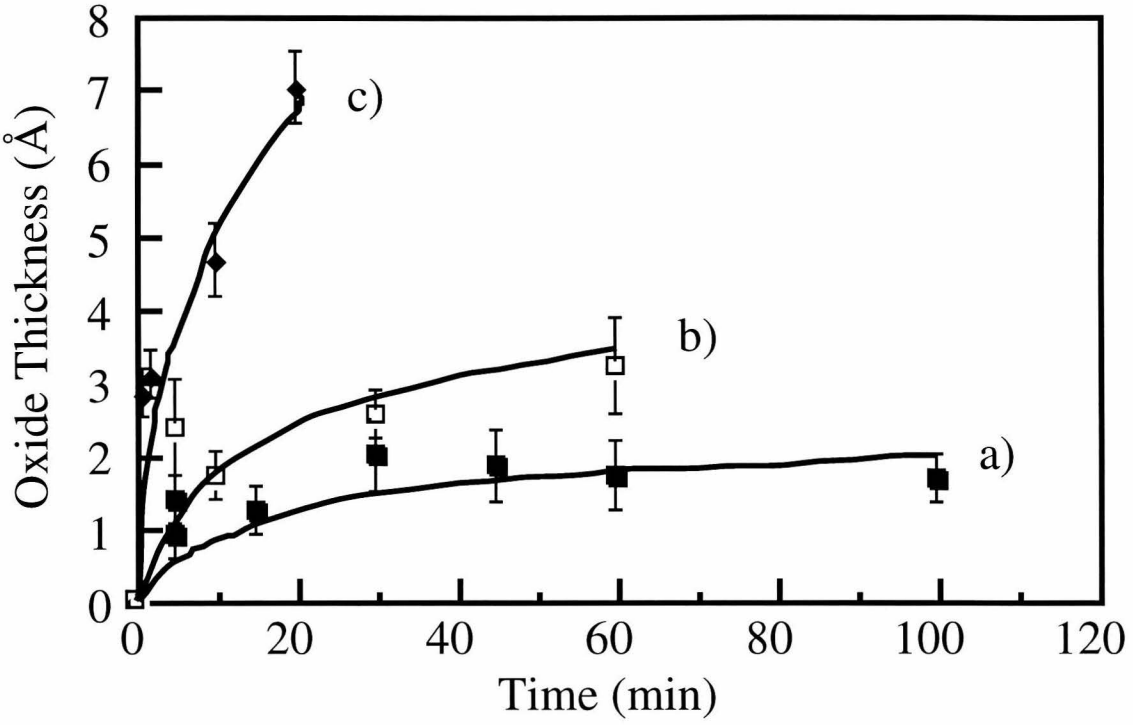
Oxide Thickness (Å)
Time (min)
0
1
2
3
4
5
6
7
8
0
20
40
60
80
100
120
a)
b)
c)

C. Barrier Height Determination for n-Si/CH_3OH-$Me_2Fc^{+/0}$ and n-Si/CH_3OH-$Co(bipy)_3^{3+/2+}$ Contacts

An important component of κ_n as expressed in the Marcus/Gerischer formalism (Equation 3.2) is the driving force for hole transfer from the valence band of the semiconductor to the stabilizing agent, $\mathbf{E}^{o'}(A/A^-)$-$\mathbf{E}_{vb}$. This energetic quantity can be determined if the band edge positions of the semiconductor can be assigned relative to the redox potential of the solution. Differential capacitance vs. voltage (Mott-Schottky) analysis was performed to independently determine $\mathbf{E}(A/A^-)$-$\mathbf{E}_{vb}$, and $\Delta G^{o'}=\mathbf{E}^{o'}(A/A^-)$-$\mathbf{E}_{vb}$, for the redox couples of concern.

Figure 3.8 shows the results of the Mott-Schottky measurements of $Me_2Fc^{+/0}$-treated Si electrodes in contact with CH_3OH-$Co(2,2'\text{-bipy})_3^{3+/2+}$ and CH_3OH-$Me_2Fc^{+/0}$ solutions. The flat-band potential, V_{fb}, for each system was obtained from the x-intercept (as $(C_{sc})^{-2}$-->0) of such plots. Values for V_{fb} were identical within experimental error when measured for n-Si/CH_3OH-$Me_2Fc^{+/0}$ and n-Si/CH_3OH-$Co(2,2'\text{-bipy})_3^{3+/2+}$ contacts, with $V_{fb}=0.637 \pm 0.007$ V. Correction of these results for the difference between the Fermi level and conduction band edge in the bulk of the sample, V_n (Figure 3.1), yielded barrier heights of $\phi_b=0.93\pm0.007$ V. Using this value for ϕ_b in Equation 3.4 resulted in a driving force $\Delta G^{o'}=-0.25$ eV for hole transfer at both of these solid/liquid contacts.

The quality of each Mott-Schottky plot was evaluated by three criteria: linearity, lack of frequency dispersion, and accuracy of the slope. Excellent linearity of C^{-2} vs. V was achieved with the linear regressions typically yielding R^2 values of 1.00, where R is the correlation coefficient for the line fit. A measure of the frequency independence was obtained by comparing the extrapolated x-intercepts for a single electrode, which fell within a range of 5 to 30 mV. Slope accuracy was determined by calculating a dopant density and comparing it to the measured dopant density of the sample. According to the Mott-Schottky equation:

$$(C_{sc})^{-2} = \frac{2}{q\varepsilon\varepsilon_0 N_D A_s^2}(V_A - V_{fb} - \frac{kT}{q}) \tag{3.6}$$

where V_A represents the applied potential, ε, the dielectric constant of the semiconductor, N_D, the dopant density of the semiconductor, and A_s, the geometric area of the electrode.[2] Therefore, plotting $(C_{sc})^{-2}$ versus V_A should yield a line of slope $(2/(q\varepsilon\varepsilon_0 N_D A_s^2))$. Independent measurements of N_D (from four-point probe conductivity data) yielded values for the dopant density of the sample that were within 2-4% of those calculated from the slope of the Mott-Schottky plots, thereby lending confidence to the validity of the driving force values obtained herein.

Figure 3.8: C^{-2} vs. V data for Si electrodes immersed in various redox couples. (a) $Co(2,2'\text{-bipy})_3^{3+/2+}$; (b) same plot as in (a), extrapolated to C^{-2} equals 0; (c) $Me_2Fc^{+/0}$; (d) same plot as in c), extrapolated to C^{-2} equals 0. Results are given for 7 frequencies between 5 and 100 kHz. Note that the x-axis in (b) and (d) has been greatly expanded to show the lack of frequency dependence on the x-intercept.

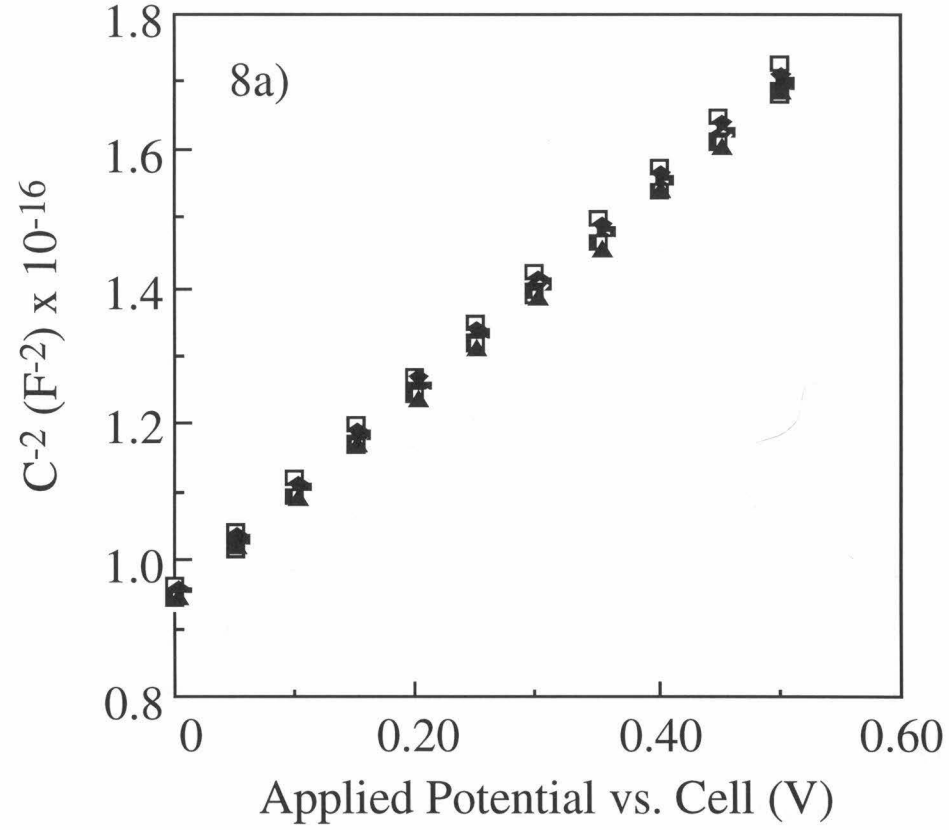
8a)
1.8
1.6
1.4
1.2
1.0
0.8
C-2 (F-2) x 10-16
0
0.20
0.40
0.60
Applied Potential vs. Cell (V)

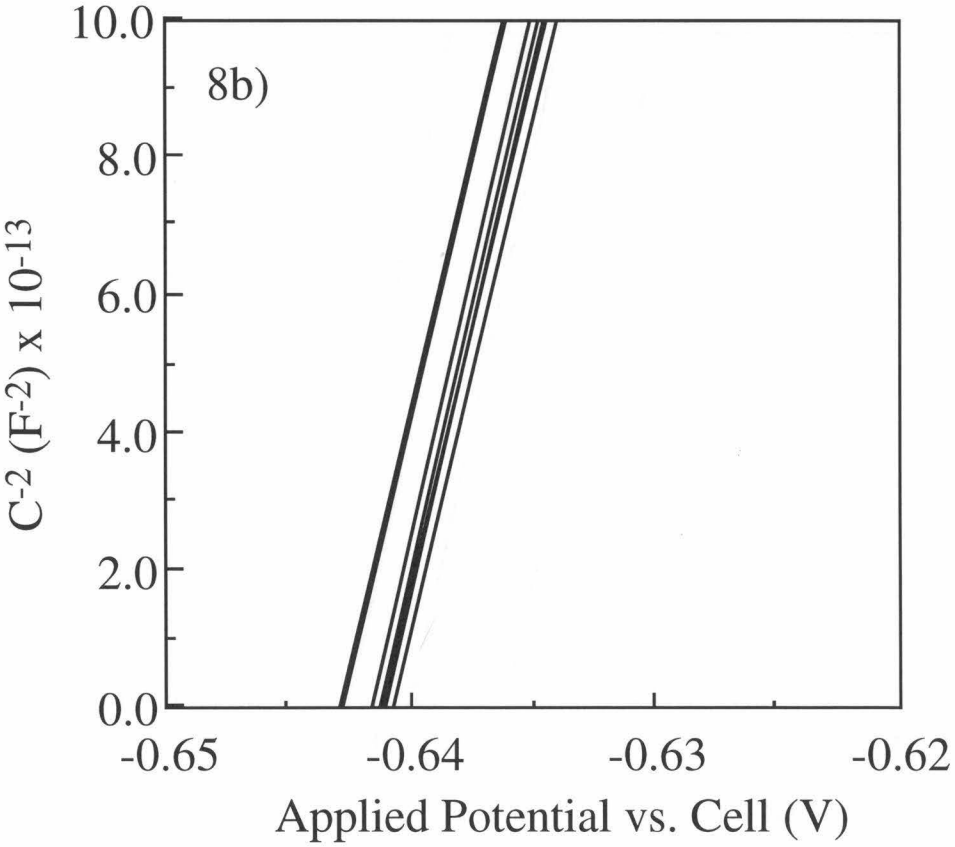
8b)
10.0
8.0
6.0
4.0
2.0
0.0
C-2 (F-2) x 10-13
-0.65
-0.64
-0.63
-0.62
Applied Potential vs. Cell (V)

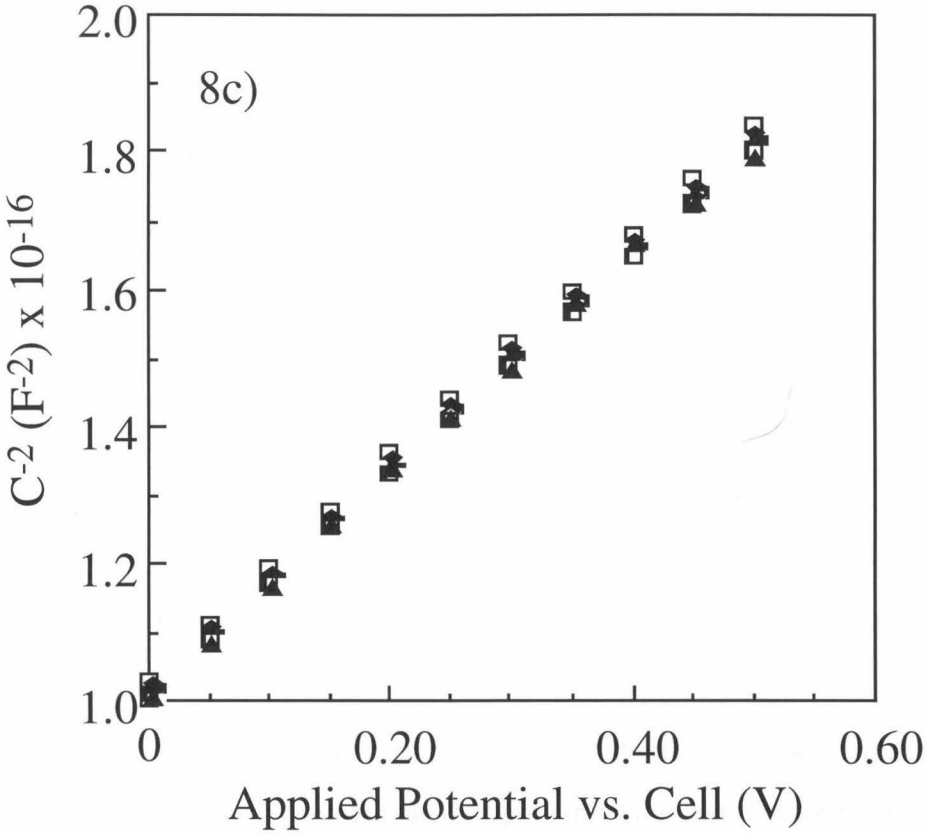
8c)
2.0
1.8
1.6
1.4
1.2
1.0
C-2 (F-2) x 10-16
0
0.20
0.40
0.60
Applied Potential vs. Cell (V)

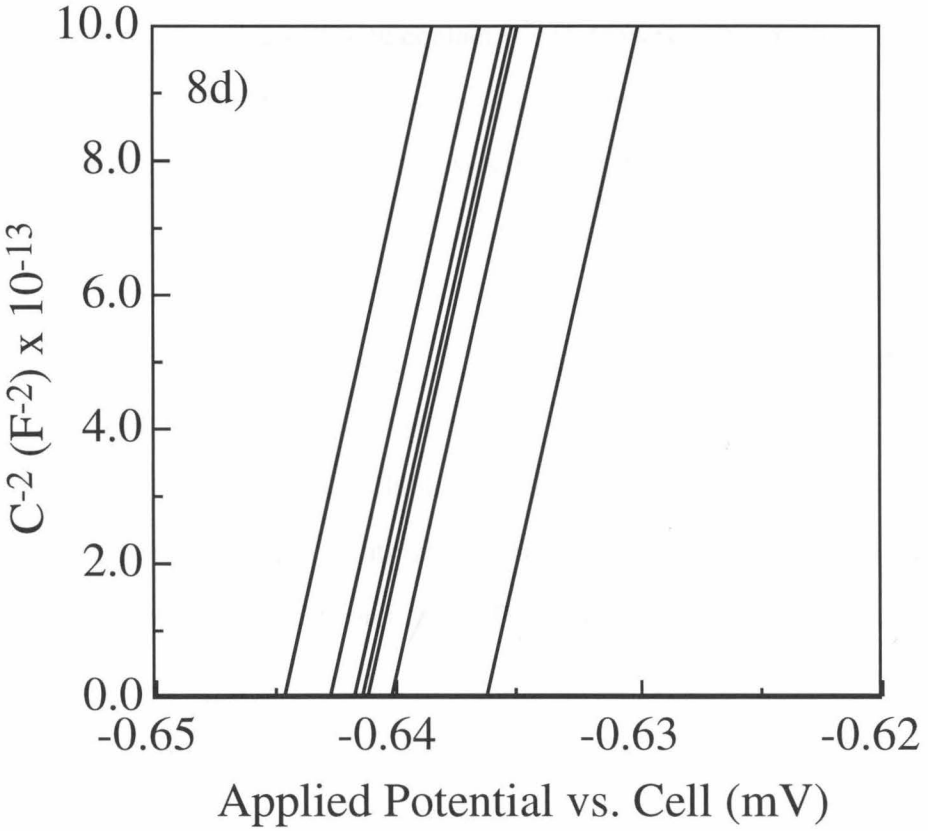
8d)
10.0
8.0
6.0
4.0
2.0
0.0
C-2 (F-2) x 10-13
-0.65
-0.64
-0.63
-0.62
Applied Potential vs. Cell (mV)

V. Discussion

The results obtained above clearly demonstrate the dependence of the stability of a silicon photoelectrochemical cell on the reorganization energy of the redox couple. As the reorganization energy of the stabilizing agent increased, the donor molecule did not compete as effectively with the water for the photogenerated holes, and the electrode passivated more rapidly. Note that the $Me_2Fc^{+/0}$ and $Ru(NH_3)_5(4,4'\text{-bipy})^{3+/2+}$ redox couples displayed approximately equal stabilization efficiencies, in accord with the observation that the self-exchange rate constants, k_{se}, for these redox couples only differ by about an order of magnitude (Table 3.1). In contrast, electrodes immersed in $Co(2,2'\text{-bipy})_3^{3+/2+}$, which has a self-exchange rate that is several orders of magnitude lower than the rate for the other two redox couples, exhibited very poor stability towards passivation. Increases in the concentration of the $Co(2,2'\text{-bipy})_3^{3+/2+}$ stabilizer did improve the electrode stability, as expected from the rate law governing competition for photogenerated holes at an n-type semiconductor/liquid contact.[5,22,28] However, even a four-fold increase in the $Co(2,2'\text{-bipy})_3^{3+/2+}$ concentration was not sufficient to yield passivation protection that was comparable to that of the other redox systems (with smaller λ values) at lower donor concentrations. Ideally, more redox couples with electrochemical potentials in this range would have been used in this study, especially ones with self-exchange rate constants on the order of 10^3-10^4 M^{-1} s^{-1}. However, it was very difficult to identify such systems, especially with the constraint that the redox couples must be outer-sphere, one-electron donors/acceptors that are reasonably soluble in methanol.

The Marcus equations can be utilized to compare the stability ratios observed experimentally to those expected theoretically. The reorganization energies can be estimated by the equation:

$$k_{se}=Z_{bi}e^{-(\lambda/4kT)} \qquad (3.7)$$

where $Z_{bi} \approx 10^{11}$ $M^{-1}s^{-1}$ is the normal collisional vibration frequency for bimolecular reactions at room temperature.[29] This treatment yields values of λ=0.96 eV, 1.2 eV, and 2.2 eV for $Me_2Fc^{+/0}$, $Ru(NH_3)_5(4,4'\text{-bipy})^{3+/2+}$, and $Co(2,2'\text{-bipy})_3^{3+/2+}$, respectively. Using Equations 3.1 and 3.2 and assuming $\nu_n = 10^{13}$ sec^{-1} and κ_{el}=1 allows calculation of the relative rate constant ratios for hole capture for the three semiconductor/liquid contacts under study. Using the experimental value of $\Delta G^{o'}$ = -0.25 eV and the values calculated above for λ implies that $k_{ht}(Ru(NH_3)_5(4,4'\text{-bipy})^{2+}) = 0.4\ k_{ht}(Me_2Fc)$ and $k_{ht}(Co(2,2'\text{-bipy})_3^{2+}) = 0.005\ k_{ht}(Me_2Fc)$. As depicted above, these relative rate constant ratios are in good agreement with the observed stabilization ratios for these three redox couples at n-Si/CH_3OH-H_2O interfaces. The excellent stability of n-Si/CH_3OH-$Me_2Fc^{+/0}$ interfaces can therefore be ascribed in part to the low reorganization energy and in part to the relatively large hole capture rate constant at this solid/liquid interface. Additional increases in stability for redox systems involving the $Co(2,2'\text{-bipy})_3^{3+/2+}$ system could be achieved, in principle, through changes in the complex to decrease $E(A/A^-)$ and thus increase $\Delta G^{o'}$. However, such an approach would produce a decrease in the overall energy conversion efficiency of the resulting photoelectrochemical cell because the free energy used to accelerate the hole capture process would not be available for collection from photogenerated carriers in the external circuit. In this respect, the n-Si/CH_3OH-$Me_2Fc^{+/0}$ interface[30] is seen to be nearly ideal for protection against Si passivation without sacrificing excessive amounts of free energy to achieve the desired faradaic stabilization process.

In summary, the predictions of the Marcus/Gerischer theory have been semi-quantitatively verified for n-Si/CH_3OH photoelectrochemical cells. By holding the electron donor concentration, the reaction driving force, and the photocurrent density constant for each cell, the effect of changing the reorganization energy of the electron donor could be isolated. Charge transfer rates from the semiconductor electrode to the electron donor are predicted to decrease as this reorganization energy is increased. This effect was investigated by adding a constant amount of water to each cell and monitoring the

competition between hole transfer to the electron donor and passivation due to hole transfer to the water. Current-voltage behavior qualitatively showed a correlation between the reorganization of the redox couple and stability of the cell. XP spectra of electrodes gave a more quantitative measure of the rates of passivation, which gave reasonable correlations with calculated rates of hole transfer to the redox stabilizer.

VI. References

(1) Memming, R. In *Electroanalytical Chemistry*; A. J. Bard, Ed.; Marcel Dekker, Inc.: New York, 1979; Vol. 11; pp 1.

(2) Morrison, S. R. *Electrochemistry at Semiconductor and Oxidized Metal Electrodes*; Plenum: New York, 1980.

(3) Koval, C. A.; Howard, J. N. *Chem. Rev.* **1992**, *92*, 411.

(4) Gerischer, H. *J. Phys. Chem.* **1991**, *95*, 1356.

(5) Lewis, N. S. *Ann. Rev. Phys. Chem.* **1991**, *42*, 543.

(6) Marcus, R. A. *J. Phys. Chem.* **1990**, *94*, 1050.

(7) Gerischer, H. *J. Electroanal. Chem.* **1977**, *82*, 133.

(8) Bard, A. J.; Wrighton, M. S. *J. Electrochem. Soc.* **1977**, *124*, 1706.

(9) Rajeshwar, K. *J. Appl. Electrochem.* **1985**, *15*, 1.

(10) Kenyon, C. N.; Ryba, G. N.; Lewis, N. S. *J. Phys. Chem.* **1993**, *97*, 12928.

(11) Rosenwaks, Y.; Thacker, B. R.; Nozik, A. J.; Ellingson, R. J.; Burr, K. C.; Tang, C. L. *J. Phys. Chem.* **1994**, *98*, 2739.

(12) Peter, L. M. *Chem. Rev.* **1990**, *90*, 753.

(13) Yang, E. S.; Chan, M.; Wahl, A. C. *J. Phys. Chem.* **1975**, *79*, 2049.

(14) Weaver, M. J.; Yee, E. L. *Inorg. Chem.* **1980**, *19*, 1936.

(15) Gomes, W. P.; Van Overmeire, F.; Vanmaekelbergh, D.; Vanden Kerchove, F. *ACS Proc.* **1981**, 119.

(16) Ginley, D. S.; Butler, M. A. In *Semiconductor Electrodes*; H. O. Finklea, Ed.; Elsevier: New York, 1988; pp 329.

(17) Schneemeyer, L. F.; Wrighton, M. S. *J. Am. Chem. Soc.* **1980**, *102*, 6964.

(18) Tufts, B. J.; Kumar, A.; Bansal, A.; Lewis, N. S. *J. Phys. Chem.* **1992**, *96*, 4581.

(19) Fleischer, E. B.; Lavallee, D. K. *J. Am. Chem. Soc.* **1972**, *94*, 2583.

(20) Burstall, F. H.; Nyholm, R. S. *J. Chem. Soc.* **1952**, 3570.

(21) Gronet, C. M.; Lewis, N. S. *J. Phys. Chem.* **1984**, *88*, 1310.

(22) Gerischer, H. In *Physical Chemistry: An Advanced Treatise*; H. Eyring; D. Henderson and W. Yost, Ed.; Academic: New York, 1970; Vol. 9A; pp 463.

(23) Bard, A. J.; Faulkner, L. R. *Electrochemical Methods: Fundamentals and Applications*; John Wiley & Sons: New York, 1980, pp 629.

(24) Fadley, C. S. *Prog. Solid State Chem.* **1976**, *11*, 265.

(25) Briggs, D.; Seah, M. P. *Auger and X-ray Photoelectron Spectroscopy;* 2nd ed.; John Wiley & Sons, Inc.: New York, 1990; Vol. 1.

(26) Hochella, M. F., Jr.; Carim, A. H. *Surf. Sci. Lett.* **1988**, *197*, L260.

(27) Lauermann, I.; Lewis, N. S. unpublished results.

(28) Marcus, R. A. *J. Phys. Chem.* **1991**, *95*, 2010.

(29) Marcus, R. A. *J. Phys. Chem.* **1963**, *67*, 853.

(30) Rosenbluth, M. L.; Lieber, C. M.; Lewis, N. S. *Appl. Phys. Lett.* **1984**, *45*, 423.

(31) Wherland, S.; Gray, H. B. *Proc. Natl. Acad. Sci. U.S.A.* **1976**, *73*, 2950.

(32) Cummins, D.; Gray, H. B. *J. Am. Chem. Soc.* **1977**, *99*, 5158.

Chapter 4: Theoretical and Experimental Upper Bounds on Interfacial Charge Transfer Rate Constants Between Semiconducting Solids and Outer-Sphere Redox Couples

All or part of this text originally appeared in: Pomykal, K. E., Fajardo, A. M., and Lewis, N. S., *J. Phys. Chem.*, **1996**, *100(9)*, pp. 3652-3664.

I. Introduction

In this section, experimental results are presented that have been designed to investigate whether k_{et} values in the range $k_{et} \approx 10^{-13}$-10^{-12} cm^4 s^{-1} are generally characteristic of semiconductor/liquid contacts. Specifically, charge transfer processes involving non-adsorbing, outer-sphere redox reagents in semiconductor/liquid contacts that provide efficient energy conversion systems are investigated. These types of interfaces are the ones for which the modified Marcus theory outlined in Chapter 1 was developed and for which experimental validation is required. In many of these systems, interfacial charge transfer is not the rate-determining recombination step, so the observed steady-state interfacial current density cannot yield a direct value for k_{et}. However, for these types of junctions, measurements of the total interfacial recombination flux at a specific potential, combined with energetic information on the barrier height of the semiconductor/liquid contact, can yield an experimentally rigorous upper bound for k_{et} for the contact of concern. The measurements in this work have been performed on semiconductor/liquid junctions with $\kappa_n \approx 1.0$ (See Equation 4.1), so any upper bounds on k_{et} should also establish upper bounds on $k_{et,max}$ at these types of contacts.

This chapter also explores analytically the implications of k_{et} values far larger than $k_{et} = 10^{-16}$ cm^4 s^{-1} for the construction of efficient photoelectrochemical energy conversion devices. In addition, slight modifications of the previous theoretical model are described herein, in which adiabaticity is explicitly incorporated into the theoretical treatment of k_{et}. We also evaluate the effects of a finite distance of approach of the ion to the electrode surface on theoretical values for $k_{et,max}$.

II. Theory

As described in Chapter 1, the Marcus treatment of electron transfer at semiconductor/liquid junctions predicts a theoretical maximum for the value of the charge transfer rate constant k_{et}, where $k_{et} = \nu_n \kappa_n \kappa_{el}$. This plateau arises from the expression for the nuclear term, κ_n:[1]

$$\kappa_n = e^{-(\lambda_A + \Delta G^{o'})^2/(4kT\lambda_A)} \tag{4.1}$$

In this term, λ_A is the total reorganization energy of the acceptor molecule, $\Delta G^{o'}$ is the free energy of reaction for the electron transfer, k is the Boltzmann constant, and T is the temperature. An estimate for the upper limit on the value of the rate constant, $k_{et,max}$, can be obtained by setting the total reorganization energy equal to $-\Delta G^{o'}$, so $\kappa_n = 1.0$ in Equation 4.1 and the condition of optimal exoergicity for k_{et} is attained. In the expression for k_{et}, the attempt frequency, ν_n, is the relevant nuclear vibrational frequency, with ν_n taken to be approximately 10^{13} s^{-1}. The numerical value of $k_{et,max}$ thus depends on the value of the electronic factor, κ_{el}:

$$\kappa_{el} = \pi\left[\frac{2(r_A + r_e)}{\beta^3} + \frac{6}{\beta^4}\right] \tag{4.2}$$

In the expression for κ_{el}, r_A and r_e are the effective radii of the acceptor in solution and the electron in the solid, respectively, and β is the electronic coupling decay constant.

To arrive at the expression in Equation 4.2 for κ_{el}, the distance dependence of the electronic coupling term was taken to be:

$$\kappa_{el}(R) = \kappa_{el,0}\, e^{-\beta(R - r_e - r_A)} \tag{4.3}$$

where $\kappa_{el,0}$ is the electronic term at the closest approach distance of the reactants and R is the distance between the electron in the solid and the acceptor in solution.[2] Integration of $\kappa_{el}(R)$ was then performed over the relevant distances and angles to describe properly a random distribution of acceptors confined to the liquid phase and a random distribution of electrons confined to the semiconducting phase.[1,2]

In the semiquantitative treatment of such processes presented previously in the literature, r_e was approximated to be the Bohr radius of an electron in the solid, and β was assumed to be $\approx 1 \times 10^{-8}$ cm^{-1}. The value for the Bohr radius is well-documented from theory and experiment on Si, GaAs and other semiconducting solids,[3] while the assumed value for β is consistent with values reported previously for the experimentally-determined distance dependence of $\kappa_{el}(R)$ through hydrocarbon glasses[4,5] as well as through proteins[6-9] and other non-conjugated chemical linkages.[10-21] Inserting $\beta = 1 \times 10^{-8}$ cm^{-1} and $r_e = 2 \times 10^{-7}$ cm for Si into Equation 4.2 and using this value for κ_{el} in Equation 4.1 yields an estimate of $k_{et,max} = 10^{-17}$ cm^4 s^{-1}. Although k_{et} is theoretically sensitive to the third power of the decay constant β, the assumed value for β is unlikely to be in error by an order of magnitude, so the uncertainty in $k_{et,max}$ is estimated to be less than a factor of 10^2. A somewhat different derivation, which used an effective reaction zone for the charge transfer process and assumed that the process proceeded with an averaged, single rate constant for all pairs that were in the zone of reaction, yielded similar values for the upper limit of the rate constant, specifically, $k_{et,max} = 10^{-16}$ cm^4 s^{-1}.[22]

Some data on charge transfer rate constants at semiconductor/liquid interfaces seem to support this theoretical model. In the few systems amenable to experimental investigation to date, measured k_{et} values, or upper limits on k_{et}, have been established as $k_{et} \leq 10^{-14}$ cm^4-s^{-1},[23] with more typical values for $k_{et} < 10^{-16}$ cm^4 s^{-1}.[24-26] However, it has been suggested recently that the prior theoretical treatments may underestimate $k_{et,max}$ by as much as 4-5 orders of magnitude.[27] This suggestion was based on experimental data that have been interpreted to indicate that k_{et} values exceeded 10^{-12} cm^4 s^{-1} for p-InP/liquid and p-GaAs/liquid contacts.[27] In addition, it has been suggested that significant increases in $k_{et,max}$ would be obtained theoretically if adiabaticity in the electron transfer process were explicitly included into the pair-weighted averaging procedure that was used to calculate κ_{el} from the functional form for $\kappa_{el}(R)$ (Equation 4.3).[28]

A. Abiabaticity and Finite Ion Size Effects on $k_{et,max}$

Adiabaticity of the interfacial charge transfer process is readily included into the treatment of k_{et} within the framework of the previous theoretical model. Adiabaticity can be included semi-quantitatively merely by adjusting the apparent radius of the electron in the solid to account for the effective distance of adiabaticity, δ. Assuming a typical Bohr radius for an electron in a semiconducting solid, $r_e = 2 \times 10^{-7}$ cm, an additional adiabatic reaction distance of 5×10^{-8} cm would only increase $k_{et,max}$ by a value of 2.5/2.0 relative to the prediction of Equation 4.2 for $r_e = 2 \times 10^{-7}$ cm. In other words, this effect would constitute a correction of less than a factor of 2 in the estimated upper limit of $k_{et,max}$.

A more rigorous treatment of adiabaticity can be obtained by re-evaluating the limits of integration in the pair-weighted calculation of κ_{el} used to obtain Equation 4.2. Modification of the integral to accommodate the possibility that $\kappa_{el} = 1.0$ for electron-ion distances $R \leq (r_e + r_A + \delta)$ yields:

$$\kappa_{el}(r_e, r_A, \delta) =$$

$$\left[\int_{R = r_e + r_A}^{r_e + r_A + \delta} \int_{r = r_e}^{R - r_A} \int_{\theta = 0}^{\theta_{max}} \int_{\phi = 0}^{2\pi} R^2 \sin\theta \, d\theta \, d\phi \, dr \, dR + \int_{R = r_e + r_A + \delta}^{\infty} \int_{r = r_e}^{R - r_A} \int_{\theta = 0}^{\theta_{max}} \int_{\phi = 0}^{2\pi} \left(R^2 e^{-\beta(R - (r_e + r_A + \delta))} \sin\theta \, d\theta \, d\phi \, dr \, dR \right) \right] \quad (4.4)$$

Integration of this function yields κ_{el} as a function of r_e, r_a, and δ:

$$\kappa_{el}(r_e, r_A, \delta) = \pi \left[\frac{6}{\beta^4} + \frac{(2r_e + 2r_A + 6\delta)}{\beta^3} + \frac{\delta^2}{\beta^2} + \frac{(r_e + r_A + \delta)\delta^2}{\beta} + \frac{(r_e + r_A)\delta^3}{3} + \frac{\delta^4}{4} \right] \quad (4.5)$$

For the chosen values of $r_e = 2 \times 10^{-7}$ cm and $r_A = 3 \times 10^{-8}$ cm, $k_{et,max}$ for $\delta = 5 \times 10^{-8}$ cm exceeds the value of $k_{et,max}$ for $\delta = 0$ by a factor of 37 (Figure 4.1, $d_H = 0$).

In addition to adiabaticity, the issue of a finite, non-zero distance of approach between the redox-active ion and the electrode surface must be considered. This effect will counteract the predicted increase in $k_{et,max}$ by tending to lower the predicted value of the optimum charge transfer rate constant. Equations 4.2-4.5 considered the ions in solution to be distributed randomly at all distances from infinity to a position of direct contact with the electrode surface. Assuming that the outer-sphere redox ion cannot penetrate the inner Helmholtz layer (of thickness d_H),[29] the value of the integral will be reduced from that calculated in Equation 4.5. Evaluation of the limits of integration with a finite d_H, assuming adiabaticity over a distance δ, yields:

$$\kappa_{el}(r_e, r_A, \delta, d_H) = \pi \left[\frac{6}{\beta^4} + \frac{(2r_e + 2r_A + 6\delta)}{\beta^3} + \frac{\delta^2}{\beta^2} + \frac{(r_e + r_A + \delta)\delta^2}{\beta} + \frac{(r_e + r_A)(\delta^3 - d_H^3)}{3} + \frac{(\delta^4 - d_H^4)}{4} \right] \quad (4.6)$$

The interplay between finite values of δ and d_H is graphically displayed in Figure 4.1. From this figure, it is evident that for reasonable values of δ and d_H, $k_{et,max}$ is expected to reach a maximum of approximately 10^{-16} to 10^{-15} cm^4 s^{-1}. Thus, when effects of adiabaticity and finite ion approach distances are simultaneously taken into account, the theoretical value of $k_{et,max}$ is similar to, but might exceed slightly, that obtained from the simple treatment presented previously.[1,30]

Further improvements in the theoretical treatment of delocalized charge carriers in the semiconducting solid will require a more sophisticated treatment of the electron in the solid as well as the extension of its wave function across the solid/liquid interface. Because of the counteracting effects of adiabatic and finite approach distance modifications to the original theory of $k_{et,max}$, upper bounds of $k_{et,max} = 10^{-16}$ to 10^{-15} cm^4 s^{-1} are thus taken

as reasonable working models until a more sophisticated theoretical treatment is available in the literature. In the results and discussion sections below, we explore the reasonableness of this upper limit for k_{et} of approximately 10^{-16} to 10^{-15} cm^4 s^{-1} in the context of experimental data for semiconductor/liquid interfaces.

Figure 4.1: Calculated values for the maximum possible charge transfer rate constant $k_{et,\,max}$ at semiconductor/liquid junctions. The various lines represent values calculated at a fixed Helmholtz layer distance d_H while varying the distance δ over which adiabatic electron transfer is allowed. The various lines are merely interpolations between the calculated points and are not intended as fits to Equation 4.6.

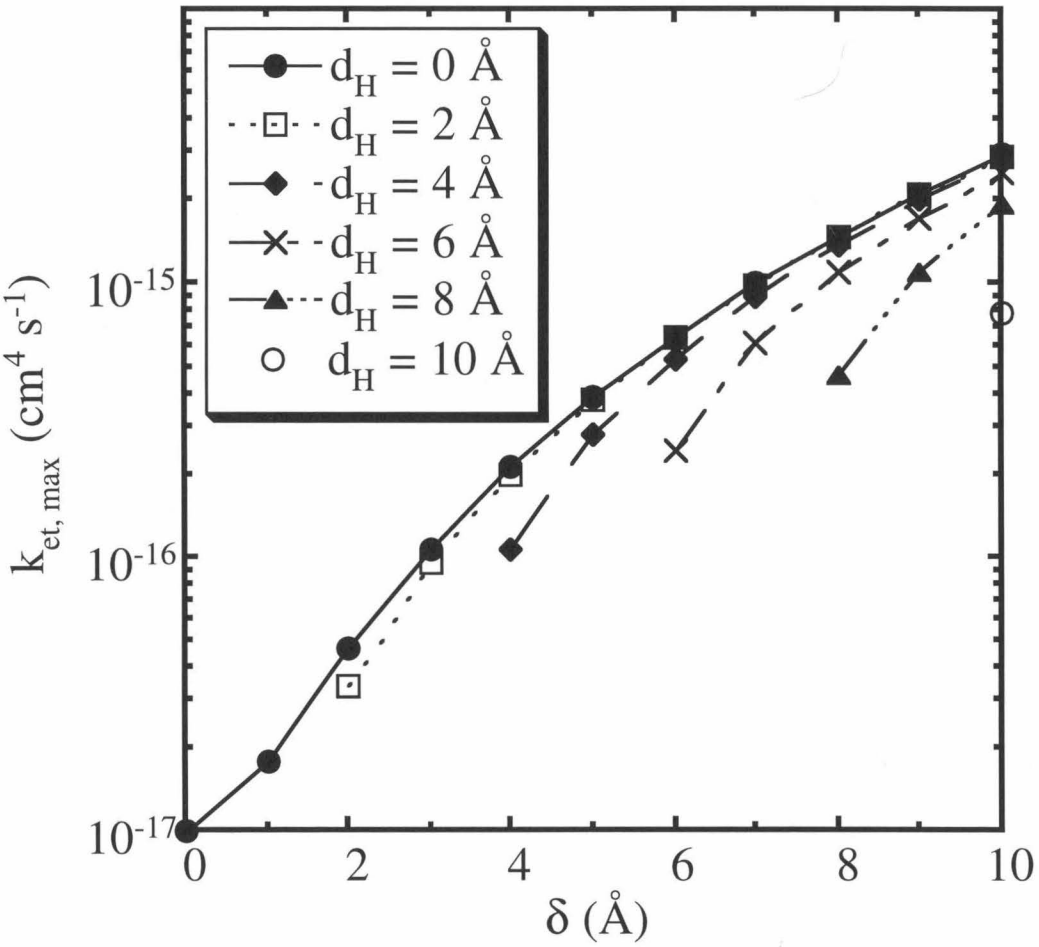
d_H = 0 Å
d_H = 2 Å
d_H = 4 Å
d_H = 6 Å
d_H = 8 Å
d_H = 10 Å
$k_{et,\,max}$ ($cm^4\ s^{-1}$)
10^{-15}
10^{-16}
10^{-17}
0
2
4
6
8
10
δ (Å)

B. Establishing an Upper Bound for Majority Carrier Charge Transfer Rate Constants at Semiconductor/Liquid Contacts

Current density vs. potential measurements, in conjunction with energetic information obtained from differential capacitance vs. potential measurements, can provide useful information on the value of k_{et} for various semiconductor/liquid contacts. For specificity, the theoretical discussion will focus on interfacial charge transfer processes for an n-type semiconductor/liquid contact under illumination. Similar expressions for p-type semiconductor/liquid contacts can be derived in terms of hole transfer rate constants, with appropriate changes in sign due to the change in direction of rectification at the semiconductor/liquid contact.

In general, the interfacial current density can be separated into a photocurrent density, $J_{ph}(E)$, and a recombination current density, $J_{rec}(E)$:[31-33]

$$J(E)= J_{rec}(E) + J_{ph}(E) \tag{4.7}$$

The potential, E, is measured relative to the Nernstian potential of the cell. The sign convention in Equation 4.7 arises because the photocurrent density $J_{ph}(E)$ produces a net flow of electrons from the liquid into the solid, whereas $J_{rec}(E)$ represents all processes that produce a net flow of electrons from the solid into the liquid (resulting from the voltage developed by illumination of the solid).

The charge transfer process related to k_{et} involves transfer of electrons from the conduction band of the n-type semiconductor into the acceptor ions of the liquid electrolyte. At an applied potential E, the expression for the current density resulting from this kinetic process is:[1,31]

$$J_{et}(E) = -q\, k_{et}\, n_s(E)\ [A] \tag{4.8}$$

where [A] is the concentration of acceptors in the interfacial region. The negative sign appears in Equation 4.8 because cathodic current flow through the interface is assigned as a negative current density by convention. If the built-in voltage, V_{bi}, of the semiconductor/liquid contact is known experimentally, $n_s(E)$ can be computed from the dopant density, N_d, of the semiconductor:[34]

$$n_s(E) = N_d e^{-\left[\frac{q(V_{bi}+E)}{kT}\right]} \tag{4.9}$$

Thus,

$$J_{et}(E) = J_{et}(0) e^{-\left(\frac{qE}{kT}\right)} \tag{4.10}$$

where

$$J_{et}(0) = -qk_{et}[A]N_d e^{-\left(\frac{qV_{bi}}{kT}\right)} \tag{4.11}$$

In general, other kinetic processes will also contribute to the interfacial current flow. These processes include tunneling of majority carriers through the depletion region, with a current density $J_{tun}(E)$.[32] In addition, several processes resulting from interfacial transfer of minority carriers, including surface recombination, with a current density $J_{ss}(E)$, recombination in the depletion region, with a current density $J_{dr}(E)$, and bulk recombination/diffusion, with a current density $J_{br}(E)$, must all be considered as possible rate-determining recombination processes (Figure 4.2).[32,34-36] The total interfacial recombination current density can then be written as:

$$J_{rec}(E) = J_{et}(E) + J_{tun}(E) + J_{dr}(E) + J_{ss}(E) + J_{br}(E) \tag{4.12}$$

If the total measured recombination current density is dominated by $J_{et}(E)$ (i.e., $J_{et}(E) \approx J_{rec}(E)$), then measurement of $J_{rec}(E)$ provides a direct measurement of k_{et} through use of Equation 4.8, provided that $n_s(E)$ (i.e., either V_{bi} or the barrier height $\phi_b = V_{bi} + (kT/q)(\ln N_c/N_d)$,[34] where N_c is the effective density of states in the conduction band) is known. Otherwise, if it can be shown that $J_{rec}(E)$ is not limited by $J_{et}(E)$ (i.e., $|J_{rec}(E)| >> |J_{et}(E)|$), then measurement of $J_{rec}(E)$ can be used with Equations 4.8 and 4.9 to establish an upper limit on the value of $J_{et}(E)$. Under these conditions, use of Equations 4.8 and 4.9 allows establishment of an upper bound for k_{et} of the semiconductor/liquid interface of concern.

Prior work from several laboratories has shown that, in contrast to directly measuring $J_{rec}(E)$, it is experimentally advantageous to measure the magnitude of the voltage at open circuit, V_{oc}, developed by a cell at a given photocurrent density.[37,38] Measurement of V_{oc} is advantageous because negligible net current flows through the interface during the measurement, so effects of uncompensated ohmic resistance losses, mass transport overpotentials, kinetic overpotentials, and other significant corrections to $J_{rec}(E)$ are minimized at $J = 0$ (i.e., at $E = -V_{oc}$ for an n-type semiconductor).[39] When $J = 0$ and $J_{rec}(E) \approx J_{et}(E)$ (and $V_{oc} >> kT/q$), Equations 4.8 and 10 yield:

$$V_{oc} = \left(\frac{kT}{q}\right)\left[\ln\left(\frac{J_{ph}}{-J_{et}(0)}\right)\right] \tag{4.13}$$

or equivalently,

$$V_{oc} = \left(\frac{kT}{q}\right)\left[\ln\left(\frac{J_{ph}}{N_d k_{et}[A]}\right)\right] + V_{bi} \tag{4.14}$$

Under these conditions, measurement of V_{oc} at a known value of J_{ph} directly yields a value for k_{et} if N_d and V_{bi} are known.

Alternatively, if it can be established that $|J_{et}(E)| << |J_{rec}(E)|$, then the inequality in Equation 4.15 must hold:

$$V_{oc} < \left(\frac{kT}{q}\right)\left[\ln\left(\frac{J_{ph}}{qN_d k_{et}[A]}\right)\right] + V_{bi} \tag{4.15}$$

In other words, when another recombination mechanism dominates V_{oc}, the experimentally determined open-circuit voltage allows establishment of an upper limit on the magnitude of the direct interfacial charge transfer current density, $|J_{et}(E)|$. This upper limit of $|J_{et}(E)|$ then provides an upper limit on k_{et}, if V_{bi} is known. Measurement of V_{oc} at a known cell temperature and photocurrent density can therefore be used to either establish k_{et} directly (Equation 4.14) or can be used to establish an upper bound on the possible value of k_{et} (Equation 4.15). Although all equations in this thesis are derived for n-type semiconductors, equivalent expressions are easily obtained for p-type semiconductors, substituting k_{ht}, N_a, and [A-] for k_{et}, N_d, and [A] respectively and making the appropriate sign changes.

Figure 4.2: Recombination currents present at the semiconductor/liquid interface. The majority carrier processes J_{et} and J_{tu} represent the current density due to electron transfer to solution acceptor ions from the conduction band edge and via partial tunneling through electric potential barrier present in the depletion layer, respectively. J_{ss}, J_{bu}, and J_{dr} represent current density due to recombination via surface-states, bulk recombination, and depletion region recombination, respectively. J_{ss}, J_{bu}, and J_{dr} result from minority carrier processes and are not expected to depend on the solution acceptor concentration.

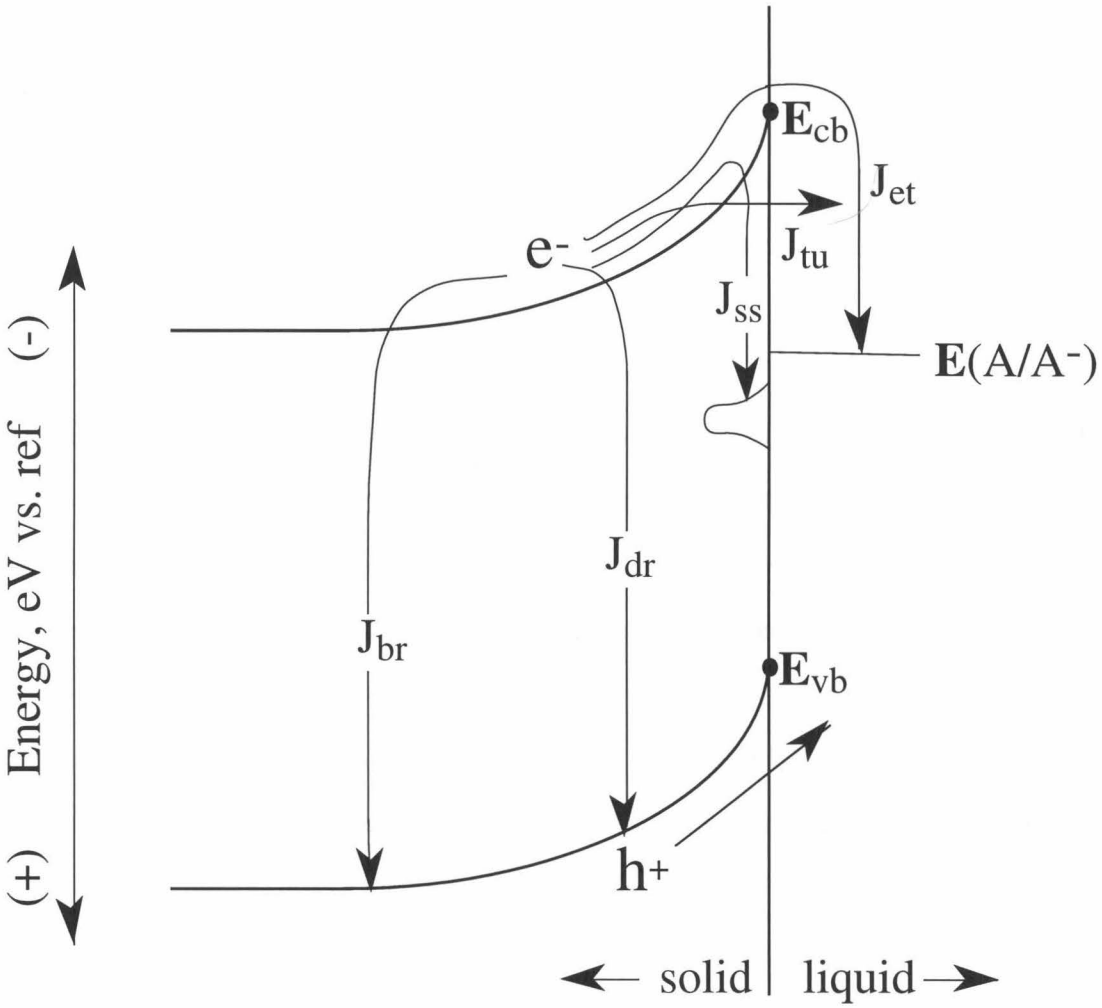
E_cb
J_et
J_tu
e-
J_ss
E(A/A-)
J_dr
J_br
E_vb
h+
Energy, eV vs. ref
(-)
(+)
solid
liquid

Figure 4.2

III. Experimental

A. Electrodes and Materials

All semiconductor electrodes were fashioned using the general procedure described below. After making an ohmic contact, each sample was attached to a Sn:Cu wire with Ag print (GC Electronics). The wire was enclosed in glass tubing, and after mounting the sample onto the wire, the back and edges of the electrode assembly were insulated from the solution by white epoxy (Dexter Corp.). Electrode areas were quantified by photographing the electrodes concurrently with a microruler, followed by magnifying the images and digitizing them.

Both n-type (nominally undoped, dopant density = 5.5 x 10^{15} cm^{-3}, (100)-orientation) and p-type (sulfur-doped, dopant density = 1.1 x 10^{17} cm^{-3}, (100)-oriented) indium phosphide wafers were obtained from Crysta-Comm, Inc. The n-type samples were contacted with a Ga:In eutectic, while p-type samples were contacted by sequential evaporation of 100 Å Au, 1000 Å Zn, and 700 Å Au[40] followed by annealing at 500 °C for 5 min under N_2(g). Indium phosphide electrodes were etched by alternately dipping the sample in solutions of 0.05% Br_2 (v/v) in CH_3OH and 4.0 M NH_3 in CH_3OH for 30 sec, with rinses of CH_3OH between immersions. This procedure was repeated twice before the electrodes were used in electrochemical experiments.

CH_3OH and CH_3CN were dried before use and were distilled under N_2(g). CH_3OH was dried over magnesium methoxide, while CH_3CN was predried over CaH_2 and then dried over P_2O_5. Dimethylferrocene (Me_2Fc, Strem) and cobaltocene ($Co(Cp)_2$, Aldrich) were purified by sublimation before use. Me_2FcBF_4 was prepared as previously described[41] and was dried in vacuo. $Co(Cp)_2PF_6$ (Aldrich) was recrystallized from CH_3CN and dried in vacuo. $LiClO_4$ (Aldrich) was dried by fusing at 240 °C under vacuum. All of the redox couples and electrolytes described above were stored in a N_2(g)-purged drybox until use. Potassium ferrocyanide, potassium ferricyanide, and potassium chloride were obtained from Aldrich and were used as received.

B. Electrochemical Cells and Instrumentation

For nonaqueous electrochemical cells, all solids were introduced into the cell inside the drybox. InP cells were sufficiently sensitive to air that standard Schlenk techniques for transferring solvents and introduction of electrodes yielded poor current density vs. potential stability. The solids and solvents for these cells were instead separately transferred into a nitrogen flushbox that contained less than 10 ppm of O_2 (as monitored by the fuming of $(CH_3CH_2)_2Zn$). The solids were dissolved in an appropriate solvent, and the electrodes were etched within the flushbox and added to the cell. All electrochemical experiments with these systems were then conducted within the flushbox.

All cells utilized a three-electrode potentiostatic setup, with a Pt wire reference electrode poised at the Nernstian solution potential and a Pt foil or Pt gauze counter electrode. The area of the counter electrode was at least ten times larger than that of the working electrode, to minimize any set-up related impedance losses and to minimize mass transport overpotentials at the counterelectrode. For nonaqueous junctions with n-type InP, the concentrations of the cell components were typically 0.100 M of the reduced form of the redox couple (A^-), 0.010 M of the oxidized form of the redox couple (A), and 1.00 M of electrolyte. These precautions (large counterelectrode, high concentrations of both forms of the redox couple, large working electrode areas, etc.) were essential to obtaining highly reproducible, minimal frequency dispersion of the differential capacitance of the semiconductor/liquid contacts studied in this work. This minimal frequency dispersion contrasts with prior reports of the impedance properties of many of these same photoelectrode systems, which apparently contained frequency-dependent features that arose from an unoptimized experimental configuration of the cells and measurement apparatus and/or unoptimal electrode etching and surface preparation. The InP/KCl(aq)-$Fe(CN)_6^{3-/4-}$ cells consisted of 0.100 M $Fe(CN)_6^{3-}$, 0.100 M $Fe(CN)_6^{4-}$, and 1.00 M KCl, while p-InP/CH_3CN-$Co(Cp)_2^{+/0}$ cells consisted of 0.0010 M $Co(Cp)_2$, 0.020 M $Co(Cp)_2^+$, and 0.70 M to 1.00 M $LiClO_4$.

All current density vs. potential experiments were performed using an EG&G Princeton Applied Research (PAR) Model 173 potentiostat in conjunction with a Houston Instruments Omnigraphic 2000 recorder and an EG&G PAR Model 175 Universal Programmer. Light intensities were controlled by the use of an ENH-type W-halogen bulb in conjunction with neutral density filters. X-ray photoelectron spectroscopy (XPS) measurements were conducted in an apparatus that has been described previously, and which consisted of an ultra-high vacuum (UHV) surface science instrument interfaced to a drybox.[42] Impedance spectra were obtained on a computer-controlled Schlumberger Model 1260 Frequency Response Analyzer equipped with a Model 1286 Electrochemical Interface.

C. Built-in Voltage Measurements and Rate Constant Calculations

For experiments with semiconductors in nonaqueous electrolytes, the current density vs. potential (J-*E*) behavior of each electrode was initially measured as a function of the incident light intensity. The J-*E* data were obtained at a scan rate of 50 mV s^{-1}, and direct measurements of V_{oc} and J_{sc} (where J_{sc} is the current density at short circuit and is assumed to be equal to J_{ph}) were taken at each light intensity by reading the appropriate quantities through a digital multimeter that had been connected to the electrochemical cell. These J-*E* measurements were repeated after each set of impedance measurements to verify that the properties of the electrode remained constant over the time scale of the impedance measurements.

The built-in voltages, V_{bi}, of the various semiconductor/liquid junctions were calculated from electrochemical impedance data. An impedance measurement consisted of 11 or 13 frequency sweeps, each with an ac voltage of 10 mV rms amplitude. Each sweep was performed at a different dc potential in reverse bias. The ac frequency range was varied for each semiconductor/liquid system in order to identify the region of purely capacitive behavior of the semiconductor/liquid contact. Impedance data were fit to an equivalent circuit consisting of a resistor R_{sc} (representing the resistance to Faradaic charge

transfer) in parallel with a capacitor C_{sc} (representing the differential capacitance of the semiconductor space charge region), both of which were in series with a resistance R_s (representing resistive losses through the solution, leads, etc.). This model assumes that the measured differential capacitance (C) equals C_{sc}. The differential space-charge capacitance was computed from the impedance data using the equation:[29]

$$2\pi f C_{diff} = \frac{1+(1-4(Z_{im}/R_{sc})^2)^{1/2}}{2Z_{im}} \tag{4.16}$$

where f is the frequency of the ac voltage and Z_{im} is the imaginary part of the measured impedance, Z, at the dc bias of interest. R_{sc} values were taken as the diameter of a semicircular fit to a Nyquist plot (Z_{im} vs. Z_{real} as a function of f, where Z_{real} is the real part of the measured impedance) at each dc bias. The differential capacitance was then related to the built-in voltage of the semiconductor/liquid junction by the Mott-Schottky equation:

$$C_{sc}^{-2} = \frac{2}{q\varepsilon\varepsilon_0 N_d A_s^2}(E - V_{bi} - \frac{kT}{q}) \tag{4.17}$$

Here ε is the dielectric constant of the semiconductor, ε_0 is the permittivity of free space, and A_s is the area of the semiconductor electrode. A plot of *E* vs. C^{-2}, followed by extrapolation of the data to infinite capacitance and application of the correction factor (kT/q) (Equation 4.17), yielded the built-in voltage of the solid/liquid contact. The validity of the equivalent circuit model used in this work was assessed by computing the slopes of the lines of C_{sc}^{-2} vs. *E* at each frequency of the ac voltage and comparing these slopes to those expected from the known dopant density, area, and dielectric constant of the electrode in question. Within a data set, only data which exhibited linear C^{-2} vs. *E* ($R^2 \geq 0.999$, where R is the correlation coefficient) plots having slopes which corresponded to the measured dopant density to within 50% were considered. Electrodes that yielded non-

linear or frequency-dependent plots for all frequency values were considered defective and were not included in the analysis.

D. Passivation/Corrosion Measurements of InP/Liquid Contacts

Unlike the other cells studied in this work, InP/$Fe(CN)_6^{3-/4-}$(aq) contacts were observed to undergo rapid passivation or corrosion processes. A series of measurements was performed to investigate these phenomena in some detail. To assess electrode stability, InP electrodes were first contacted with a redox couple/electrolyte solution known to display stable J-*E* properties, and the J-*E* behavior was measured in the presence of band gap illumination of the solid. The electrodes were then immersed into a KCl(aq)-$Fe(CN)_6^{3-/4-}$ solution, and J-*E* measurements were performed. In an attempt to minimize electrode oxidation, data in aqueous solutions were obtained in the dark for n-type electrodes and in the light for p-type electrodes. Finally, the electrodes were reimmersed into the first (stable) redox couple-electrolyte solution and the resulting J-*E* behavior was measured. For example, in the case of p-type InP electrodes, J-*E* curves were measured in the light in CH_3CN-0.70 M $LiClO_4$-0.100 M $Co(Cp)_2^+$-0.0010 M $Co(Cp)_2$ solutions before and after J-*E* curves were measured in the light in a 1.00 M KCl(aq)-0.100 M $Fe(CN)_6^{3-}$-0.100 M $Fe(CN)_6^{4-}$ electrolyte.

Surface science techniques were used to determine the oxide levels on various InP electrodes. The J-*E* data for a freshly etched n-type InP electrode were first obtained under band gap illumination in a N_2(g)-purged CH_3OH-1.00 M $LiClO_4$-0.100 M Me_2Fc-0.010 M Me_2FcBF_4 solution. This n-type InP electrode was then rinsed and immediately placed into a nitrogen-purged Schlenk tube as a control. Another freshly-etched electrode was also placed in this Schlenk tube as a second control. A third electrode was etched and immersed into the CH_3OH-$Me_2Fc^{+/0}$ solution, and J-*E* data were collected on this specimen in the presence of band gap illumination. This electrode was then rinsed with CH_3OH and was immediately immersed into a nitrogen-purged 1.00 M KCl(aq)-0.100 M $Fe(CN)_6^{3-}$-0.100 M $Fe(CN)_6^{4-}$ solution. The J-*E* behavior of this contact was then

determined in the dark. The electrode was then rinsed and was immediately reimmersed into the CH_3OH-$Me_2Fc^{+/0}$ solution. J-*E* data were collected (again in the presence of band gap illumination) to assess the stability of the electrode in the KCl(aq)-$Fe(CN)_6^{3-/4-}$ solution. This InP electrode was then rinsed and placed in the Schlenk tube. This series of experiments was then repeated with a fourth electrode, except that instead of 1.00 M KCl(aq) as the electrolyte in the $Fe(CN)_6^{3-/4-}$ solution, 1.00 M HCl(aq) was used. The Schlenk tube containing the four electrodes was then introduced into a nitrogen flushbox equipped with a load-lock into the UHV chamber. The electrodes were removed from the Schlenk tube, mounted onto UHV sample studs, and introduced into the UHV chamber for XPS studies. Impedance measurements as described above were also attempted for both the neutral and acidic solutions.

The thicknesses of any oxide layers resulting from the procedure described above were determined using standard overlayer models.[43] The thickness of an overlayer, d, on the InP sample is related to the XPS signals for the overlayer and the substrate by:

$$d = (\lambda \sin\beta) \ln\left(\frac{I_o n_s}{I_s n_o} + 1\right) \tag{4.18}$$

where I_o and I_s are the areas under the peaks for the overlayer and the substrate, respectively. Here λ is the electron escape depth from the material (23 Å for InP[43,44]), β is the angle of the detector from the substrate (35°), and n_o and n_s are the number of P atoms per unit volume in the overlayer and substrate, respectively. The ratio n_s/n_o thus corrects for the difference between the densities of the substrate and overlayer, with $n_s/n_o = 1.42$ for pure InP referenced to oxidized InP. This model assumes that the sensitivity factors and escape depths are the same for the overlayer and substrate, which is reasonable since both the overlayer and substrate signals originate from the same type of atom.

IV. Results

A. Barrier Height Measurements and Upper Bounds on k_{et}/k_{ht} for Semiconductors in Contact with Nonaqueous Solvents

In conjunction with the work described below for InP, built-in voltages were measured for two other efficient, stable, n-type semiconductor/electrolyte combinations, and upper limits on the rate constant were calculated. Differential capacitance vs. potential data were used to measure V_{bi} for these contacts. In conjunction with Equation 4.15, these V_{bi} values allow establishment of upper bounds on k_{et} for the n-type semiconductor/liquid interfaces. The barrier height of the junction, ϕ_b, is related to the built-in voltage by the equation:[34]

$$\phi_b = V_{bi} + \frac{kT}{q}\ln\left(\frac{N_c}{N_d}\right) \tag{4.19}$$

for an n-type semiconductor. Combination of Equation 4.19 with Equations 4.8 and 9 yields the expression:

$$V_{oc} < \left(\frac{kT}{q}\right)\left[\ln\left(\frac{J_{sc}}{qN_c k_{et}[A]}\right)\right] + \phi_b \tag{4.20}$$

The results of these experiments are summarized in Table 1. Note that in both cases it has been shown that electron transfer from the conduction band edge is not the rate-limiting recombination mechanism in these systems, and thus the values in Table 1 represent upper limits on the electron transfer rate constant.

p-InP photoelectrodes also provide well-behaved, efficient energy conversion systems in nonaqueous solvents.[45] The p-type InP/CH_3CN-$Co(Cp)_2^{+/0}$ junction thus provided a semiconductor/liquid contact that was suitable for investigation of interfacial charge transfer rate constants. This system is valuable in that it provides an upper bound

on the charge transfer rate constant for hole transfer, k_{ht}, as opposed to the upper bounds on k_{et} that were obtained from the studies of n-type photoanodes described above.

Figure 4.3 displays the current density-potential data at varying light intensities for a p-InP/CH_3CN-$Co(Cp)_2^{+/0}$ junction. The J-*E* curves were rectifying and displayed high photovoltages (Figure 4.3), consistent with prior cyclic voltammetry studies of p-InP photocathodes in contact with outer-sphere redox couples in CH_3CN.[45,46]

Figure 4.4 displays the C^{-2} vs. *E* data for the p-InP/CH_3CN-$Co(Cp)_2^{+/0}$ system. The plots were linear and were in good agreement with each other for $1 \times 10^3 < f < 1 \times 10^5$ Hz. The slopes were within 25% of the manufacturer-quoted values for the dopant density of the samples, and the intercepts yielded $V_{bi} = 1.04 \pm 0.02$ V for these contacts. Use of the manufacturer-reported dopant density $N_A = 1.1 \times 10^{17}$ cm^{-3} to calculate a barrier height for this system yielded $\phi_b = 1.16$ V. This value is in reasonable agreement with previous capacitance vs. potential measurements on p-InP samples of slightly different dopant densities. These previous measurements yielded $\phi_b = 1.23$ V ($N_A = 1.86 \times 10^{18}$ cm^{-3}) or $\phi_b = 1.03$ V ($N_A = 1.87 \times 10^{16}$ cm^{-3}).[47]

Use of Equation 4.15, modified for a p-type semiconductor, yielded an upper bound for $k_{ht} \leq 10^{-13}$ cm^4 s^{-1} for this system. The limited solubility of $Co(Cp)_2$ in most solvents precluded determination of whether the recombination rate was limited by hole (majority carrier) transfer to the $Co(Cp)_2$ donor species. If the donor concentration could have been increased further, a more rigorous upper limit could be placed on the charge transfer rate constant for this system.

Table 4.1 Summary of built-in voltages and upper limits on the rate constants for n-type semiconductors in contact with nonaqueous electrolytes. Data is taken from Pomykal, K. E., Fajardo, A. M., and Lewis, N. S., *J. Phys. Chem.*, **1996**, *100(9)*, pp. 3652-3664.
$Me_2Fc^{+/0}$ = 1,1'-dimethylferrocenium/1,1'-dimethylferrocene; $Fc^{+/0}$ = ferrocenium/ferrocene.

System	V_{bi} (V)	ϕ_b (eV)	$k_{et,\ max}$ ($cm^4\ s^{-1}$)
n-Si/CH_3OH-$Me_2Fc^{+/0}$	0.884±0.014	1.03	10^{-15}
n-GaAs/CH_3CN-$Fc^{+/0}$	1.053±0.023	----------	10^{-14}

Table 4.1

Figure 4.3: (a) Current density vs. voltage data for a p-InP/CH_3CN-$Co(Cp)_2^{+/0}$(0.025 M / 0.0010 M) junction at various light intensities. The scan rate was 50 mV s^{-1}. (b) Natural logarithm of the photocurrent density vs. the open circuit voltage for the junction represented in (a). The line is a fit to the equation: $\ln(J_{ph}) = \ln(|J_{et}(0)|) + (qV_{oc}/AkT)$. The diode quality factor, A, is calculated to be 1.2 from this plot.

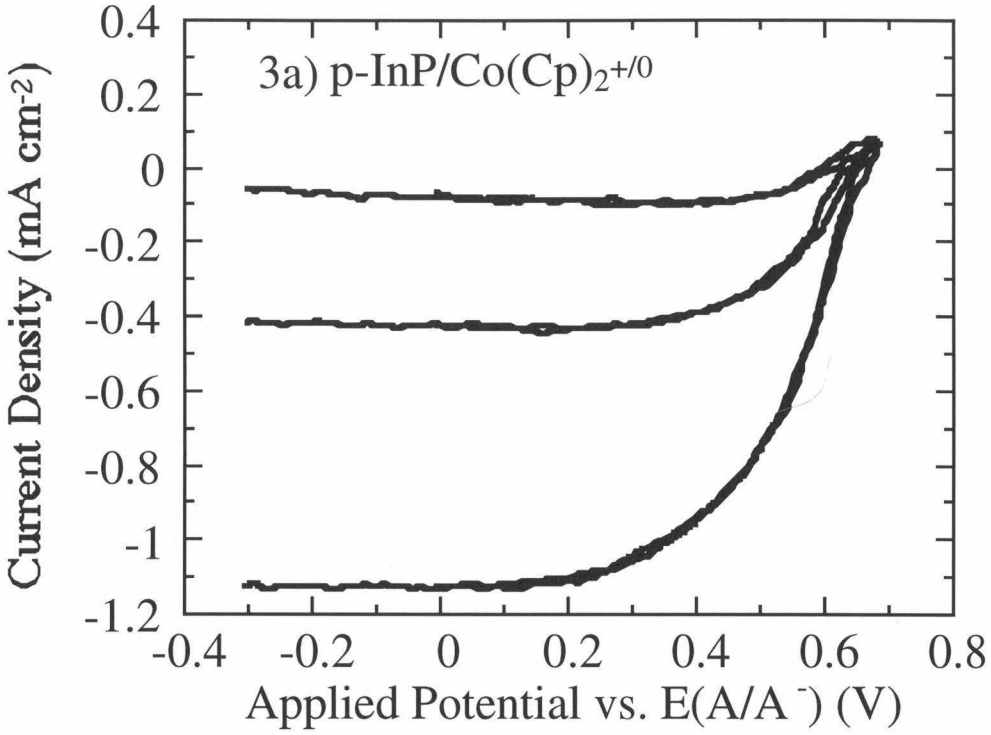
3a) p-InP/Co(Cp)2+/0
Current Density (mA cm-2)
0.4
0.2
0
-0.2
-0.4
-0.6
-0.8
-1
-1.2
-0.4
-0.2
0
0.2
0.4
0.6
0.8
Applied Potential vs. E(A/A-) (V)

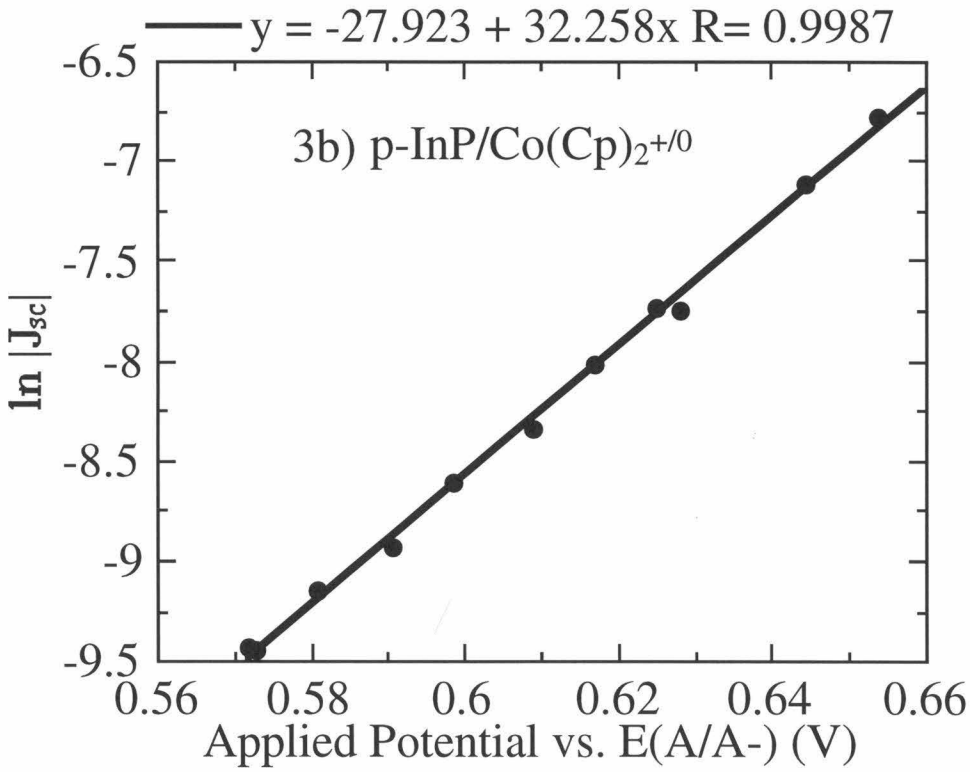
y = -27.923 + 32.258x R= 0.9987
3b) p-InP/Co(Cp)2+/0
ln |Jsc|
-6.5
-7
-7.5
-8
-8.5
-9
-9.5
0.56
0.58
0.6
0.62
0.64
0.66
Applied Potential vs. E(A/A-) (V)

Figure 4.4: (a) C^{-2} vs. applied dc potential for the p-InP/CH_3CN-$Co(Cp)_2^{+/0}$ junction in Figure 3. The points represent data taken at seven frequencies between 0.5 and 15 kHz. (b) The extrapolation of the data points in (a).

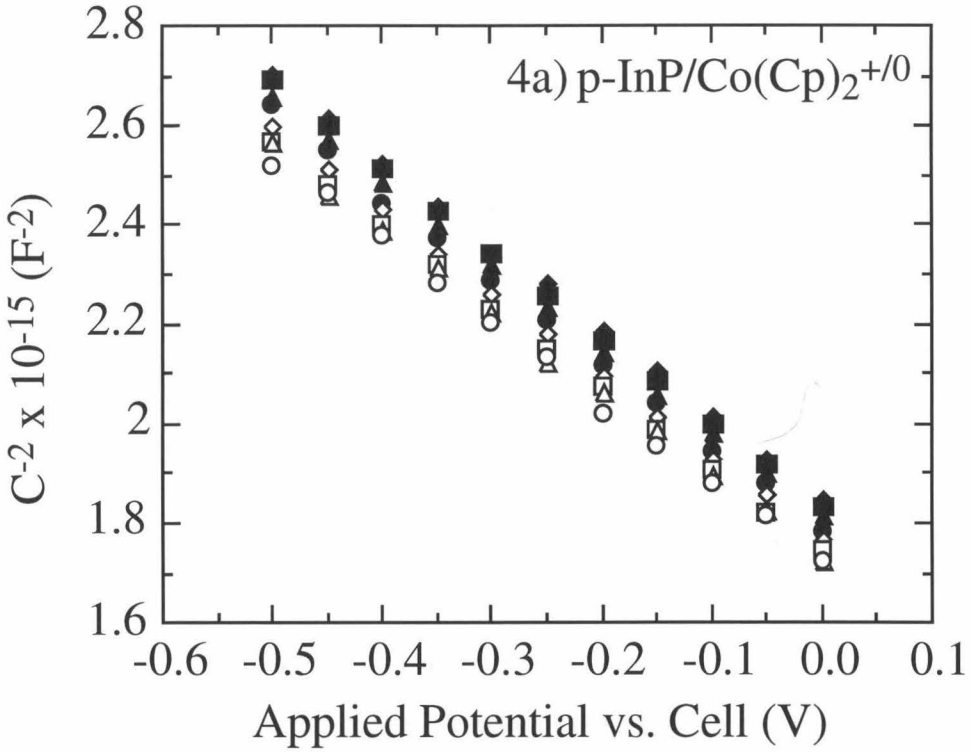
4a) p-InP/Co(Cp)2+/0
C-2 x 10-15 (F-2)
2.8
2.6
2.4
2.2
2
1.8
1.6
-0.6 -0.5 -0.4 -0.3 -0.2 -0.1 0.0 0.1
Applied Potential vs. Cell (V)

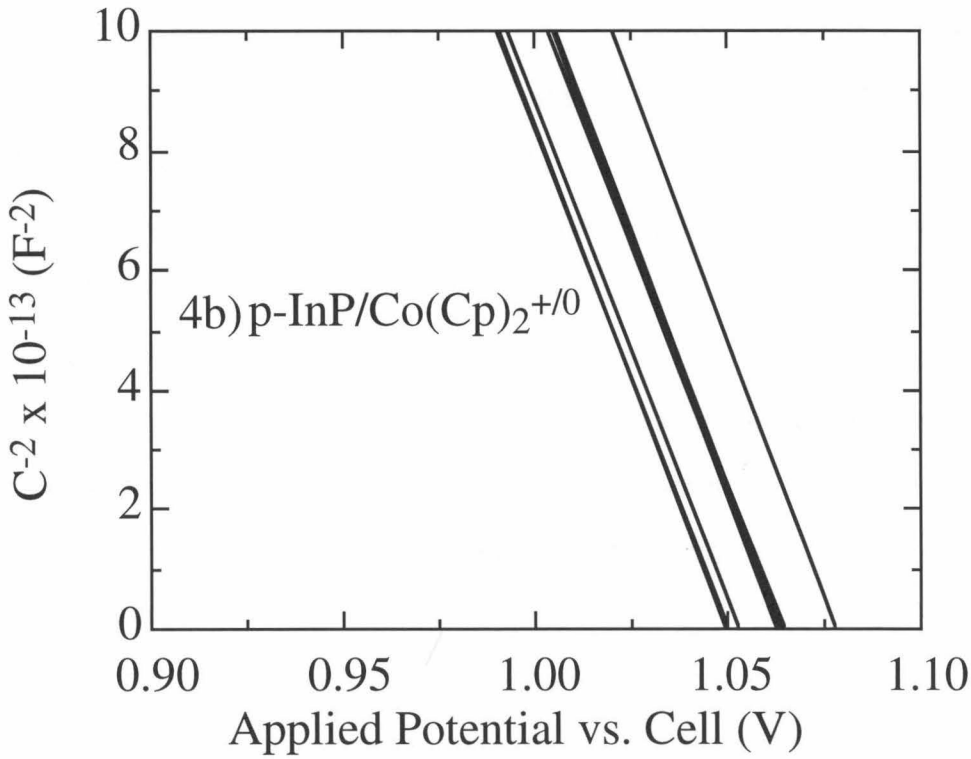
4b) p-InP/Co(Cp)2+/0
C-2 x 10-13 (F-2)
10
8
6
4
2
0
0.90 0.95 1.00 1.05 1.10
Applied Potential vs. Cell (V)

B. Steady-State J-*E* Behavior of n-InP/H_2O-$Fe(CN)_6^{3-/4-}$ Contacts

1. *J-E Data for n-InP Electrodes in KCl(aq)-$Fe(CN)_6^{3-/4-}$ Solutions*

Figure 4.5 displays the J-*E* data for n-InP anodes in contact with KCl(aq)-0.100 M $Fe(CN)_6^{4-}$ 0.100 M $Fe(CN)_6^{3-}$. When compared to data on n-InP/CH_3OH-$Me_2Fc^{+/0}$ contacts studied previously[48] and re-evaluated in the course of this work (Figure 4.5a), the current densities in Figure 4.5b were extremely small at low forward bias. Even at an electrode potential of -1.0 V vs. $E(A/A^-)$, the current density at the n-InP/KCl(aq)-$Fe(CN)_6^{3-/4-}$ junction was only on the order of 10^{-3} A cm^{-2}. The low current densities indicated that the electron transfer rate was very small for n-InP/KCl(aq)-$Fe(CN)_6^{3-/4-}$ contacts.

Although the short-circuit current density was zero at n-InP/CH_3OH/$Me_2Fc^{+/0}$ contacts, a non-zero short-circuit current density of 0.5 μA cm^{-2} was observed for n-InP/KCl(aq)-$Fe(CN)_6^{3-/4-}$ junctions. The presence of a finite current density at short circuit indicated the presence of a chemical passivation or corrosion reaction at the n-InP/KCl(aq)-$Fe(CN)_6^{3-/4-}$ contact. Consistently, the open-circuit voltage of this interface was ≈ 350 mV even in the absence of illumination.

2. *Effects of Exposure to KCl(aq)-$Fe(CN)_6^{3-/4-}$ Solutions on the Behavior of n-InP/CH_3OH-$Me_2Fc^{+/0}$ Contacts*

Since the oxides of InP are insoluble at near-neutral pH in H_2O,[49] corrosion of the InP induced by the presence of $Fe(CN)_6^{3-}$ should produce an insoluble oxide overlayer on the electrode surface. The formation of such an overlayer was investigated by evaluation of the J-*E* properties of the n-InP/CH_3OH-$Me_2Fc^{+/0}$ interface. Figure 4.5a displays the J-*E* behavior of a freshly etched n-InP electrode in contact with the CH_3OH/$Me_2Fc^{+/0}$ solution. Consistent with prior work,[48] the J-*E* curves in this electrolyte were stable and reproducible, exhibiting large V_{oc} values and excellent fill factors. In contrast, Figure 4.5c displays the J-*E* behavior of the same n-InP/CH_3OH-$Me_2Fc^{+/0}$ junction in Figure 4.5a after the electrode had been exposed to the potential scans in the dark shown in Figure

4.5b. After exposure to the KCl(aq)-$Fe(CN)_6^{3-/4-}$ electrolyte, the open-circuit voltage of the n-InP/CH_3OH-$Me_2Fc^{+/0}$ junction decreased by 100 mV, the fill factor decreased from 0.7 to 0.2, and the forward bias current density decreased significantly at all potentials. This behavior indicated that exposure to the KCl(aq)-$Fe(CN)_6^{3-/4-}$ electrolyte was deleterious to the performance of n-InP photoanodes, causing J-*E* properties characteristic of electrodes possessing electrically insulating overlayers on their surfaces.

3. *J-E Data for n-InP Electrodes in HCl(aq)-$Fe(CN)_6^{3-/4-}$ Solutions*

Further evidence for the presence of a chemical reaction between InP and KCl(aq)-$Fe(CN)_6^{3-/4-}$ was obtained by investigation of the J-*E* properties of n-InP electrodes in contact with acidic HCl(aq)-$Fe(CN)_6^{3-/4-}$ electrolytes (Figure 4.6). In and P oxides are soluble in strongly acidic solutions of HCl(aq),[47,49-51] implying that active etching, as opposed to formation of an insoluble insulating oxide overlayer, should occur under these acidic conditions. In accord with these predictions, the J-*E* behavior of n-InP/HCl(aq)-$Fe(CN)_6^{3-/4-}$ junctions at pH=0 showed a significant open-circuit voltage, with $V_{oc} \approx 400$ mV (Figure 4.6b). A non-zero short-circuit current density was also observed for this system, and its value was much larger than that for n-InP/KCl(aq)-$Fe(CN)_6^{3-/4-}$ contacts measured at neutral pH values (Figures 4.5b, 4.6b). These observations signaled that the InP was undergoing a corrosion reaction with the acidic electrolyte. However, as displayed in Figure 4.6c, the chemical reaction did not induce significant changes in the J-*E* behavior of subsequently formed n-InP/CH_3OH-$Me_2Fc^{+/0}$ contacts. Additionally, the J-*E* behavior in the aqueous acidic medium was much less resistive than was observed at neutral pH (Figures 5b, 6b), indicating the absence of insulating oxide overlayers on InP surfaces in contact with the acidic solutions. The non-zero short-circuit current densities, finite open-circuit voltages, and absence of an insulating overlayer on the InP during immersion into acidic HCl(aq)-$Fe(CN)_6^{3-/4-}$ solutions (Figure 4.6) are precisely the behaviors expected for an etching reaction that yields a soluble oxide product.

4. *XPS Studies of Oxide Formation and Estimates of k_{et} for n-InP/KCl(aq)-$Fe(CN)_6^{3-/4-}$ and n-InP/HCl(aq)-$Fe(CN)_6^{3-/4-}$ Interfaces*

XPS studies were performed to confirm further the presence of corrosion reactions at n-InP/KCl(aq)-$Fe(CN)_6^{3-/4-}$ contacts. Figure 4.7 shows XP spectra of the phosphorus region for electrodes that had been etched (4.7a), etched and exposed to CH_3OH-$Me_2Fc^{+/0}$ (4.7b), etched and exposed to KCl(aq)-$Fe(CN)_6^{3-/4-}$ at neutral pH (4.7c), and etched and exposed to HCl(aq)-$Fe(CN)_6^{3-/4-}$ at acidic pH (4.7d). All electrodes except those that had been exposed to KCl(aq)-$Fe(CN)_6^{3-/4-}$ at neutral pH exhibited negligible oxide signals in the phosphorus region. Figures 4.7a-c show only the XPS signal expected for pure InP, at a binding energy of about 129-130 eV.[52] In contrast, the electrodes that had been exposed to neutral pH solutions of KCl(aq)-$Fe(CN)_6^{3-/4-}$ showed an additional signal at 134 eV, whose area indicated the presence of 7.5 Å of phosphate (phosphorus oxide) on the electrode surface (Equation 4.18).[52]

Despite the presence of the oxide overlayer on n-InP/KCl(aq)-$Fe(CN)_6^{3-/4-}$ contacts, impedance measurements were performed to provide an estimate of k_{et} through use of Equations 4.10 and 4.11. Although this analysis will clearly underestimate the actual k_{et} value relevant to the contact in the absence of the insulating oxide overlayer, such a calculation was of interest with respect to the value of k_{et} reported from luminescence decay data that have been collected on InP surfaces in this same redox system.[27] Figure 4.8 displays a Bode plot for an n-type InP electrode at E=+0.25 V vs. $E(A/A^-)$ in contact with a 1.00 M KCl -0.100 M $Fe(CN)_6^{3-}$-0.100 M $Fe(CN)_6^{4-}$ solution. Even though oxidation of the InP was probably occurring on the time scale of these measurements, the Bode plot (log $|\mathbf{Z}|$ vs. log f, where $|\mathbf{Z}|$ is the magnitude of the impedance vector) showed ideal behavior, with a slope of 0.97±0.01 for frequencies of 0.01 kHz < f < 100 kHz. The C^{-2} vs. E data for this system are shown in Figure 4.9. The plots were linear for 400 < f < 1 x 10^4 Hz, and the slopes of the lines agreed to within 50% of those expected from the manufacturer's specified dopant densities of the samples.[53]

Extrapolation of the Mott-Schottky data of Figure 4.9 to $C^{-2} = 0$ yielded $V_{bi} = 0.97 \pm 0.02$ V. For n-InP/KCl(aq)-$Fe(CN)_6^{3-/4-}$ contacts, J = 0.17 mA cm^{-2} at *E*= -0.8 V vs. *E*(A/A^-), so Equations 4.10 and 4.11 yielded an upper limit on k_{et} of 10^{-18} cm^4 s^{-1}. Because the J-*E* data were so resistive for the oxide-coated n-InP electrodes, the apparent rate constants were a function of the applied potential. At potentials more negative than -0.8 V vs. *E*(A/A^-), the apparent rate constant was even smaller; using the value of J = 2 mA cm^{-2} at *E*=-1.0 V in Equations 4.10 and 4.11 yielded a maximum value for k_{et} of 10^{-20} cm^4 s^{-1}. These bounds on k_{et} were directly obtained from the steady-state J-*E* data and therefore are essentially independent of kinetic models for the actual charge transfer process; in this regard, it is notable that the bounds on k_{et} determined herein are significantly smaller than the values of k_{et} (10^{-15} to 10^{-12} cm^4 s^{-1}, at various potentials) that were obtained from a model-dependent (oxide-free, defect-free surface) interpretation of the luminescence decay data for p-InP cathodes in contact with this same redox system.[27]

Impedance plots for n-InP/HCl(aq)-$Fe(CN)_6^{3-/4-}$ contacts were non-ideal, possibly due to the higher faradaic current at these electrodes. No useful information about the built-in voltage for this system could be obtained from a conventional Mott-Schottky analysis of the impedance data. However, assuming a similar value of V_{bi} for n-InP/KCl(aq)-$Fe(CN)_6^{3-/4-}$ contacts at neutral and acidic pH, an upper bound for k_{et} in acidic media can be estimated from the data of Figure 4.6b. Taking a value of 1.2 mA cm^{-2} at *E* = 0.70 V vs. *E*(A/A-) from the data of Figure 4.6b and making the same assumptions as above, k_{et} was bounded at $< 10^{-15}$ cm^4 s^{-1} for this system.

Figure 4.5: (a) J vs. *E* data for a n-InP/CH_3OH-$Me_2Fc^{+/0}$(0.100 M / 0.0100 M) junction in the light at two different light intensities. (b) J vs. *E* data for the same n-InP electrode contacting a H_2O-$Fe(CN)_6^{3-/4-}$(0.100 M / 0.100 M)-KCl(1.00 M) solution in the dark. Note that ideal diode behavior is not observed for this system; i.e., the curves for the two current scales do not show the ideal 0.059 V separation in voltage. (c) J vs. *E* data for the same n-InP/CH_3OH-$Me_2Fc^{+/0}$ junction in the light after this electrode had been cycled in the H_2O-$Fe(CN)_6^{3-/4-}$-KCl solution in the dark. Although the photocurrent densities are the same as in (a), the open circuit voltages are much lower and the curves are more resistive. In all cases the scan rate was 50 mV s^{-1}.

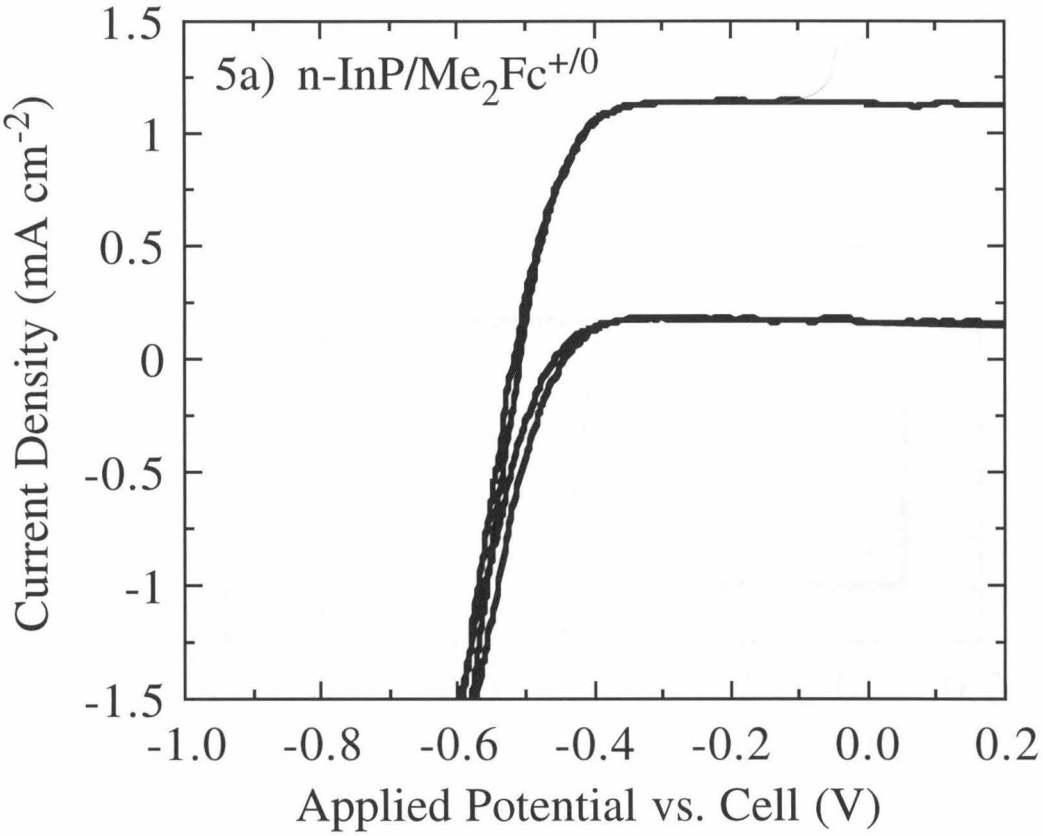
5a) n-InP/Me2Fc+/0
Current Density (mA cm-2)
1.5
1
0.5
0
-0.5
-1
-1.5
-1.0
-0.8
-0.6
-0.4
-0.2
0.0
0.2
Applied Potential vs. Cell (V)

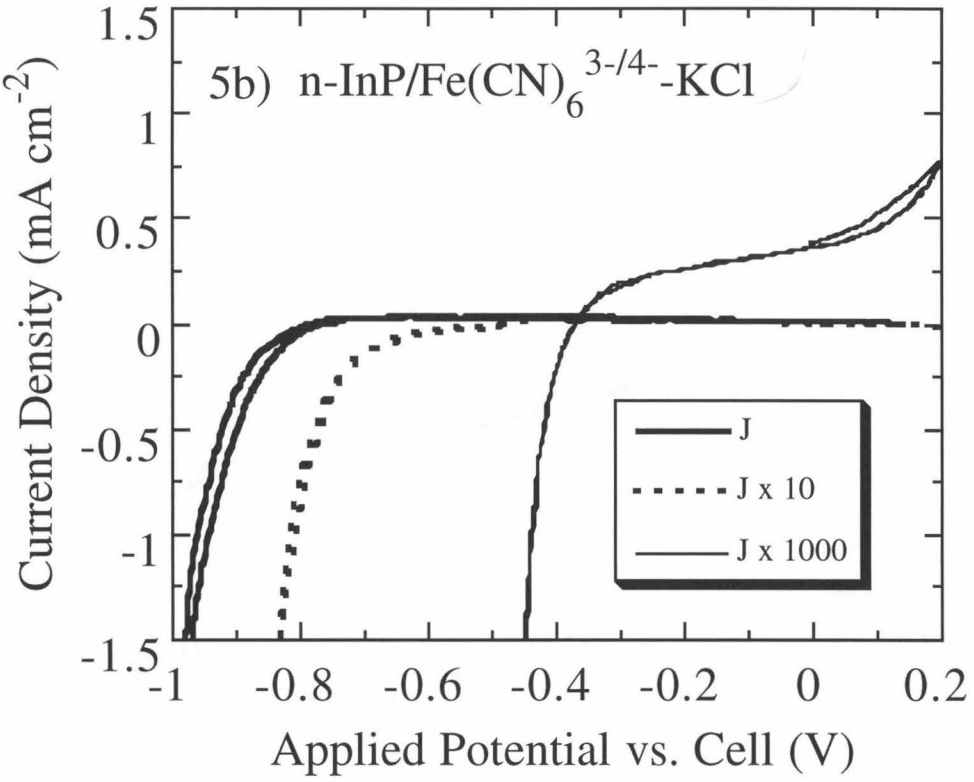
5b) n-InP/Fe(CN)6 3-/4--KCl
Current Density (mA cm-2)
Applied Potential vs. Cell (V)
1.5
1
0.5
0
-0.5
-1
-1.5
-1
-0.8
-0.6
-0.4
-0.2
0
0.2
J
J x 10
J x 1000

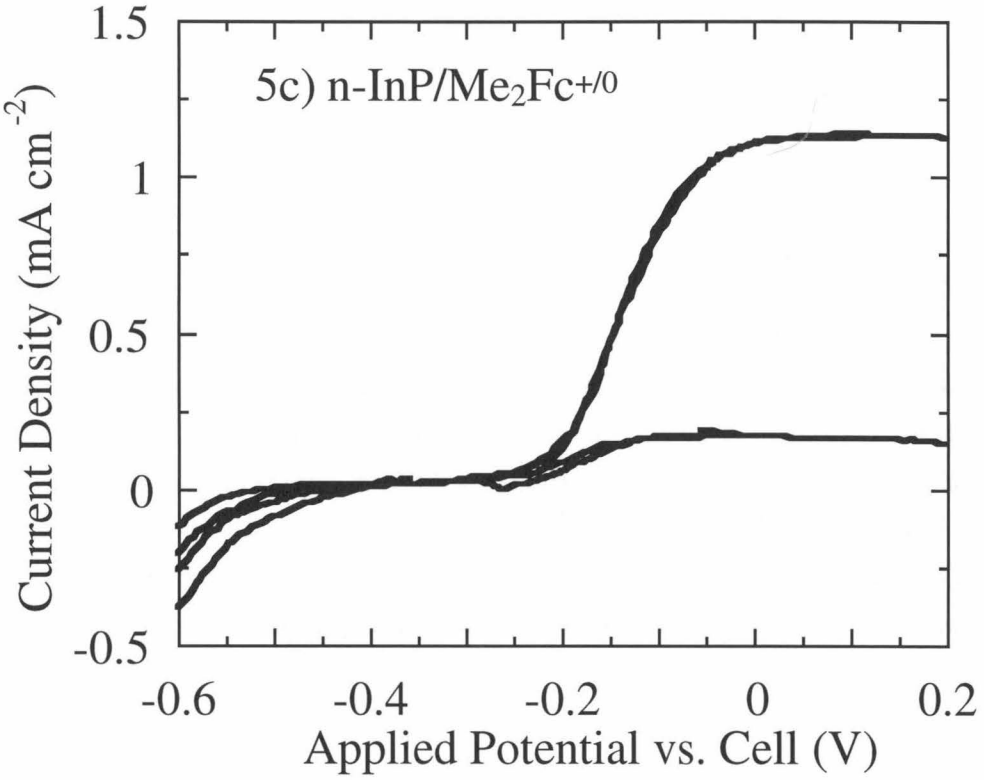
5c) n-InP/Me2Fc+/0
Current Density (mA cm-2)
1.5
1
0.5
0
-0.5
-0.6
-0.4
-0.2
0
0.2
Applied Potential vs. Cell (V)

Figure 4.6: (a) J vs. *E* data for a n-InP/CH_3OH-$Me_2Fc^{+/0}$(0.100 M / 0.0100 M) junction in the light at two different light intensities. (b) J vs. *E* data for the same n-InP electrode contacting a H_2O-$Fe(CN)_6^{3-/4-}$(0.100 M / 0.100 M)-HCl(1.00 M) solution in the dark. In this case, the curves for the two current scales show a much lower separation in voltage, closer to ideal diode behavior. (c) J vs. *E* data for the same n-InP/CH_3OH-$Me_2Fc^{+/0}$ junction in the light after this electrode had been cycled in the H_2O-$Fe(CN)_6^{3-/4-}$-HCl solution in the dark. Note that here the curves in (a) and (c) are nearly superimposable. In all cases the scan rate was 50 mV s^{-1}.

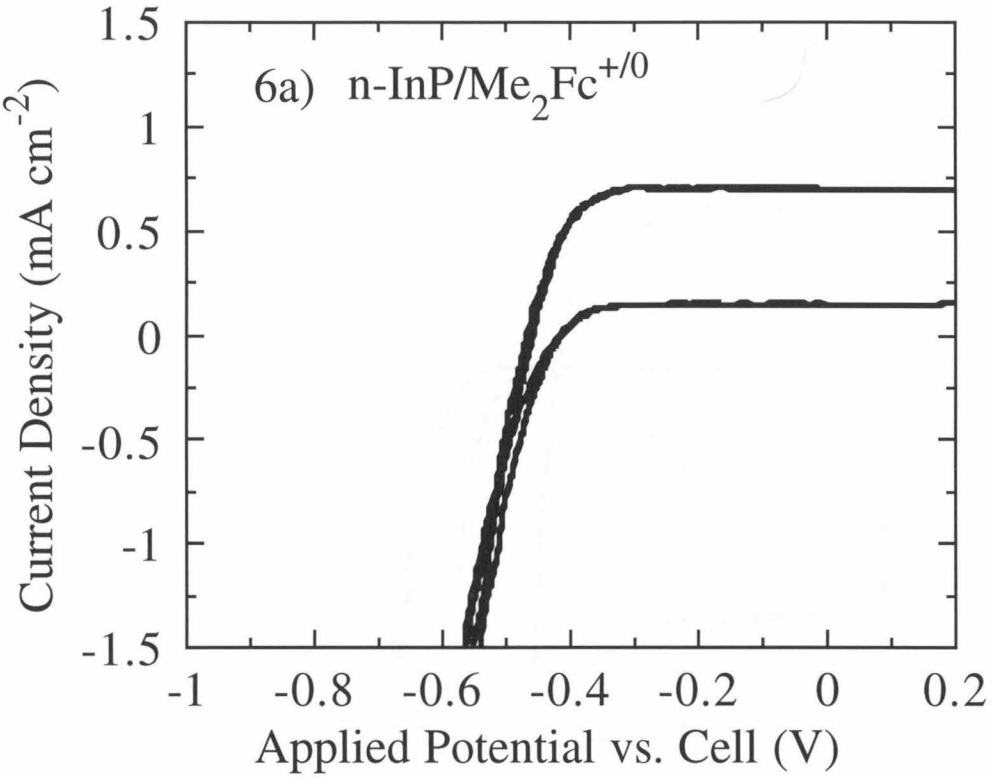
6a) n-InP/Me2Fc+/0
Current Density (mA cm-2)
Applied Potential vs. Cell (V)
1.5
1
0.5
0
-0.5
-1
-1.5
-1
-0.8
-0.6
-0.4
-0.2
0
0.2

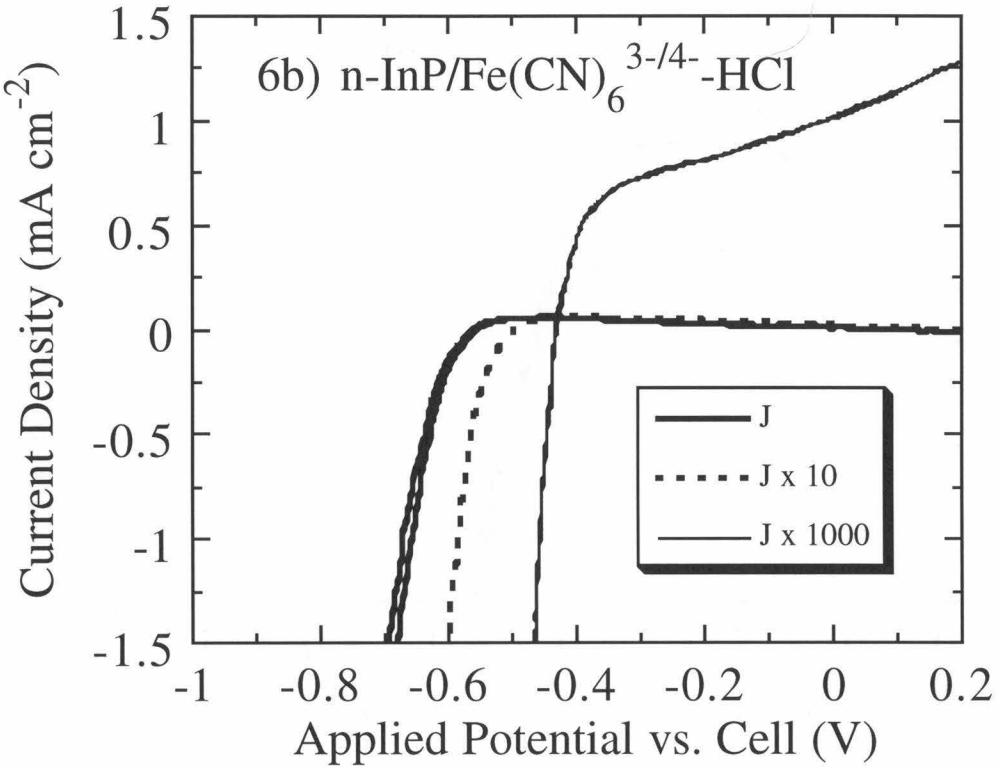
6b) n-InP/Fe(CN)6 3-/4--HCl
Current Density (mA cm-2)
Applied Potential vs. Cell (V)
1.5
1
0.5
0
-0.5
-1
-1.5
-1
-0.8
-0.6
-0.4
-0.2
0
0.2
J
J x 10
J x 1000

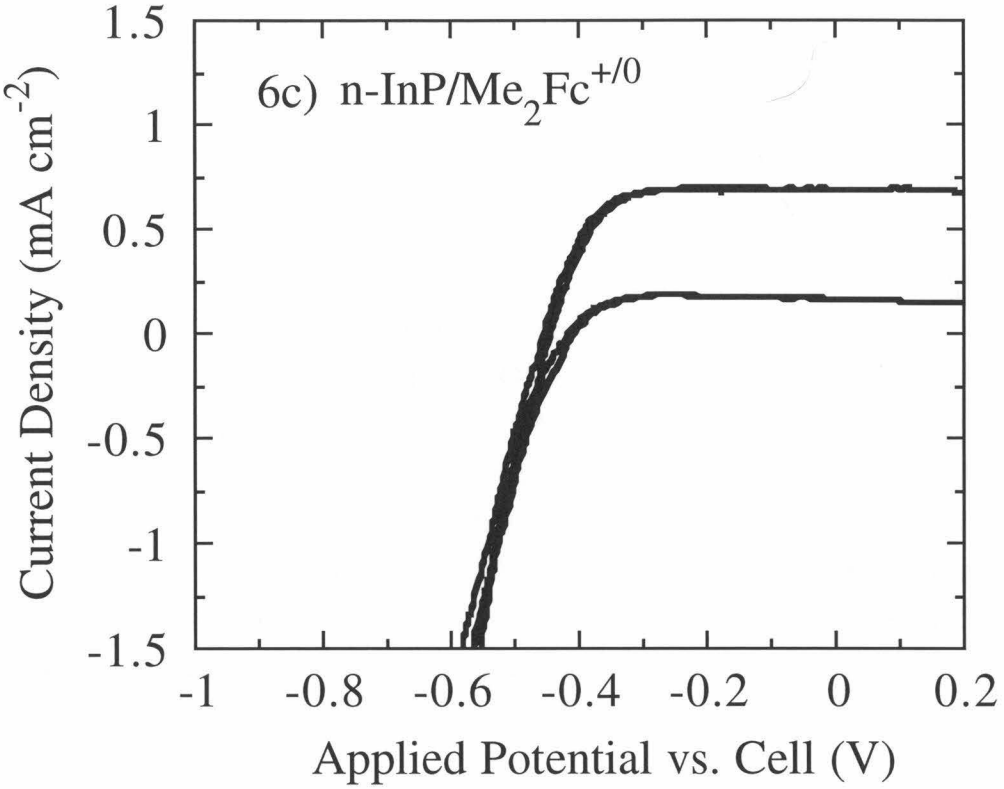
6c) n-InP/Me2Fc+/0
Current Density (mA cm-2)
Applied Potential vs. Cell (V)
1.5
1
0.5
0
-0.5
-1
-1.5
-1
-0.8
-0.6
-0.4
-0.2
0
0.2

Figure 4.7: Phosphorus (2p) region of XP spectra of electrodes after treatments described in Figures 4.5 and 4.6. The normal, unoxidized P(2p) signal for InP occurs at about 130.5 eV. (a) control 1: n-InP electrode etched in Br_2/CH_3OH and NH_3/CH_3OH (vide infra). (b) control 2: n-InP electrode cycled in a CH_3OH-$Me_2Fc^{+/0}$(0.100 M / 0.0100 M) solution in the light. (c) n-InP electrode cycled in a $H_2O/Fe(CN)_6^{3-/4-}$(0.100 M / 0.100 M)-HCl(1.00 M) solution in the dark (Figure 4.6). (d) n-InP electrode cycled in a $H_2O/Fe(CN)_6^{3-/4-}$(0.100 M / 0.0100 M)-KCl(1.00 M) solution in the dark (Figure 4.5). Of the four spectra, only Figure 4.7d shows a significant signal at 134.5 eV, evidence of a thick oxide layer on the surface of the electrode.

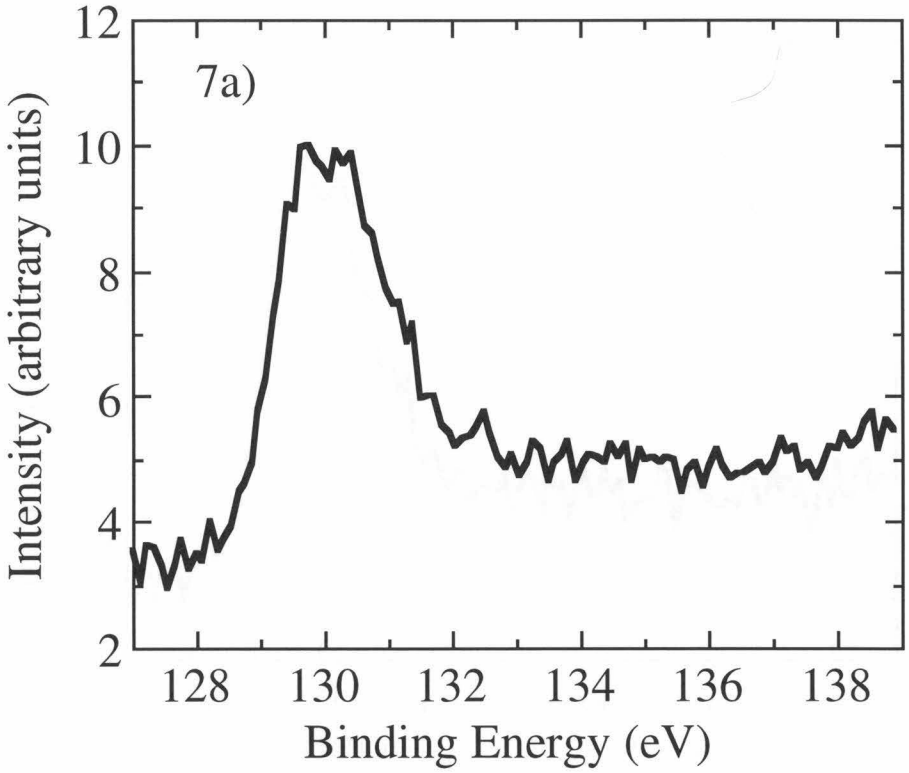
7a)
Intensity (arbitrary units)
Binding Energy (eV)
12
10
8
6
4
2
128
130
132
134
136
138

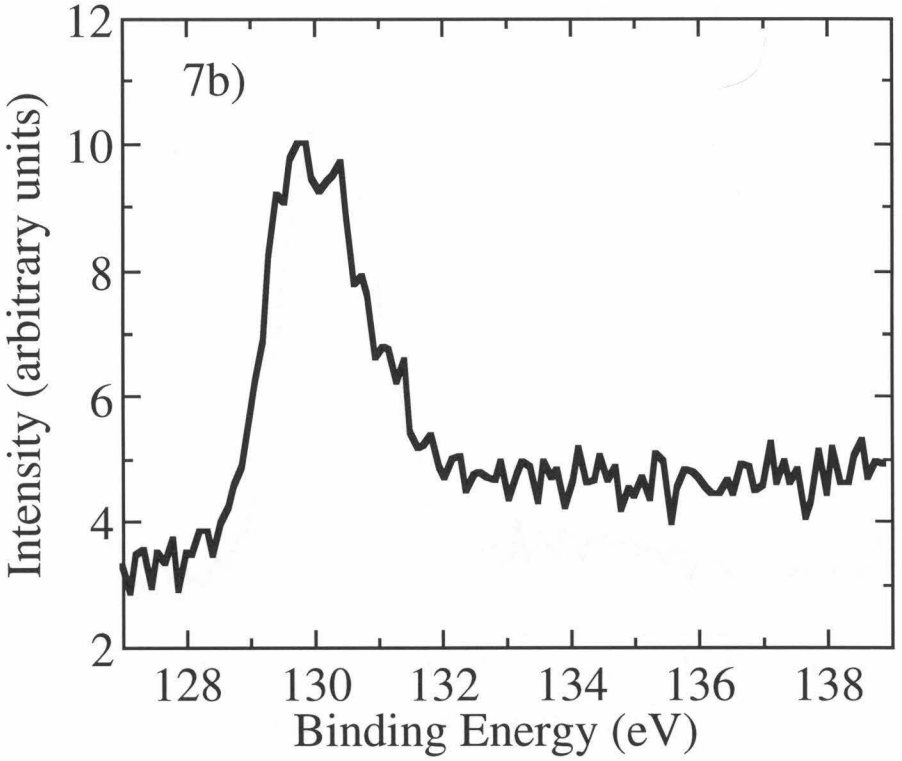
7b)
Intensity (arbitrary units)
Binding Energy (eV)
12
10
8
6
4
2
128
130
132
134
136
138

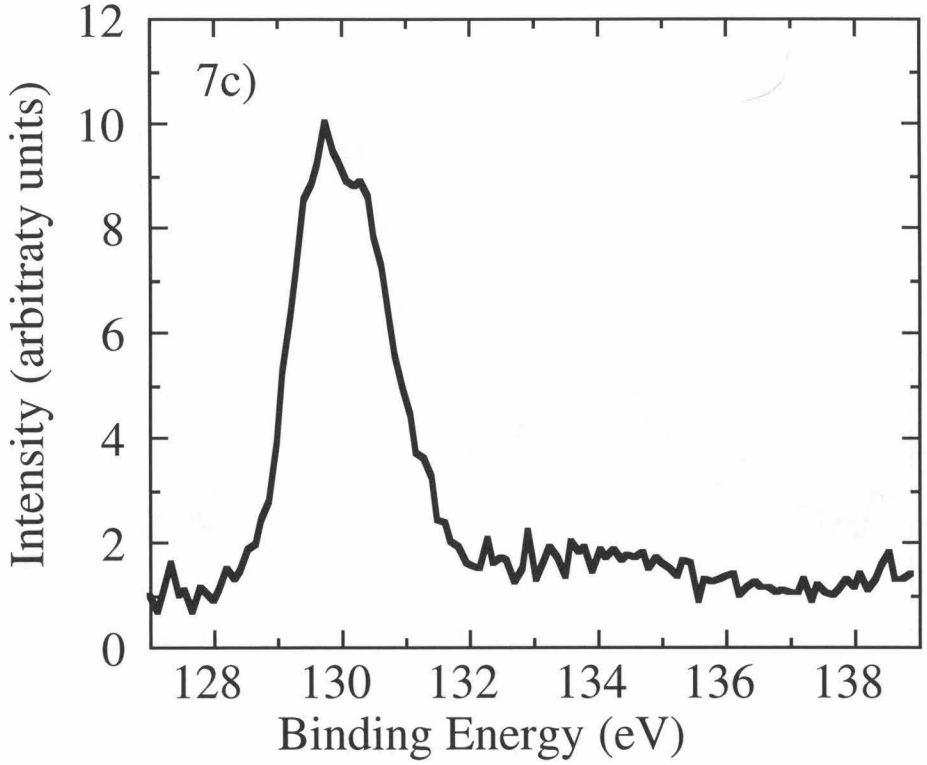
7c)
Intensity (arbitraty units)
Binding Energy (eV)
0
2
4
6
8
10
12
128
130
132
134
136
138

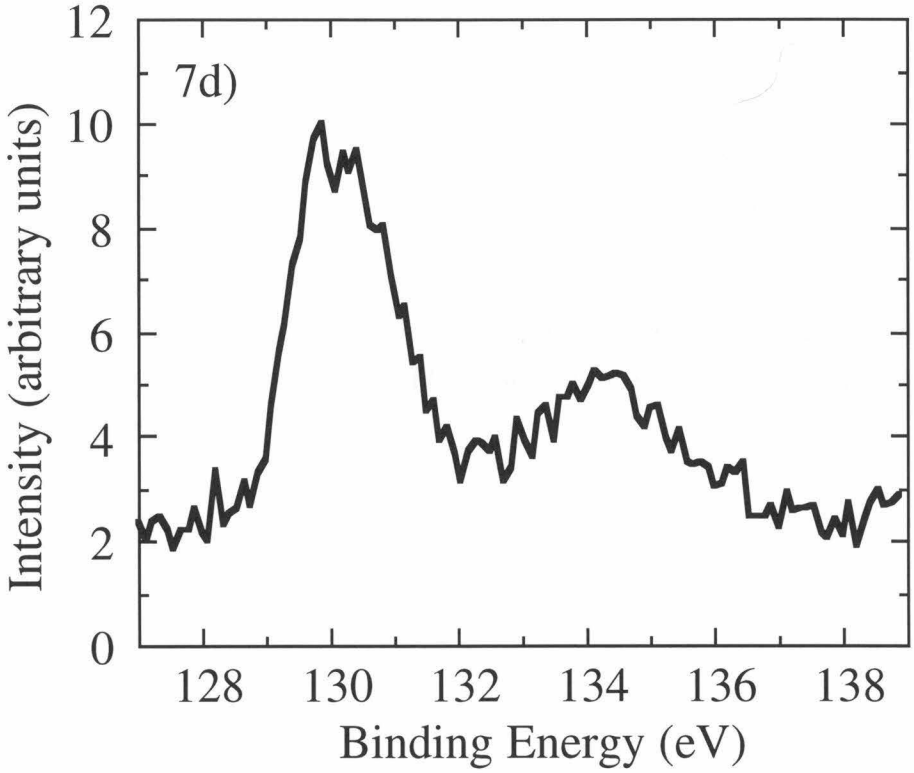
7d)
Intensity (arbitrary units)
Binding Energy (eV)
0
2
4
6
8
10
12
128
130
132
134
136
138

Figure 4.8: Bode plot for impedance data taken at 0.25 V dc bias for the n-InP/H_2O/$Fe(CN)_6^{3-/4-}$(0.100 M / 0.100 M)-KCl(1.00 M) junction. Fitting the curve to a power law shows the ideal dependence of impedance on frequency, with an exponent of 0.97, where the slope of a log |**Z**| vs. log f plot should be 1.0.

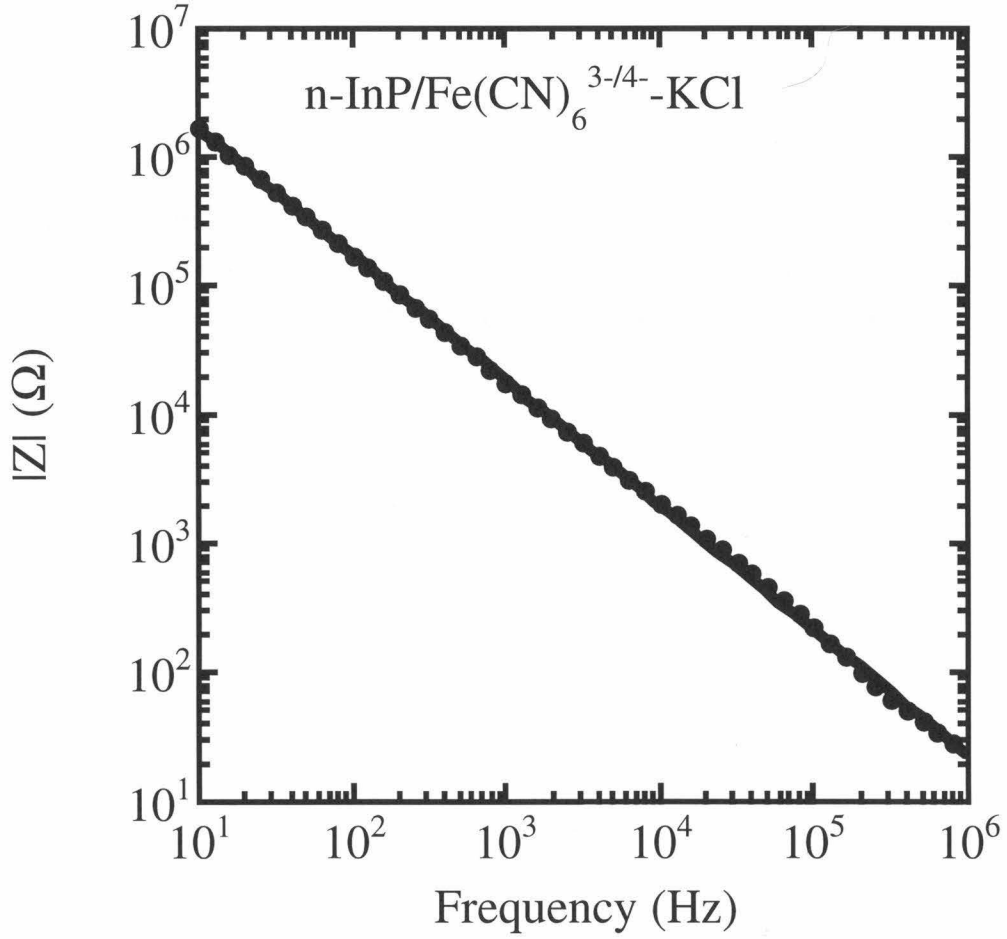
n-InP/Fe(CN)6 3-/4--KCl
|Z| (Ω)
Frequency (Hz)
10^7
10^6
10^5
10^4
10^3
10^2
10^1
10^1
10^2
10^3
10^4
10^5
10^6

Figure 4.8

Figure 4.9: (a) C^{-2} vs. applied dc potential for the n-InP/H_2O-$Fe(CN)_6^{3-/4-}$ junction in Figure 4.8. The points represent data taken at six frequencies between 0.1 and 1.2 kHz. (b) Extrapolation of the data points in (a).

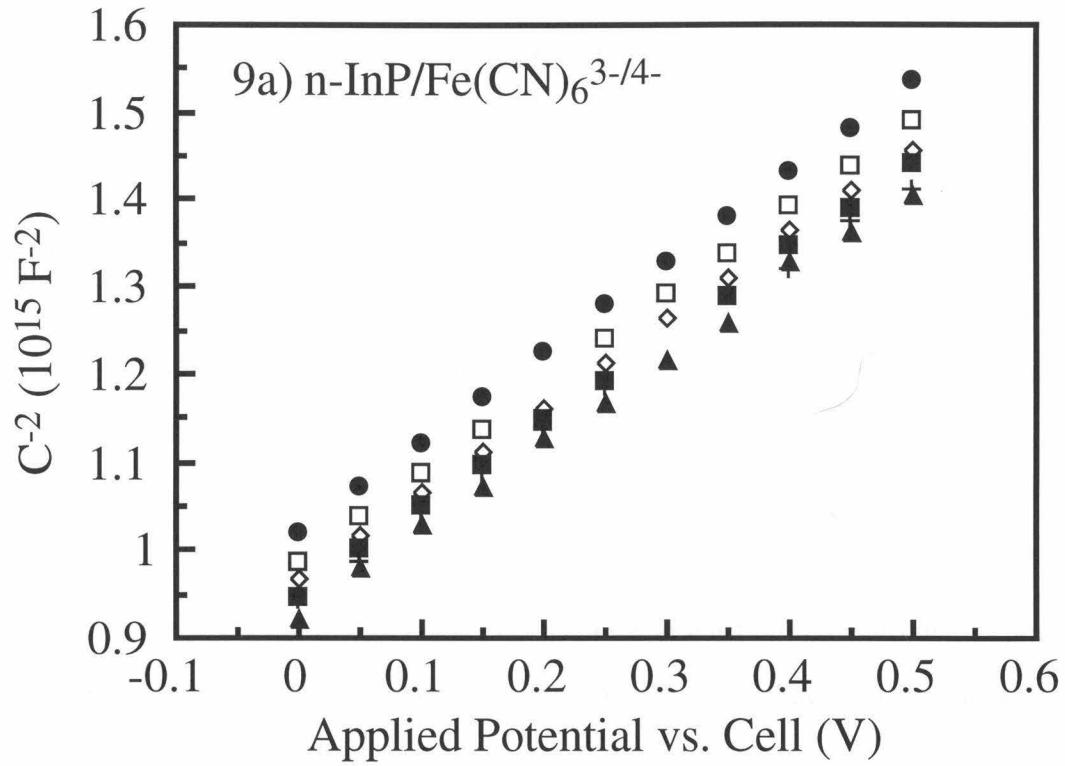
9a) n-InP/Fe(CN)6 3-/4-
C-2 (10 15 F-2)
1.6
1.5
1.4
1.3
1.2
1.1
1
0.9
-0.1
0
0.1
0.2
0.3
0.4
0.5
0.6
Applied Potential vs. Cell (V)

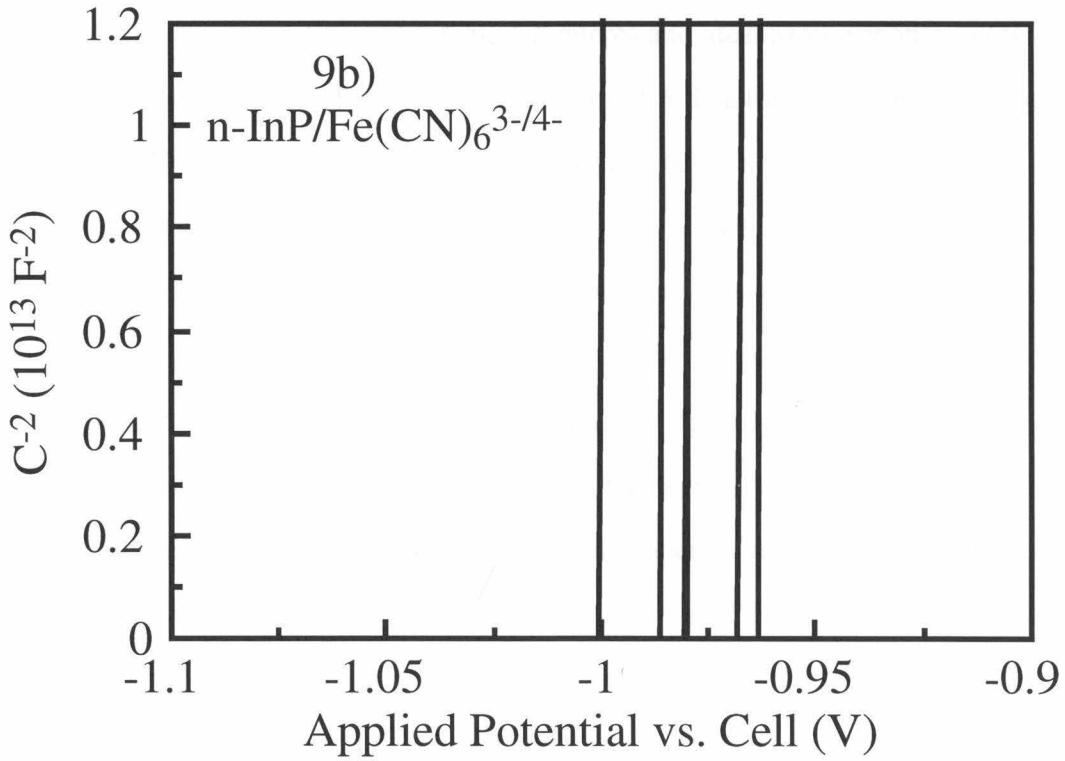
9b)
n-InP/Fe(CN)6 3-/4-
C-2 (10 13 F-2)
1.2
1
0.8
0.6
0.4
0.2
0
-1.1
-1.05
-1
-0.95
-0.9
Applied Potential vs. Cell (V)

C. Steady-State J-*E* Behavior of p-InP/H_2O-$Fe(CN)_6^{3-/4-}$ Contacts

Since anodic oxidation can be minimized on photocathodes that are continuously illuminated with band gap light and maintained in depletion,[54,55] the J-*E* behavior of p-InP electrodes was investigated directly in contact with KCl(aq)-$Fe(CN)_6^{3-/4-}$ solutions in the light. The goal of these studies was to evaluate whether the results obtained above, indicating the presence of irreversible chemical reactions on InP surfaces in contact with KCl(aq)-$Fe(CN)_6^{3-/4-}$, were applicable to illuminated p-type InP photocathode surfaces.[27] A protocol established previously,[56] and utilized in the studies of the electrochemistry of n-InP described above, was also used to evaluate the chemical reactivity of p-type InP surfaces. In this method, the J-*E* properties of an inert, stable, semiconductor/liquid contact are used to evaluate whether deleterious chemical reactions have occurred upon immersion and subsequent electrochemical experiments of the semiconductor surface with the electrolyte of interest.[56]

CH_3CN-$Co(Cp)_2^{+/0}$ solutions were used as the test electrolyte in this work, since p-InP electrodes were found to yield stable J-*E* curves and ideal Mott-Schottky plots in contact with these solutions. Figure 4.10a shows the J-*E* data for electrodes illuminated in contact with CH_3CN-0.100 M $Co(Cp)_2^+$-0.0010 M $Co(Cp)_2$ solutions. For such surfaces, V_{oc} values of 690 mV were obtained at J_{sc} = 1.1 mA cm^{-2} at T = 300 K. This J-*E* behavior is consistent with prior cyclic voltammetry studies on p-InP surfaces[45,46] in that large V_{oc} values are expected in contact with the $Co(Cp)_2^{+/0}$ redox couple. In addition, the p-InP photoelectrode of Figure 4.10a yielded significant optical-to-electrical energy conversion, displaying stable light-limited photocurrents in forward bias.

In contrast, the current density vs. potential properties of p-InP/1.00 M KCl(aq)-$Fe(CN)_6^{3-/4-}$- contacts were very poor (Figure 4.10b). This J-*E* behavior is in qualitative accord with that described in a prior report of the behavior of p-InP/1.00 M KCl(aq)-$Fe(CN)_6^{3-/4-}$ contacts at neutral pH.[27] In Figure 4.10b, negligible cathodic current densities were observed in forward bias, and applied voltages >0.5 V into reverse bias

were required in order to achieve a significant photocurrent density. Comparison of Figures 10a and 10b indicates that an overpotential of >1 V relative to V_{oc} was required on the p-InP/1.00 M KCl(aq)-$Fe(CN)_6^{3-/4-}$ contact to produce photocurrent densities that were comparable to those of the p-InP/CH_3CN-$Co(Cp)_2^{+/0}$ contact.

When the p-InP photocathode of Figure 4.10b was reimmersed, without etching, into the CH_3CN-$Co(Cp)_2^{+/0}$ electrolyte, significant changes were observed in the J-*E* properties of this system. Comparison of Figures 10a and 10c illustrates that immersion of the p-InP electrode into the 1.00 M KCl(aq)-$Fe(CN)_6^{3-/4-}$ electrolyte produced irreversible changes in the photoelectrode properties, and converted an efficient, energy-storing photoelectrode into a photoelectrode that required both illumination and an applied bias relative to the equilibrium solution potential in order to sustain significant interfacial photocurrent. This behavior is consistent with the formation of an insulating oxide overlayer on the p-InP surface in contact with 1.00 M KCl(aq)-$Fe(CN)_6^{3-/4-}$ solutions, as was identified above for n-InP electrodes. The use of CH_3CN-$Co(Cp)_2^{+/0}$ as a test electrolyte thus clearly revealed that the p-InP/1.00 M KCl(aq)-$Fe(CN)_6^{3-/4-}$-system is unstable and produces irreversible changes in the surface electrical properties of the p-InP photocathode.

Figure 4.10: (a) J vs. *E* data for a p-InP/CH_3CN-$Co(Cp)_2^{+/0}$(0.025 M / 0.0010 M) junction in the light at three different light intensities. (b) J vs. *E* data for the same p-InP electrode contacting a H_2O-$Fe(CN)_6^{3-/4-}$(0.100 M / 0.100 M)-KCl(1.00 M) solution at approximately identical light intensities. The photovoltages are extremely low in comparison with (a), and the curves are very resistive. (c) J vs. *E* data for the same p-InP/CH_3CN-$Co(Cp)_2$ junction at the same light intensities in (a) and (b) after this electrode had been cycled in the H_2O-$Fe(CN)_6^{3-/4-}$-KCl solution. In all cases the scan rate was 50 mV s^{-1}.

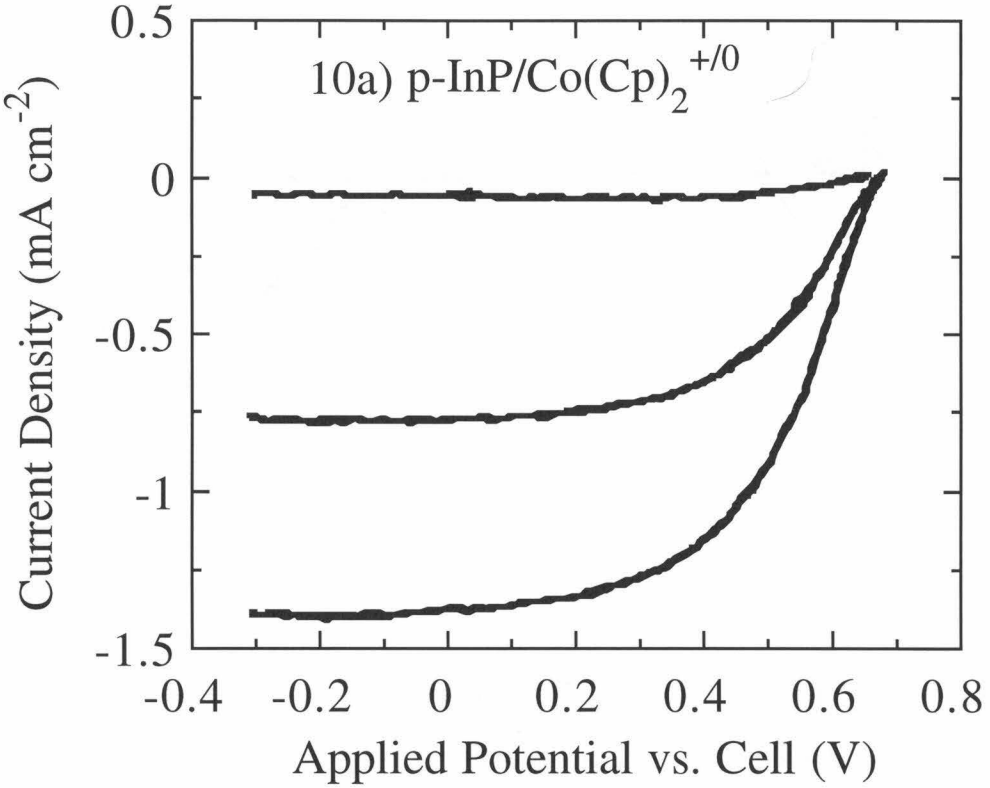
10a) p-InP/Co(Cp)2+/0
Current Density (mA cm-2)
Applied Potential vs. Cell (V)
0.5
0
-0.5
-1
-1.5
-0.4
-0.2
0
0.2
0.4
0.6
0.8

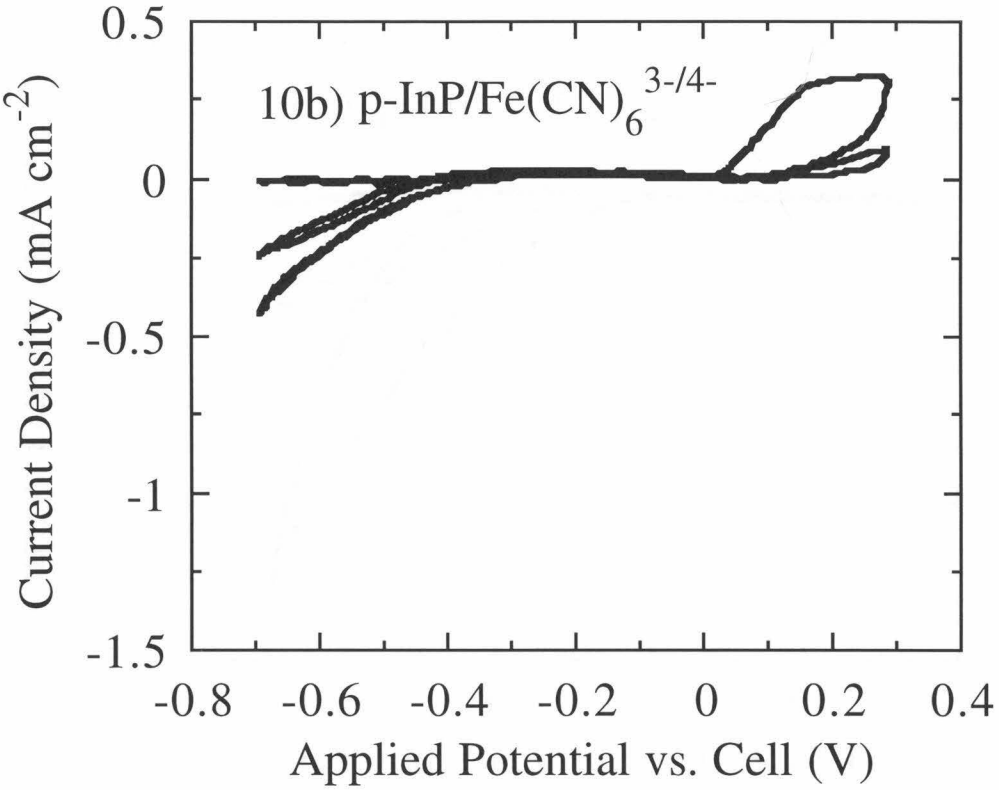
10b) p-InP/Fe(CN)6 3-/4-
Current Density (mA cm-2)
0.5
0
-0.5
-1
-1.5
-0.8
-0.6
-0.4
-0.2
0
0.2
0.4
Applied Potential vs. Cell (V)

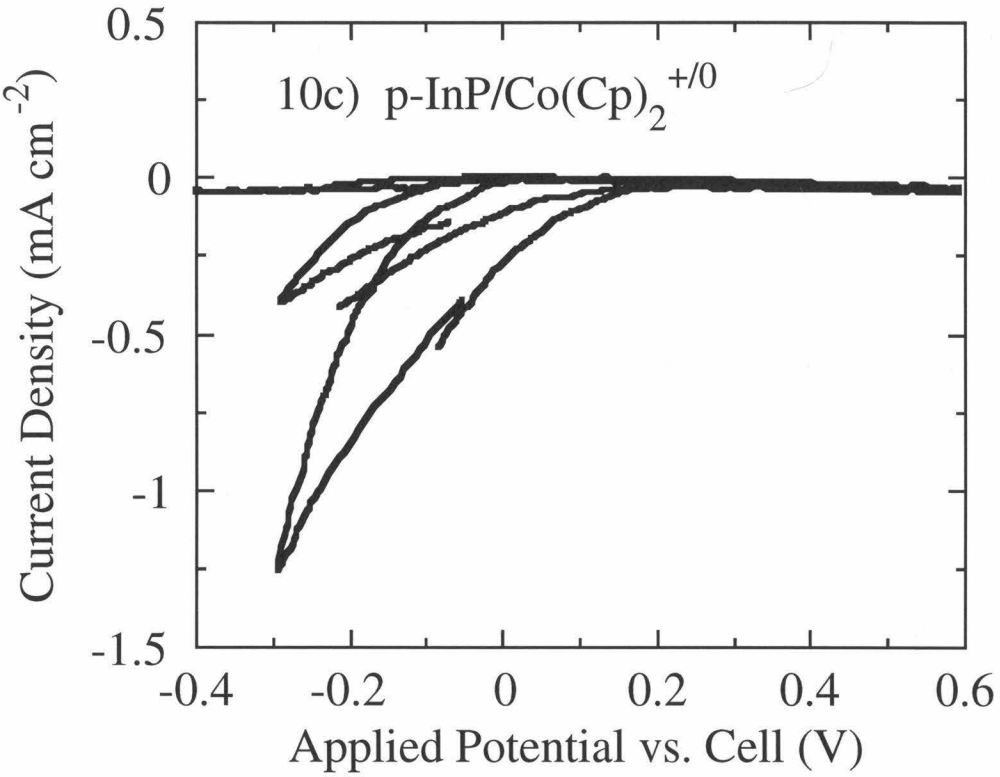
10c) p-InP/Co(Cp)2 +/0
Current Density (mA cm-2)
0.5
0
-0.5
-1
-1.5
-0.4
-0.2
0
0.2
0.4
0.6
Applied Potential vs. Cell (V)

V. Discussion

Although the data described herein do not establish absolute values for k_{et}, they do allow definition of upper bounds on k_{et} of less than 10^{-13} cm^4 s^{-1} for the entire collection of semiconductor/liquid contacts and upper bounds on k_{et} of less than 10^{-14} cm^4 s^{-1} for the n-Si and n-GaAs semiconductor/liquid interfaces that have been investigated. The approach used herein also extends a previously proposed protocol for establishing which interfaces are suitable for use in a comparison between the theoretical predictions and the experimental data.[56] Estimates of λ and measurements of V_{bi} for these well-behaved semiconductor/liquid junctions indicate that κ_n is on the order of 10^{-1}-10^{0} for the contacts discussed herein. These data therefore serve to establish semi-quantitative upper bounds on $k_{et,max}$ for these systems. The measurements and calculations discussed above are also in agreement with recent determinations of k_{et} for p-WS_2/H_2O-$Ru(NH_3)_6^{3+/2+}$ contacts,[24] with measurements of k_{et} for n-WSe_2/CH_3CN-$Me_2Fc^{+/0}$ contacts,[57] and with upper limits on k_{et} that have been estimated previously for n-Si/liquid contacts.[1,26,33,39]

The maximum possible value of the bimolecular interfacial charge transfer rate constant is pertinent to optimal efficiencies for photoelectrochemical solar energy conversion devices. Specifically, a large majority carrier charge transfer rate constant is undesirable for the construction of efficient photoelectrochemical energy conversion devices. For example, from Equation 4.11, with $k_{et} = 10^{-12}$ cm^4 s^{-1}, $N_d = 10^{16}$ cm^{-3} and [A] = 0.10 M, $|J_{et}(0)| = (1 \times 10^5) \exp(-qV_{bi}/kT)$. Setting $J_{rec} = J_{et}$ in Equation 4.12, and taking $J_{ph} = 20$ mA cm^{-2} (Equation 4.15) allows calculation of the maximum possible V_{oc} under these conditions. Such a calculation implies that $V_{oc} - V_{bi} = -0.40$ V, and that the difference between ϕ_b and V_{oc} is 0.55-0.65 V. Thus, even in the optimized situation of extremely high barrier heights, with $\phi_b \approx \mathbf{E}_g/q$, V_{oc} would be much less than $(\mathbf{E}_g/q)$ due to efficient majority carrier capture process. Losses in quantum yield would also be observed in the short-wavelength spectral response of such semiconductor/liquid contacts,[58] due to the efficient competition between drift-induced charge separation and concentration-gradient

driven charge recombination processes that would occur with such a large majority carrier collection velocity.[58] The construction of efficient photoelectrochemical cells, such as those reported in the literature using n-Si/CH_3OH-$Me_2Fc^{+/0}$,[38,59,60] n-GaAs/CH_3CN-$Fc^{+/0}$,[61,62] p-Si/CH_3CN-cobaltocene$^{+/0}$,[63] and other semiconductor/liquid contacts[48] would not appear to be possible with this value of the bimolecular rate constant for interfacial majority carrier charge transfer.[64]

It is also interesting to explore the implications of rate constants greater than the upper bounds established in the systems studied herein with respect to the physical behavior of semiconductor/liquid contacts. A value of $k_{et}=10^{-12}$ cm^4 s^{-1} was assigned to a luminescence decay time of ~1 ps for InP cathodes injected with 10^{12} carriers cm^{-3} in contact with 0.10 M $Fe(CN)_6^{3-}$-0.10 M $Fe(CN)_6^{4-}$.[27] A bimolecular rate law interpretation of this data would therefore predict a luminescence decay time of ≈ 100 ps at 1.0 mM of acceptor species. At [A] = 1.0 mM = 10^{17} cm^{-3}, the volume defined by a 1 cm x 1 cm area of solution extending 10^{-7} cm from the electrode surface contains 10^{10} molecules. Because the large scale ion movements are essentially frozen on short timescales, in order to collect 10^{12} charge carriers cm^{-2} through interfacial charge transfer in 100 ps, a significant fraction of the photogenerated charge carriers would have to be injected 0.1 μm into the solution during this 100 ps time period. Such rates have no precedent in molecular charge transfer systems;[65-68] thus, a bimolecular charge transfer rate constant of 10^{-12} cm^4-s^{-1} would require that the semiconductor electrode drastically modify the electron tunneling properties of the solvent in order for the electron transfer to occur over such large distances on such short timescales.

The unusual electrical junction properties predicted at very large interfacial charge transfer rate constants are underscored by comparison of the predicted recombination current density at semiconductor/liquid interfaces with various values of k_{et} to the recombination current density observed for semiconductor/metal Schottky barriers.[34] For semiconductor/metal contacts, essentially every carrier that reaches the semiconductor/metal

junction is captured by the metal phase.[34] The thermionic emission-diffusion current density for semiconductor/metal contacts, which describes this charge carrier capture process, is:[34]

$$J_{th}(0) = -A^{*}T^{2}e^{-\left(\frac{q\phi_b}{kT}\right)} \tag{4.21}$$

where A^* is the effective Richardson constant for thermionic emission. Combining Equations 4.10 and 21 therefore yields the ratio between the charge transfer current densities for semiconductor/metal and semiconductor/liquid contacts of identical barrier heights:

$$\frac{J_{et}(0)}{J_{th}(0)} = \left[\frac{qk_{et}[A]N_c}{A^{*}T^{2}}\right] \tag{4.22}$$

With $k_{et} = 10^{-12}$ cm^4 s^{-1} and [A] = 0.10 M = 6 x 10^{19} cm^{-3} (a typical value for operating photoelectrochemical cells), Equation 4.22 predicts that $J_{et} \approx J_{th}$. In other words, with such a large bimolecular charge transfer rate constant, the steady-state majority carrier recombination losses from an interfacial electron transfer process would be as severe as those for semiconductor/metal contacts, in which essentially every majority carrier that reaches the surface is collected in a deleterious recombination event. This efficient capture by the redox ions in the solution would be occurring at only [A] = 0.10 M, i.e., under conditions when > 99% of the volume of the solution, and > 99% of the geometric cross sectional area presented to the electron, was occupied by inert, spectator species such as the electrolyte ions and the solvent molecules. Smaller values of k_{et}, such as those established in this work, therefore correspond more closely to the expected situation in which the capture cross section of the acceptor species is approximately its geometric cross section.[69]

Small majority carrier interfacial rate constants are thus desirable for the construction of efficient photoelectrochemical cells.

The system in which bias-dependent luminescence decay dynamics have been reported and interpreted in terms of field-dependent charge transfer velocities is the p-InP/KCl(aq)-$Fe(CN)_6^{3-/4-}$ interface.[27] In the present work, InP/KCl(aq)-$Fe(CN)_6^{3-/4-}$ interfaces have been shown to be unstable to passivation and corrosion processes both in the dark and under illumination. The presence of an insulating oxide would require the application of large reverse bias potentials in order to obtain significant photocurrent flow through the layer. The presence of such an oxide would thus provide a consistent explanation of the high overpotential J-*E* behavior observed in this work and in prior work for p-InP/KCl(aq)-$Fe(CN)_6^{3-/4-}$ contacts[27] and would explain the poor J-*E* behavior observed for p-InP photocathodes in contact with CH_3CN-$Co(Cp)_2^{+/0}$ contacts after exposure to the passivating KCl(aq)-$Fe(CN)_6^{3-/4-}$ solution. A quantitative analysis of the behavior of the charge transfer dynamics in the p-InP/KCl-$Fe(CN)_6^{3-/4-}$ system would therefore require rigorous inclusion of the transmission coefficients and voltage drops across the insulating oxide overlayer as a function of the applied potential. Notably, the field-dependent minority carrier charge transfer effects identified to date, if validated experimentally while accounting for the presence of the InP oxide overlayer, would not appear to be of concern in efficient energy conversion systems, for which the band bending under illumination must be minimized in order to obtain maximal photovoltages from the semiconductor/liquid contact.

Another contributing factor to produce apparently large k_{et} values in transient relaxation processes of semiconductor/liquid contacts involves adsorption of the redox ions on the semiconductor surface. Strong adsorption increases the effective surface concentration of acceptor species above that calculated for a random distribution of acceptors, thereby facilitating increased charge carrier capture rates. Additionally, intermediate capture of charge carriers by surface states prior to subsequent transfer into the

acceptor ion,[22,25,57] inner sphere bridges to the redox center from the electrode, and other such processes might also be important in producing very high apparent k_{et} values.[70,71] Experiments conducted under such situations do not measure the rate constant for transfer to outer-sphere, non-adsorbed, randomly distributed acceptors at inert semiconductor surfaces, but measure the capture velocity for a fundamentally different charge transfer process. Adsorption appears to be of concern in a previously investigated system for which real-time luminescence quenching measurements of the charge carrier decay dynamics had been interpreted as exhibiting k_{et} values larger than theoretically expected,[56,72] and possibly could affect rate constants for InP/KCl(aq)$Fe(CN)_6^{3-/4-}$ contacts in the absence of an oxide overlayer or could establish the upper limit for charge transport through the InP oxide overlayer. The direct steady-state methods employed herein place an upper bound on the charge transfer rate constant that is ≈8 orders of magnitude lower than those obtained from an interpretation of transient luminescence decay experiments, underscoring the difficulty in interpreting transient luminescence decay data in the absence of well-defined, oxide-free and defect-free surfaces with defined band bending and carrier injection levels.

In summary, upper limits on k_{et} or k_{ht} have been experimentally determined for three semiconductor/solution systems which have been shown to exhibit stable, non-resistive, diode behavior. The limits on bimolecular interfacial charge transfer rate constants determined for these systems are consistent with theoretical expectations. In contrast, it has been shown that n- and p-type InP/KCl(aq)-$Fe(CN)_6^{3-/4-}$ contacts are unstable and thus unsuitable for these types of measurements. Further quantitative study involving charge transfer rate constants requires identification of systems in which the recombination current is dominated by charge transfer across the barrier or demands exploiting another reliable technique by which these rate constants can be measured.

VI. References and Notes

(1) Lewis, N. S. *Ann. Rev. Phys. Chem.* **1991**, *42*, 543.

(2) Marcus, R. A. *J. Phys. Chem.* **1991**, *95*, 2010.

(3) Ibach, H.; Luth, H. *Solid-State Physics*; Springer Verlag: Berlin, 1990.

(4) Miller, J. R.; Beitz, J. V.; Huddleston, R. K. *J. Am. Chem. Soc.* **1984**, *106*, 5057.

(5) Domingue, R. P.; Fayer, M. D. *J. Chem. Phys.* **1985**, *83*, 2242.

(6) Bowler, B. E.; Raphael, A. L.; Gray, H. B. *Prog. Inorg. Chem.* **1990**, *38*, 259.

(7) Axup, A. W.; Albin, M.; Mayo, S. L.; Crutchley, R. J.; Gray, H. B. *J. Am. Chem. Soc.* **1988**, *110*, 435.

(8) Elias, H.; Chou, M. H.; Winkler, J. R. *J. Am. Chem. Soc.* **1988**, *110*, 429.

(9) Mayo, S. L.; Ellis, W. R.; Crutchley, R. J.; Gray, H. B. *Science* **1986**, *233*, 948.

(10) Oevering, H.; Paddon-Row, M. N.; Heppener, M.; Oliver, A. M.; Cotsaris, E.; Verhoeven, J. W.; Hush, N. S. *J. Am. Chem. Soc.* **1987**, *109*, 3258.

(11) Paddon-Row, M. N.; Oliver, A. M.; Warman, J. M.; Smit, K. J.; de Haas, M. P.; Oevering, H.; Verhoevern, J. W. *Phys. Chem.* **1988**, *92*, 6958.

(12) Closs, G. L.; Miller, J. R. *Science* **1988**, *240*, 440.

(13) Penfield, K. W.; Miller, J. R.; Paddon-Row, M. N.; Cotsaris, E.; Oliver, A. M.; Hush, N. S. *J. Am. Chem. Soc.* **1987**, *109*, 5061.

(14) Isied, S. S.; Vassilian, A.; Wishart, J. F.; Creutz, C.; Schwarz, H. A.; Sutin, N. *J. Am. Chem. Soc.* **1988**, *110*, 635.

(15) Schanze, K. S.; Sauer, K. *J. Am. Chem. Soc.* **1988**, *110*, 1180.

(16) Leland, B. A.; Joran, A. D.; Felker, P. M.; Hopfield, J. J.; Zewail, A. H.; Dervan, P. B. *J. Phys. Chem.* **1985**, *89*, 5571.

(17) Geno, M. J. K.; Dawson, J. H. *Inorg. Chem.* **1984**, *23*, 1182.

(18) Finckh, P.; Heitele, H.; Volk, M.; Michelbeyerle, M. E. *J. Phys. Chem.* **1988**, *92*, 6584.

(19) Woitellier, S.; Launay, J. P.; Spangler, C. W. *Inorg. Chem.* **1989**, *28*, 758.

(20) Finklea, H. O.; Hanshew, D. D. *J. Am. Chem. Soc.* **1992**, *114*, 3173.

(21) Carter, M. T.; Rowe, G. K.; Richardson, J. N.; Tender, L. M.; Terrill, R. H.; Murray, R. W. *J. Am. Chem. Soc.* **1995**, *117*, 2896.

(22) Gerischer, H. *J. Phys. Chem.* **1991**, *95*, 1356.

(23) Shreve, G. A. Thesis, California Institute of Technology, 1994.

(24) Bard, A. J.; Mirkin, M. V.; Horrocks, B. R. *J. Phys. Chem.* **1994**, *98*, 2739.

(25) Morrison, S. R. *Surface Science* **1969**, *15*, 363.

(26) Forbes, M. D. E.; Lewis, N. S. *J. Am. Chem. Soc.* **1990**, *112*, 3682.

(27) Rosenwaks, Y.; Thacker, B. R.; Nozik, A. J.; Ellingson, R. J.; Burr, K. C.; Tang, C. L. *J. Phys. Chem.* **1994**, *98*, 2739.

(28) Smith, B. B.; Nozik, A. J. In *19th D. O. E. Solar Photochemistry Research Conference*; Washington, D. C., 1995.

(29) Bard, A. J.; Faulkner, L. R. *Electrochemical Methods: Fundamentals and Applications*; John Wiley & Sons: New York, 1980, pp 629.

(30) Kesselman, J.; Hoffman, M. R.; Shreve, G. A.; Lewis, N. S. *J. Phys. Chem.* **1995**, *98*, 13385.

(31) Morrison, S. R. *Electrochemistry at Semiconductor and Oxidized Metal Electrodes*; Plenum: New York, 1980.

(32) Fonash, S. J. *Solar Cell Device Physics*; Academic: New York, 1981.

(33) Laibinis, P. E.; Stanton, C. E.; Lewis, N. S. *J. Phys. Chem.* **1994**, *98*, 8765.

(34) Sze, S. M. *The Physics of Semiconductor Devices;* 2nd ed.; Wiley: New York, 1981.

(35) Lewis, N. S. *J. Electrochem. Soc.* **1984**, *131*, 2496.

(36) Lewis, N. S. *Acc. Chem. Res.* **1990**, *23*, 176.

(37) Rosenbluth, M. L.; Lewis, N. S. *J. Am. Chem. Soc.* **1986**, *108*, 4689.

(38) Kobayashi, H.; Chigami, A.; Takeda, N.; Tsubomura, H. *J. Electroanal. Chem.* **1990**, *287*, 239.

(39) Kumar, A.; Lewis, N. S. *J. Phys. Chem.* **1991**, *95*, 7021.

(40) Kuphal, E. *Sol. St. Electron.* **1981**, *24*, 69.

(41) Hendrickson, D. H.; Sohn, Y. S.; Gray, H. B. *Inorg. Chem.* **1971**, *10*, 1559.

(42) Pomykal, K. E.; Fajardo, A. M.; Lewis, N. S. *J. Phys. Chem.* **1995**, *99*, 8302.

(43) Briggs, D.; Seah, M. P. *Auger and X-ray Photoelectron Spectroscopy;* 2nd ed.; John Wiley & Sons, Inc.: New York, 1990; Vol. 1.

(44) Tanuma, S.; Powell, C. J.; Penn, D. R. *Surf. Interface Anal.* **1991**, *17*, 927.

(45) Dominey, R. N.; Lewis, N. S.; Wrighton, M. S. *J. Am. Chem. Soc.* **1981**, *103*, 1261.

(46) Koval, C. A.; Austermann, R. L.; Turner, J. A.; Parkinson, B. A. *J. Electrochem. Soc.* **1985**, *132*, 613.

(47) Segar, P. R.; Koval, C. A.; Koel, B. E.; Gebhard, S. C. *J. Electrochem. Soc.* **1990**, *137*, 544.

(48) Heben, M. J.; Kumar, A.; Zheng, C.; Lewis, N. S. *Nature* **1989**, *340*, 621.

(49) Pourbaix, M. *Atlas of Electrochemical Equilibria in Aqueous Solution*; Pergammon: New York, 1966.

(50) Aspnes, D. E.; Studna, A. A. *Appl. Phys. Lett.* **1981**, *39*, 316.

(51) Kobayashi, H.; Mizuno, F.; Nakato, Y.; Tsubomura, H. *J. Phys. Chem.* **1991**, *95*, 819.

(52) Massies, J.; Turco, F.; Contour, J.-P. *Jpn. J. Appl. Phys.* **1986**, *25*, L664.

(53) The poorer agreement of the slopes of the lines with those calculated using the dopant density specified by the manufacturer may be partially due to the concurrent passivation of the electrode with the impedance measurements. As the electrode is oxidized, less of the applied voltage will be dropped across the semiconductor depletion region, so the calculated V_{bi} may be even higher than the actual V_{bi}. Due to the problems

inherent in this system, these values should be viewed as only rough estimates, where the parameters have been chosen to yield the highest rate constant estimates that are consistent with the data.

(54) Heller, A.; Miller, B.; Lewerenz, H. J.; Bachmann, K. J. *J. Am. Chem. Soc.* **1980**, *102*, 6555.

(55) Finklea, H. O. *Semiconductor Electrodes*; Elsevier: New York, 1988.

(56) Bansal, A.; Tan, M. X.; Tufts, B. J.; Lewis, N. S. *J. Phys. Chem.* **1993**, *97*, 7309.

(57) Howard, J. N.; Koval, C. A. *Anal. Chem.* **1994**, *66*, 4525.

(58) Kumar, A.; Lewis, N. S. *J. Phys. Chem.* **1990**, *94*, 6002.

(59) Rosenbluth, M. L.; Lieber, C. M.; Lewis, N. S. *Appl. Phys. Lett.* **1984**, *45*, 423.

(60) Gibbons, J. F.; Cogan, G. W.; Gronet, C. M.; Lewis, N. S. *Appl. Phys. Lett.* **1984**, *45*, 1095.

(61) Kohl, P. A.; Bard, A. J. *J. Electrochem. Soc.* **1979**, *126*, 603.

(62) Gronet, C. M.; Lewis, N. S. *Appl. Phys. Lett.* **1983**, *43*, 115.

(63) Lieber, C. M.; Gronet, C. M.; Lewis, N. S. *Nature* **1984**, *307*, 533.

(64) These upper bounds on $k_{et,\,max}$ are conservative because effects of band edge movement under illumination, which would tend to yield lower barrier heights and thus even smaller upper bounds on $k_{et,max}$, have not been included in computing this $k_{et,max}$ value. For the outer sphere redox couples used in this work, band edge movement is expected to be minimal, as shown by a direct measurement on the illuminated n-Si/CH_3OH-$Me_2Fc^{+/0}$ contact, for which the quasi-Fermi level of holes was equal, within experimental error, to the Nernstian potential of the solution.[73] A differential capacitance measurement on an illuminated (J_{sc}=20 mA/cm^2) n-Si/CH_3OH-$Me_2Fc^{+/0}$ contact yielded a barrier height of 0.89 V; using this value yields an upper bound on $k_{et,max}$ that is on the same order of magnitude as that determined from use of ϕ_b value determined for this system in the dark.

(65) Closs, G. L.; Calcaterra, L. T.; Green, N. J.; Penfield, K. W.; Miller, J. R. *J. Phys. Chem.* **1986**, *90*, 3673.

(66) McClendon, G.; Miller, J. R. *J. Am. Chem. Soc.* **1985**, *107*, 7811.

(67) Marcus, R. A.; Sutin, N. *Biochim. Biophys. Acta* **1985**, *811*, 265.

(68) Fox, L. S.; Kozik, M.; Winkler, J. R.; Gray, H. B. *Science* **1990**, *247*, 1069.

(69) It is possible to speculate that effects of an extremely strong interfacial electric field could increase k_{et} for minority carriers above those described herein while not affecting the interfacial rate constant for majority carriers. There appears to date to be no theoretical or experimental support for a process in which interfacial electric fields would accelerate the electron into a liquid sufficiently rapidly to produce a significant increase in the capture cross section from ions that are generally at distances in excess of the electron mean free path in the liquid phase.

A semiclassical collision theory approach to estimate k_{et} yields:

$$k_{et} = \sigma \, v \, \delta \tag{4.23}$$

where σ is the cross section for reaction, v is the relative velocity of the reactants, and d is the effective zone of reaction. For a typical molecular dimension of 3×10^{-8} cm, with a relative velocity of 10^7 cm s^{-1} (dominated by the thermal velocity of the charge carrier in the solid) and an effective distance for electron transfer of 10^{-7} cm, $k_{et} = 10^{-12}$ cm^4-s^{-1} implies a value for the cross section of $\sigma = 10^{-12}$ cm^2. Thus, $k_{et} = 10^{-12}$ cm^4 s^{-1} implies that ions which participate in the charge transfer process (presumably proceeding off-resonance) would exhibit the curious behavior of possessing capture cross sections that far exceeded their geometric cross sections. "Giant" cross sections for carrier capture of this magnitude have been reported for the solid state, but such processes are dominated by Coulombic attraction effects.[74] Coulombic attractions will be minimized in interfacial charge transfer processes by the presence of the electrolyte and the correspondingly small Debye screening lengths in the liquid phase.

(70) Gronet, C. M.; Lewis, N. S. *J. Phys. Chem.* **1984**, *88*, 1310.

(71) Ryba, G. N.; Kenyon, C. N.; Lewis, N. S. *J. Phys. Chem.* **1993**, *97*, 13814.

(72) Rosenwaks, Y.; Thacker, B. R.; Ahrenkiel, R. K.; Nozik, A. J. *J. Phys. Chem.* **1992**, *96*, 10096.

(73) Tan, M. X.; Kenyon, C. N.; Lewis, N. S. *J. Phys. Chem.* **1994**, *98*, 4959.

(74) Fahrenbruch, A. L.; Bube, R. H. *Fundamentals of Solar Cells: Photovoltaic Solar Energy Conversion*; Academic: New York, 1983.

Chapter 5: Measurement of Interfacial Charge Transfer Rate Constants at n-type InP/CH_3OH Junctions

All or part of this text originally appeared in Pomykal, K. E., and Lewis, N. S., *J. Phys. Chem.*, **1997**, *101(14)*, pp 2476-2484.

I. Introduction

In this chapter, experimental measurements of interfacial charge transfer rate constants for n-type InP electrodes in contact with a series of one electron, outer-sphere redox reagents are reported. These reagents have been chosen because they allow variation in the driving force for the interfacial charge transfer process while controlling variation in other solvent-related reorganization parameters. In addition, many of these redox couples have been used in efficient InP-based photoelectrochemical cells,[1-3] so understanding the factors that control the interfacial rates at these contacts provides a direct understanding of the factors that control the efficiency losses in such photoelectrochemical energy conversion devices.

As described in the preceding chapter, a model based on an adaptation of Marcus' theory for liquid/liquid interfaces has recently been used to estimate values of the electron transfer rate constant, k_{et}, for semiconductor/liquid contacts.[4,5] Although upper limits on k_{et} have been established experimentally[5-7] and are consistent with estimates of k_{et} produced by the available theories,[4,5] the use of any approach currently available in the literature to estimate k_{et} for such systems has recently been criticized.[8,9] To date, there appears to be little direct experimental data on values of k_{et} at well-defined semiconductor/liquid interfaces.[4,10-12] We describe such measurements, using n-InP electrodes and a series of outer-sphere redox couples, in this chapter.

The flux of electrons from the conduction band edge of a semiconductor to a molecular electron acceptor species dissolved in the solution is given by:[13]

$$J_{et}(E) = qk_{et}n_s(E)[A] \tag{5.1}$$

where J_{et} (A cm^{-2}) is the current density due to the direct charge transfer process, E (V) is the applied potential, q (C) is the elementary charge, n_s (cm^{-3}) is the electron concentration at the surface of the semiconductor, and [A] (cm^{-3}) is the concentration of acceptors that participate in the electron transfer process. The surface electron concentration is measured

in units of cm^{-3} rather than cm^{-2}, because it is related to the electron concentration in the bulk, n_b, through a Boltzmann relationship:[14]

$$n_s(E) = N_d e^{-q(E+V_{bi})/(kT)} \tag{5.2}$$

In Equation 5.1, V_{bi} is the built-in voltage developed across the space charge layer in the semiconductor at charge transfer equilibrium of the semiconductor/liquid contact and n_b is taken to be equal to the dopant density of the semiconductor, N_d.

Thus, the two variables in a semiconductor/liquid system that must be measured in order to evaluate the electron transfer rate constant using steady-state methods are V_{bi} and $J_{et}(E)$. As outlined in Chapter 4, only J_{et} varies linearly with n_s (i.e., exponentially with E, under forward bias) and varies linearly with [A]. Only a system in which direct-electron transfer is the dominant recombination current exhibits both of these characteristics. When these criteria are obeyed, Equations 5.2 and 5.3 can be used to determine the value of k_{et}, provided that V_{bi} can be determined experimentally. Measurements of k_{et} for solid/liquid contacts having various values of $\Delta G^{o'}$ can then yield a value for $k_{et,max}$ and, in turn, can allow estimation of κ_{el}.

II. Experimental Section

A. Electrodes and Materials

Nominally undoped ($N_d = 6.4 \times 10^{15}$ cm^{-3}) (100)-oriented, n-type InP wafers were obtained from Crysta-Comm, Inc., and Sumitomo Electric Industries, LTD. The samples were sliced into pieces ranging from 0.1 to 0.3 cm^2 in area, and were fashioned into electrodes using procedures that have been described previously in the literature.[5] Cross-sectional areas of the electrodes were determined photographically, and the roughness factor of these electrodes was assumed to be negligible. Electrodes were etched by alternately immersing the sample two times each for 30 s into solutions of 0.05% Br_2 (v/v) in CH_3OH and 4.0 M NH_3 in CH_3OH, followed by rinsing with CH_3OH after each immersion.[15] Each electrode was etched immediately before use in electrochemical experiments.

All solvents were dried and distilled under $N_2(g)$ and were then stored under an anaerobic atmosphere. CH_3OH (EM Science) was dried over magnesium methoxide. Tetrahydrofuran (THF) (EM Science) was pre-dried over KOH pellets, then transferred to the solvent still, dried over sodium metal (with benzophenone as an indicator), and distilled. The ferrocenes (ferrocene, Fc; 1,1'-dimethylferrocene, Me_2Fc; and decamethylferrocene, $Me_{10}Fc$) were obtained from Strem or Aldrich and were purified by sublimation. The tetrafluoroborate salts of each ferrocene ($FcBF_4$, Me_2FcBF_4, and $Me_{10}FcBF_4$) were prepared using the method of Hendrickson *et al.*[16] The dichloride salt of 1,1'-diphenyl-4,4'-dipyridinium ($PVCl_2$) was prepared using the synthesis of Kamogawa *et al.*[17] 1,1'-diphenyl-4,4'-dipyridinium radical cation ($PV^{+\bullet}$) was produced by electrolysis (vide infra). $LiClO_4$ was dried by fusion at 240 °C in vacuo, and LiCl was dried by heating at 220 °C for at least 6 hours in vacuo. All redox couples and electrolytes were stored in a nitrogen-purged drybox until use.

B. Electrochemical Cells and Instrumentation

Electrochemical cells were prepared inside a nitrogen-purged drybox by introducing the solid components of the solution into the cell. The cells were then transferred to the anaerobic atmosphere and the appropriate solvent was introduced. CH_3OH was used as the solvent for all redox systems except $Me_{10}Fc^{+/0}$, for which a solution of 25% CH_3OH-75% THF (v/v) was required to dissolve the redox species at the desired concentrations. $LiClO_4$ was used as the electrolyte in all solutions except in CH_3OH-$PV^{2+/+\bullet}$ cells, where LiCl was required in order to avoid precipitation of the redox species. In all cases, 1.00 M electrolyte was used. All experiments were conducted within the anaerobic atmosphere, which contained less than 10 ppm of O_2 as monitored by the lack of any visibly detectable fumes arising from diethyl zinc.

In the CH_3OH-$PV^{2+/+\bullet}$ cells, the reduced form of the redox couple was generated electrochemically. A platinum gauze electrode was used as the working electrode and a second platinum gauze electrode, separated from the main solution by a glass frit, was used

as the counter electrode. A reference electrode (a methanolic saturated calomel electrode, MSCE) with a potential of -50.0 mV vs. SCE was made according to conventional SCE fabrication procedures, except that CH_3OH saturated with LiCl was substituted for the more conventional saturated KCl(aq) solution.[18] The $PV^{+\bullet}$ was generated by applying a potential of -100 to -200 mV vs. MSCE across the cell (more negative potentials produced some PV^0). The progress of the electrolysis was monitored both by counting the number of coulombs passed through the cell and by periodically checking the cell potential vs. the MSCE reference electrode.

In all electrochemical experiments, after the desired ratio of the oxidized to reduced forms of the redox couple was obtained, the n-InP electrode was etched and immersed into the electrolyte. All electrochemical experiments with semiconducting electrodes were conducted in a three-electrode set-up, with a Pt gauze counter electrode and a Pt wire reference. An EG&G Princeton Applied Research (PAR) Model 173 potentiostat in conjunction with an EG&G PAR Model 175 Universal Programmer was used for all current density vs. potential measurements. The data were collected on a Houston Instruments Omnigraphic 2000 recorder and in some cases were also fed directly into a computer. Data acquisition and analysis were performed using LabView software (National Instruments, Inc.). Impedance spectra were obtained on a computer-controlled Schlumberger Model 1260 frequency response analyzer equipped with a Model 1286 electrochemical interface. After each set of experiments, the solution potential was measured to insure that the cell composition had not changed significantly during the course of the experiment.

C. Current Density vs. Potential and Built-in Voltage Measurements

For kinetic studies, the current density vs. potential (J-*E*) behavior of each electrode was measured in the dark in a cell containing the desired concentration of the redox acceptor species. The J-*E* data were collected at a scan rate of 50 mV s^{-1}. Each electrode was then re-etched and the series of experiments was repeated, changing the redox acceptor

concentration by tenfold. In some cases, instead of just lowering the acceptor concentration by a factor of ten, the entire solution was diluted with solvent containing 1.00 M electrolyte in order to maintain a constant cell potential. This procedure was necessary for $PV^{2+/+\bullet}$ cells because changing only the acceptor concentration made the cell potential sufficiently negative to form an ohmic contact to the n-InP. Also, in the case of n-InP/$Fc^{+/0}$ contacts, the band edges were found to shift upon increasing the acceptor concentration, so the dilution method was used to examine the concentration dependence of the interfacial kinetics at fixed V_{bi} values. For some experiments, the electrodes were not etched between J-*E* experiments; in such instances, after running J-*E* curves in the second solution, the electrodes were returned to the original solution, again without etching, and a third set of J-*E* data was obtained. The purpose of these experiments was to determine whether a shift in the J-*E* behavior was due to the changing acceptor concentration or to some irreversible reaction occurring at the electrode surface. All J-*E* curves were corrected for the series resistance present in the cell, with the series resistance either determined from impedance measurements (vide infra) or from the J-*E* behavior of a platinum electrode of similar size and shape to that of the n-InP electrode positioned in the same cell geometry.

The built-in voltage of each n-InP/liquid junction was calculated from the electrochemical impedance data. Data were only collected for cells containing at least 0.010 M of both the oxidized and reduced forms of the redox couple and which contained a counter electrode having at least ten times the surface area of the working electrode. These precautions were necessary to obtain reliable impedance data.[5] Impedance data were fit to an equivalent circuit consisting of a resistor R_{sc} (representing the resistance to Faradaic charge transfer) in parallel with a capacitor C_{sc} (representing the differential capacitance of the semiconductor space charge region), both in series with a resistance R_s (representing the series resistance due to resistive losses through the cell, leads, etc.). The differential capacitance of the space charge layer is related to the built-in voltage of the junction through the Mott-Schottky equation:[13,14]

$$C_{sc}^{-2} = \frac{2}{q\varepsilon\varepsilon_0 N_d A_s^2}(E + V_{bi} - \frac{kT}{q}) \tag{5.4}$$

where ε_0 is the permittivity of free space, ε is the dielectric constant, and A_s is the area of the semiconductor electrode. Thus, by measuring the impedance data at several different potentials, V_{bi} was determined for the semiconductor/liquid interface of interest.

For each dc bias, the impedance, Z, of the cell was measured by superimposing an ac signal of 10 mV rms amplitude on the applied dc potential. The ac frequency was varied from 0.1 to 10^3 kHz, but only data which were almost purely capacitive in nature (phase angle > 80°) were used in the Mott-Schottky analyses. The differential capacitance, assumed in this equivalent circuit model to be equal to the differential space-charge capacitance of the semiconductor, C_{sc}, was extracted from Z_{im}, the imaginary part of the measured Z, from the equation:[19]

$$2\pi f C_{sc} = \frac{1 + (1 - 4(Z_{im} / R_{sc})^2)^{1/2}}{2Z_{im}} \tag{5.5}$$

In the above expression, f is the frequency of the ac voltage and R_{sc} was taken as the diameter of the semicircle formed by plotting Z_{im} vs. Z_{real} for the whole frequency range, where Z_{real} is the real component of the measured impedance.

The equivalent circuit used to model the data was validated by two methods. First, since the Mott-Schottky expression should be independent of the measurement frequency, electrodes which did not show measured capacitances that were independent of frequency (over at least one order of magnitude in frequency) were considered defective and were discarded. Second, the slope of the Mott-Schottky plot should be dependent only on the properties of the semiconductor itself (Equation 5.4). The validity of the equivalent circuit model was thus assessed by extracting the dopant density from the slope of the Mott-Schottky plot and comparing it to the value reported by the manufacturer. Only data which showed linear Mott-Schottky plots ($R^2 \geq 0.999$, where R is the correlation coefficient) with calculated dopant densities within 50% of the reported dopant density were considered valid.

III. Results

A. Rate Constant Measurements for n-InP/CH_3OH-$Me_2Fc^{+/0}$ Contacts

Figure 5.1a shows the J-*E* behavior of several n-InP/CH_3OH-$Me_2Fc^{+/0}$ contacts in the absence of illumination. In this series of experiments, the concentration of Me_2Fc was held constant at 0.100 M while the concentration of Me_2Fc^+ was either 0.100, 0.010, or 0.001 M. The data were corrected for series resistance and referenced to MSCE for all three concentrations of Me_2Fc^+.

The data of Figure 5.1a can be fit to the diode equation:[20]

$$J = J_o\left(e^{-qE/AkT} - 1\right) \tag{5.6}$$

where A is the diode quality factor and J_o is the exchange current density of the semiconductor/liquid contact. In sufficiently far forward bias (-*E*>>AkT/q), the exponential term dominates the right-hand side of Equation 5.6, and the expression can be rewritten as:

$$\ln J = \ln J_o - \frac{qE}{AkT} \tag{5.7}$$

Fitting the data of Figure 5.1a to Equation 5.7 yielded diode quality factors of 1.15, 1.28, and 1.34 for Me_2Fc^+ concentrations of 0.001 M, 0.010 M and 0.100 M, respectively. The deviation from the ideally expected value of A = 1.0 for these junctions may arise from a different recombination mechanism contributing to the current density at lower potentials, but the general behavior was in accord with the first-order kinetic dependence of J on the concentration of electrons at the surface of the semiconductor.

For the two higher concentrations of Me_2Fc^+, the separation of the data along the abscissa was 75 ± 5 mV, which is close to the ideally expected 59 mV value derived from Equations 5.2 and 5.3.[21] Changing the acceptor concentration by two orders of magnitude resulted in a potential difference in the J-*E* data of 125 ± 5 mV relative to a MSCE reference, compared to the ideal shift of 118 mV. These data verify a first-order dependence of J on the concentration of acceptors in the solution, thus the interfacial flux at

this solid/liquid contact was dominated by electron transfer from the conduction band to the redox acceptor in the solution phase.

Figure 5.1b displays the C_{sc}^{-2}-*E* data for an n-InP/CH_3OH-0.100 M Me_2Fc-0.010 M Me_2Fc^+ contact. In this plot, C_{sc} was extracted from the impedance data obtained at f = 100 kHz and f = 10 kHz. The C_{sc}^{-2}-*E* data were linear and essentially independent of frequency over the measurement range. The calculated dopant density was 8.7 x 10^{15} cm^{-3} while that reported by the supplier of this wafer was 6.4 x 10^{15} cm^{-3}. Use of Equation 5.4 yielded a built-in voltage of $V_{bi} = 0.64 \pm 0.01$ V for the solid/liquid contact of Figure 5.1b.

The impedance analysis was also performed for solutions having a higher concentration of $Me_2Fc^{+/0}$ in order to insure that the band edge positions of the semiconductor were relatively fixed as the solution acceptor concentration was changed. Figure 5.1c displays the results of a C^{-2}-*E* plot for an n-InP/CH_3OH-0.100 M Me_2Fc-0.100 M Me_2Fc^+ contact. These data yielded $V_{bi} = 0.69 \pm 0.01$ V. These Mott-Schottky plots also were in good agreement with the reported dopant density and were independent of frequency over the range of frequencies probed in this work. Since the Nernstian potential of the cell, $E(A/A^-)$, in Figure 5.1c was more positive than that of Figure 5.1b by 59 mV, the built-in voltage of the contact of Figure 5.1c was expected to be 59 mV greater than that of Figure 5.1b. The actual difference was just slightly less than this ideal separation, but was in the correct direction, so that a positive shift in $E(A/A^-)$ led to an increase in the built-in voltage of the semiconductor/liquid contact.

The energetic information from the C^{-2}-*E* analysis of Figures 5.1b and 5.1c was then combined with the kinetic information from the J-*E* data of Figure 5.1a to evaluate the value of k_{et} for this system. To perform this computation, the built-in voltage obtained from the Mott-Schottky plots was used with Equation 5.3 to compute the surface electron concentration at a given potential in forward bias. Using Equation 5.2, a rate constant value was then computed from the current density observed at the chosen potential. The

potentials chosen for evaluation of k_{et} were all ones for which the J-*E* data were linearly dependent on the acceptor concentration.

For the n-InP-CH_3OH-0.100 M Me_2Fc -0.100 M Me_2Fc^+ interface of Figure 5.1, this procedure yielded $k_{et} = 6.2 \times 10^{-17}$ cm^4 s^{-1} at E = -0.45 V vs. $E(A/A^-)$. Since the diode quality factors for these junctions were not exactly unity, the calculated values of k_{et} depended slightly on the potential chosen for the kinetic measurements. For instance, a value of $k_{et} = 1.7 \times 10^{-16}$ cm^4 s^{-1} was obtained for the same electrode at a potential of -0.25 V vs. $E(A/A^-)$. Since kinetic processes with diode quality factors of 1.0 tend to dominate the interfacial flux further into forward bias, the charge transfer rate constants calculated at the more negative potentials are more likely to reflect the true rate constant.[22]

For the n-InP/CH_3OH-0.100 M Me_2Fc-0.010 M Me_2Fc^+ contact, the computed electron transfer rate constant varied from 2.2×10^{-17} cm^4 s^{-1} to 1.2×10^{-16} cm^4 s^{-1} over a potential range of E = -0.45 to -0.25 V vs. $E(A/A^-)$. Thus, these k_{et} values were consistent with the ones derived for the higher Me_2Fc^+ acceptor concentration, confirming the bimolecular nature of the observed interfacial kinetic process.

At any individual potential, repeated determinations of J-*E* and C_{sc}^{-2}-*E* were performed, and the resulting values for k_{et} were analyzed using conventional statistical procedures. Results from many different electrodes yielded an average charge transfer rate constant of $(8.5 \pm 7.7) \times 10^{-17}$ cm^4 s^{-1} for n-InP/CH_3OH-0.100 M Me_2Fc- 0.100 M Me_2Fc^+ contacts and yielded $k_{et} = 1.1 \times 10^{-16}$ cm^4 s^{-1} for InP/CH_3OH-0.100 M Me_2Fc-0.0100 M Me_2Fc^+ contacts. The standard deviation in the case of the InP/CH_3OH-0.100 M Me_2Fc- 0.0100 M Me_2Fc^+ system was slightly larger than the mean, with individual k_{et} values ranging from 1.5×10^{-18} cm^4 s^{-1} to 9.9×10^{-16} cm^4 s^{-1}. The second highest (of 24 values) calculated rate constant was 3.6×10^{-16} cm^4 s^{-1}. Given the error present in the measurements, k_{et} for the n-InP/CH_3OH-$Me_2Fc^{+/0}$ junction was estimated to be between (1-10) x 10^{-17} cm^4 s^{-1}.

Figure 5.1: Current density-potential and differential capacitance-potential data for n-type InP/CH_3OH-$Me_2Fc^{+/0}$ contacts. (a) ln J vs. *E* for n-InP/CH_3OH-1.00 M $LiClO_4$-0.100 M Me_2Fc interfaces having Me_2Fc^+ (electron acceptor) concentrations of: (i) 0.001 M ($E(A/A^-)$ = 0.130 V vs. MSCE), (ii) 0.010 M ($E(A/A^-)$ = 0.192 V vs. MSCE), and (iii) 0.100 M ($E(A/A^-)$ = 0.252 V vs. MSCE). The diode quality factor, A, was extracted from linear fits of these data to Equation 5.7. (b) Mott-Schottky plots taken at two ac measuring frequencies, 10 kHz (dashed line, solid squares) and 100 kHz (solid line, open circles), for an n-InP/CH_3OH-1.00 M $LiClO_4$-0.100 M Me_2Fc-0.010 M Me_2Fc^+ contact. The potentials are referenced to the Nernstian potential of the cell, $E(A/A^-)$. The average dopant density extracted from the slopes of these lines was 8.7 x 10^{15} cm^{-3}, compared to the reported dopant density of 6.4 x 10^{15} cm^{-3}. The built-in voltages, V_{bi}, are listed for each frequency. (c) Mott-Schottky plots for two ac measuring frequencies, 10 kHz (dashed line, solid squares) and 100 kHz (solid line, open circles), for an n-InP/CH_3OH-1.00 M $LiClO_4$-0.100 M Me_2Fc-0.100 M Me_2Fc^+ contact. The average dopant density extracted from the slopes of these lines was 8.7 x 10^{15} cm^{-3}.

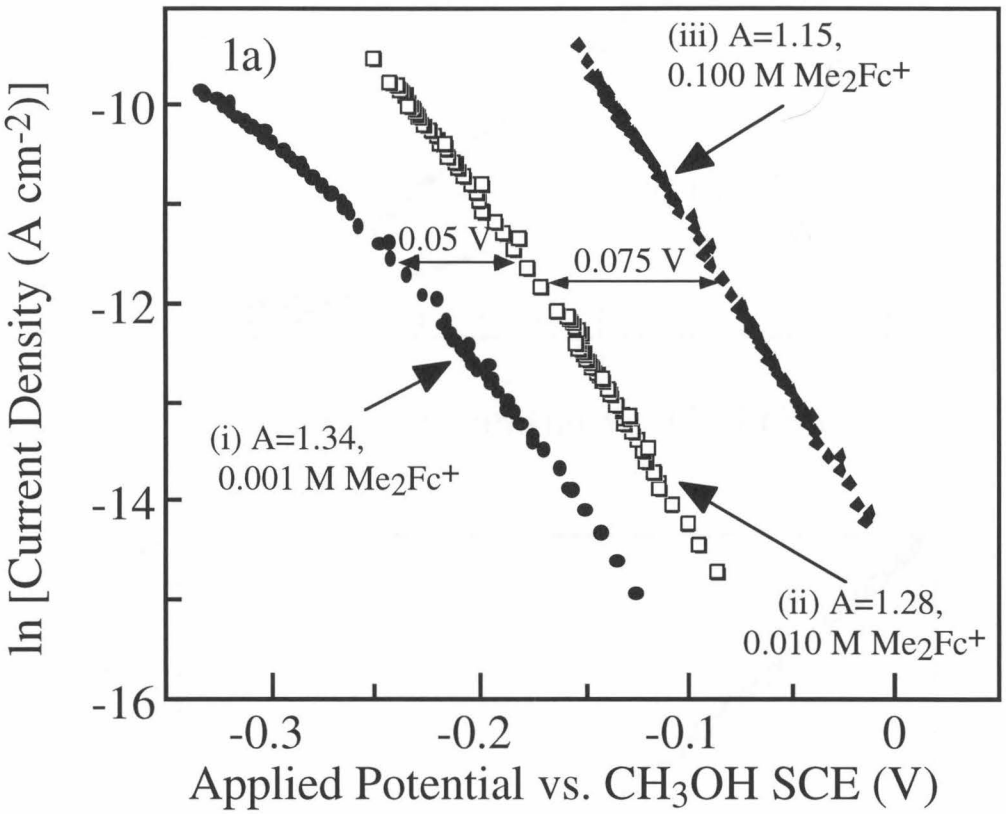
1a)
(iii) A=1.15,
0.100 M Me2Fc+
0.05 V
0.075 V
(i) A=1.34,
0.001 M Me2Fc+
(ii) A=1.28,
0.010 M Me2Fc+
ln [Current Density (A cm-2)]
-10
-12
-14
-16
-0.3
-0.2
-0.1
0
Applied Potential vs. CH3OH SCE (V)

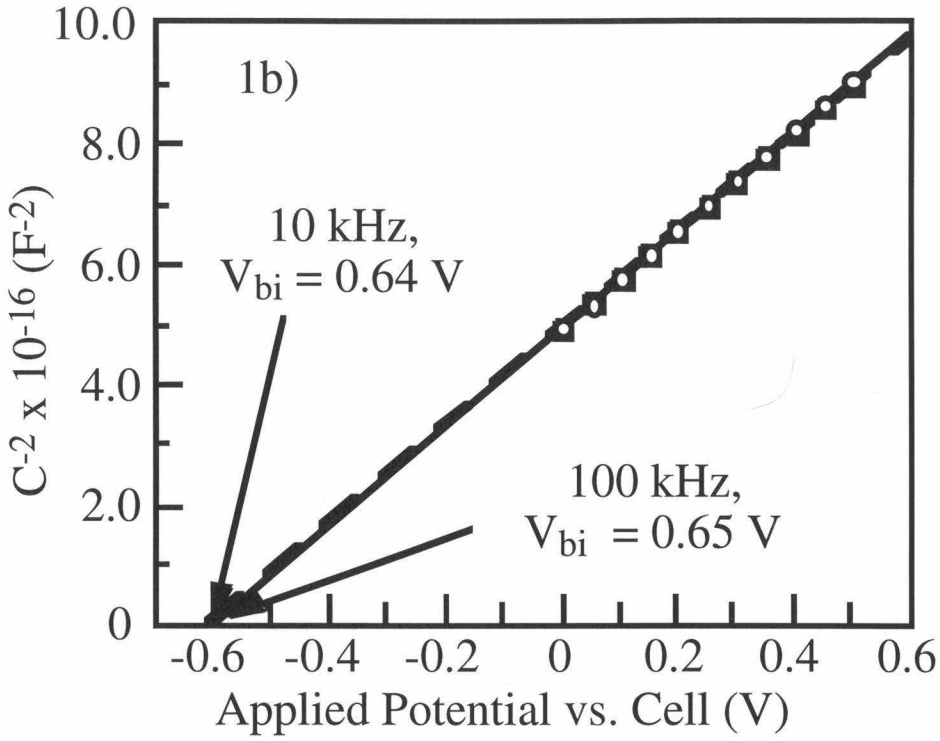
1b)
10 kHz,
V_{bi} = 0.64 V
100 kHz,
V_{bi} = 0.65 V
C^{-2} x 10^{-16} (F^{-2})
10.0
8.0
6.0
4.0
2.0
0
-0.6 -0.4 -0.2 0 0.2 0.4 0.6
Applied Potential vs. Cell (V)

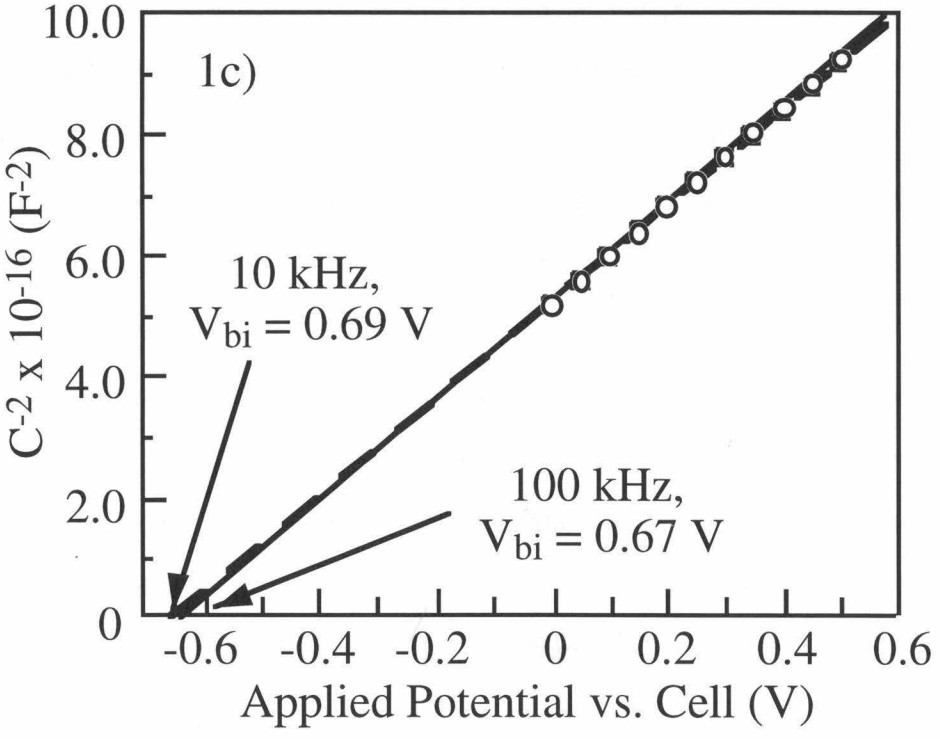
1c)
10 kHz,
V_{bi} = 0.69 V
100 kHz,
V_{bi} = 0.67 V
C^{-2} x 10^{-16} (F^{-2})
10.0
8.0
6.0
4.0
2.0
0
-0.6 -0.4 -0.2 0 0.2 0.4 0.6
Applied Potential vs. Cell (V)

B. Rate Constant Measurements for n-InP/CH_3OH(25%)-THF(75%)-$Me_{10}Fc^{+/0}$ Contacts

Analogous experiments were performed for n-InP/$Me_{10}Fc^{+/0}$ contacts. In this system, due to the poor solubility of $Me_{10}Fc$ in pure CH_3OH, the solvent was 25% CH_3OH/75% THF (v/v). J-*E* data were collected for [$Me_{10}Fc$] = 0.025 M with the acceptor concentration adjusted to produce [$Me_{10}Fc^+$]=0.025 M or [$Me_{10}Fc^+$] = 0.0025 M (Figure 5.2a). Although the diode quality factors of these contacts deviated somewhat from unity, the data for the two $Me_{10}Fc^+$ concentrations were separated by the expected 60 mV relative to MSCE. Thus, the reaction was kinetically first order in the concentration of solution acceptors and in the electron concentration at the semiconductor surface, as predicted by the rate law of Equation 5.2.

Figure 5.2b displays the Mott-Schottky plots for n-InP/CH_3OH-THF-0.025 M Me_2Fc-0.025 M $Me_{10}Fc^+$ contacts at f = 39.811 kHz and f = 3.981 kHz. For these contacts, the range over which the impedance data were independent of frequency was somewhat smaller than that observed for n-InP/CH_3OH-$Me_2Fc^{+/0}$ contacts, but the impedance data were nevertheless essentially independent of frequency over an order of magnitude of f. Over this frequency range, the dopant density computed from the C^{-2}-*E* data was in good agreement with the known dopant density of the sample. The built-in voltage obtained from the C^{-2}-*E* analysis of this sample was 0.49 ± 0.01 V.[23]

The same procedure as described in section IV.A above, in which the analyses of C^{-2}-*E* and J-*E* data were combined, was used to compute the value of k_{et} for the n-InP/CH_3OH-THF-$Me_{10}Fc^{+/0}$ contacts. For the data shown in Figure 5.2, k_{et} = 1.2 x 10^{-17} cm^4 s^{-1} at *E* = -0.35 V vs. *E*(A/A-) and k_{et} = 4.9 x 10^{-17} cm^4 s^{-1} at *E* = -0.15 V vs. *E*(A/A^-). Over several trials, the average electron transfer rate constant for this system was found to be 5.3 x 10^{-17} cm^4 s^{-1}, but individual values ranged from 9.3 x 10^{-18} cm^4 s^{-1} to 6.6 x 10^{-17} cm^4 s^{-1}. Within the experimental error afforded by the relatively small uncertainties in V_{bi} (propagating into larger uncertainties in n_s), along with differences in

k_{et} determined at different measurement potentials (due to the deviation of A from the ideal value of A = 1.0), these k_{et} values were indistinguishable from those reported above for n-InP/CH_3OH- $Me_2Fc^{+/0}$ contacts.

Figure 5.2: Data for n-InP/CH_3OH-THF-$Me_{10}Fc^{+/0}$ contacts. (a) ln J vs. *E* data for n-InP/CH_3OH-THF-1.00 M $LiClO_4$-0.025 M $Me_{10}Fc$ contacts having $Me_{10}Fc^+$ concentrations of: (i) 0.0025 M ($E(A/A^-)$ = -0.042 V vs. MSCE), and (ii) 0.025 M ($E(A/A^-)$ = 0.010 V vs. MSCE). The diode quality factor, A, was extracted from linear fits of these data to Equation 5.7. (b) Mott-Schottky plots for two ac measuring frequencies, 3.981 kHz (dashed line, solid squares) and 39.811 kHz (solid line, open circles), for an n-InP/CH_3OH-THF-1.00 M $LiClO_4$-0.025 M $Me_{10}Fc$-0.025 M $Me_{10}Fc^+$ contact. The average dopant density extracted from the slopes of these lines was 9.5 x 10^{15} cm^{-3}. The built-in voltages, V_{bi}, are listed for each frequency.

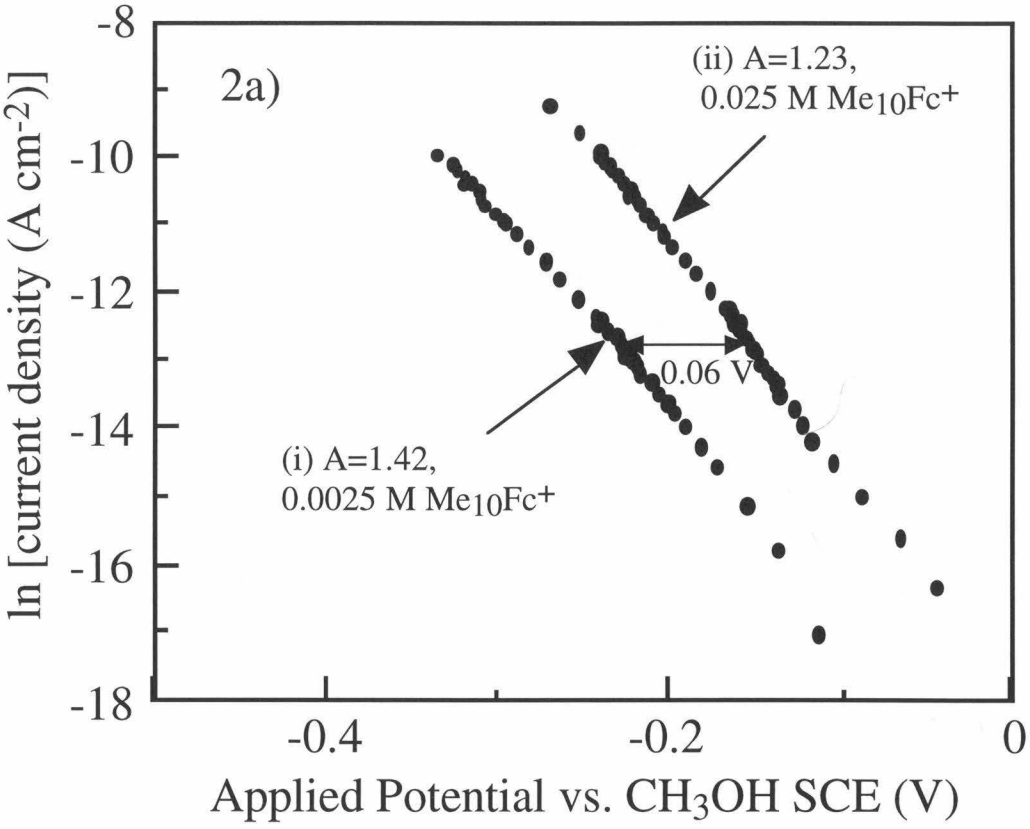
2a)
(ii) A=1.23,
0.025 M Me10Fc+
0.06 V
(i) A=1.42,
0.0025 M Me10Fc+
ln [current density (A cm-2)]
-8
-10
-12
-14
-16
-18
-0.4
-0.2
0
Applied Potential vs. CH3OH SCE (V)

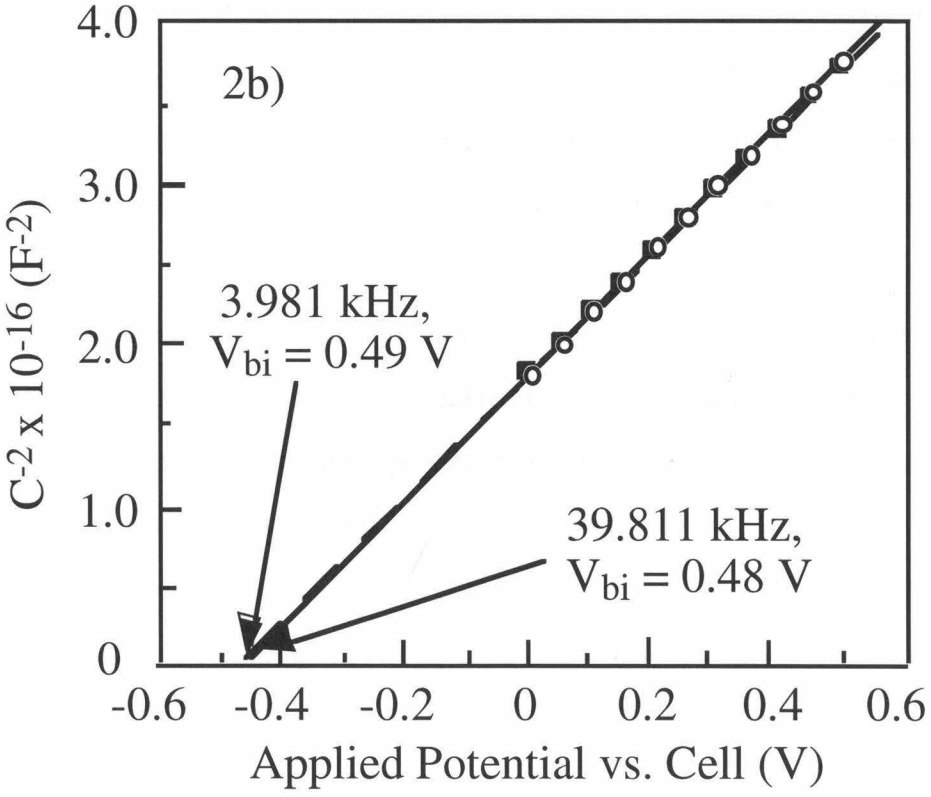
2b)
3.981 kHz,
Vbi = 0.49 V
39.811 kHz,
Vbi = 0.48 V
C-2 x 10-16 (F-2)
4.0
3.0
2.0
1.0
0
-0.6
-0.4
-0.2
0
0.2
0.4
0.6
Applied Potential vs. Cell (V)

C. Rate Constant Data for n-InP/CH_3OH-$PV^{2+/+\bullet}$ Contacts

Cyclic voltammetric data showed that $PV^{2+/+\bullet}$ exhibited reversible, one electron redox behavior in CH_3OH at a Pt electrode. This redox couple displayed a formal potential, $E^{o'}(A/A^-)$, of -180 mV vs. MSCE, which was >200 mV more negative than $E^{o'}(A/A^-)$ for $Me_{10}Fc^{+/0}$ (in CH_3OH-THF). Consequently, the more negative value of $E^{o'}(A/A^-)$ for $PV^{2+/+\bullet}$ should produce smaller built-in voltages, and therefore lower values of $\Delta G^{o'}$, for n-InP/CH_3OH-$PV^{2+/+\bullet}$ contacts relative to those of n-InP/CH_3OH-$Me_2Fc^{+/0}$ or n-InP/CH_3OH-THF-$Me_{10}Fc^{+/0}$ junctions.

Figure 5.3a shows the J-*E* data for an n-InP electrode in contact with CH_3OH-1.00 M LiCl-0.050 M PV^{2+}-0.010 M $PV^{+\bullet}$. In this system, J_o was sufficiently large that the condition $-E > AkT/q$ was not satisfied over the entire potential range of interest. Thus, the simplifications that allow Equation 5.6 to be transformed into Equation 5.7 were not appropriate for this system. The kinetic data of Figure 5.3a were therefore fit to Equation 5.6 to yield J_o, and then k_{et} was computed using Equation 5.2, with $n_s(E) = n_s(0)$.

Since the redox potential of the solution was near the InP conduction band edge energy at the semiconductor surface, the J-*E* behavior for this n-InP/liquid contact was very sensitive to the value of $E(A/A^-)$. For example, at even slightly more negative potentials than $E(A/A^-)$ = -0.150 mV vs. MSCE, the n-InP/liquid contact exhibited nonrectifying, near-ohmic behavior. It was therefore not possible to perform an experiment analogous to that described in Figure 5.1 with the n-InP/$PV^{2+/+\bullet}$ contacts, in which the acceptor concentration was decreased in order to reveal the kinetic dependence of J on [A] while [A^-] was held constant. Instead, the J-*E* properties of an n-InP electrode were recorded in contact with a CH_3OH-1.00 M LiCl-0.010 M PV^{2+}-0.050 M $PV^{+\bullet}$ solution and then in contact with a CH_3OH-1.00 M LiCl-0.0010 M PV^{2+}-0.0050 M $PV^{+\bullet}$ solution. The latter solution was prepared by diluting part of the more concentrated solution with 1.00 M LiCl in CH_3OH. This procedure allowed investigation of the desired kinetic behavior but required a slightly different analysis of the data, as described below.

The results of this experiment are shown in Figure 5.3b. In this figure, the current scale for the electrode in the more dilute solution is multiplied by a factor of ten. These data clearly show the first-order dependence of the current density on the concentration of acceptor species dissolved in the solution, as expected from Equation 5.2.

The Mott-Schottky plots for two ac frequencies applied to the CH_3OH-1.00 M LiCl-0.010 M PV^{2+}-0.050 M $PV^{+\bullet}$ interface are shown in Figure 5.3c. The impedance data for this junction exhibited more frequency dispersion than is evident in Figures 5.1c-d or 2c, possibly due to the large Faradaic current that was present during the impedance measurements of this low barrier height system. Despite this complication, the dopant density obtained from the C^{-2}-*E* plots over the frequency range 158.489 kHz to 15.849 kHz was within 30% of the value specified by the manufacturer. Additionally, although the slopes varied slightly over this range of frequencies, the x-intercepts of the C^{-2}-*E* plots were in agreement to within ± 15 mV. The built-in voltage of this junction was calculated to be 0.28 V, yielding an electron transfer rate constant of 3.3×10^{-16} cm^4 s^{-1}. Over many measurements of this system, the average electron transfer rate constant was $k_{et} = (3.3 \pm 2.4) \times 10^{-16}$ cm^4 s^{-1}. In this case, the range of values for the electron transfer rate constant was higher than those reported for the n-InP/CH_3OH-$Me_2Fc^{+/0}$ and n-InP/CH_3OH-THF-$Me_{10}Fc^{+/0}$ interfaces, with k_{et} ranging from 1×10^{-16} cm^4 s^{-1} to 9×10^{-16} cm^4 s^{-1}. It should be noted, however, that the reorganization energies for the viologens in homogeneous solution are significantly lower than those of the ferrocenes,[24-26] hence the decreased outer-sphere reorganization energies of this redox system somewhat counteracted the effects of the lower driving force at the n-InP/$PV^{2+/+\bullet}$ contact.

Figure 5.3: Data for n-InP/CH_3OH-1.00 M LiCl-$PV^{2+/+\bullet}$ contacts. (a) J-*E* data for an n-InP/CH_3OH-1.00 M LiCl-0.050 M PV^{2+}- 0.010 M $PV^{+\bullet}$ contact ($E(A/A^-)$ = -0.146 V vs. MSCE). The data were fit to Equation 5.8 and yielded a diode quality factor of 1.1. (b) J-*E* data for n-InP/CH_3OH-1.00 M LiCl-0.050 M PV^{2+}- 0.010 M $PV^{+\bullet}$ and n-InP/CH_3OH-1.00 M LiCl-0.0050 M PV^{2+}- 0.0010 M $PV^{+\bullet}$ contacts. The current density data for the n-InP/CH_3OH-1.00 M LiCl-0.0050 M PV^{2+}- 0.0010 M $PV^{+\bullet}$ contact (triangles) has been multiplied by ten for better comparison to the data for the CH_3OH-1.00 M LiCl-0.050 M PV^{2+}- 0.010 M $PV^{+\bullet}$ solution (open squares). (c) Mott-Schottky plots for the system in (a) at two ac measuring frequencies, 15.849 kHz (dashed line, open circles) and 158.489 kHz (solid line, filled circles). The dopant density predicted from the slope of the 15.849 kHz line was 9.9 x 10^{15} cm^{-3}, while the dopant density extracted from the slope of the 158.489 kHz line was 8.9 x 10^{15} cm^{-3}. The built-in voltages, V_{bi}, are listed for each frequency.

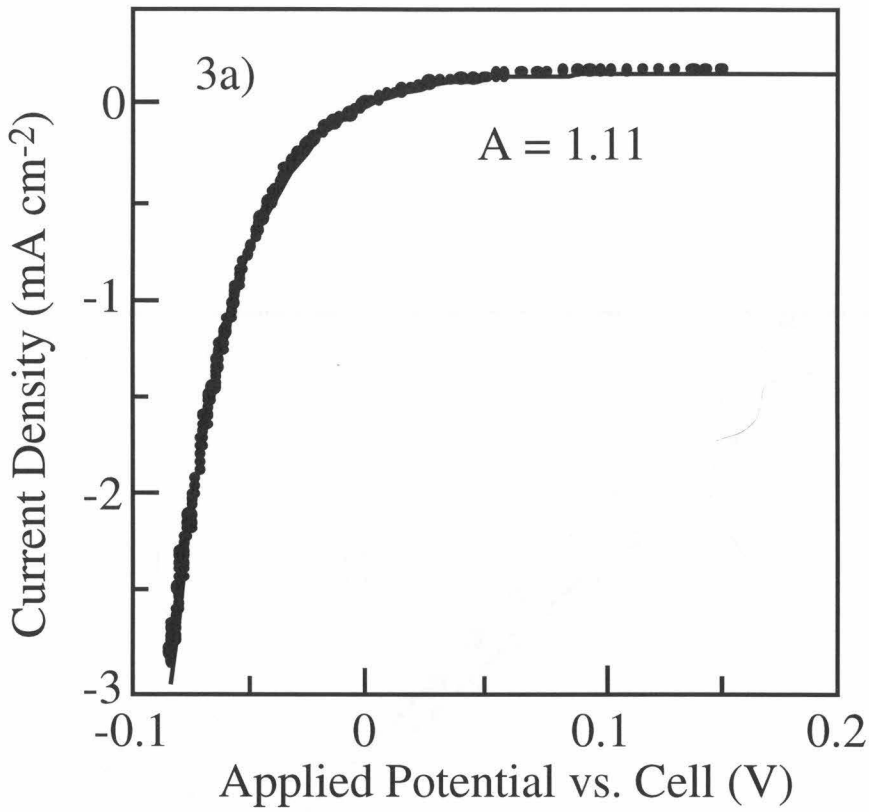
3a)
A = 1.11
Current Density (mA cm-2)
0
-1
-2
-3
-0.1
0
0.1
0.2
Applied Potential vs. Cell (V)

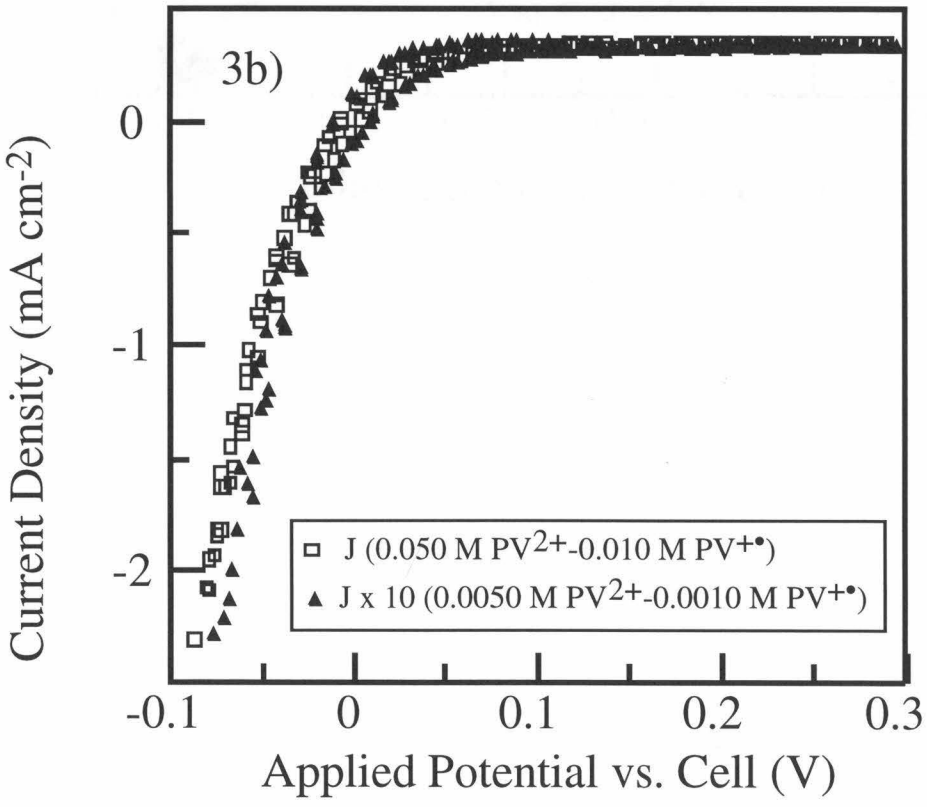
3b)
Current Density (mA cm-2)
0
-1
-2
J (0.050 M PV2+-0.010 M PV+•)
J x 10 (0.0050 M PV2+-0.0010 M PV+•)
-0.1
0
0.1
0.2
0.3
Applied Potential vs. Cell (V)

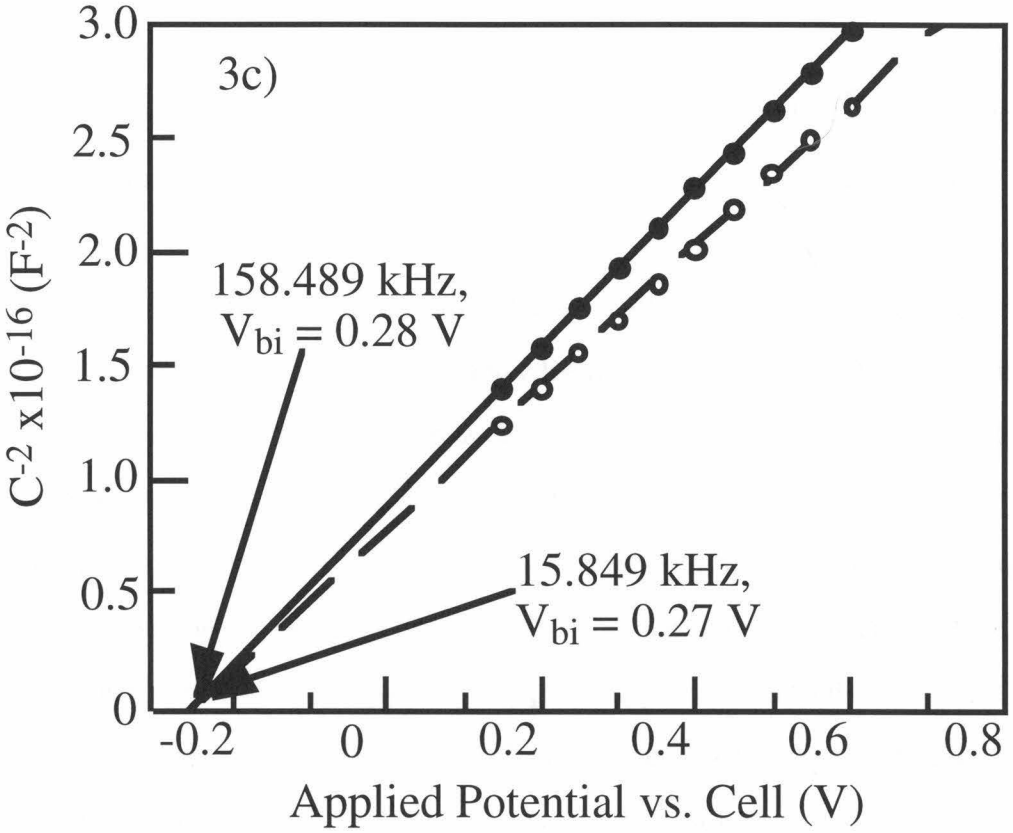
3c)
158.489 kHz,
V_{bi} = 0.28 V
15.849 kHz,
V_{bi} = 0.27 V
C^{-2} x10^{-16} (F^{-2})
3.0
2.5
2.0
1.5
1.0
0.5
0
-0.2
0
0.2
0.4
0.6
0.8
Applied Potential vs. Cell (V)

D. n-InP/CH_3OH-$Fc^{+/0}$ Contacts

Figure 5.4a depicts the J-*E* characteristics of n-InP/CH_3OH-0.010 M Fc-0.100 M Fc^+ and n-InP/CH_3OH-0.010 M Fc-0.010 M Fc^+ contacts. In contrast to the behavior of the n-InP/CH_3OH interfaces described above, the n-InP/CH_3OH-$Fc^{+/0}$ junction showed a shift in its J-*E* properties of 120 mV vs. MSCE upon increasing the acceptor concentration by an order of magnitude. This shift was approximately twice as large as the ≈60 mV shift that was observed for the other redox systems (Figures 5.1-5.2), and is twice as large as that expected from the rate law of Equation 5.2. This J-*E* behavior indicated a shift in the band edge positions of the semiconductor as the Nernstian potential of the $Fc^{+/0}$ solution increased, and precluded a straightforward justification of the second-order rate law by variation of [A] with constant [A^-]. This band edge movement may arise from a number of sources, including surface state charging or carrier inversion, and does not necessarily indicate any adsorption of the Fc^+ ion on the electrode surface.

To minimize such band-edge shifts, the concentrations of Fc^+ and Fc were changed simultaneously but the [A]/[A^-] ratio was held fixed, so that Nernstian potential of the solution was held constant. To implement this process, part of a CH_3OH-1.00 M $LiClO_4$-0.010 M Fc-0.100 M Fc^+ solution was diluted with sufficient CH_3OH-1.00 M $LiClO_4$ to form a CH_3OH-1.00 M $LiClO_4$-0.0010 M Fc-0.010 M Fc^+ solution. This method is identical to the one used to prove second-order kinetics for the n-InP/CH_3OH-$PV^{2+/+\bullet}$ system (vide supra). Figure 5.4b shows the J-*E* behavior for an n-InP electrode in contact with each solution, and illustrates the 70 mV potential shift of the J-*E* behavior, relative to a MSCE reference, that was observed when this experimental protocol was used.

Impedance data were again used to obtain the energetics for the n-InP/CH_3OH-$Fc^{+/0}$ interface. Figures 5.4c and d display the impedance data for representative n-InP/CH_3OH-0.010 M Fc-0.100 M Fc^+ and n-InP/CH_3OH-0.010 M Fc-0.010 M Fc^+ contacts, respectively, in the form of Mott-Schottky plots. These C^{-2}-*E* plots showed little frequency dispersion and had slopes that were consistent with those computed from the

dopant density reported by the manufacturer of the InP samples. In addition, the built-in voltages of these two n-InP/CH_3OH-$Fc^{+/0}$ contacts were essentially indistinguishable from each other. This effect was observed for several different electrodes; in fact, the mean value of V_{bi} for the n-InP/CH_3OH-0.010 M Fc-0.100 M Fc^+ contact, V_{bi} = 0.78 V, was slightly lower than the mean value of V_{bi} = 0.81 V measured for the n-InP/CH_3OH-0.010 M Fc-0.010 M Fc^+ contact. The 120 mV shift observed in the J-*E* data when [Fc^+] was varied but [Fc] was held constant is thus readily understood in the context of the band edge movement revealed by the C^{-2}-*E* data. As displayed in Figures 5.4c-d, the built-in voltage of the more concentrated Fc^+ solution is lower than expected by ≈60 mV, due to a band edge shift that is consistent with prior studies of n-InP/nonaqueous liquid contacts having such positive Nernstian solution potentials.[3] This band edge movement results in an additional 60 mV shift in the J-*E* curves for these solutions relative to that expected from the rate law of Equation 5.2 assuming fixed band edge positions, thus resulting in the 120 mV shift in J-*E* behavior (vs. the MSCE reference) observed in Figure 5.4a.

With the energetics available from the impedance analysis, k_{et} could be computed for each n-InP/CH_3OH-$Fc^{+/0}$ solution from the combined analysis of C^{-2}-*E* and J-*E* data. For the n-InP/CH_3OH-0.010 M Fc-0.100 M Fc^+ contact, the average electron transfer rate constant was found to be $(5.3 \pm 3.2) \times 10^{-17}$ cm^4 s^{-1}, while for the n-InP/CH_3OH-0.010 M Fc-0.010 M Fc^+ contact, the average k_{et} value was $(1.6 \pm 1.1) \times 10^{-16}$ cm^4 s^{-1}. Table 1 summarizes the kinetic data for all of the InP/liquid contacts studied in this work.

Figure 5.4: Data for n-InP/CH_3OH-$Fc^{+/0}$ contacts. (a) J-*E* data for n-InP/CH_3OH-1.00 M $LiClO_4$-0.010 M Fc contacts having Fc^+ concentrations of: (i) 0.010 M ($E(A/A^-)$ = 0.350 V vs. MSCE), and (ii) 0.100 M ($E(A/A^-)$ = 0.407 V vs. MSCE). (b) ln J vs. *E* data for an n-InP/CH_3OH-1.00 M $LiClO_4$-0.010 M Fc-0.100 M Fc^+ contact (filled circles) and for an n-InP/CH_3OH-1.00 M $LiClO_4$-0.0010 M Fc-0.010 M Fc^+ contact (open circles). (c) Mott-Schottky plots for two ac measuring frequencies, 10 kHz (dashed line, open squares) and 100 kHz (solid line, filled circles), for an n-InP/CH_3OH-1.00 M $LiClO_4$-0.010 M Fc-0.010 M Fc^+ interface. The average dopant density extracted from the slopes of these lines was 8.1 x 10^{15} cm^{-3}. The built-in voltages, V_{bi}, are listed for each frequency. (d) Mott-Schottky plots for two ac measuring frequencies, 3.981 kHz (dashed line, filled circles) and 39.811 kHz (solid line, open circles), for an n-InP/CH_3OH-1.00 M $LiClO_4$-0.010 M Fc-0.100 M Fc^+ contact. The average dopant density extracted from the slopes of these lines was 8.2 x 10^{15} cm^{-3}.

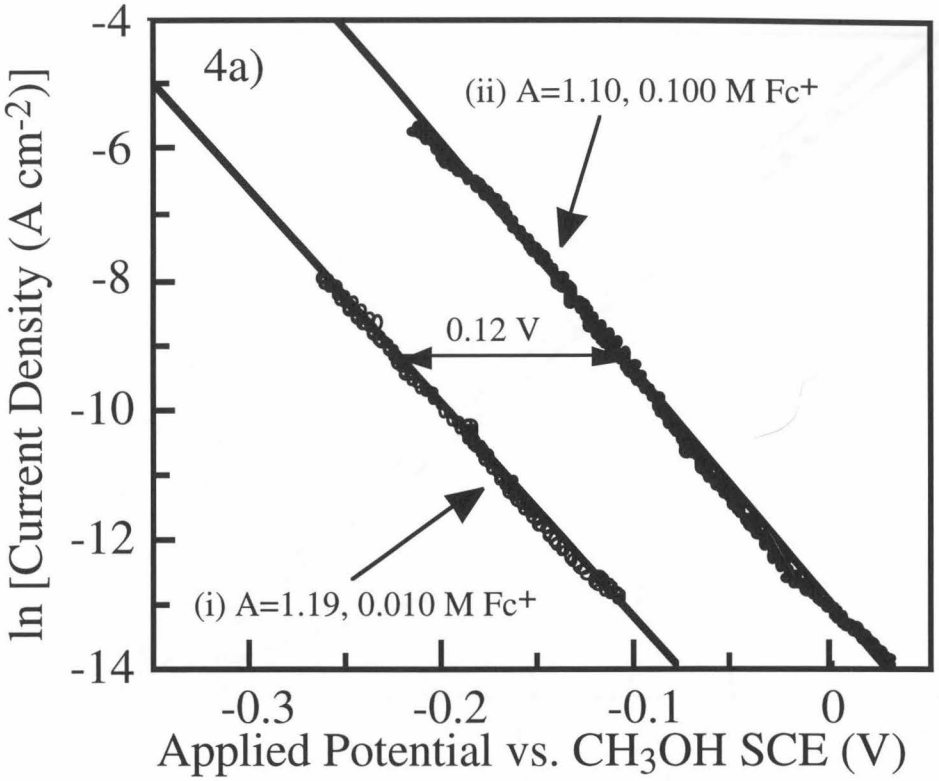
4a)
(ii) A=1.10, 0.100 M Fc+
0.12 V
(i) A=1.19, 0.010 M Fc+
ln [Current Density (A cm-2)]
-4
-6
-8
-10
-12
-14
-0.3
-0.2
-0.1
0
Applied Potential vs. CH3OH SCE (V)

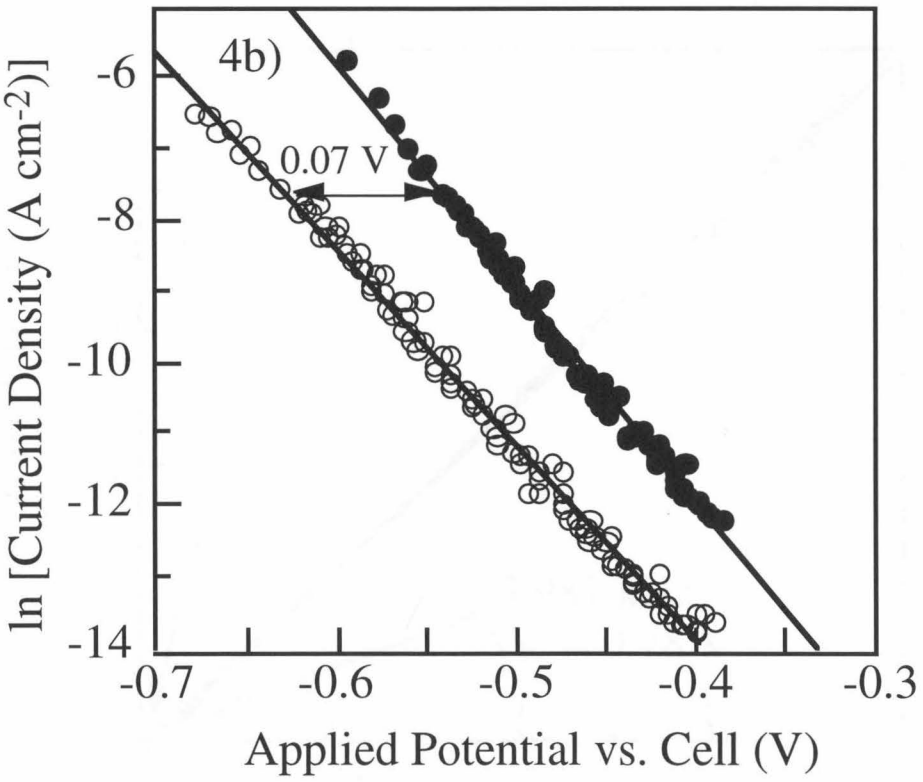
4b)
0.07 V
ln [Current Density (A cm-2)]
-6
-8
-10
-12
-14
-0.7
-0.6
-0.5
-0.4
-0.3
Applied Potential vs. Cell (V)

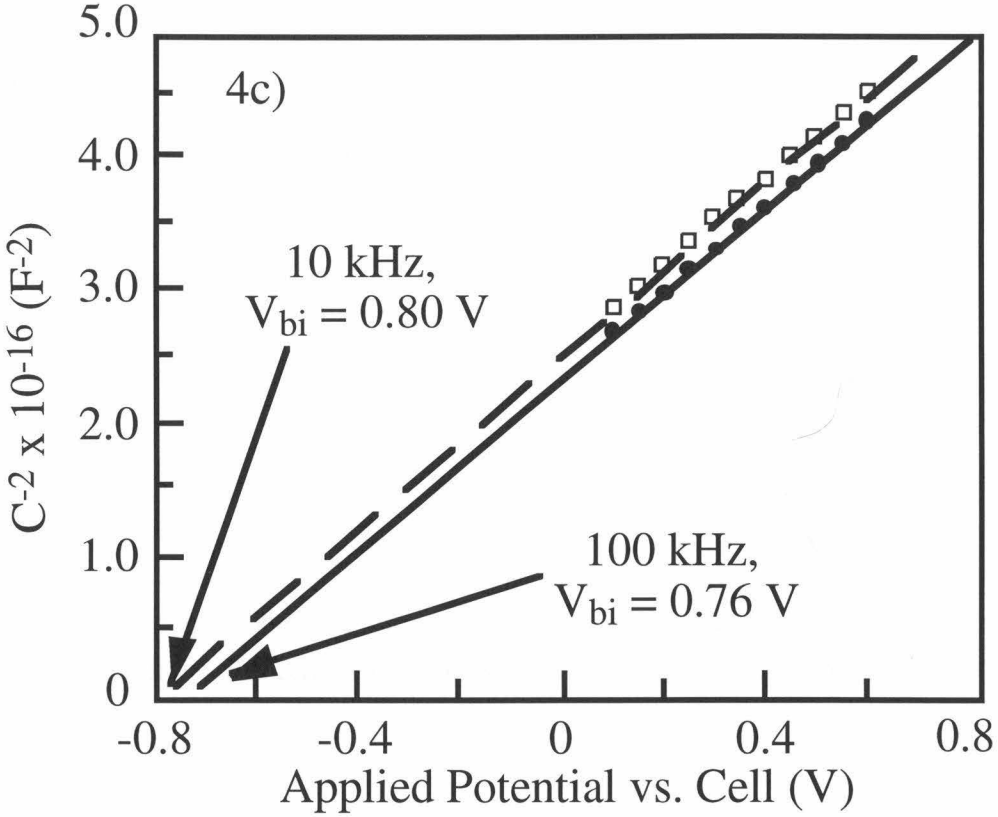
4c)
10 kHz,
V_{bi} = 0.80 V
100 kHz,
V_{bi} = 0.76 V
C^{-2} x 10^{-16} (F^{-2})
5.0
4.0
3.0
2.0
1.0
0
-0.8
-0.4
0
0.4
0.8
Applied Potential vs. Cell (V)

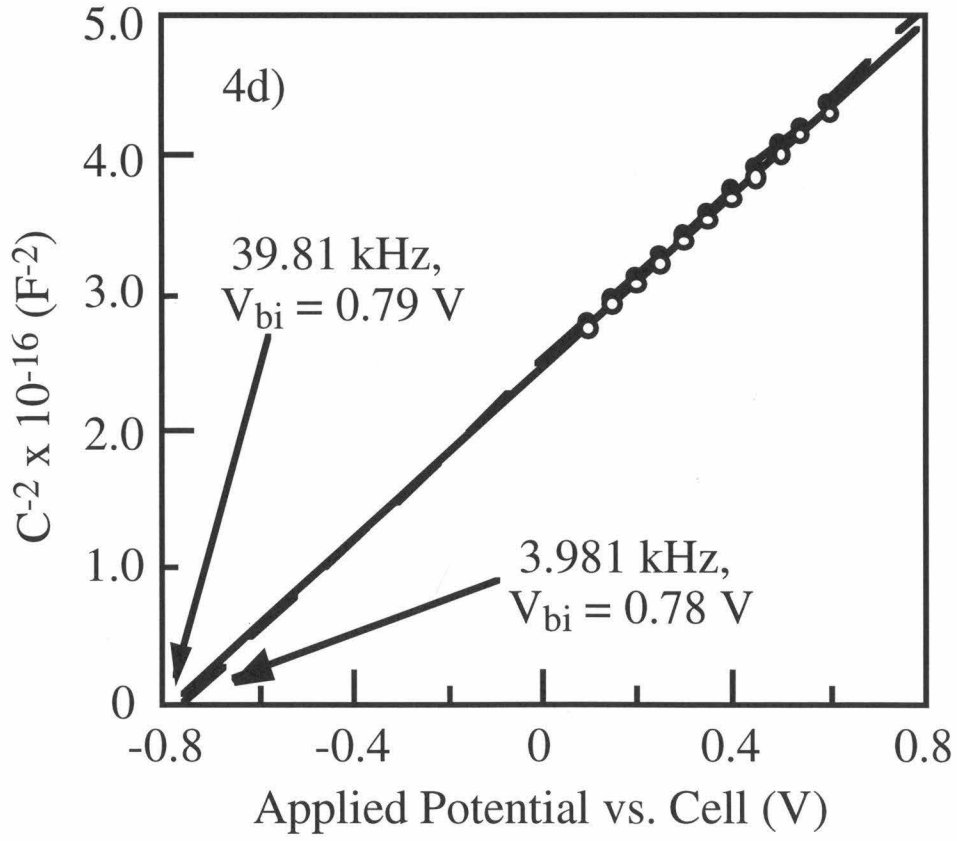
4d)
39.81 kHz,
V_{bi} = 0.79 V
3.981 kHz,
V_{bi} = 0.78 V
C^{-2} x 10^{-16} (F^{-2})
5.0
4.0
3.0
2.0
1.0
0
-0.8
-0.4
0
0.4
0.8
Applied Potential vs. Cell (V)

Table 5.1. Summary of electron transfer rate constants. Values listed for k_{et} are averages obtained for each redox couple at each electron acceptor concentration. The error present in each average is listed in the text.

Redox Couple	[A] (M)	k_{et} (cm^4 s^{-1})
$Me_2Fc^{+/0}$	0.100	8.5×10^{-17}
$Me_2Fc^{+/0}$	0.010	1.1×10^{-16}
$Me_{10}Fc^{+/0}$	0.025	5.3×10^{-17}
$PV^{2+/+\bullet}$	0.050	3.3×10^{-16}
$Fc^{+/0}$	0.100	5.3×10^{-17}
$Fc^{+/0}$	0.010	1.6×10^{-16}

Table 5.1

IV. Discussion

The most significant feature of the n-InP/liquid contacts discussed herein is that they exhibited not only nearly-ideal energetic but also nearly-ideal kinetic behavior. Ideal energetic behavior, in which the C^{-2}-*E* plots are well-behaved and the resulting band edge positions are invariant for a wide range of redox potentials, has been observed previously for some n-InP/CH_3CN contacts.[3] The above data document this behavior in detail for a series of outer-sphere redox couples and extend these observations to CH_3OH as the solvent. In addition, the n-InP contacts studied in this work exhibited nearly ideal kinetic behavior in that their current density-potential relationships were observed to obey the rate law behavior expected from Equation 5.2 for a simple interfacial electron transfer event acting as dominant recombination rate to produce current flow through the semiconductor/liquid interface. Such behavior has not been reported previously for a series of outer-sphere, one-electron redox couples at a semiconductor surface except in a very few cases,[27] yet this combination of behaviors is required in order to determine directly the values of the heterogeneous charge transfer rate constants for semiconductor electrodes from steady-state J-*E* data.

The ideal energetic behavior reported herein is significant in view of prior hypotheses that n-type InP surfaces exhibit Fermi level pinning in contact with nonaqueous electrolytes.[1,28] In the absence of Fermi-level pinning, the difference in the built-in voltage of two semiconductor/liquid junctions should be equal to the difference in the Nernstian potentials of the two electrolyte solutions. Figure 5.5 shows the built-in voltage as a function of $E(A/A^-)$ for the junctions examined in this work. The points define a straight line, with the exception of those for the CH_3OH-1.00 M $LiClO_4$-0.010 M Fc-0.100 M Fc^+ solution, where the junction is no longer sensitive to the cell potential, and the $Me_{10}Fc^{+/0}$ solution, where a different solvent system was used because of solubility constraints. Fitting the remaining points to a line yielded a slope of 1.1, indicating that these junctions behave nearly ideally over this potential range. Thus, for this series of contacts, the

equilibrium band bending and equilibrium electric field strength in the n-InP are not dominated by surface states, but instead respond completely to variation of the thermodynamic properties of the redox species in the liquid phase. This conclusion is in agreement with the photovoltage behavior of n-InP/CH_3CN contacts,[2] but contrasts with earlier, nonideal C^{-2}-E data that were interpreted within a complex equivalent circuit model to indicate nearly complete Fermi level pinning for n-type InP electrodes in contact wth CH_3CN solvent.[28] It also contrasts with the well-documented Fermi level pinning behavior of metal-semiconductor Schottky contacts formed on n-type InP surfaces.[29,30]

The kinetic behavior of these n-InP/CH_3OH contacts is also significant in the context of theoretical expectations for heterogeneous charge transfer rate constants at semiconductor/liquid interfaces. Since the $\Delta G^{o'}$ values for the reported contacts were between -0.4 and -0.9 eV, and the reorganization energies of the redox couples used in this work were ≈0.5-1.0 eV,[24-26] the value of k_{et} is expected to be dominated by the electronic terms of the rate constant expression, as opposed to the nuclear (Franck-Condon) factors. For example, for the $Me_{10}Fc^{+/0}$ redox couple, the reorganization energy is predicted to be about 0.80 eV,[26,31] while n-InP in contact with this redox system yielded $\Delta G^{o'}$ = -0.6 eV. Substituting these numbers into Equation 5.1 yields $\kappa_n = 0.52$, indicating k_{et} for this system is only expected to be about a factor of 2 lower than $k_{et,\,max}$. Performing a similar calculation for the n-InP/CH_3OH-$PV^{2+/+\bullet}$ system using $\lambda = 0.5$ eV[25,31] and $\Delta G^{o'} = 0.4$ eV yields $\kappa_n = 0.82$. The value of κ_{el} has been previously estimated to be 10^{-30} cm^4 for a typical semiconductor,[4,5] which yields a value of $k_{et,max} = 10^{-17}$ cm^4 s^{-1} at optimal exoergicity, assuming that $v_n = 10^{13}$ s^{-1}. The expectations for $k_{et,max}$ and κ_{el} are thus in excellent agreement with the kinetic behavior observed for the n-InP/liquid contacts investigated in this work.

Considering the theoretical prediction in more detail, the value of κ_{el} has been related to the Bohr radius of the electron in the solid. In this approach, the Bohr radius was taken as a qualitative measure of the delocalization length of the wavefunction for the

electron in the conduction band of the semiconductor. Due to the very low effective mass of electrons in the conduction band of n-InP,[14] the Bohr radius of electrons in InP is a factor of 10 larger than that of electrons in Si (or than that of carriers in most other common semiconductors),[32] so the existing model implies that the k_{et} values for n-InP/liquid contacts should be larger, by about an order of magnitude, than those for otherwise identical contacts using other types of semiconductor electrodes. This prediction seems to be borne out experimentally from the available data, because recent steady-state kinetic data obtained on n-type Si/CH_3OH interfaces has yielded $k_{et,max}$ values of $\approx 5 \times 10^{-17}$ cm^4 s^{-1} for a series of viologen acceptors.[27] Due to the significant error of these types of J-*E* and C^{-2}-*E* kinetic measurements at present, which limits the precision of the determination of $k_{et,max}$ to factors of 5-10, further work would be required to evaluate definitively any experimental relationship between the Bohr radius of the carrier in the solid and the charge transfer rate constant at the semiconductor/liquid contact. Nevertheless, the data available to date seem to be in qualitative agreement with this prediction of the model for interfacial charge transfer at semiconductor/liquid junctions.[4]

In summary, a combination of energetic and kinetic measurements has been used to determine values of the interfacial charge rate constants for a series of n-InP/liquid contacts. In all cases, the J-*E* behavior was in accord with the ideally expected rate law for interfacial charge transfer, being first order in the concentration of acceptors in the solution and first order in the concentration of electrons at the surface of the semiconductor. Mott-Schottky plots derived from impedance measurements were essentially independent of frequency, yielded the theoretically expected slopes, and produced reliable measurements of the built-in voltages and band edge positions of the solid/liquid contacts. The built-in voltages of n-InP/CH_3OH interfaces were found to be controlled by the Nernstian potential of the solution, indicating a lack of Fermi level pinning over most of the potential range investigated. Electron transfer rate constants for these semiconductor/liquid junctions were determined to be on the order of 10^{-17}-10^{-16} cm^4 s^{-1}. These values are in excellent

agreement with theoretical models available in the literature for such charge transfer processes. Taken together with upper limits on $k_{et,max}$ that have been established recently for a wide range of semiconductor/liquid junctions, these data therefore strongly support the theoretical prediction that optimally exoergic steady-state interfacial charge transfer rate constants are in the range 10^{-17}-10^{-16} cm^4 s^{-1} for semiconductor surfaces in contact with randomly dissolved, nonadsorbing, outer-sphere redox couples.

Figure 5.5: Dependence of the built-in voltage of n-InP electrodes on the Nernstian potential, $E(A/A^-)$, of various contacts having outer-sphere redox systems dissolved in the solution phase. The Nernstian potentials are referenced vs. SCE and differ from the MSCE values by 50.0 mV. The equation for the best fit line (omitting the point for $Me_{10}Fc^{+/0}$, which was obtained in a different solvent system) yields a slope of 1.09. Extrapolating the graph to V_{bi} = 0 V and correcting for the difference between the potential of the conduction band edge, E_{cb}, and the Fermi level in the semiconductor yields E_{cb} = -0.52 V relative to SCE. However, since the slope is not exactly 1.0, at higher built-in voltages the apparent conduction band edge position is slightly different; for example, taking the specific point determined for n-InP/CH_3OH--1.00 M $LiClO_4$-0.100 M Me_2Fc-0.100 M Me_2Fc^+ of V_{bi} = 0.69 V at $E(A/A^-)$ = 0.19 V vs. SCE, E_{cb} = -0.62 V.

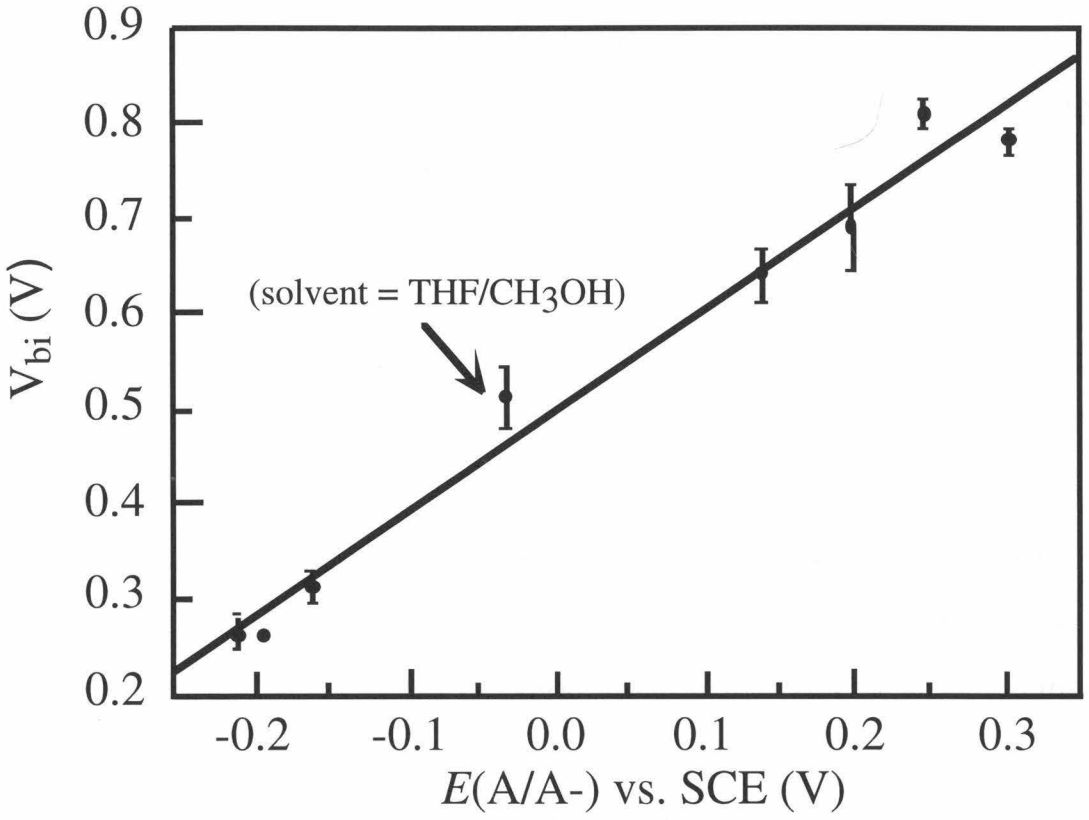
0.9
0.8
0.7
0.6
0.5
0.4
0.3
0.2
V_{bi} (V)
(solvent = THF/CH_3OH)
-0.2
-0.1
0.0
0.1
0.2
0.3
E(A/A-) vs. SCE (V)

Figure 5.5

V. References

(1) Dominey, R. N.; Lewis, N. S.; Wrighton, M. S. *J. Am. Chem. Soc.* **1981**, *103*, 1261.

(2) Heben, M. J.; Kumar, A.; Zheng, C.; Lewis, N. S. *Nature* **1989**, *340*, 621.

(3) Koval, C.; Austermann, R. *J. Electrochem. Soc.* **1985**, *132*, 2656.

(4) Lewis, N. S. *Ann. Rev. Phys. Chem.* **1991**, *42*, 543.

(5) Pomykal, K. E.; Fajardo, A. M.; Lewis, N. S. *J. Phys. Chem.* **1996**, *100*, 3652.

(6) Forbes, M. D. E.; Lewis, N. S. *J. Am. Chem. Soc.* **1990**, *112*, 3682.

(7) Howard, J. N.; Koval, C. A. *Anal. Chem.* **1994**, *66*, 4525.

(8) Rosenwaks, Y.; Thacker, B. R.; Nozik, A. J.; Ellingson, R. J.; Burr, K. C.; Tang, C. L. *J. Phys. Chem.* **1994**, *98*, 2739.

(9) Smith, B. B.; Nozik, A. J. *Chem. Phys.* **1996**, *205*, 47.

(10) Koval, C. A.; Howard, J. N. *Chem. Rev.* **1992**, *92*, 411.

(11) Horrocks, B. R.; Mirkin, M. V.; Bard, A. J. *J. Phys. Chem.* **1994**, *98*, 9106.

(12) Uhlendorf, I.; Reinekekoch, R.; Memming, R. *J. Phys. Chem.* **1996**, *100*, 4930.

(13) Morrison, S. R. *Electrochemistry at Semiconductor and Oxidized Metal Electrodes*; Plenum: New York, 1980.

(14) Sze, S. M. *The Physics of Semiconductor Devices;* 2nd ed.; Wiley: New York, 1981.

(15) Aspnes, D. E.; Studna, A. A. *Appl. Phys. Lett.* **1981**, *39*, 316.

(16) Hendrickson, D. H.; Sohn, Y. S.; Gray, H. B. *Inorg. Chem.* **1971**, *10*, 1559.

(17) Kamogawa, H.; Sato, S. *Bull. Chem. Soc. Jpn.* **1991**, *64*, 321.

(18) Pomykal, K. E.; Fajardo, A. M.; Lewis, N. S. *J. Phys. Chem.* **1995**, *99*, 8302.

(19) Bard, A. J.; Faulkner, L. R. *Electrochemical Methods: Fundamentals and Applications*; John Wiley & Sons: New York, 1980, pp 629.

(20) Tan, M. X.; Laibinis, P. E.; Nguyen, S. T.; Kesselman, J. M.; Stanton, C. E.; Lewis, N. S. *Prog. Inorg. Chem.* **1994**, *41*, 21.

(21) Rosenbluth, M. L.; Lewis, N. S. *J. Phys. Chem.* **1989**, *93*, 3735.

(22) The observed current at the semiconductor interface is given by the sum of the currents for all possible processes. Since the diode quality factor, A, appears in the denominator of the exponential in Equation 6, at sufficiently large potentials a process with a smaller value of A can dominate the total interfacial flux even if the exchange current density, J_o, is larger for other parallel kinetic processes having larger A values.

(23) The cell potential was 20 mV vs. MSCE, nearly 200 mV more negative than that of the $Me_2Fc^{+/0}$ system, but the built-in voltage was only 150 mV smaller for the n-InP/CH_3OH-THF-$Me_{10}Fc^{+/0}$ contact than for the n-InP/CH_3OH-$Me_2Fc^{+/0}$ contact. This is likely due to the slight difference in the apparent band edge positions between the two different solvent systems that were required for these measurements.

(24) Yang, E. S.; Chan, M.; Wahl, A. C. *J. Phys. Chem.* **1975**, *79*, 2049.

(25) Dai, S. Thesis, University of Tennessee, 1990.

(26) Nielson, R. M.; McManis, G. E.; Safford, L. K.; Weaver, M. J. *J. Phys. Chem.* **1989**, *93*, 2152. In this work, the self-exchange rate constant, k_{se}, for $Me_{10}Fc^{+/0}$ was not reported in methanol. However, k_{se} for $Fc^{+/0}$ was reported in methanol as well as in some solvents for which k_{se} for $Me_{10}Fc^{+/0}$ was also reported. In most cases, k_{se} of $Me_{10}Fc^{+/0}$ exceeded that of $Fc^{+/0}$ by about a factor of three. To arrive at a reorganization energy for $Me_{10}Fc^{+/0}$ in methanol, k_{se} of $Fc^{+/0}$ in methanol was multiplied by three and converted to a reorganization energy by the equation: $k_{se} = Z_{bi}\, e^{-(\lambda/4kT)}$ where $Z_{bi} \approx 10^{11}$ $M^{-1}\, s^{-1}$ is the normal collisional vibration frequency for bimolecular reactions at room temperature.[31]

(27) Fajardo, A. M.; Lewis, N. S. *Science* **1996**, *274*, 969.

(28) Nagasubramanian, G.; Wheeler, B. L.; Bard, A. J. *J. Electrochem. Soc.* **1983**, *130*, 1680.

(29) Mead, C. A.; Spitzer, W. G. *Phys. Rev.* **1964**, *134*, A713.

(30) Newman, N.; Kendelewicz, T.; Bowman, L.; Spicer, W. E. *Appl. Phys. Lett.* **1985**, *46*, 1176.

(31) Marcus, R. A. *J. Phys. Chem.* **1963**, *67*, 853.

(32) Ibach, H.; Luth, H. *Solid-State Physics*; Springer Verlag: Berlin, 1990.